

UNIVERSITÉ DE REIMS CHAMPAGNE-ARDENNE

ÉCOLE DOCTORALE SCIENCES FONDAMENTALES - SANTÉ N°619

# THÈSE EN CO-TUTELLE

Pour obtenir le grade de

DOCTEUR DE L'UNIVERSITÉ DE REIMS CHAMPAGNE-ARDENNE

*Discipline : SCIENCES DE LA VIE ET DE LA SANTE*

*Spécialité : La biophysique*

*Et*

DOCTEUR DE L'UNIVERSITÉ DE CENTRAL LANCASHIRE

*Spécialité : Les sciences bioanalytiques*

Présentée et soutenue à huis clos par

**SHAWN HUSSAIN**

Le 22 mars 2019

---

## Développement de méthodes biophotoniques appliquées aux biofluides pour le diagnostic rapide et non-invasif du cancer

---

Thèse dirigée par **Dr. ALLISON E JONES**, Université de Central Lancashire

Et par **Dr. MATTHEW J BAKER**, Université de Strathclyde

Thèse dirigée par **Pr. GANESH D SOCKALINGUM**, Université de Reims Champagne-Ardenne

### JURY

M. Chris SAMMON	Professeur,	Université de Sheffield Hallam	<b>Rapporteur</b>
M. Ludovic DUPONCHEL	Professeur,	Université de Lille	<b>Rapporteur</b>
M. Kamalinder SINGH	Professeur	Université de Central Lancashire	<b>Examineur</b>
M. Frederic VELARD	Ingenieur de recherche HDR,	Université de Reims Champagne-Ardenne	<b>Examineur</b>

---

## **Développement de méthodes biophotoniques appliquées aux biofluides pour le diagnostic rapide et non-invasif du cancer**

---

La spectroscopie vibrationnelle englobe les techniques optiques spécifiques de la spectroscopie infrarouge à transformée de Fourier (IRTF) et Raman (RS). Ces techniques sondent les vibrations moléculaires de l'échantillon lorsque la lumière interagit avec celui-ci, ce qui représente des 'empreintes moléculaires' de la composition chimique globale. Les deux techniques sont très prometteuses pour le diagnostic en santé, notamment dans le cadre des 'biopsies liquides', en particulier les biofluides. Cette étude a porté sur le développement des méthodologies bio-spectroscopiques pour l'analyse biochimique du sérum à visée diagnostic rapide et détection de pathologies. Le but était double. i) développer des méthodologies IRTF et RS pour étudier les variations pré-analytiques du sérum et ii) utiliser l'approche RS liquide couplée à une analyse chimiométrique pour évaluer le potentiel diagnostique sur des cas réels de données patients. Au-delà de la preuve-de-concept et des études sur les variations préanalytiques (qui n'ont montré aucun effet sur le profil spectral sérique) par la congélation/décongélation du sérum et le séchage en milieu ambiant, trois études diagnostiques ont été menées sur des sérums provenant de patients avec différentes pathologies : cirrhotiques avec ou sans un carcinome hépatocellulaire, différents stades de fibrose et différents stades de tumeurs cérébrales. Tout au long de cette thèse, une série de techniques spectroscopiques IRTF et Raman ont été développées/utilisées, telles que l'ATR, et IRTF à haut débit spectroscopie et Raman sur sérums humains séchés et liquides. Des approches chimiométriques avancées ont été utilisées telles que cluster (PCA, HCA), partial least squares, linear discriminant analysis avancé, support vector machine with leave-one-out cross validation avec fonction de base radiale et classifieurs random forest, avec pour but de développer un classificateur robuste de diagnostic d'une pathologie. Dans toutes les études de diagnostic, les résultats ont montré une capacité diagnostique modérée à bonne. Ces travaux démontrent que la spectroscopie vibrationnelle associée à des méthodes chimiométriques avancées peut constituer une approche complémentaire pour le diagnostic clinique, tels que les zones de soins.

---

Mots-clés : Spectroscopie vibrationnelle ; biofluides, cancer ; diagnostique ; technologie point-of-care

---

### **Developing biophotonic techniques for the rapid and non-invasive diagnosis of cancer from biofluids**

---

Vibrational spectroscopy relates to the specific optical techniques of Fourier-transform infrared (FTIR) and Raman spectroscopy (RS). These techniques probe molecular vibrations of the sample when light interacts with it, which present 'fingerprints' of the global chemical composition. Both techniques hold great promise in disease diagnostics, especially with 'liquid biopsies' for biofluids. This study developed bio-spectroscopic methodologies to query the serum biochemistry towards rapid diagnosis and detection of diseases. The aim was two-fold; i) to develop FTIR and RS methodologies to analyse sera for pre-analytical variation. Secondly, to use liquid RS combined with chemometric analysis to interpret pathological data for its diagnostic potential. Beyond the proof-of-concept, with investigations into preanalytical variations (which proved no effect is seen on the serum profile) *via* serum freeze-thawing and environmental drying, three diagnostic studies were sought; from patient cases, *i.e.* cirrhotic sera with and without hepatocellular carcinoma, sera with different levels of fibrosis, and with varying stages of brain tumours. Throughout the thesis, a suite of FTIR and Raman spectroscopy techniques were developed/employed, such as attenuated total reflectance, high throughput FTIR, and Raman spectroscopy on liquid and dried human sera. Advanced chemometric approaches were employed such as clustering (PCA, HCA), partial least squares, and forward linear discriminant analysis, radial basis function support vector machine with leave-one-out cross validation, random forest classifiers, all towards developing a robust disease classifier. Across all diagnostic studies, results showed moderate-to-good diagnostic abilities. It was shown that vibrational spectroscopy combined with advanced chemometric methods can provide a good adjunct to clinical screening settings, such as point-of-care areas.

---

Keywords : Vibrational spectroscopy ; biofluids; cancer ; diagnostics ; point-of-care technology

---

**Discipline : SCIENCES DE LA VIE ET DE LA SANTE**

---

**Spécialité : La Biophysique**

---

Université de Reims Champagne-Ardenne  
Biospectroscopie Translationnelle : BioSpecT  
51 rue Cognacq-Jay, 51096 Reims Cedex, France

---

## **DEDICATION**

This thesis is dedicated to my life partner and soulmate Paul, for his indubitable enthusiasm, kind heart and emotional support and patience throughout all my wants, needs and desires, whether it be the biggest decision in my life to quit my well-paying job and live like an eternal student, again...

To my late parents, Christine and Imtiaz, brothers, Adam and Carl, and my niece and nephew, Phoebe and Lewis, for their downtimes and family fun.

Mum and Dad, this is for you!

## STUDENT DECLARATION

### Concurrent registration for two or more academic awards

I declare that while registered for the research degree, I was with the University's specific permission, a registered candidate for the following award:

*Doctor of Philosophy* at the Universite de Reims, Champagne-Ardenne, France.

### Material submitted for another award

I declare that no material contained in the thesis has been used in any other submission for an academic award and is solely my own work.

### Collaboration

Where a candidate's research programme is part of a collaborative project, the thesis must indicate in addition clearly the candidate's contribution and the extent of the collaboration. Please state below:

**Signature of Candidate:**



**Type of Award:** Doctor of Philosophy (FR)

**School :** Ecole Doctorale Sciences Technologie et Santé

# TABLE OF CONTENTS

## TABLE DES MATIERES

RESUME	2
DEDICATION	3
STUDENT DECLARATION	4
TABLE OF CONTENTS /TABLE DES MATIÈRES	5
ABBREVIATIONS AND SYMBOLS	12
ACKNOWLEDGEMENTS / REMERCIEMENTS	14
<b>CHAPTER 1: GENERAL INTRODUCTION</b>	<b>15</b>
<b>CHAPITRE I: INTRODUCTION GÉNÉRALE</b>	<b>15</b>
<i>Vibrational Spectroscopy Fundamentals</i>	15
I.1 RÉSUMÉ	16
I.1.1 Principes fondamentaux de la spectroscopie vibrationnelle	16
I.1.1-1 La spectroscopie infrarouge	17
I.1.1-2 La spectroscopie Raman	17
I.1.2 Biofluides et marqueurs de maladies	18
I.1.2-1 Cancer	19
I.1.2-2 Fibrose et cirrhose hépatique, carcinome hépatocellulaire et gliomes	20
I.1.3 Objectifs de l'étude	22
<b>CHAPTER OVERVIEW</b>	<b>23</b>
1.1 INTRODUCTION TO ELECTROMAGNETIC RADIATION	23
1.2. PRINCIPLES OF VIBRATIONAL SPECTROSCOPY	26
1.2.1 Infrared Spectroscopy	26
1.2.1.1 IR Selection Rule	26
1.2.2 Raman Spectroscopy	26
1.2.2.1 Raman Selection Rule	27
1.2.3 Fundamental Molecular Vibrations	27
1.2.3.1 Normal Modes and Bond Vibrations	30
1.2.3.2 Complementarity of Infrared and Raman Spectroscopy	31
1.3. PRINCIPLES OF SPECTROSCOPIC INSTRUMENTATION	33
1.3.1 FTIR Spectroscopic Instrumentation	33
1.3.1.1 Michelson Interferometer	33
1.3.1.2 FTIR Sampling Modalities	35
1.3.1.2.1 Transmission mode	37
1.3.1.2.2 Transflection mode	38
1.3.1.2.3 ATR mode	38
1.3.1.2.3.1 Principles of ATR	38
1.3.2 Raman Spectroscopic Instrumentation	39
1.3.2.1 Instrument Components	40
1.4. SIGNAL PRE-PROCESSING & QUALITY ASSESSMENT	43
1.4.1 Wavelength Truncation	43
1.4.2 Normalisation	44

1.4.2.1	Vector Normalisation	44
1.4.2.2	Standard Normal Variance	44
1.4.2.3	Offset Scale Correction	45
1.4.3	FTIR Spectral Quality	45
1.4.3.1	FTIR Spectral Quality Assessment	45
1.4.3.2	FTIR Baseline Correction	46
1.4.3.2.1	Rubber-band Correction	46
1.4.3.2.2	Extended Multiplicative Signal Correction (EMSC)	46
1.4.4	Raman Spectral Quality	47
1.4.4.1	Raman Spectral Quality Assessment	47
1.4.4.2	Wavelength/Intensity Calibrations and CCD Checks	47
1.4.4.3	Raman Baseline Correction	48
1.5.	CHEMOMETRICS FOR SPECTROSCOPY	49
1.5.1	Principal Component Analysis (PCA)	49
1.5.2	Hierarchical Cluster Analysis (HCA)	51
1.5.3	K means Cluster Analysis (KM)	52
1.5.4	Principal Component - Discriminant Function Analysis (PC-DFA)	53
1.5.5	Support Vector Machine (SVM)	54
1.5.6	Random Forest Classifiers (RF)	56
	<u>Introduction to Clinical Biospectroscopy</u>	58
1.6.	BIOMEDICAL VIBRATIONAL SPECTROSCOPY	58
1.7.	BIOFLUIDS AND DISEASE	58
1.7.1	Biofluids and Disease Markers	59
1.8.	CANCER	59
1.8.1	Cancer Prevalence, Survival and Mortality	59
1.8.2	Cancer Biology	60
1.8.3	Hallmarks of Cancer	61
1.9.	LIVER DISEASE & PRIMARY LIVER CANCER	62
1.9.1	Hepatic Fibrosis and Cirrhosis	62
1.9.2	Hepatocellular Carcinoma (HCC)	64
1.9.2.1	Hepatocarcinogenesis	64
1.9.2.2	HCC Tumour Staging	65
1.10.	PRIMARY BRAIN TUMOURS	66
1.10.1	Tumour Classification and Grading	67
1.11.	CURRENT CLINICAL VIBRATIONAL SPECTROSCOPY	69
1.11.1	Clinical Infrared Biofluid Spectroscopy	69
1.11.2	Clinical Raman Biofluid Spectroscopy	71
1.12.	SUMMARY, WORKING HYPOTHESIS, MAIN AIMS & OBJECTIVES	73
1.12.1	Summary	73

1.12.2 Working Hypothesis	73
1.12.3 Main Aim	73
1.12.4 Specific Aims & Objectives	73
<b>CHAPTER 2: EXPERIMENTAL METHODS &amp; INSTRUMENTATION</b>	<b>74</b>
<b>CHAPITRE II: METHODES EXPERIMENTALES ET INSTRUMENTATION</b>	<b>74</b>
<b>II.1 RÉSUMÉ</b>	<b>75</b>
2.1. CHAPTER OVERVIEW	75
2.2. SPECTRAL METHOD DEVELOPMENT & SERUM ANALYSIS	77
2.2.1 FTIR Spectrometers	77
2.2.1.1 Agilent Cary 670 FTIR Spectrometer	77
2.2.1.1.1 ATR-FTIR Serum Approach	77
2.2.1.1.2 Transmission FTIR Serum Approach	78
2.2.1.2 Bruker FTIR-HTS Tensor 27 Spectrometer	79
2.2.1.2.1 High Throughput Transmission (HT) FTIR Serum Approach	79
2.2.1.3 Perkin Elmer Spotlight 400 FTIR Spectroscopic Imaging System	80
2.2.1.3.1 FTIR Microspectroscopy of Dried Serum Drops	80
2.2.1.3.2 FTIR Imaging of Dried Serum Drops	80
2.2.2 Raman Spectrometers	81
2.2.2.1 Horiba Jobin-Yvon LabRAM HR800 Microspectrometer	82
2.2.2.1.1 Raman Microspectroscopy for Dried Serum Analysis	82
2.2.2.2 Horiba Jobin-Yvon LabRAM ARAMIS Microspectrometer	82
2.2.2.2.1 Raman Microspectroscopy for Liquid & Dried Serum	84
2.2.2.3 Horiba Jobin-Yvon LabRAM 1 Microspectrometer	84
2.2.2.3.1 Dried Centre and Periphery Measurements and Liquid Analysis	87
2.2.2.4 Horiba Jobin-Yvon LabRAM HR300 Spectrometer	87
2.2.2.4.1 Macro Liquid Raman Serum Analysis	88
2.2.2.5 Horiba Jobin-Yvon HE Raman Spectrograph & Fibreoptic Raman Probe	89
2.2.2.5.1 Fibreoptic Raman Serum Measurements	90
2.3. SPECTRAL QUALITY & VARIANCE ASSESSMENTS	91
2.3.1 Spectral Quality Testing	92
2.3.2 Variance Analysis	92
2.3.3 Statistical Data Analysis	95
2.4. FTIR & RAMAN SERUM DIAGNOSTIC APPLICATIONS	96
2.4.1 FTIR Serum Diagnostics	96
2.4.1.1 Patient Sera for HT-FTIR Spectroscopy	97
2.4.1.1.1 Hepatic Fibrosis Patient Biobank	97
2.4.1.1.2 BTNW Patient Biobank	97
2.4.2 Raman Serum Diagnostics	98
2.4.2.1 Patient Sera for Liquid Macro Raman Spectroscopy	98

<b>CHAPTER 3: FTIR SERUM SPECTROSCOPY SAMPLE STABILITY &amp; DIAGNOSTIC APPLICATIONS</b>	<b>100</b>
<b>CHAPITRE III: SPECTROSCOPIE IRTF SERIQUE, STABILITE DES ECHANTILLONS, APPLICATIONS DIAGNOSTIQUES</b>	<b>100</b>
III.1 RÉSUMÉ	101
III.2 CONCLUSION	101
<hr/>	
3.1 INTRODUCTION	104
3.1.1 Introduction to Hepatic Fibrosis	105
3.1.2 Introduction to Gliomas	106
3.2 MATERIALS & METHODS	107
3.2.1 Serum Samples	107
3.2.2 Preanalytical Variation Studies	107
3.2.2.1 ATR-FTIR Serum Analysis	108
3.2.2.2 HT-FTIR Serum Analysis	108
3.2.2.3 FTIR Transmission Microspectroscopy Serum Analysis	108
3.2.3 Diagnostic Screening Studies	109
3.2.3.1 Diagnostic HT-FTIR Spectroscopy	110
3.2.4 Spectral Quality Testing and Variance Analysis	110
3.2.5 Spectral Pre-processing & MVA Strategies	111
3.2.5.1 Pre-processing Strategies	111
3.2.5.2 MVA Strategies	111
3.3 RESULTS & DISCUSSION	112
3.3.1 Freeze-Thaw Study	112
3.3.1.1 ATR-FTIR Spectral Variance	112
3.3.1.2 ATR-FTIR Principal Component Analysis	113
3.3.1.3 HT-FTIR Spectral Variance	117
3.3.1.4 HT-FTIR Principal Component Analysis	118
3.3.2 Environmental Drying Study	121
3.3.2.1 FTIR Spectral Variance	121
3.3.2.2 Principal Component Analysis	124
3.3.3 Diagnostic Serum Fibrosis Study	128
3.3.3.1 Serum Fibrosis Spectral Variance	128
3.3.3.2 Serum Fibrosis Principal Component Analysis	130
3.3.3.3 Serum Fibrosis Discriminant Function Analysis	132
3.3.4 Diagnostic Serum Glioma Study	133
3.3.4.1 Serum Glioma Spectral Variance	133
3.3.4.2 Serum Glioma Principal Component Analysis	135
3.3.4.3 Serum Glioma Discriminant Function Analysis	137
3.4 CONCLUSION	139
<hr/>	

<b>CHAPTER 4: RAMAN SERUM SPECTROSCOPY SAMPLE STABILITY AND LIQUID DIAGNOSTIC APPLICATION</b>	<b>142</b>
<b>CHAPITRE IV: SPECTROSCOPIE RAMAN DU SERUM, STABILITE DES ECHANTILLON ET APPLICATION AU DIAGNOSTIC EN PHASE LIQUIDE</b>	<b>142</b>
IV.1 RÉSUMÉ	143
IV.2 CONCLUSION	143
4.1 INTRODUCTION	145
4.2. MATERIALS & METHODS	147
4.2.1 Serum Samples	147
4.2.2 Preanalytical Variation Studies	147
4.2.2.1 Freeze-Thaw Cycles (FTC)	147
4.2.2.2 Environmental Air-Drying (ED)	148
4.2.3 Raman Spectroscopic Optimisation and Calibrations	148
4.2.4 Raman Microscopic DCDD Serum Analysis	149
4.2.4.1 Instrument 1: LabRAM HR800	150
4.2.4.2 Instrument 2: LabRAM ARAMIS	150
4.2.4.3 Instrument 3: LabRAM 1	151
4.2.4.3.1 Drop Dried Spatial Distribution: Centre <i>versus</i> Periphery Study	151
4.2.4.3.2 Macroscopic Liquid Serum Development	151
4.2.4.4 Instrument 4: LabRAM HR300	152
4.2.5 Macroscopic Diagnostic Liquid Raman	152
4.2.6 Spectral Pre-processing and MVA Strategies	154
4.2.6.1 Pre-processing Strategies	154
4.2.6.2 MVA Strategies	154
4.3. RESULTS & DISCUSSION	154
4.3.1 Serum Sampling Observations	154
4.3.2 Raman Spectral Variance	155
4.3.3 Instrument 1 Results	157
4.3.3.1 Principal Component Analysis	157
4.3.4 Instrument 2 Results	159
4.3.4.1 Principal Component Analysis	159
4.3.5 Instrument 3 Results	161
4.3.5.1 Instrument 3: Centre vs. Periphery Study	161
4.3.6 Environmental Air Drying	166
4.3.6.1 Principal Component Analysis	170
4.3.7 Preanalytical Variation Discussion	171
4.3.8 Liquid Serum Raman Fibrosis Study	173
4.3.8.1 Spectral Variance Analysis	173
4.3.8.2 Principal Component Analysis	175
4.3.8.3 Discriminant Function Analysis	176
4.3.8.4 Random Forest Classifiers & RBF-SVM	178

4.3.8.4 Forward Linear Discriminant Analysis	180
4.4 CONCLUSION	183
<hr/>	
<b>CHAPTER 5: SPECTROSCOPIC SCREENING OF HCC FROM CIRRHOTIC PATIENTS VIA MACRO RAMAN ANALYSIS OF LIQUID PATIENT SERUM</b>	<b>185</b>
<b>CHAPITRE V: DÉPISTAGE PAR ANALY SPECTROSCOPIQUE MACRO-RAMAN DU SERUM LIQUIDE DE PATIENTS CIRRHOTIQUES ATTIENT D'UN CHC</b>	<b>185</b>
V.1 RÉSUMÉ	186
V.2 CONCLUSIONS	186
<hr/>	
5.1 INTRODUCTION	187
5.2 EXPERIMENTAL METHODOLOGY	190
5.2.1 Serum Biobank	190
5.2.2 Sample Processing	190
5.2.3 Macro Liquid Raman Spectroscopy	191
5.2.4 Raman Spectral Quality Testing	192
5.2.5 Spectral Pre-processing and Chemometrics	192
5.2.6 MVA Workflow	193
5.3 RESULTS & DISCUSSION	193
5.3.1 Spectral Quality & Variance Study	193
5.3.2 Explorative PCA of Cirrhotic, HCC and F0 Patients	198
5.3.3 DFA: Semi-supervised Data Analysis	201
5.3.4 PC-DFA: Supervised Cluster Analysis	205
5.3.5 Supervised Machine Learning: RF and SVM	208
5.4 CONCLUSIONS	211
<hr/>	
<b>CHAPTER 6: GENERAL CONCLUSION &amp; PERSPECTIVES</b>	<b>212</b>
<b>CHAPITRE VI: CONCLUSION GÉNÉRALE ET PERSPECTIVES</b>	<b>212</b>
VI.1 RÉSUMÉ	213
VI.2 CONCLUSION : La portée des études futures	213
<hr/>	
6.1 THESIS CONCLUSION	214
6.2 SCOPE FOR FUTURE STUDIES	218
<hr/>	
<b>REFERENCES</b>	<b>219</b>
<b>PRESENTATIONS AND PUBLICATION</b>	<b>231</b>
<b>Poster</b> - Freeze-thaw Sample Preparation for use in Vibrational Biospectroscopy: Proof of Principle Study for Serum Stability and Kinetics, Windermere, UK	232
<b>Poster</b> - Serum Spectroscopy: Freeze-Thaw and Drying Sample Preparation, Exeter University, UK	233
<b>Poster</b> - A Spectroscopic Investigation of Liver Fibrosis <i>via</i> a Liquid Macro Raman Approach, CLIRCON17, Manchester University, UK, Raman4Clinics, Castelldefels, Spain	234
<b>Poster</b> -Monitoring the Effects of Freeze-thaw Liquid and Dried Drop Serum by Micro-Raman Spectroscopy, SPEC Conference 2016, Montreal, Canada	234

**Publication** - Developing and understanding biofluid vibrational spectroscopy:  
a critical review. *Chem. Soc. Rev.*, 2016, 45, 1803-1818

236

# ABBREVIATIONS & SYMBOLS

## General

ATR	Attenuated Total Reflection
ATR-FTIR	Attenuated Total Reflection-Fourier Transform Infrared
BTNW	Brain Tumour North West
Cost	Cost ( <i>C</i> )
CNS	Central Nervous System
CT	Computed Tomography
CV	Cross Validation
Di	Diamond
DNA	Deoxyribonucleic Acid
DTGS	Deuterated Triglycine Sulphate
EM	Electromagnetic
EMR	Electromagnetic Radiation
EtOH	Ethanol
F	Female
FIR	Far-Infrared
GA	Genetic Algorithm
GA-SVM	Genetic Algorithm-Support Vector Machine
Ge	Germanium
GBM	Glioblastoma Multiforme
GUI	Graphic User Interface
HCC	Hepatocellular Carcinoma
HGG	High-grade Glioma
HT	Hight-throughput Screening
HT-FTIR	Hight-throughput-Fourier Transform Infrared Spectroscopy
IR	Infrared
IRE	Internal Reflection Element
LGG	Low-grade Glioma
M	Male
MCT	Mercury Cadmium Telluride
MRI	Magnetic Resonance Imaging
MIR	Mid-Infrared
MVA	Multivariate Analysis
NHS	National Health Service
NICE	National Institute of Health and Care Excellence

NIR	Near-Infrared
NR	Noise Reduction
OPD	Optical Path Difference
PC(s)	Principal Component(s)
PCA	Principal Component Analysis
PCD	Programmed Cell Death
PET	Positron Emission Tomography
QCL	Quantum Cascade Laser
RBF	Radial Basis Function
RBF-SVM	Radial Basis Function-Support Vector Machine
RI	Refractive Index
RMS	Root Mean Square
Se	Sensitivity
Sp	Specificity
STD/RSD	Standard Deviation/Relative Standard Deviation
SNR	Signal-Noise Ratio
SVM	Support Vector Machine
UK	United Kingdom
VN	Vector Normalisation
WHO	World Health Organisation
W	Wavenumber ( $\nu/\text{cm}^{-1}$ )

## Symbols

$\lambda$	Gamma
$\lambda_{\text{em}}$	Emission wavelength/ nm
$\lambda_{\text{ex}}$	Excitation wavelength/ nm
$\lambda_{\text{max}}$	Wavelength of maximum absorbance or emission/ nm

## Constants

c	Speed of light, $2.998 \times 10^8 \text{ ms}^{-1}$
h	Planck constant, $6.626 \times 10^{-34} \text{ Js}^{-1}$

## ACKNOWLEDGEMENTS / REMERCIEMENTS

*C'est avec grand plaisir que je saisis cette occasion pour exprimer mes sincères remerciements à de nombreuses personnes qui ont rendu cette thèse possible. Ce travail n'aurait pas été possible sans le soutien financier de l'Université de Central Lancashire à Preston, Grande Bretagne, de l'Université de Reims Champagne-Ardenne à Reims et du Conseil Régional de Champagne-Ardenne, France. Mes remerciements vont également aux deux laboratoires qui m'ont accueilli pendant cette thèse ainsi qu'à leurs personnels. Je suis reconnaissant à tous ceux avec qui j'ai eu le plaisir de travailler pendant ce projet et d'autres projets associés, y compris les deux groupes de recherche ici et de l'autre côté de la Manche.*

I would like to thank both Dr. Matthew Baker and Professor Ganesh Sockalingum for choosing me to conduct this research and for changing my life's course back in 2014.

Special thanks go to Dr. Allison Jones for all the support and guidance throughout my research career. It is because of you I was able to visit new parts of the world to present my research at colloquia's. I would especially like to thank Professor Jaipaul Singh for being supportive and available in my hours of need. Thank you for taking me on as my DoS at the last minute. His guidance helped me in the times of writing of this thesis.

Finally, to my honorary Northern family, June and Colin for putting up with me and my literal 'skeletons'. Thank you for accepting me in to your home, I hope your life has been enriched just as much as mine for your presence.

*Mon séjour à Reims a été une longue période d'apprentissage et je voudrais remercier le Professeur Gérard Thiéfin pour ses conseils et pour avoir fourni des échantillons pour cette recherche. Mention spéciale à mes collègues de bureau et de chambre à Reims: Dr Louis Lao Honghui (Louis), Dr Nathalie Mainreck, Dr Que Nguyen - merci de m'avoir accueilli en France et de m'avoir laissé de bons souvenirs. Une mention spéciale au Dr. Dominique Bertrand pour son soutien technique et son expertise pour certaines méthodes chimométriques avancées d'analyse de données.*

Nobody has been more important to me in the pursuit of this project than the members of my family. I would like to thank my late parents; whose love and guidance are with me in whatever I pursue. They are both the ultimate role models. Most importantly, I wish to thank my loving and supportive partner Paul, who allows me to be the person I am today. Thank you!

**| CHAPTER 1 |**

**GENERAL  
INTRODUCTION**

---

**| CHAPITRE I |**

**INTRODUCTION  
GÉNÉRALE**

# VIBRATIONAL SPECTROSCOPY FUNDAMENTALS PRINCIPES DE SPECTROSCOPIE VIBRATIONNELLE FONDAMENTAUX

## I.1 RÉSUMÉ

Ce chapitre présente les bases fondamentales de la théorie de la lumière et de son interaction avec la matière. Il traite aussi la spectroscopie de biofluides et illustre comment celle-ci est en mesure de fournir un excellent complément aux paramètres biomédicaux à visée diagnostic et de dépistage d'une pathologie. Des maladies telles que le cancer, à savoir le cancer primitif du foie (carcinome hépatocellulaire) et les gliomes cérébraux sont introduites et discutées. Les étapes pathologiques telles que la fibrose hépatique et la cirrhose du foie en phase terminale sont détaillées et le lecteur est guidé à travers les objectifs du projet doctoral et les objectifs spécifiques de l'étude. Le chapitre comporte une introduction et une discussion sur l'état-de-l'art des techniques IRFT et Raman dans le domaine de la biospectroscopie clinique.

### I.1.1 Principes fondamentaux de la spectroscopie vibrationnelle

Les changements d'énergie détectés suite à l'interaction du rayonnement incident avec une molécule donnée dans la spectroscopie de vibration sont ceux qui sont nécessaires pour provoquer un mouvement nucléaire, que ce soit par absorption, transmission, diffusion ou réflexion [2-3]. C'est la base de la spectroscopie vibrationnelle [3-6]. Les spectroscopies IR et Raman en font partie et elles sondent les vibrations moléculaires de l'échantillon irradié par la lumière (monochromatique pour la diffusion Raman et polychromatique pour la spectroscopie IR). Certaines fréquences de vibration, dites « fréquences de groupe », sont caractéristiques de la présence d'un groupement chimique dans la molécule étudiée. La théorie mécanique des vibrations permet de prévoir l'existence des fréquences de groupe à partir des ordres de grandeur des différents types de constante de force. La fréquence vibrationnelle dépend de la nature des liaisons, de la masse des atomes concernés et de l'environnement proche du groupement considéré. Ainsi, en utilisant ces techniques, on peut obtenir une empreinte chimique de l'échantillon analysé.

Les spectroscopies IR et Raman sont complémentaires car elles fournissent toutes deux une « empreinte digitale » ou une « signature » des molécules d'un échantillon, selon que leurs liaisons présentent des activités Raman ou IR. En raison des empreintes moléculaires caractéristiques obtenues, les spectroscopies Raman et infrarouge sont très prometteuses pour le diagnostic des maladies. Elles sont largement utilisées dans la recherche et le développement de nouveaux outils dans le domaine de la santé ; avec plus d'une décennie dédiée à chercher des marqueurs spectroscopiques associés à des mécanismes pathologiques au niveau cellulaire et

tissulaire [68]. Les recherches ont donné lieu aux concepts de la « cytologie spectrale » et de « l'histologie spectrale » [8, 67-69]. Cependant, il y a un manque de standardisation, de validation lors d'essais cliniques à grande échelle et d'actions multicentriques, associé aux limites de l'approbation éthique des essais de données à grande échelle. Cela signifie que la traduction clinique réelle est quelque peu entravée. Néanmoins, la recherche de marqueurs d'une maladie *via* des 'biopsies liquides' devient rapidement une technologie émergente au potentiel considérable.

Il est courant de dépister des maladies dans le sang et seules quelques études ont exploré les approches spectroscopiques. Les avancées au niveau instrumentation, le gain de sensibilité des détecteurs, l'utilisation de nouvelles techniques de traitement des données plus pointues ont amélioré la capacité de détecter rapidement et de façon non-invasive les signatures spectrales liées à des maladies. Par conséquent, ces approches représentent un potentiel de s'intégrer à la pratique clinique actuelle. En fin de compte, cela apporterait des services publics plus efficaces, des économies substantielles, une prise en charge efficace pour les patients et une réduction marquée de la morbidité et de la mortalité.

#### *1.1.1-1 La spectroscopie infrarouge*

Lorsque la lumière infrarouge interagit avec la matière, plusieurs phénomènes physiques peuvent avoir lieu mais principalement, elle peut être absorbée, transmise, réfléchi, réfractée ou diffractée. Quand la lumière incidente a la bonne énergie correspondant à la différence entre deux niveaux d'énergie de vibration, elle sera absorbée. Ceci provoque le passage d'une molécule à un état d'énergie plus élevé en raison du transfert d'énergie. Par conséquent, il est décrit comme un processus quantifié et donne lieu à un spectre composé de pics / bandes pouvant être interprété qualitativement (position du pic) et quantitativement (intensité / surface du pic, intensité relative) [2,5]. De part sa nature, l'énergie d'absorption du rayonnement infrarouge est inférieure aux énergies mises en jeu en spectroscopie Raman, comme illustré dans la Figure 1.4.

#### *1.1.1-2 La spectroscopie Raman*

Lorsque des photons d'une lumière monochromatique interagissent avec des molécules, le faisceau incident est soit diffusé sans changement de longueur d'onde (diffusion de Rayleigh), soit avec un changement de longueur d'onde, connu sous le nom de diffusion Raman. La diffusion de Rayleigh (dite élastique) se produit lorsqu'un électron est excité de l'état fondamental à un état virtuel avec une énergie plus élevée, avant de revenir à l'état fondamental. Cet effet représente une proportion importante des interactions photoniques qui ne présentent aucune information moléculaire car la même longueur d'onde est recouverte [6]. Lorsque les photons transfèrent de l'énergie aux molécules sous forme d'énergie de vibration, il se produit

une perte d'énergie et un décalage vers une longueur d'onde plus longue avec une intensité supérieure, par exemple, la lumière est décalée vers le rouge. Ceci est connu sous le nom de diffusion Raman-Stokes. Cependant, les photons incidents peuvent recevoir de l'énergie de molécules vibrantes, entraînant une augmentation fréquence / énergie, se déplaçant vers une longueur d'onde plus courte avec une intensité moindre, par exemple, la lumière est décalée vers le bleu. C'est ce que l'on appelle la diffusion Raman anti-Stokes, dont le signal est globalement moins intense que celui des raies Stokes (différence de population des niveaux) car seules les molécules déjà excitées avant l'irradiation peuvent provoquer ce phénomène [6-7]. Les diffusions Stokes et anti-Stokes sont appelées « inélastiques » et l'information moléculaire contenue est la même. Dans la pratique usuelle, le signal anti-Stokes et la raie Rayleigh sont filtrés pour ne garder que le signal Raman-Stokes. La Figure 1.4 montre les transitions impliquées au cours de ces processus.

### **I.1.2 Biofluides et marqueurs de maladies**

Les composants sanguins tels que le sérum et le plasma sont couramment utilisés dans en analyse clinique car ils contiennent des biomarqueurs utiles au diagnostic de la maladie [7]. Dans le domaine du diagnostic du cancer, ils sont connus pour être une source riche d'informations et représentent une lecture des événements cellulaires et extracellulaires en cours [70]. De plus, ils sont facilement accessibles et peu invasifs pour les patients, ce qui rend possible des études plus grandes. Les tendances récentes indiquent que l'utilisation d'un seul ou de quelques biomarqueurs est en recul par rapport à l'utilisation de plusieurs biomarqueurs pour la progression de la maladie [71]. Dans ce contexte, le rôle des méthodes de spectroscopies vibrationnelles peut être déterminant car les informations fournies par la signature spectrale du biofluide reflètent, *via* la composition biomoléculaire ou empreinte chimique, le statut physiopathologique du patient. La capacité de détecter des changements biochimiques ou morphologiques au stade prodromique de la maladie est essentielle pour une thérapie efficace. De plus, la détection de biomarqueurs joue un rôle important dans cette exploration. Plus une maladie est détectée précocement, plus le traitement peut tirer pleinement parti de l'intervention thérapeutique. Pour le cancer en particulier, il existe un large éventail d'entités biochimiques, notamment des protéines, des acides nucléiques, des lipides, des glucides, de petits métabolites et des paramètres cytogénétiques et cytocinétiques, ainsi que des cellules tumorales circulantes (CTC) entières logées dans des biofluides. La recherche de marqueurs de maladie émerge rapidement en spectroscopie vibrationnelle. L'accent a été mis sur le sérum et le plasma, en raison de la prévalence de ces échantillons dans les biobanques actuelles et du fait que l'approbation éthique est déjà bien établie pour la collecte et l'utilisation de ces échantillons biologiques dans la détection de nouveaux marqueurs associés à des maladies.

### **I.1.2-1 Cancer**

La prévalence du cancer a considérablement changé au cours des cinq dernières années et devrait atteindre 4 millions de personnes au Royaume-Uni d'ici 2030 [72]. À l'heure actuelle, 2,5 millions de personnes vivent avec le cancer au Royaume-Uni, dont 80% en Angleterre [73]. On dit que la maladie sera diagnostiquée chez 1 personne sur 2 à un moment de leur vie et que la survie au cancer est trois fois plus élevée lorsqu'elle est diagnostiquée tôt [74].

Selon la Fondation mondiale de recherche sur le cancer, la France a la deuxième incidence la plus élevée ; ayant l'incidence la plus élevée chez les hommes (360,6). C'est le 6<sup>ème</sup> rang mondial (300,4), alors que le Royaume-Uni se classe 22<sup>ème</sup> (266,9) au niveau mondial [76]. Bien que les taux de mortalité par cancer aient diminué en France au cours des vingt dernières années, il reste la principale cause de décès, avec 148 000 décès en 2012 [75].

Le cancer est la croissance incontrôlée des cellules, due aux mutations de notre processus de renouvellement cellulaire normal. Des erreurs au stade de la réplication de l'ADN peuvent entraîner une instabilité génétique et éventuellement des modifications physiques dans le corps. De tels changements affectent les nucléotides. Ces molécules de sucre azoté fournissent les éléments constitutifs de la vie et sont souvent désignées par A (adénine), T (thymine), C (cytosine) et G (guanine) dans l'ADN. Une accumulation de changements au sein de ces molécules peut conduire au développement d'un cancer qui se manifeste dans le cycle cellulaire (voir Figure 1.23). Par conséquent, la plupart des médicaments anticancéreux ciblent des zones sélectives du cycle cellulaire pour inhiber la croissance [77]. Notre appareil cellulaire interne a mis au point des « points de contrôle » permettant d'appréhender de telles mutations avant et après la réplication génétique. Ces phases appelées G (lacunes / croissance) sont le signal des cellules pour arrêter tous les processus si des dommages génétiques sont détectés. Au renouvellement cellulaire, le cycle cellulaire subit les phases suivantes G1, S, G2, appelées collectivement Interphase, suivies de la mitose chez les eucaryotes. Avant d'entrer en mitose, ces points de contrôle vérifient régulièrement l'existence de modifications inconnues au sein de l'architecture de l'ADN et proposent des modifications correctives ou un arrêt cellulaire (G0). Si des dommages à l'ADN ne sont pas observés, il en résulte souvent un ADN anormal avec un nombre incorrect de chromosomes et une division aberrante continue menant à des mutations géniques, d'où la formation de tumeurs.

### **I.1.2-2 Fibrose et cirrhose hépatique, carcinome hépatocellulaire et gliomes**

La fibrose hépatique (FH) résulte de la réponse cicatrisante du foie à des lésions répétées [82], telles que l'hépatite virale ou la stéatohépatite non alcoolique (NASH) [83]. La défense naturelle du corps déclenche une réponse inflammatoire, ce qui entraîne une diminution des quantités de protéines de la matrice extracellulaire au site de la lésion, permettant ainsi aux cellules nécrotiques / apoptotiques d'être remplacées par de nouvelles cellules parenchymateuses du foie. Cependant, si la lésion persiste, la régénération du foie échoue éventuellement ; les hépatocytes sont remplacés par une abondance de MEC, telle que le collagène fibrillaire. La FH passe des bandes de collagène à la fibrose de pontage en cirrhose en phase terminale [84]. La fibrose est caractérisée par une gradation sur une échelle allant de F0 à F4. L'activité, qui correspond à la quantité d'inflammation (en particulier l'intensité des lésions nécro-inflammatoires), est notée sur une échelle de 4 points allant de A0 à A3 (Tableau 1.2).

La cirrhose se caractérise par une hypertrophie du foie, cicatrisante et difficile à toucher, qui est élargie et correspond à la nécrose des unités fonctionnelles du foie ou des hépatocytes. En raison des dommages au foie, les hépatocytes forment des nodules régénératifs (colonies de cellules), entourés de tissu fibreux et d'un excès de collagène. Les cellules responsables de cette formation sont les cellules étoilées qui, dans les tissus en fonctionnement, sont des réserves de vitamine A en sommeil. Habituellement, les cellules sont logées dans l'espace péri-sinusoïdal (entre le canal biliaire et la triade porte). Les hépatocytes sont situés autour du canal biliaire et d'un côté de la triade porte. La triade porte est la zone sinusoïdale où la veine porte et l'artère hépatique convergent toutes les deux vers la veine centrale, située au centre de chaque hépatocyte [88].

Le carcinome hépatocellulaire (CHC) est un cancer primitif du foie. Il est considéré comme l'un des cancers les plus répandus dans le monde et la troisième cause de mortalité par cancer [89]. En France, il s'agit du deuxième cancer digestif après le cancer colorectal. Au cours des dernières décennies, son incidence a augmenté chez les deux sexes en France (4,8% chez les hommes et 3,4% chez les femmes, respectivement) [89]. Le CHC est la principale cause de mortalité en cas de cirrhose et se développe en plusieurs étapes : hépatite chronique, fibrose et cirrhose (environ 80% des cas deviennent cancéreux) [89-91]. Connue pour sa pathogenèse moléculaire complexe, la durée de vie hépatocarcinogénétique est comprise entre 10 et 30 ans [96-97] avec initiation primaire de stimuli externes excluant les modifications génétiques au sein des hépatocytes.

Un diagnostic précoce équivaut à une meilleure fenêtre thérapeutique et se traduit par un pronostic plus probant de l'évolution de la maladie. Il existe un protocole accepté pour classer

une tumeur en fonction de la taille de la masse et de l'apparence histologique. Cependant, la mise en scène du CHC présente de nombreuses autres distinctions. Selon les récentes directives de l'EASL [101], quatre aspects connexes sont proposés en raison de l'évolution très complexe du cancer et des patients atteints de cirrhose insidieuse. Celles-ci comprennent le stade tumoral, la sévérité de l'altération de la fonction hépatique, le bien-être du patient et l'efficacité du traitement [101]. Lorsque la tumeur est non résécable, elle ne peut pas être complètement enlevée par une chirurgie. Un plan de traitement en fonction des besoins nécessite d'être mis en place pour le patient.

Les néoplasmes intracrâniens primaires (NIC ou tumeurs cérébrales) sont des tumeurs dont l'origine est le cerveau, et les tumeurs gliales ou gliomes représentent 30 à 40% de tous les ICN [106]. Les gliomes sont différenciés en fonction de l'emplacement des tumeurs gliales [107]. La Figure 1.26 présente un organigramme des différents types de gliomes et de non-gliomes à base de tumeurs cérébrales primitives.

La plupart des cancers du cerveau résultent de l'invasion de tissus voisins et de métastases distales. Celles-ci sont environ 10 fois plus courantes que les tumeurs cérébrales primitives. En règle générale, les ICN sont très différents sur le plan histologique et sont classés en fonction de leur degré de croissance élevé (croissance agressive et rapide / propagation) ou bas degré (croissance lente contrôlée). Cependant, les tumeurs de bas grade peuvent ne pas être caractéristiques et peuvent ne pas répondre efficacement au traitement. Par conséquent, la raison en est qu'il n'y a pas de ligne de démarcation nette entre bénigne et maligne lors du discernement des NIC. Les tumeurs de bas grade sont les plus nombreuses, telles que les tumeurs hypophysaires, les neurinomes de l'acoustiques, les méningiomes et les tumeurs de la région pinéale, tandis que les tumeurs de haut grade sont essentiellement des gliomes et du GBM, des médulloblastomes et des lymphomes cérébraux primitifs, avec des croissances très agressives et une mortalité très élevée. [107-109].

Dépendant de la présentation précoce des symptômes de toute tumeur cérébrale, le patient est soumis à une série de régimes de traitement. Celles-ci comprennent de nombreux tests sanguins, techniques d'imagerie permettant de visualiser et d'aider au diagnostic, tels que l'IRM, les tomodensitogrammes, et la chirurgie invasive pour réaliser des biopsies ou une résection tumorale. Celles-ci sont souvent suivies d'un cocktail de médicaments, de radiations (parfois de thérapie par émission de positrons) et d'autres thérapies adjuvantes telles que la thérapie photodynamique. Cependant, actuellement, il ne rentre pas dans les paramètres définis par d'autres études [110].

### **I.1.3 Objectif de l'étude**

L'objectif principal de cette thèse est de développer une méthodologie spectroscopique capable de dépister ou de diagnostiquer rapidement un état pathologique cancéreux à partir de biofluides. Celle-ci pourrait éventuellement devenir un test de diagnostic utilisable au lit du patient. Cet objectif est composé de plusieurs étapes comme mentionné ci-dessous :

1. Effectuer une recherche documentaire approfondie dans le domaine d'étude proposé de la biospectroscopie des biofluides
2. Etudier et analyser les effets pré-analytiques tels les cycles de congélation-décongélation de sérum humain et du séchage du biofluide à l'air ambiant par les micro-spectroscopies Raman et IRTF
3. Etudier et mettre au point une méthodologie rapide pour les tests sur sérums liquides et par gouttes séchées par spectroscopies Raman et IRTF, à partir de sérums de patients : hépatite avec fibrose hépatique et cirrhose et patients atteints d'une tumeur au cerveau présentant divers degrés de gliomes primitifs de bas et de haut grade et de métastases cancers
4. Choisir la technique optimale pour l'analyse spectroscopique du sérum liquide développée et l'utiliser sur une large cohorte de patients : cirrhotiques présentant un CHC ou non et différenciation des différentes étapes de la fibrose

## CHAPTER OVERVIEW

This introduction explains the fundamental principles of vibrational spectroscopy along with the principles of spectroscopic instrumentation, signal pre-processing and chemometrics for biomedical analysis.

### 1.1 INTRODUCTION TO ELECTROMAGNETIC RADIATION

Electromagnetic radiation (EMR) consists of both electric and magnetic vectors, which oscillate at right angles to one another as shown in Figure 1.1. The wave-particle duality theory states that light can behave both as a wave and a particle. Particles of light or photons travel at  $3 \times 10^8 \text{ ms}^{-1}$  ( $c$ ) and have discrete quantised energy. Photonic absorption promotes an electron shift in energy levels. There is an inverse relationship between photonic energy and wavelength. Higher energy photons produce shorter wavelengths. These photonic-wave interactions with matter are of importance to the field of spectroscopy.

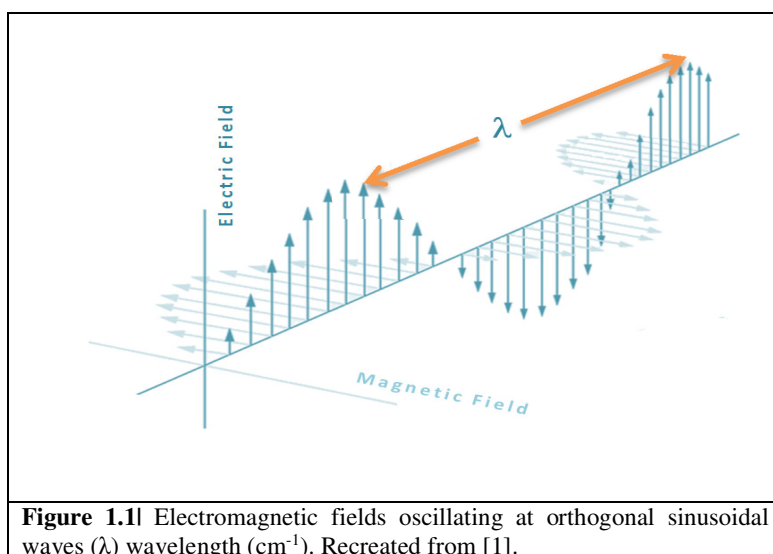


**Figure 1.1** Electromagnetic fields oscillating at orthogonal sinusoidal waves ( $\lambda$  wavelength ( $\text{cm}^{-1}$ )). Recreated from [1].

EMR waves have certain characteristics, including amplitude, wavelength, and frequency as shown in Figure 1.2. Light can travel through a vacuum and undergoes repetitive cycles, that is, the wave travels from zero amplitude to zero amplitude after three passes through the zero position, sinusoidally. EMR is grouped based upon its wavelength in to the electromagnetic spectrum (EMS), as shown in Figure 1.3, *i.e.*, visible, infrared (IR), ultraviolet (UV) etc.

Since the field moves one wavelength in time  $\lambda/c$ , the wavelength, frequency and speed of a wave are related (eq. 1a) [1].

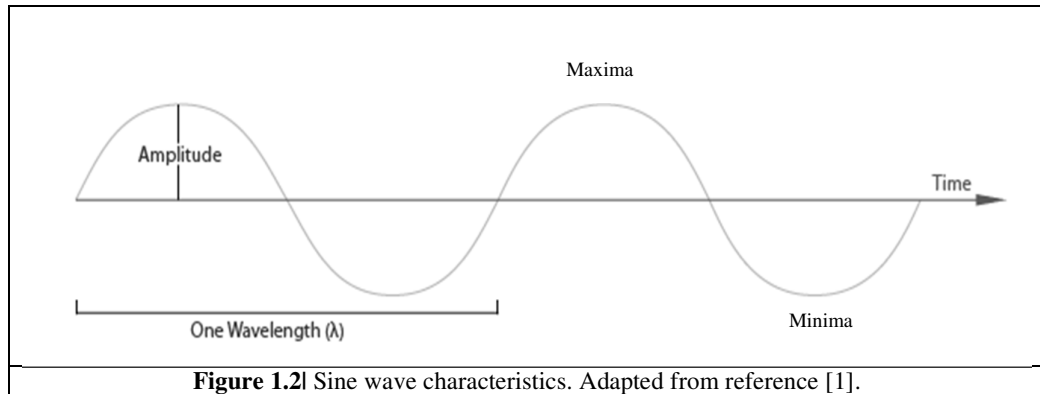


**Figure 1.2|** Sine wave characteristics. Adapted from reference [1].

$$c = \frac{\lambda}{\nu}$$

**Eq. 1a**

Frequency,  $\nu$  is defined as the number of cycles in a second and is measured in Hertz (Hz) or  $s^{-1}$ . The relationship between energy  $E$  and its frequency  $\nu$ , is proportional and is expressed using Planck's constant  $h$ , (eq. 1b) [1-2]. Hence, the higher the frequency, the higher the energy.

$$E = h\nu$$

**Eq. 1b**

Where,

$E$  is energy (J),

$h$  is Planck's constant, ( $h= 6.62607 \times 10^{-34}$  Js)

$\nu$  is frequency ( $s^{-1}$ )

The energy of EM waves is proportional to the frequency or inversely proportional to the wavelength (eq. 1c). This tells us that the shorter the wavelength of light, the higher the energy.

$$E = h\nu = \frac{hc}{\lambda}$$

**Eq. 1c**

Furthermore, wavelength is inversely related to wavenumber  $\tilde{\nu}$ , measured in reciprocal centimetres ( $\text{cm}^{-1}$ ), as it measures the number of cycles which a wave encounters per unit length (eq. 1d) [1-2].

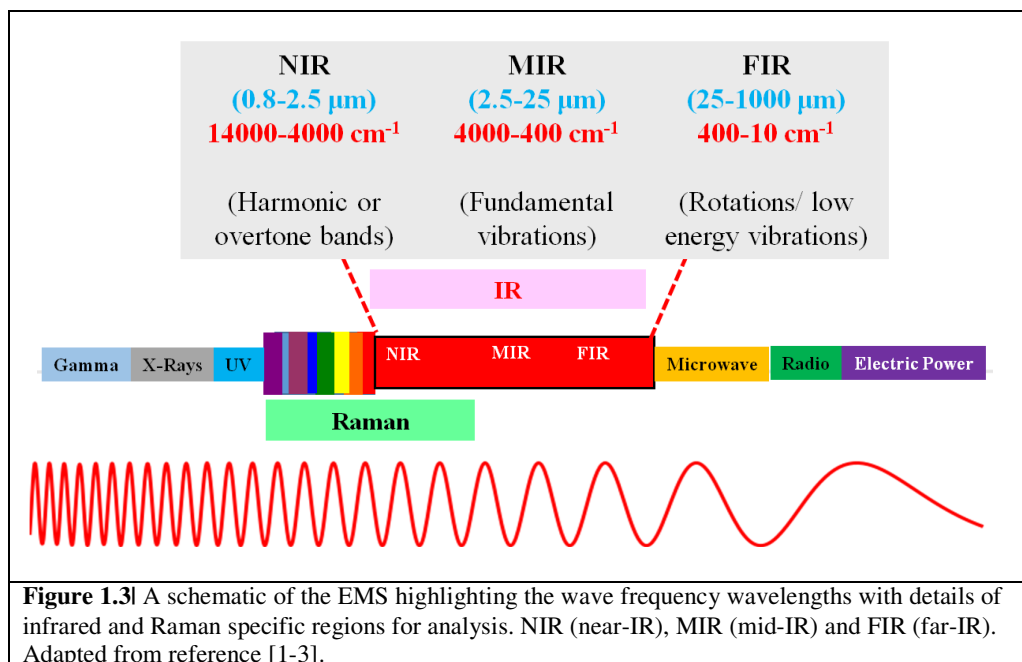
$$\tilde{\nu} = \frac{1}{\lambda}$$

**Eq. 1d**

Visible light wavelengths are expressed in nanometres, whilst the IR region is measured in micrometres and has a longer wavelength with comparatively lower energy. The IR spectrum is split into three regions named for their relation to the visible light spectrum (Figure 1.3).

Vibrational spectroscopy techniques such as Raman spectroscopy and IR spectroscopy allows for the detection of chemical bonds or molecular vibrations from the visible light region, small aspects of ultraviolet (UV) region, and the full IR spectrum, depending on the technique used.

Fundamental molecular vibrations often occur in the 2.5-25  $\mu\text{m}$  region, known as the mid-IR (MIR) region and provides measurements across the 4000-400  $\text{cm}^{-1}$  [2-3]. In Raman spectroscopy, which is based on light scattering rather than absorption of light, such vibrations occur within the visible – NIR region (Figure 1.3).



## 1.2. PRINCIPLES OF VIBRATIONAL SPECTROSCOPY

The energy changes detected from incident radiation interaction with a given molecule are those which are required to cause nuclear motion, either by absorption, transmission, scattering or reflection [2-3]. This is the basis of vibrational spectroscopy [2-4]. IR and Raman spectroscopy probe molecular vibrations of a sample when irradiated with light (monochromatic for Raman scattering and polychromatic for IR spectroscopy). When employing these techniques, one can derive a chemical fingerprint of the sample under observation.

### 1.2.1 Infrared Spectroscopy

When IR light interacts with matter, it can be absorbed, transmitted, reflected, refracted or diffracted as well as with other properties. Light of the right energy that corresponds to the difference between two vibrational energy levels will be absorbed causing a molecule to be promoted to a higher vibrational state. Therefore, it is described as a quantised process and results in a spectrum of peaks/bands that can be interpreted qualitatively (peak position) and quantitatively (peak intensity/area, relative intensity) [2-5]. The absorption energy of IR radiation is less than the Raman energies as shown in Figure 1.4.

#### 1.2.1.1 IR Selection Rule

If photons of polychromatic light from the electric vector exactly matches that of a specific molecular vibration of covalent bonds (*i.e.*, in resonance with the specific energy gap between the ground state and virtual excited states of the molecule), and it induces a change in dipole moment, this causes an electron to jump to the outer higher energy shell and a photon is emitted when the electron returns to its ground state [3-4, 7]. The IR signal intensity is equal to the square of the change in dipole moment [2-3].

### 1.2.2 Raman Spectroscopy

When photons of monochromatic light interact with molecules the incident beam is either scattered with no change in wavelength (Rayleigh scattering), or with a change in wavelength, known as Raman scattering. Rayleigh (elastic) scattering occurs when an electron is excited from the ground state to a virtual state with higher energy, before returning to the ground state. This effect accounts for a high proportion of the photonic interactions that present no molecular information [7]. When photons transfer energy to the molecules as vibrational energy, there is a loss of energy and a shift to a longer wavelength with higher intensity, *e.g.*, the light is blue shifted. This is known as the Raman-Stokes scattering. However, the incident photons can receive energy from vibrating molecules, causing an increase in frequency/energy, shifting to a shorter wavelength with less intensity, *e.g.* the light is red shifted. This is known as Raman anti-

Stokes scattering, which has an overall less intense signal than the Stokes line because only molecules that are vibrationally excited prior to irradiation can give rise to this [5-7]. More often, the anti-Stokes line is used in other Raman systems for intensely fluorescent models, whereas, in conventional spontaneous Raman spectroscopy, Stokes blue shifted frequencies are seen. Figure 1.4 shows the transitions involved during these processes.

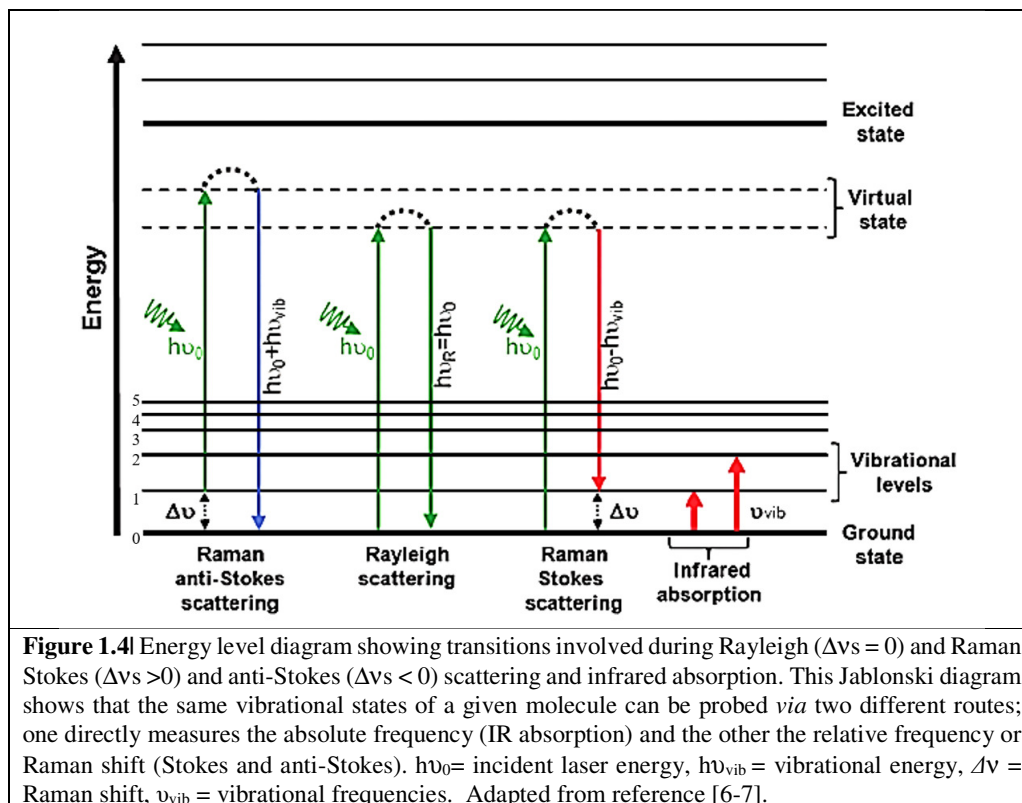


**Figure 1.4** Energy level diagram showing transitions involved during Rayleigh ( $\Delta\nu_s = 0$ ) and Raman Stokes ( $\Delta\nu_s > 0$ ) and anti-Stokes ( $\Delta\nu_s < 0$ ) scattering and infrared absorption. This Jablonski diagram shows that the same vibrational states of a given molecule can be probed *via* two different routes; one directly measures the absolute frequency (IR absorption) and the other the relative frequency or Raman shift (Stokes and anti-Stokes).  $h\nu_0$  = incident laser energy,  $h\nu_{vib}$  = vibrational energy,  $\Delta\nu$  = Raman shift,  $\nu_{vib}$  = vibrational frequencies. Adapted from reference [6-7].

### 1.2.2.1 Raman Selection Rule

Raman scattering is associated with a change in the molecular polarisability of the molecules, that is, a net change in the electron cloud distribution surrounding the nuclei [7-8] when the electric vector interacts with the molecular bond, which results in an induced electric dipole moment in the molecule [2]. This is termed the selection rule for Raman scattering. Raman intensity is equal to the square of the change in molecular polarisability [2, 4, 8].

### 1.2.3 Fundamental Molecular Vibrations

Molecular stretching, bending and rotations occur in a molecule undergoing interaction with incident light, which give rise to specific frequency characteristics of a molecule's vibrational state. If the energy is in resonance with a molecular bond vibration, then as the molecule transition to a higher energy level, the vibrational energies are quantised, meaning that specific frequencies are needed to increase defined energy levels within a molecule [6-8].

When a molecule is in a stable state, *i.e.*, no incident external radiation, the chemical bonds of a molecule are analogous to springs holding the atoms in place at their equilibrium position with only minute oscillations occurring. However, any atomic displacement from such equilibrium causes the molecular structure to vibrate and depending on the technique used for detection (Raman or IR spectroscopy), the molecules are excited to a higher energy state.

For a fundamental understanding of the energetics of molecular vibrations, Hooke's law is used. For a diatomic heteronuclear molecule (homonuclear are IR inactive), it vibrates somewhat like two masses on a spring, with a potential energy that is dependent on the square of equilibrium displacement [2, 4, 7]. If the bond is considered to behave like a spring, then the restoring force is proportional to the displacement from the equilibrium length, which is Hooke's law (eq. 2a).

$$F = -kx$$

**Eq. 2a**

Where,

- $F$  is the restoring force
- $k$  is the force constant or a measure of bond stiffness, and
- $x$  is the internuclear distance

When the atoms are displaced from their equilibrium positions, an opposite restoring force is produced, which increases proportionally with displacement. Equation 2b allows us to understand the natural frequency vibration of a bond and radiation required to successfully quantise diatomic molecules of two different atoms.

$$\nu = \frac{1}{2\pi c} \sqrt{\frac{k}{\mu}}$$

**Eq. 2b**

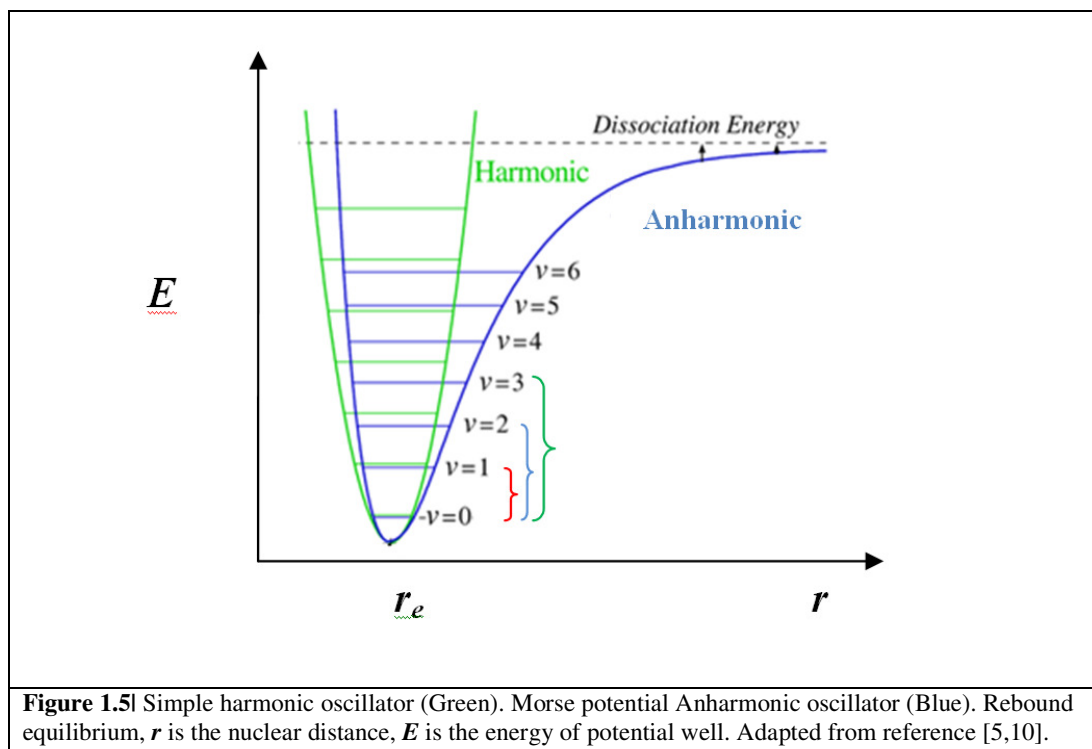
Where,

- $\nu$  is the vibrational frequency
- $\mu$  is the reduced masses of the atoms, *i.e.*,  $m_1m_2/(m_1+m_2)$
- $c$  is the velocity of light
- $k$  is a constant that varies from one bond to another, *i.e.*,  $k$  is greater for triple bonds than single bonds [7-8]

Importantly, a change to either the atoms' masses or the bond force has the potential to alter a molecule's wavenumber position on a spectrum. Stronger bonds have a large  $k$  value and vibrate at higher frequencies with more energy, and the greater the mass of the atoms, the lower the vibrational frequency. With the harmonic oscillator, we can see that a transition is understood in terms of the quantum number being  $\Delta\nu = \pm 1$ , and a fundamental transition is defined as the result of the molecular energy going from its ground state to the first excited vibrational state ( $\nu_0 \rightarrow 1$ ). See Figure 1.5 [highlighted in red].

However, Hooke's law is not a strong approximation for real molecules and only holds true for low values of the quantum number. As the force required to compress a bond by a definite distance is larger than the force which is required to stretch a bond, the energy potential is rather anharmonic. Perturbation theory is used to calculate the anharmonicity from the harmonic oscillator model [7-8]. So, in contrast, the relationship between the force and displacement is non-linear, but dependent upon displacement amplitude and thus has non-equidistant energy levels. With this, the vibrational quantum numbers become ( $\Delta\nu = >1$ ) and decreases in oscillation frequency are allowed, which explains the presence of overtone bands with lower energies than twice the fundamental [2, 5]. The transition from  $\nu_0 - \nu_2$  and  $\nu_0 - \nu_3$  are called first and second overtones, respectively and decrease in energy progressively (see in Figure 1.5) [highlighted in blue and green, respectively].

Combinations bands can also arise, whereby two vibrational frequencies ( $\nu_1$  and  $\nu_2$ ) in a molecule couple to give rise to a new IR active frequency. This band is the sum of the two interacting bands ( $\nu_{\text{comb}} = \nu_1 + \nu_2$ ) [3, 7, 8].



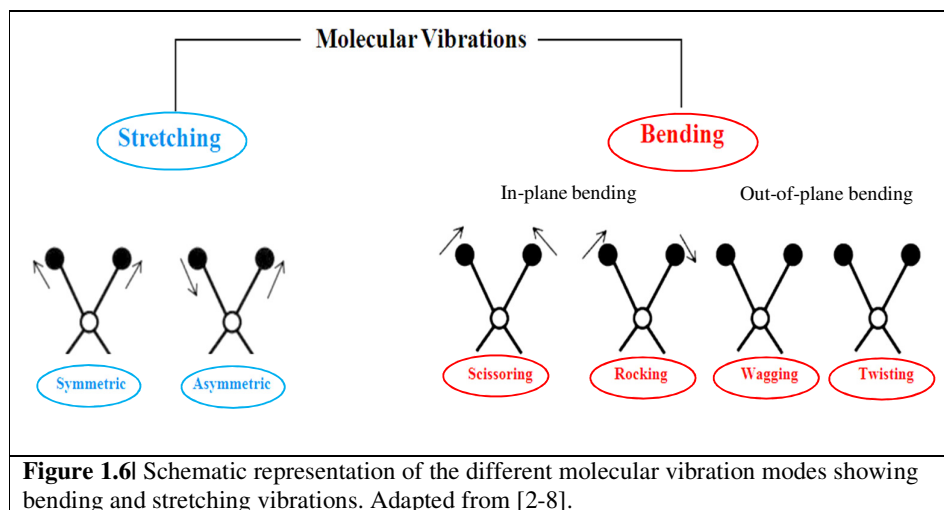
### 1.2.3.1 Normal Modes and Bond Vibrations

The vibrational energy of a molecule can be divided into a number of parts, called ‘degrees of freedom’. There are three coordinates to describe the translational motion around the center of mass, three coordinates for the rotational motion in non-linear molecules ; for linear molecules only two are required. The remaining coordinates are used to describe the vibrational motion of a molecule. Therefore, it can be stated that molecules with  $N$  atoms have  $3N-6$  vibrations for non-linear molecules, whilst for linear molecules it’s  $3N-5$  vibrations (see Table 1.1).

There are 2 fundamental types of bond vibrations: stretching and bending. Stretching modes can be further classified into symmetric or antisymmetric. Bending or deformation modes can be sub-categorised into four actions as shown in Figure 1.6. Antisymmetric stretches occur at a higher frequency than symmetric ones, which in turn occur higher up the spectrum than the group of bending vibrations [2, 4, 10-11].

**Table 1.1** Overview of degrees of freedom (DOF).

	Total DoF	Translational DoF	Rotational DoF	Vibrational DoF
<i>Non-linear Molecules</i>	$3N$	3	3	$3N-6$
<i>Linear Molecules</i>	$3N$	3	2	$3N-5$



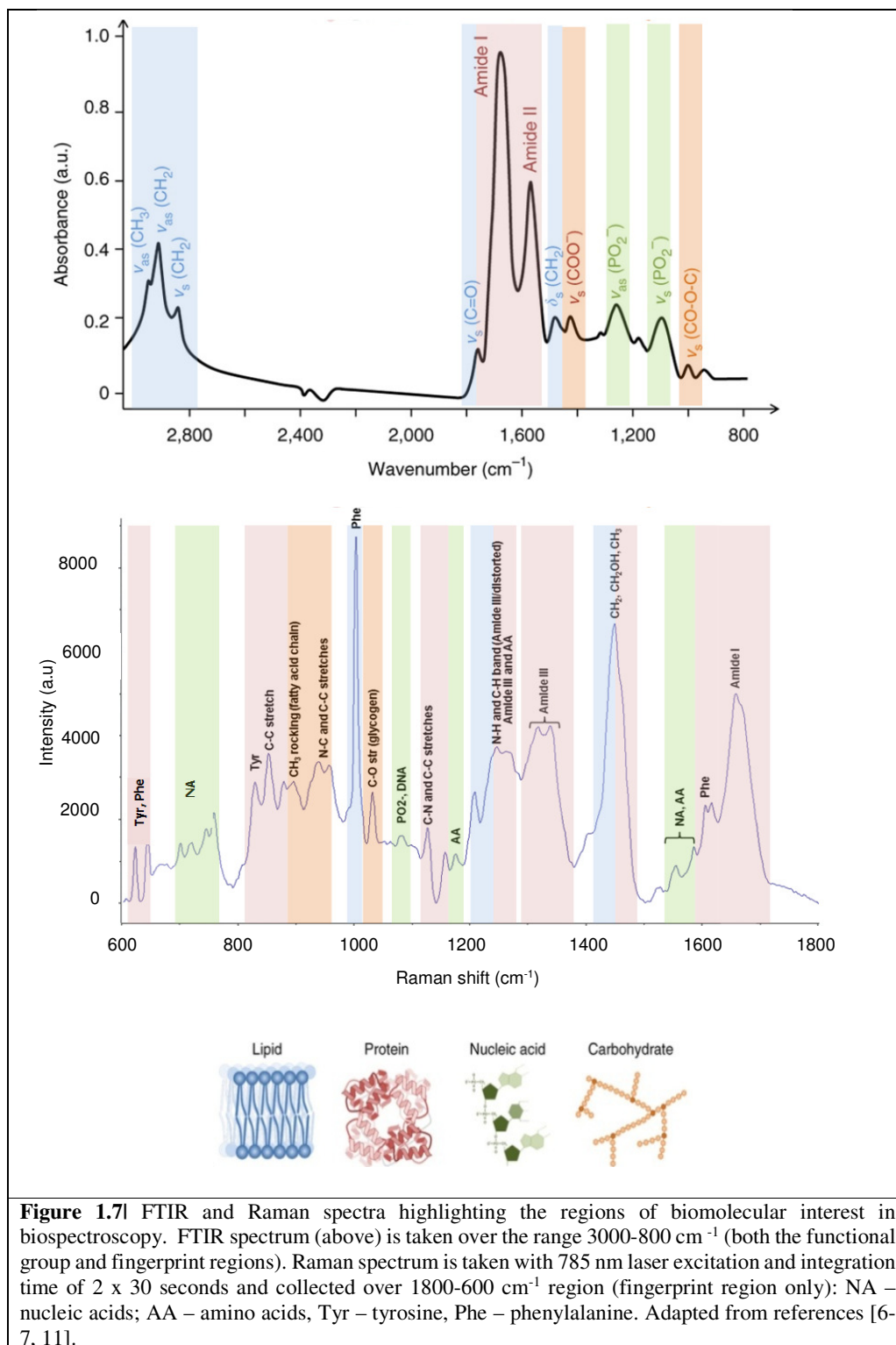
### 1.2.3.2 Complementarity of Infrared and Raman Spectroscopy

If a molecule has a centre of symmetry or an inversion centre, then IR active vibrations are Raman in-active and *vice versa*. There may be modes in-active in both. If a molecule has no centre of symmetry, then some (not all) vibrations may be both IR and Raman active. This is called the ‘*principle of mutual exclusion*’ in vibrational spectroscopy.

For example, carbon dioxide is a centrosymmetric molecule ( $\text{CO}_2$ ). It has 4 normal modes of vibrations. The IR and Raman active modes are given in brief below:

- The Raman active mode is a symmetrical stretch as there is a change in polarizability, but it is IR inactive as there is no change in dipole moment.
- The remaining three are IR active and Raman inactive modes (antisymmetric stretch, in-plane bending and out-of-plane bending; but a degenerate, i.e they appear at the same spectral region, as the vibrations are owed to a change in dipole moment [2-3,10].

$\text{CO}_2$  has 2 peaks on an FTIR spectrum: one antisymmetric ( $\sim 2350 \text{ cm}^{-1}$ ) and two degenerate deformation stretches ( $\sim 666 \text{ cm}^{-1}$ ) and only one symmetric peak ( $\sim 1330 \text{ cm}^{-1}$ ) on a Raman spectrum [8, 10]. When the information gained from a Raman and FTIR spectrum is taken as whole, one can see a fuller picture of biological spectra. Figure 1.7 shows an IR and Raman spectrum that is assigned to the biological features of interest for biospectroscopy.



### 1.3. PRINCIPLES OF SPECTROSCOPIC INSTRUMENTATION

#### 1.3.1 FTIR Spectroscopic Instrumentation

A modern FTIR spectrometer consists of a source, interferometer, sample compartment, detector, amplifier, A/D converter, and a computer (see Figure 1.8). The source is usually a Globar™ source (a silicon carbide rod). The Globar™ is supplied with an electric current, which induces a rapid heating and emission of IR radiation [3, 11-13].

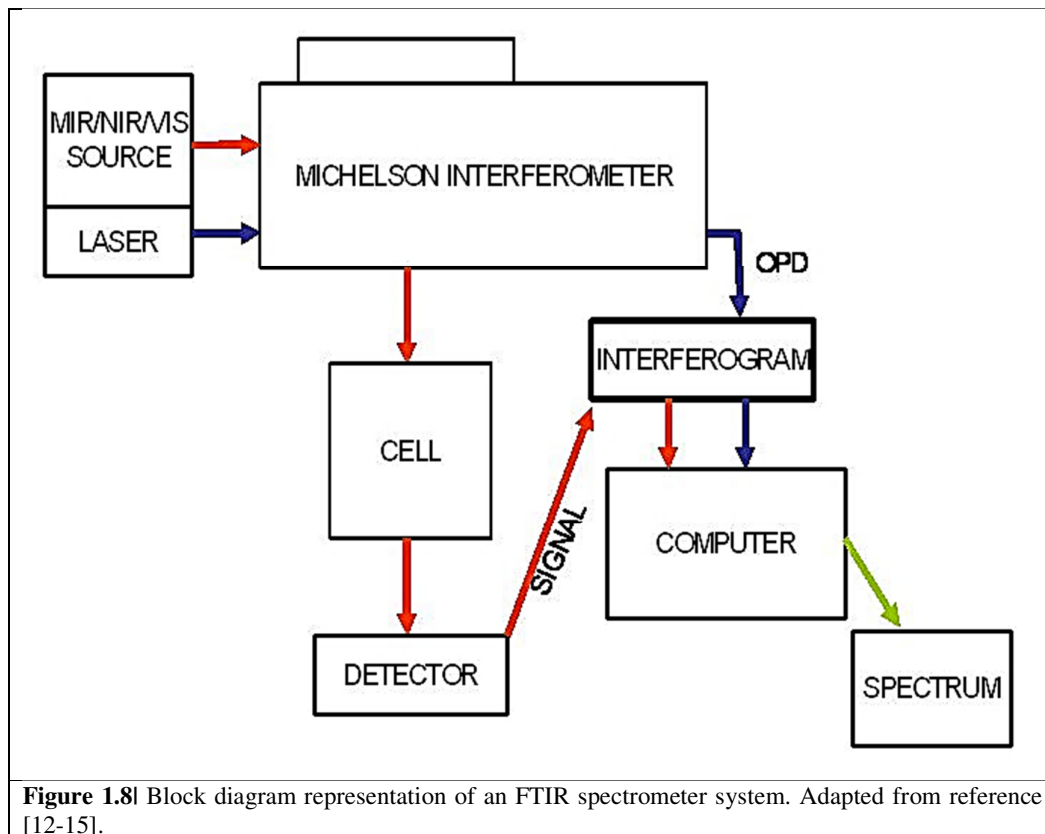


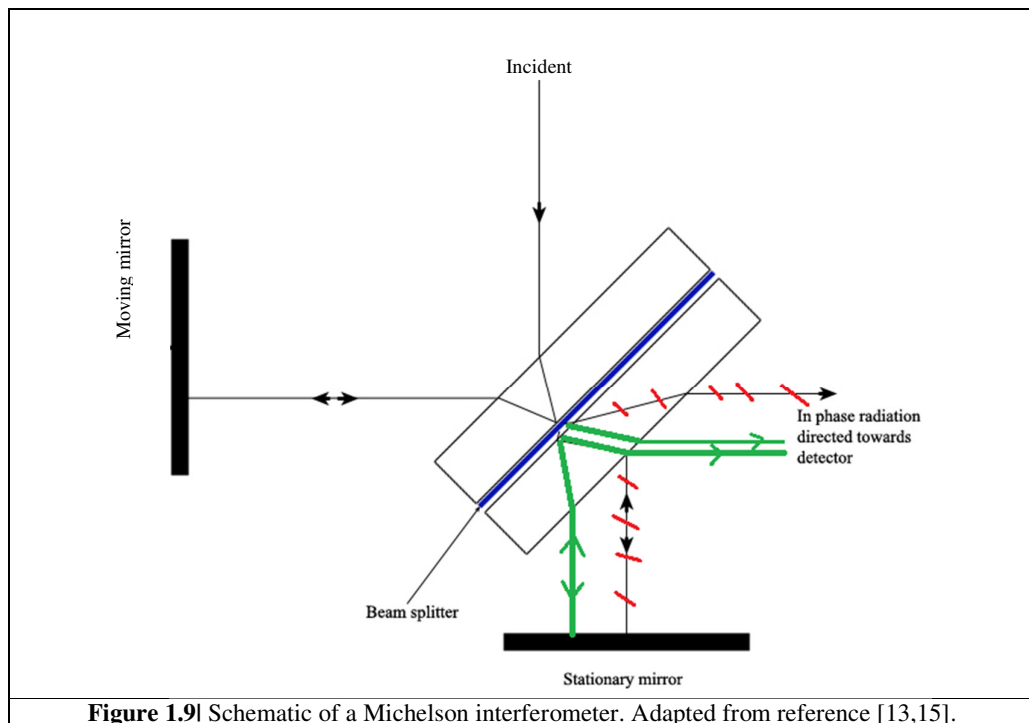
**Figure 1.8** Block diagram representation of an FTIR spectrometer system. Adapted from reference [12-15].

Infrared detectors are either thermal or quantum models. A thermal detector uses the IR beam as heat, while the quantum mechanical detector uses it as light, which provides for an increase in detector sensitivity. Upon detection, the signal is amplified and converted to a digital signal by the amplifier and analogue-to-digital converter (A/D), respectively. The computer then transforms the signal *via* a Fourier transform calculation.

##### 1.3.1.1 Michelson Interferometer

A major component of modern FTIR spectrometers is the Michelson interferometer. It is used to split one beam of polychromatic light into two so that the paths of the two beams are different,

recombining the two beams and directing them into the detector where the difference in the intensities are measured as a function of the difference of the path lengths. Figure 1.9 is a schematic of the Michelson interferometer [13-15]. It consists of two perpendicular mirrors and a beam splitter and acts to modulate the signal prior to Fourier transformation. One mirror is stationary and the other is moving, this causes a difference in path length of the travelling radiation (signal). The beam splitter functions to transmit half of the light and reflect the other half. Basically, the transmitted light and the reflected light strike the stationary mirror and the movable mirror, respectively. When reflected by the mirrors, two beams of light recombine with different phase delays causing interferences with each other at the beam splitter.



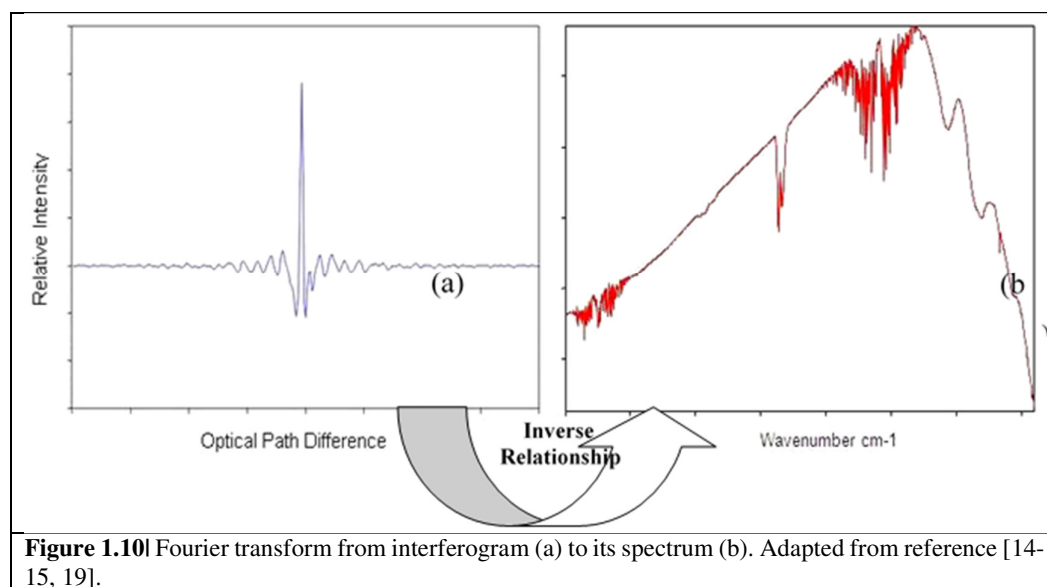
If the distances travelled by the two beams are the same, which means the distances between the two mirrors and beam splitter are the same, this is known as zero path difference (ZPD). However, if the distance from the moving mirror is greater or less than the distance travelled from the stationary mirror, then the resulting signal produced is known as optical path difference (OPD). This is a summation of cosine and sine contributions that display the signal intensity as a function of path length. Then the interferogram is Fourier-transformed which produces the sample spectrogram [15-16].

Optical retardation or OPD occurs when there is a phase difference in beams recombining. This specific feature is the only dependant factor for FTIR spectral resolution, *i.e.*, the larger the

distance travelled by the moving mirror, the greater the spectral resolution. This is directly related to an increase in scan time. Some scan times for an FTIR spectrometer are 0.25 cm, 5 cm and 1 cm, which are equivalent to spectral resolutions of  $4\text{ cm}^{-1}$ ,  $2\text{ cm}^{-1}$  and  $1\text{ cm}^{-1}$ , respectively [14-16].

The resulting interferogram is a measure of relative intensity against OPD. Fourier transformation takes a signal in a time domain and converts it to get a frequency or spatial domain, which is deconvolved to produce a spectrum of intensities per unit wavelength. Figure 1.11 shows the Fourier transform from an interferogram of polychromatic source to its spectrum. In the absence of sample, this is what is known as a background reference spectrum (see Figure 1.10 (b)).

Fourier transform of the interferogram can be viewed as the inversion of OPD; since the units of OPD is centimetres, the inversion of such has a unit of inverse centimetres ( $\text{cm}^{-1}$ ) or wavenumbers. This results as a plot of intensity versus wavenumbers (an FTIR spectrum).



### 1.3.1.2 FTIR Sampling Modalities

There are three main sampling modalities of FTIR spectroscopy: transmission, attenuated total reflectance (ATR) and transfection (see Figure 1.11). There are two more methods, namely specular reflectance and diffuse reflectance modalities, but will not be detailed here in depth, as they were not used in this biological research. Diffuse reflectance is commonly used for both organic and inorganic samples that are finely ground in a powder (less than 10 microns) and mixed in a matrix, *i.e.*, KBr. Using an accessory to direct the IR beam into a sample cup filled-

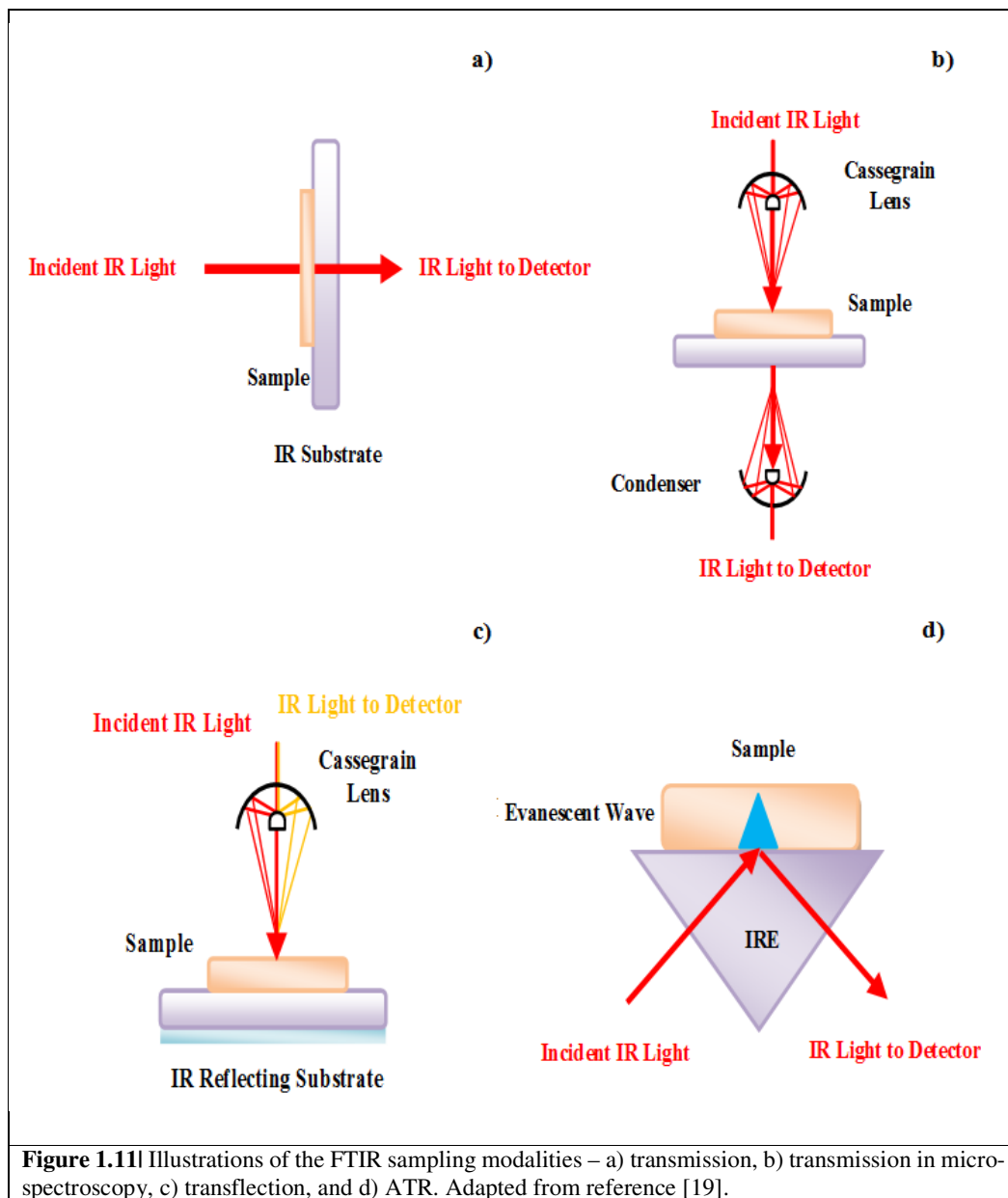
mixture, the IR energy interacts with particles and then reflects off their surface, causing the light to diffuse as it passes through the sample. Specular reflection or reflection-absorption spectroscopy requires the use of a reflective surface, *i.e.*, gold, aluminium with a thin sample layer surface coated. The beam then interacts with the surface at an angle and bounces off at a different angle (in effect passing the sample layer twice ; hence reflection-absorption). For this sampling technique, the angle of incidence is important for increased sensitivity. The steeper the angle entering the sample, the longer it will interact with the sample [19].

#### *1.3.1.2.1 Transmission mode*

To measure a sample in transmission mode, the sample can be mounted onto an IR transparent substrate; usually calcium fluoride ( $\text{CaF}_2$ ). The IR light is shone onto the sample and passes through with some of the frequencies of light being absorbed. The transmitted light is detected. Whilst this method is effective for bulk analyses, sample preparations can be time-consuming, and substrates are costlier than ones used in transfection mode.

### 1.3.1.2.2 Transflection mode

In transflection mode, the sample is placed on an IR-reflective surface, which is usually coated with a coated material that conducts, commonly a silver-tin oxide complex layered on glass, known as low e (emissivity), or MirrIR (Kevely Technologies) substrates. The substrate is reflective to IR radiation but transmits visible light. A Schwarzschild-Cassegrain objective is used to both focus the beam on to the sample and capture the returning light.



The beam being bounced off the IR reflective window and transmitted back through the sample and up to the same Cassegrain objective. Transflection mode does suffer spectral perturbations, such as Mie scattering and the electric field standing wave artefact (EFSW) [18]. Mie scattering is due scattering particles being larger than the wavelength of interacting light, whilst EFSW is due to non-linear changes in absorbance with sample thickness differences, when in contact with metallic surface [16-17, 19].

#### 1.3.1.2.3 ATR mode

In ATR mode, the sample can be placed directly on to the internal reflection element (IRE), *e.g.* diamond, germanium and zinc selenide crystal, as they all have a higher refractive index (RI) than the sample, or a surface. The sample can be liquid or solid. The major benefit of using ATR is the ease of analysis with liquid samples with a biomedical or clinical importance, as it is rapid, non-destructive (exception of removal of dried biofilm build up upon drying of liquid), easy to use, and cost effective.

##### 1.3.1.2.3.1 Principles of ATR

In ATR mode, an IR beam is directed onto an optically dense IRE crystal with relatively higher RI than the sample. The beam enters the crystal and is totally reflected from its internal surface, which creates an evanescent wave that penetrates the sample (on the crystal) by a few microns (0.5 - 5 $\mu$ m). The sample absorbs a small proportion of energy the evanescent wave becomes attenuated. [17, 19]. In regions of the IR spectrum where the sample absorbs energy, the evanescent wave becomes attenuated or altered; and the energy from the wave is passed back to the IR beam and exits the opposite end of the IRE for detection *via* the detector.

Given that ATR is a surface-sensitive technique, to ensure the analyst is able to acquire quality spectra the following two requirements must be met:

- An intimate contact between the sample and IRE is integral, because the evanescent wave only extends up to 5  $\mu$ m max and between ~ 0.2-3  $\mu$ m in MIR [19]
- The RI must be sufficiently greater for the IRE than the sample of interest for total internal reflection to occur

Fundamentally, ATR spectroscopy is dependent on the critical angle  $\theta_c$  and the depth of penetration ( $d_p$ ), which is wavelength dependent.  $d_p$  is technically defined as the distance required for the electric field amplitude to fall to  $e^{-1}$  of its value at the surface [17, 19]. Equation 3a demonstrates the calculation of the  $\theta_c$  based upon the RI of the sample ( $n_2$ ) and the IRE ( $n_1$ ).

$$\theta_c = \sin^{-1} \left( \frac{n_2 (\text{sample})}{n_1 (\text{IRE})} \right)$$

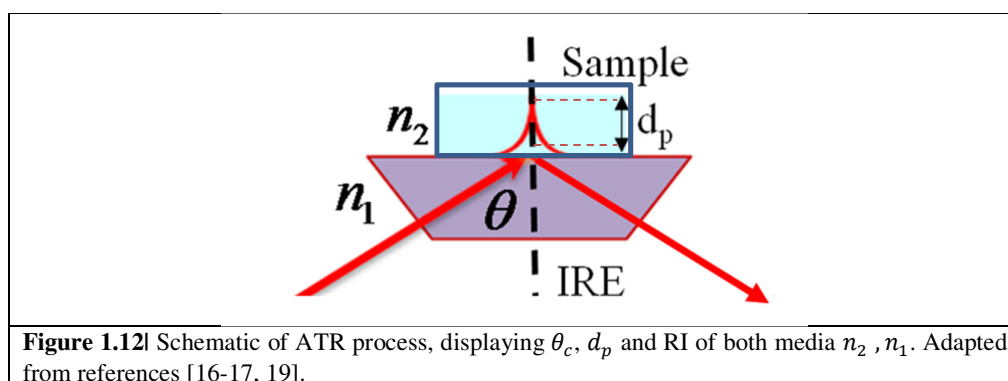
Eq. 3a

Total internal reflection can only occur if the  $\theta_c = \theta_i$  (angle of incidence). Thus, as the  $\theta_i$  increases eventually no light is refracted, so does the  $\theta_{ref}$  (angle of refraction), until it reaches  $90^\circ$ , where only reflection occurs. Now the light is totally internally reflected. So, taking equation 3a [17, 19] to form the  $d_p$  formula, we get:

$$d_p = \frac{\lambda}{2\pi(n_1^2 \sin^2 \theta - n_2^2)^{1/2}}$$

Eq. 3b

We can see that  $d_p$  entirely  $\lambda$  dependent, RI  $n_2$  (sample),  $n_1$  (IRE) and both angles ( $\theta_i, \theta_c$ ). This is shown diagrammatically in Figure 1.12.



### 1.3.2 Raman Spectroscopic Instrumentation

The Raman effect is a very weak phenomenon, due to the inelastic light scattering process that accounts for the phenomenon. Rayleigh elastic scattering does not involve a change in energy and is therefore a much more energetically favorable process. A monochromatic laser is employed, and sensitive detectors are required to capture the photons [4-5, 8, 20].

The difference in wavelength in between the incident and scattered visible radiation corresponds to the wavelength in the MIR. Thus, the frequency difference is measured by the detector and is presented as a spectrum of intensity vs. wavelength shift [20-24]. Raman instruments measure wavenumber shifts over  $4000-10 \text{ cm}^{-1}$  and can be dispersive or non-dispersive, such as Fourier transform Raman spectroscopy, which comprises a Michelson interferometer [24].

Raman spectrometers are commonly coupled with an optical microscope to enable analysis at the micron level. A Raman microspectrometer comprises an excitation laser, a beam expander,

a series of mirrors, an optical microscope, filters and prism gratings and a charge coupled device (CCD) detector. Figure 1.14 shows the basic components to a dispersive Raman spectrometer coupled to an optical microscope.

### 1.3.2.1 Instrument Components

In Raman instruments, a laser source is nearly always used, this is owed to the high intensity needed to produce the Raman scattering to be measured with a reasonable signal-noise ratio (SNR). The Raman scattering intensity varies as the fourth power of the frequency [5, 22]. This means the shorter the wavelength, the more intense the Raman scatter produced, but larger risk of photodamage to the sample. Conversely, as one increases the wavelength (green – red), the scattering efficiency decreases, and longer integration times are needed. Lasers often used in a Raman experiment range from the UV to the NIR. The choice of laser source is vitally important as it is not only directly related to the scattering intensity, but to spatial resolution and confounding fluorescence perturbations.

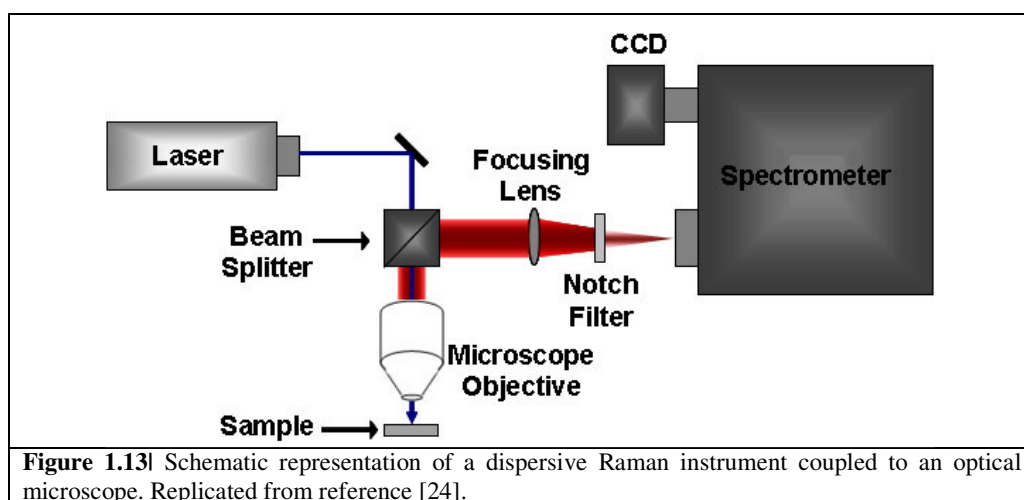


**Figure 1.13|** Schematic representation of a dispersive Raman instrument coupled to an optical microscope. Replicated from reference [24].

Some common laser sources include Argon ion (488 or 514.5 nm; Krypton ion (530.9 or 647.1 nm); Helium-neon (He-Ne) (632.8 nm); Diode (785 or 830 nm) or Neodymium-doped Yttrium Aluminium Garnet (Nd-YAG) (1064 nm). Nd-YAG sources have an advantage of lessening the fluorescence phenomenon as the energy required for a change in the excitation energy of the molecule is lower than the energies of the organic systems [23-24].

The spatial resolution of Raman spectroscopy is based on the wavelength and the numerical aperture used in a confocal system. It is given by equation 4a [5].

$$\text{Spatial Resolution} = \frac{1.22 \lambda}{NA}$$

**Eq. 4a**

The Raman spectrometer houses a range of optics including a beam splitter, mirrors, slits and lenses, which are used to focus the laser into the spectrometer, to the sample and used to collect the scattered light and direct it *via* a filter, a diffraction grating to be detected on CDD [24-26].

The two types of Rayleigh filters within a Raman system are notch and edge filters. The notch filter blocks a range of wavelengths (a few nm wide) around the central absorption of laser line, in effect blocking the laser line and allowing the Raman signal (both Stokes and anti-Stokes). Whereas, edge filters only permit Stokes scattering, as all wavelengths are blocked a couple of nm above that of the excitation wavelength.

Before the signal is sent to the CDD, it encounters a diffraction grating, which disperses the light at varying angles based on the wavelength, separating the light from polychromatic to monochromatic components [24-26]. There are many grating choices for Raman spectroscopy and the number of lines/grooves is the deciding factor for spectral resolution. Common gratings include 300 g/mm, 600 g/mm, 1200 g/mm and 1800 g/mm. The greater the groove density the better the spectral resolution. Overall spectral resolution within a dispersive Raman system is determined by four main factors, including the grating and wavelength:

- Spectrometer focal length, which is the distance between the grating and CDD. The greater the distance the higher the spectral resolution. Typically, focal lengths are between 200 mm (low/medium resolution) to over 800 mm (high resolution). Such choice should be factored in with grating choice, [25-26].
- Lastly, the detector pixel size has a bearing on spectral resolution. Essentially, the smaller the pixel size the higher the spectral resolution achievable. Spectral resolution is the resolving power to separate spectral features and bands into their separate components within a spectrum [22-24, 26].

The signal is then passed on to the CCD; a silicon-based multichannel array detector of UV, visible and NIR light. Fundamentally, each channel houses individual light-sensitive detector elements (pixels) and when they interact with incoming light they build up a charge. The charge is collected, registered then measured. When light is dispersed from the grating it is projected on to the long axis of the CCD array, which means the first pixel will detect light from low

wavenumber region, finishing with the highest wavenumber light captured at the corresponding end (see Figure 1.14).

A fundamental requirement for successful Raman analysis is achievement of a usable SNR with the highest scattering efficiency possible whilst avoiding photo-degradation of the sample. A challenge to achieving this is often an overwhelming fluorescence contribution, which masks the weak Raman signal in most cases. Fluorescence and Raman scattering are competing phenomena; however, one is a ‘real’ electronic transition (fluorescence) and the other is a ‘virtual’ electro-vibrational transitions (Raman). Fluorescence is an absorption-emission resonant process, *i.e.*, energy of incident photon is equal to the energy difference between ground energy state and one of the excited states of the molecules akin to IR spectroscopy. Whereas, Raman is a non-resonant process and is instead almost instantaneous. Fluorescence has a characteristic lifetime of nanoseconds; and can overwhelm the Raman signal.

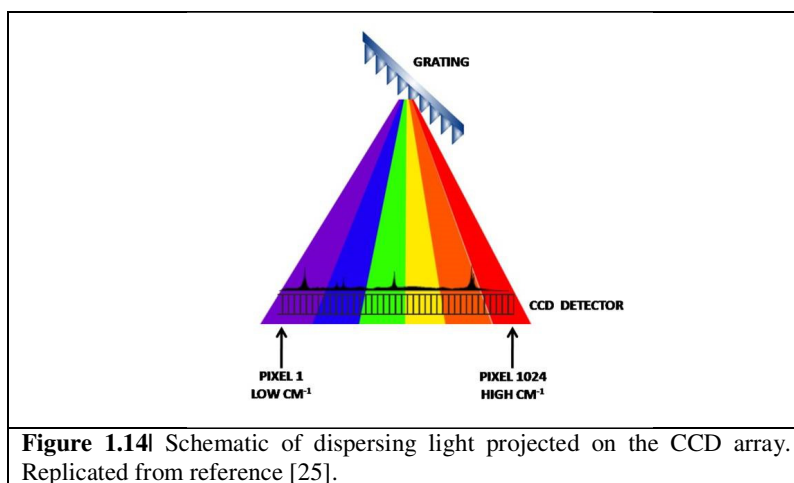


**Figure 1.14** Schematic of dispersing light projected on the CCD array. Replicated from reference [25].

Raman spectroscopy can be used to analyse almost any type of sample. However, major parameters to ensure a fully optimised and robust system are substrate choice, optical alignment of laser beam, gratings and optical components, excitation laser choice, laser exposure and confocal hole and slit size. Moreover, due to the sensitive nature of the instrument, prior to any testing, a series of optical calibrations, power checks and instrument response measurements are required to ensure correct signal alignment and no occurrence of band shifting.

## **1.4. SIGNAL PRE-PROCESSING AND QUALITY ASSESSMENT**

This section focuses on the pre-processing and data analysis methods performed during this research project. Firstly, common methods will be described, followed by technique-specific methods.

Data processing applied prior to univariate/multivariate analysis (MVA) is known as pre-processing. It aims to eliminate the effects of unwanted signals such as detector noise, calibration errors, cosmic ray artefacts (CRA), confounding fluorescence, Mie scattering, laser power fluctuations, drift, stray light and possible substrate contributions and sample thickness differences [26-27]. Spectral collection results in a combination of the pure signal that is exploitable and residual degree of instrumentation and environmental effects.

As IR and Raman spectroscopies exploit fundamentally different phenomena, the extraneous noise and unwanted signal are also different and as such pre-treatment of different steps are required. However, there are some parallels in the data analysis workflow for both Raman spectroscopy and FTIR spectroscopy. Ultimately, there is a myriad of techniques and applications available for spectral pre-processing, but the most fundamentals steps across both techniques are truncation of the spectral range and normalization of the signal to a common scale, prior to exploitation with chemometrics.

### **1.4.1 Spectral Wavelength Truncation**

One the simplest ways to pre-process spectroscopic data is to reduce the spectral range. Since most of the salient biochemical information is found in the fingerprint region of the spectrum, it is reasonable to remove any area of the spectrum that is not of interest for further analysis as it is effectively computationally-redundant This usually includes the tail ends of the spectrum whereby it could have interferences from the cut-off limits of the detector or transmission range of the substrates [9, 11]. The FTIR fingerprint is reported to be 1800-950  $\text{cm}^{-1}$  for FTIR spectroscopy and 1800-600  $\text{cm}^{-1}$  for Raman spectroscopy.

Accordingly, some studies show little differences between the application of spectral quality tests, normalization methods, baseline correction or spectral filtering techniques across Raman and FTIR datasets. However, the low SNR of biological Raman analysis should be considered when applying smoothing filters/derivatives techniques according to some [25-27].

### **1.4.2 Normalisation**

Variations owed to sample thickness or intensity differences cause slight changes to the data. Following baseline correction, the data often needs to be scaled. Vector normalization (VN), standard normal variate (SNV), min-max and offset scale correction (OSC) are popular methods,

as well as normalization to amide I band [11]. In this research, VN and SNV followed by an offset correction were carried on all spectroscopic data.

#### 1.4.2.1 Vector Normalisation

VN or (2-norm) reduces the thickness/width between the minimum and maximum spectra on the absorbance axis across all spectra. Equation 5a demonstrates the formula for VN [31].

$$S_i^{,d} = \frac{S_i^d - \bar{S}_i}{\sqrt{\sum_{d=1}^D (S_i^d - \bar{S}_i)^2}}$$

**Eq. 5a**

It achieves this by firstly mean centering the data and dividing by the square root of the sum of the mean-centred intensities squared, meaning that the sum of all the intensity values squared is equal to 1.

#### 1.4.2.2 Standard Normal Variance

SNV normalization starts with mean centred data and divides it by the root mean square (RMS) over the spectral intensities, resulting in spectra with a unit standard deviation of 1 [26-28]. This is given by equation 5b.

$$S_i^d = \frac{S_i^d - \bar{S}_i}{\sqrt{\frac{1}{D-1} \sum_{d=1}^D (S_i^d - \bar{S}_i)^2}}$$

**Eq. 5b**

#### 1.4.2.3 Offset Scale Correction

OSC is an adjustment of the normalised spectrum so that at least one of the minima points goes through the zero axes. This helps subsequent interpretation.

### 1.4.3 FTIR Spectral Quality Assessment

An internal instrument calibration is carried out automatically within the spectrometer, plus and a weekly external calibration following an in-house protocol.

#### 1.4.3.1 FTIR Spectral Quality Assessment

Raw spectra from the FTIR experiments should be submitted to a spectral quality test to check SNR, control absorbance intensity, and observe water vapour. The spectral quality test [27-28] carried out with FTIR data is detailed below.

- Absorbance linearity check: FTIR Spectra should be discarded if the spectral absorbance  $< 0.35$  a. u or  $> 1.8$  a.u. For ATR-FTIR this is slightly amended based on the attenuation of the signal. Spectral intensities between  $0.02 - 1.2$  a.u are kept.
- SNR calculation threshold (S1, S2): The maximum absorbance of two characteristics bands are chosen, i.e amide  $\sim 1700-1600$   $\text{cm}^{-1}$  (S1), and a sugar-ring vibration  $\sim 1260-1170$   $\text{cm}^{-1}$  (S2), followed by a first-order derivation to assign the maximum values. Noise is evaluated at a molecularly silent region within the mid-IR range  $\sim 2100-2000$   $\text{cm}^{-1}$  and is calculated based on its maximum value of the first derivative.
- Water vapour check (W): The water vapour content can be seen in the spectral range  $\sim 1847-1837$   $\text{cm}^{-1}$ .

Raw FTIR spectra should only pass this quality assessment if the SNR =  $>50$  and  $10$ , respectively for each of the regions, and the S1, S2-W ratio  $= < 20$  but  $> 4$ .

#### 1.4.3.2 Baseline Correction for FTIR

Generally, an FTIR spectrum should lie on a straight baseline; however, occasionally some perturbations can be seen, i.e a rising baseline owed to reflection, scattering, temperature, concentration differences and some physical effects from the instrument [29]. Essentially, variations from the background/sample and the interaction of light with matter give rise to variations in the spectral baseline [9, 30-32].

Whilst there are many mathematical algorithms available for FTIR baseline correction, in this research, a rubber-band correction was used with FTIR single point data and extended multiplicative signal correction (EMSC) model algorithm with mapping and imaging data.

##### 1.4.3.2.1 Rubber-band Correction

This technique defines a rubber-band of a given length, which is wrapped around the tail ends of the spectrum or if a specific region is selected, to that. A convex curve profile based on a polynomial approximation is carried out and subtracted from the raw spectrum to reveal a baseline corrected spectrum. This method was employed for all FTIR data except mapping and imaging.

#### 1.4.3.2.2 Extended Multiplicative Signal Correction (EMSC)

This model-based method is both a baseline and normalization approach to spectral pre-processing, but as the added advantage of being able to quantify different types of chemical and physical variations in vibrational spectra [29-31]. The EMSC method [28-30] deals with additive, *i.e.*, seen across the whole spectrum scale, and multiplicative effects, *i.e.*, seen often as variations in scattering at the higher wavenumbers, which can overwhelm FTIR signal. For information, multiplicative effects in Raman are owed to variations in sampling volume, laser intensity and positioning and focusing on the sample [31-32]. It does this by removing the physical effects of particle size and scattering from the spectra. Here, an in-house written EMSC method is given by equation 6a, b.

$$\mathbf{s}_i = \mathbf{a}_i \hat{\mathbf{s}} + \mathbf{c}_i \mathbf{P} + \mathbf{e}_i$$

Eq. 6a

It models the mid-IR light signal by a linear combination of the reference spectrum, i.e target reference spectrum or mean of data ( $\mathbf{a}_i \hat{\mathbf{s}}$ ), a polynomial model is fitted for the light scattering (baseline) ( $\mathbf{c}_i \mathbf{P}$ ), plus an estimation of the residual error model ( $\mathbf{e}_i$ ). Where  $\mathbf{a}_i$  and  $\mathbf{c}_i$  are the coefficients,  $\hat{\mathbf{s}}$  is selected as the average of the dataset (when the correct estimation of a reference spectrum is not available). The spectrum corrected by the EMSC is then calculated by equation 7b.

$$\mathbf{s}_{iEMSC} = \frac{\hat{\mathbf{s}} + \mathbf{e}_i}{\mathbf{a}_i}$$

Eq. 6b

The model can be used as an outlier detection process as the residual  $\mathbf{e}_i$  must be smaller than an empirically determined threshold, to exclude the spectra with noise and/or having a particularly odd spectral shape.

### 1.4.4 Raman Spectral Quality Assessment

One of the fundamental steps for Raman analysis is ensuring that prior to any experimentation, extraneous contributions from detector drift, noise (shot, flicker noise etc.), laser power fluctuations are kept to a minimum, if not diminished completely.

#### 1.4.4.1 Raman Spectral Quality Assessment

A Raman spectral quality test (QT) was designed to evaluate the S/N of the datasets on MATLAB software (version R2015a, The Math Works, Inc., USA). Two spectral regions ( $\sim 990\text{-}1010\text{ cm}^{-1}$  and  $1720\text{-}1780\text{ cm}^{-1}$ ) were respectively chosen to represent the spectral aspects

for signal (S) and noise (N). A spectrum passed the QT threshold if it exceeded a ratio value of 30, which is accepted for biological data and in line with previous studies [137].

The noise is generally taken as being from the higher frequency part of the Raman fingerprint region, where it usually devoid of any biochemical signal. Some regard the noise to be at the base of the peak of the signal, that is the difference between the corrected baseline and the actual baseline that the spectrum lies upon. However, here the 1720-1800  $\text{cm}^{-1}$  was chosen. Additionally, sometimes, depending on the visual appearance of the spectrum, if such a region did not have the lowest value, then another lower region was used; as was the case for the fiberoptic testing. The signal was defined as one of the most bio-characteristic intense peaks found within a Raman spectrum; *i.e.*, the ring breathing mode of Phenylalanine at  $\sim 990\text{-}1010$   $\text{cm}^{-1}$  (such a range was chosen to allow for potential minor peak shifts).

Raman spectra should only pass this quality assessment if the SNR if all spectra per test is minimally varied and is generally above 30.

#### *1.4.4.2 Wavelength/Intensity Calibrations and CCD Checks*

This is usually done with an optimised, optically aligned instrument. Generally, the follow spectral and intensity calibration steps are carried out:

- **Dark current of the CCD detector:** involves the subtraction of measured CCD signal in the absence of laser light and sample. Dark current is the residual noise from the spectrometer and components when no photons are present; often left over from the CCD detector.
- **Optical response of the spectrometer:** a signal is collected under laser illumination but in the absence of any sample for subsequent signal correction.
- **Detector response:** atomic emission lines from a polychromatic source *e.g.* a Ne, Hg, Kr lamp is read by the CCD and subsequently corrected [30, 32, 35].
- **Intensity calibration:** usually a national institute of standards technology (NIST) fluorescence standard for the excitation wavelength is placed at the sample area for spectral collection and subsequent signal correction.

Following routine detector and optical checks (above), it is necessary to complete power checks of the laser line with a power meter and to note triplicate measurements at the start and close of experimentation per day. Power checks are generally done with and without a microscope objective.

Secondly, verification of the Rayleigh line by zeroing the spectrometer position is necessary to monitor the spectrometer performance and observe shifts in the calibration of the silicon (Si

~520.8 cm<sup>-1</sup>) wavelength calibration; recording in triplicate to ensure a reliable Raman shift axis and comparable intensity scale per day.

All routine calibration data is averaged and corrected in MATLAB later and the data pre-processing stage.

#### *1.4.4.3 Baseline Correction for Raman Spectroscopy*

Sometimes inherent with Raman spectral collection are high-energy cosmic particles. These cosmic ray artefacts (CRAs) are random events recorded on the CCD and manifest themselves as non-reproducible, sharp and intense superimposed spectral spikes on the spectrum. Such spikes represent unwanted signal and should be removed. Whilst there are a number approaches which have been suggested for locating and removing CRA [32-36], signal averaging also works to limit such occurrences, when spectra are repeated.

Whilst the literature supports many methods for background removal, such as time-gated Raman spectroscopy, anti-Stokes Raman spectroscopy [37], and physical removal of fluorophores from the sample by washing and filtering [38]. Most are accomplished using advanced mathematical algorithms at the pre-processing stage. Such methods include baseline subtraction procedures using polynomial detrends [39-40], derivatisation filters [42] and have the added advantage of being efficient, relatively easy to perform and inexpensive in comparison for use of extra optical components and or instrumentation [26, 32].

In this research, a polynomial baseline detrend was employed. This method finds a least squares estimation of the baseline, ensuring the fit goes through the minima of the signal on the baseline. Employing this approach has an advantage of preserving the Raman line shape, which makes spectral interpretation easier, as the signal is not changed too drastically. User inputted values of the points and polynomial order is generally done, or it can be automated, but it does allow a good approximation for baseline correction. On the other hand, caution should be taken as not to over or underestimate as this could introduce further aberrations in to the data [11, 32]. The use of Savitzky-Golay [42] smoothing filter in combination with a polynomial detrend and derivatisation was also undertaken. It should be noted that over-smoothing degrades the signal, so caution should be taken.

### **1.5. CHEMOMETRICS FOR SPECTROSCOPY**

Chemometrics are a branch of mathematics that deals with statistical evaluation methods to extract pertinent and discriminating chemical information by finding patterns within the data and aid the interpretation of biophysical /analytical chemistry data. Vibrational spectroscopies

specifically produce many variables in multispectral domains, *i.e.*, 100s to 1000s of variables, whereby each wavenumber has a corresponding intensity associated.

Following initial quality checks, instrument response and pre-processing regimes, the data was submitted to unsupervised and supervised clustering approaches, *i.e.*, without and with *a priori* group membership information.

### 1.5.1 Principal Component Analysis (PCA)

Principal Component Analysis (PCA) [43-44] is an unsupervised dimension reduction technique, which finds classifications of data groups without *a priori* information. In unsupervised learning, the requirement is to discover significant patterns of the data without the use of labelling. PCA aims to find the underlying structure of the data, that is the directions where there is the most variance, *i.e.*, where the data is most spread. From a set of data points, PCA deconstructs it into eigenvectors and eigenvalues. An eigenvector is a direction of the data and its corresponding eigenvalue is an amount of variance within that direction. Principal component 1 (PC1) is also known as the eigenvector with the highest eigenvalue. The total number of dimensions or variables in a dataset is equal to the total number of eigenvector/value pairing [45-47].

Within vibrational spectroscopy, the data sets are sometimes 100s or even 1000s of variables that are measured simultaneously, thus spectroscopic PCA would demonstrate 100s or 1000s of eigenvector/value pairs. These new underlying directions of the data are oriented orthogonally, where by the first PC explains the greatest variance within the dataset, followed by the second, third and so on, until all dimensions (eigenvector/value pairings) have been accounted.

PCA reduces the overall data as it continues the eigenvector/value pairing, until a point whereby such eigen vector/value pairing is no longer explaining anything meaningful. At that point retaining only the meaningful latent components within the data best describes the data and the meaningless values are redundant [47]. One can then reconstruct the data based on eigen vector/value pairings that explain 99.99% of the data.

Extracting linear factors for relationship analysis is the fundamental theory behind PCA. By finding the maximised sum of the squares within a data matrix of  $p \times n$  ( $p$  = variables or columns *i.e.* wavenumbers, and  $n$  = observations (objects) or rows, *i.e.* the associated IR absorbance/Raman intensity), the original data is decomposed into new variables ( $V^T$  and  $U$ ), which best describe the greatest variation in ascending order (see Figure 1.15), whereby the new variable or dimension is termed principal component 1 (PC1) ( $k$ ). Decomposition of the data matrix

finds its pure components of the acquired spectrum, *e.g.* wavenumbers, spectrum of interest, plus noise [44-47]. Generally, PCA describes the pattern of covariance between classes of data.

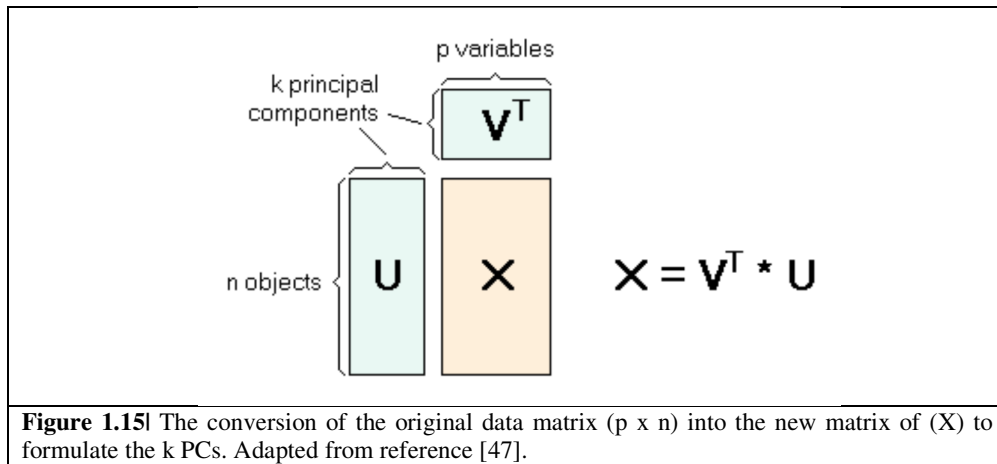
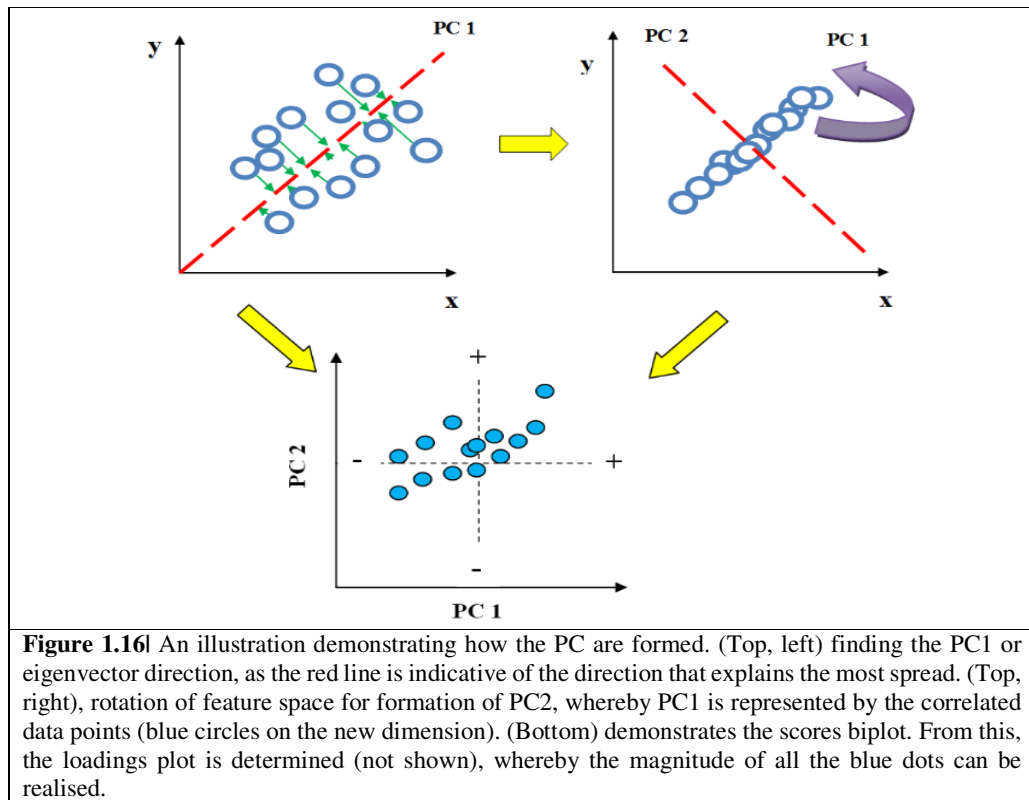


**Figure 1.15!** The conversion of the original data matrix ( $p \times n$ ) into the new matrix of ( $X$ ) to formulate the  $k$  PCs. Adapted from reference [47].

For PCA interpretation, eigenvector plots can be termed '*scores*' and correspondingly, its eigenvalues are its '*loadings*'. To relate this back to spectroscopy, the superimposable and complementary scores and loadings correlate to the row and column vectors, respectively [47].

PCA can achieve this by firstly taking the mean centre of the data, so to move the zero point to the centre of the data cloud. It then transforms the cloud of data points in  $k$  space and rotates the space until the data is uncorrelated and creates a new singular dimension (the eigenvector/value pairings), acts like a ruler line, whereby the new data points lie on the planes' direction. Figure 1.16 demonstrates how the new orthogonal directions are found in PCA.



### 1.5.2 Hierarchical Cluster Analysis (HCA)

Hierarchical Cluster Analysis (HCA) is unsupervised ensemble clustering technique which finds classifications of data groups without *a priori* information. It clusters the data into a dendrogram (tree) and each object is compared with the each other *via* the Euclidean distance calculation and in our case Ward's algorithm for agglomerative dendrograms [48]. Essentially clustering similar distance measurements under one branch of the tree until it finds the most heterogeneous data clusters in a graphical representation. Figure 1.17 demonstrates a graphical representation of HCA.

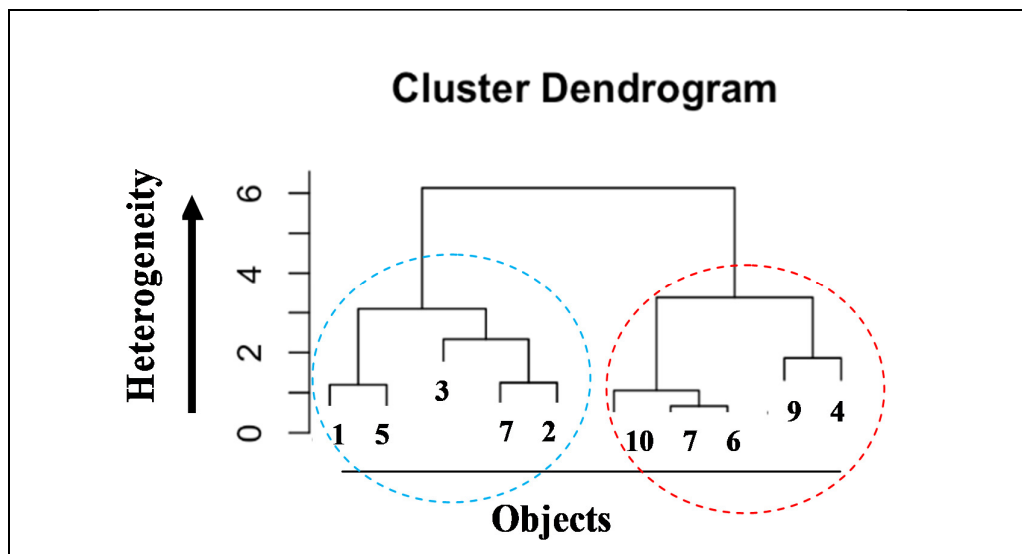
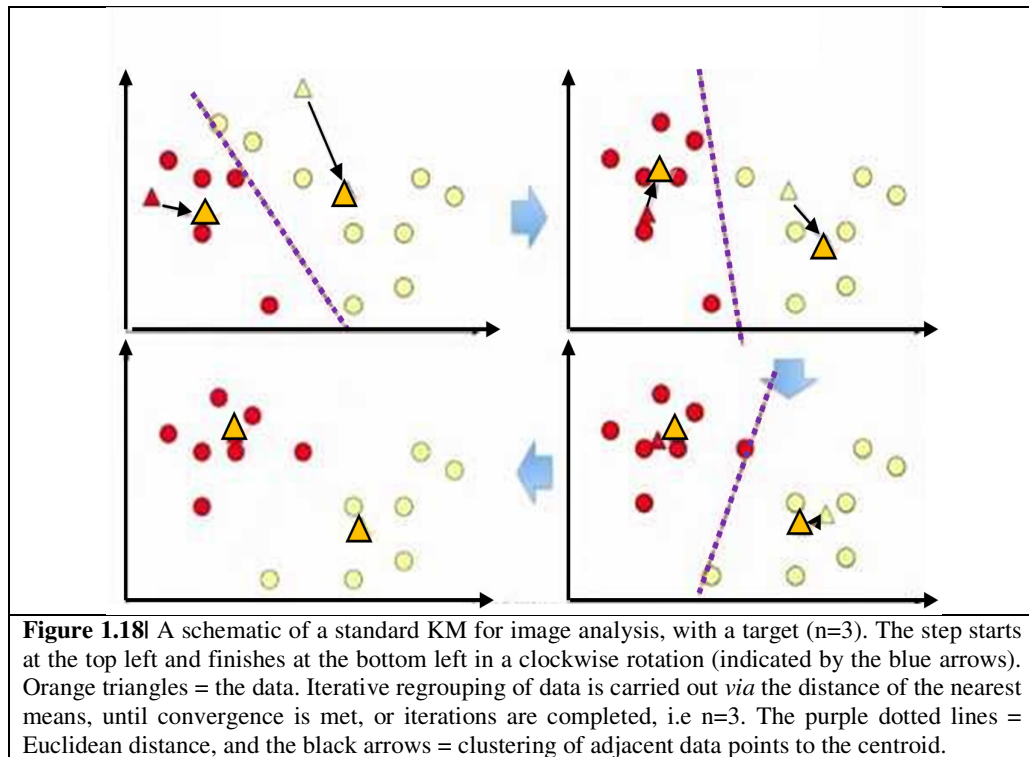


**Figure 1.17** An example of an HCA dendrogram using Ward's algorithm [48]. The objects are classified based on the degree of dissimilarity as a function of Euclidean distance; increasing heterogeneity until convergence of both clusters is reached.

### 1.5.3 K means Cluster Analysis (KM)

*K*-means clustering (KM) [49] is an unsupervised data clustering technique, which aims at partitioning the data into *k* clusters in which each data point belongs to the cluster with the nearest mean. The initial *k*-means are randomly assigned based on the user input of the number of target *k* clusters. This indicates the number of centroids the model looks for, which then uses the Euclidean distance in an iterative approach to group cases in a dataset into clusters. Such clusters contain similar features/characteristics. The algorithm achieves this while minimising the within-cluster sum of squares. The process is halted, and no more refinements of the centroids are computed when a point of convergence is reached, or the algorithm completes the target number. Once completed, for image analysis, the algorithm randomly assigns colours to the clusters, building a visual representation of the physical/chemical homogeneities within the sample. Figure 1.18 shows a step-wise approach to KM clustering.



#### 1.5.4 Principal Components - Discriminant Function Analysis (PC-DFA)

DFA is a supervised data prediction technique, which uses linear combinations inherent within the data matrix to help determine the greatest separation, whilst accounting for *a priori* information, such as class, disease state, or sample differences due to pre-analytical variation, *i.e.*, freeze-thaw and drying etc. The orientation of the combinations means that it increases class membership and reduces class variation, *i.e.*, maximizes between (B) and minimizes within (W) the data groups (Figure 1.19). DFA, canonical variates analysis (CVA) and linear discriminant analysis (LDA) are all very similar as they are based on Fisher's linear discrimination, but there is no assumption of normally distributed classes in DFA [50].

As PCs are orthogonal aspects of the data, when combining with DFA, DFs are combinations of those PCs that best describe an *a priori* class structure, or more simply, DFA identifies proportions of the PCs that best match known classes of samples.

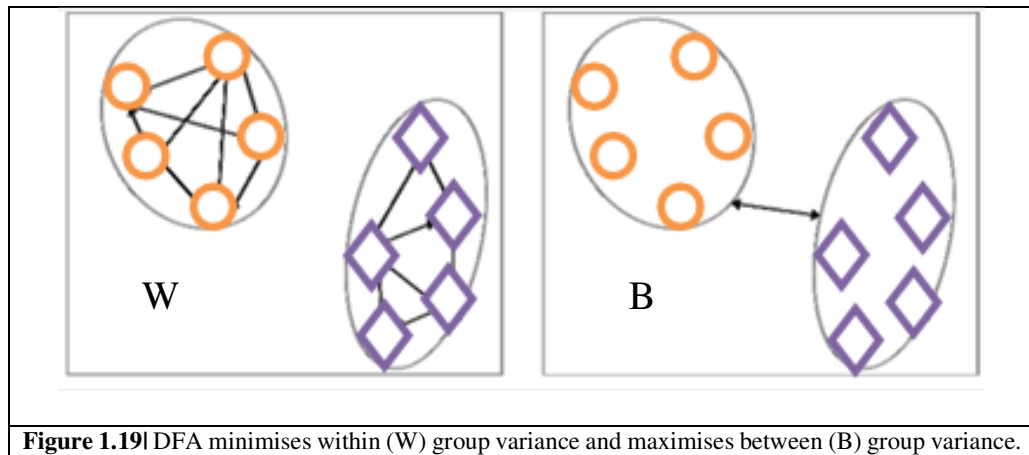
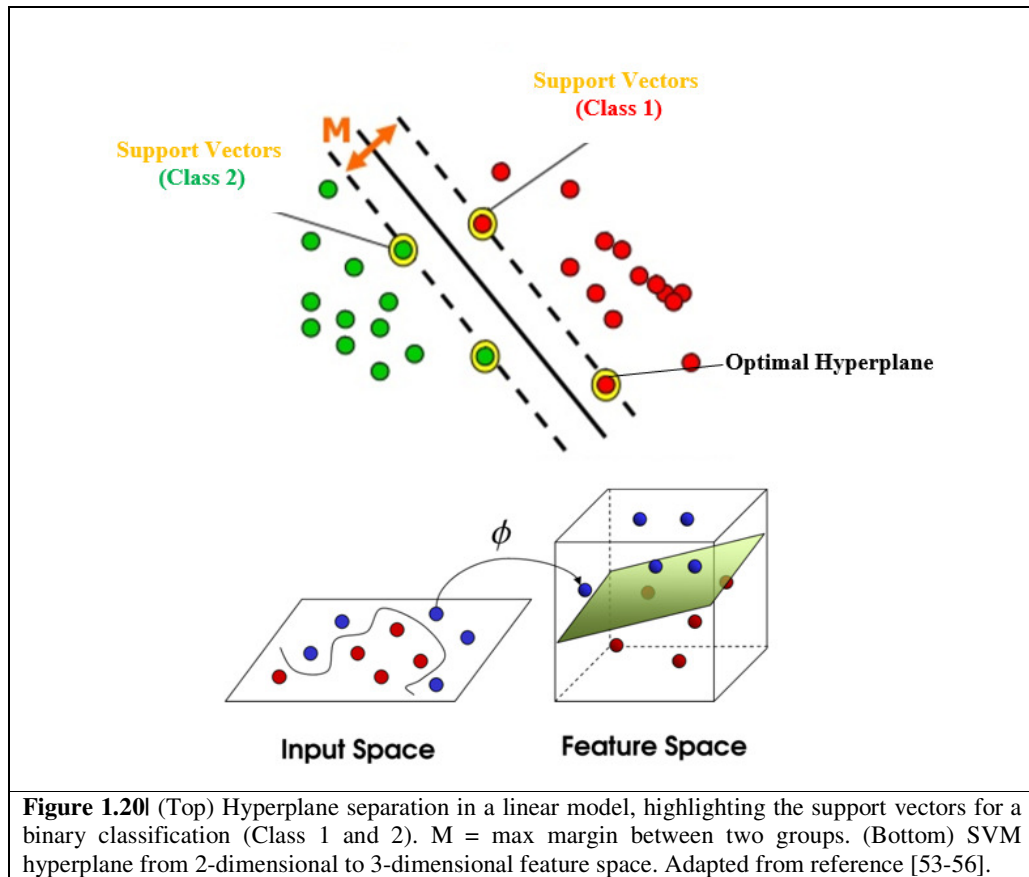


**Figure 1.19** DFA minimises within (W) group variance and maximises between (B) group variance.

PC-DFA is carried out by firstly, randomly forming testing and training groups (in our case – a 1/3 test and 2/3 train). The training data is used to build the model. The test data is then projected in to the DF space and the correct matches of test on train per data/patient etc., are noted. It is important to keep in mind that the user should define the number of PCs to be projected in to the prediction, as well as the number of DF feature spaces. Like LDA, DFA has been heavily debated in deciding which is the correct number to choose. One method to use is Cattell’s scree plot, or selection of the PCs that account for a fixed level of variance, such as 99.99% explained variance [51-52]. Additional methods include Kaiser’s rule or variable ranking methods; whatever is employed, careful consideration is important, as the data will appear not as true in some respects. For example, PC-DFA always aims to find some element of separation, that is the basis of the algorithm, but one should keep in mind that a good choice of the correct parameters will enable more robust predictions/classifications.

### 1.5.5 Support Vector Machine (SVM)

A Support Vector Machine (SVM) [53] is a supervised method for pattern recognition whereby a hyperplane is fitted between the groups of data based upon the best discrimination of a training set. This hyperplane can be visualised as a wave line but when transposed to the feature space it represents a 3-dimensional plane between the groups. Figure 1.20 shows the hyperplane in both 2-dimensional input space and 3-dimensional feature space.



Support vectors are the boundary data points lying closest to the hyperplane. These eventually become the training set for the classification. The hyperplane is significant as a choice lying closest to one group and not the other does not generalise well and will easily misclassify. The best hyperplane is found at the point furthest away from the groups.

Often in real world examples, data will not be so easily separated and a non-linear SVM is required. To deal with this a kernel is used. A kernel is a similarity function that allows one to observe how similar one class is to another. The most common kernels available are radial basis function (RBF), polynomial and sigmoidal [55-56]. SVMs can be further divided into two categories; hard and soft margin SVMs. The first requires two classes of data to be entirely separable, whereas the latter allows more misclassification with the use of slack variables, whilst still maintaining the robustness of the classification degree.

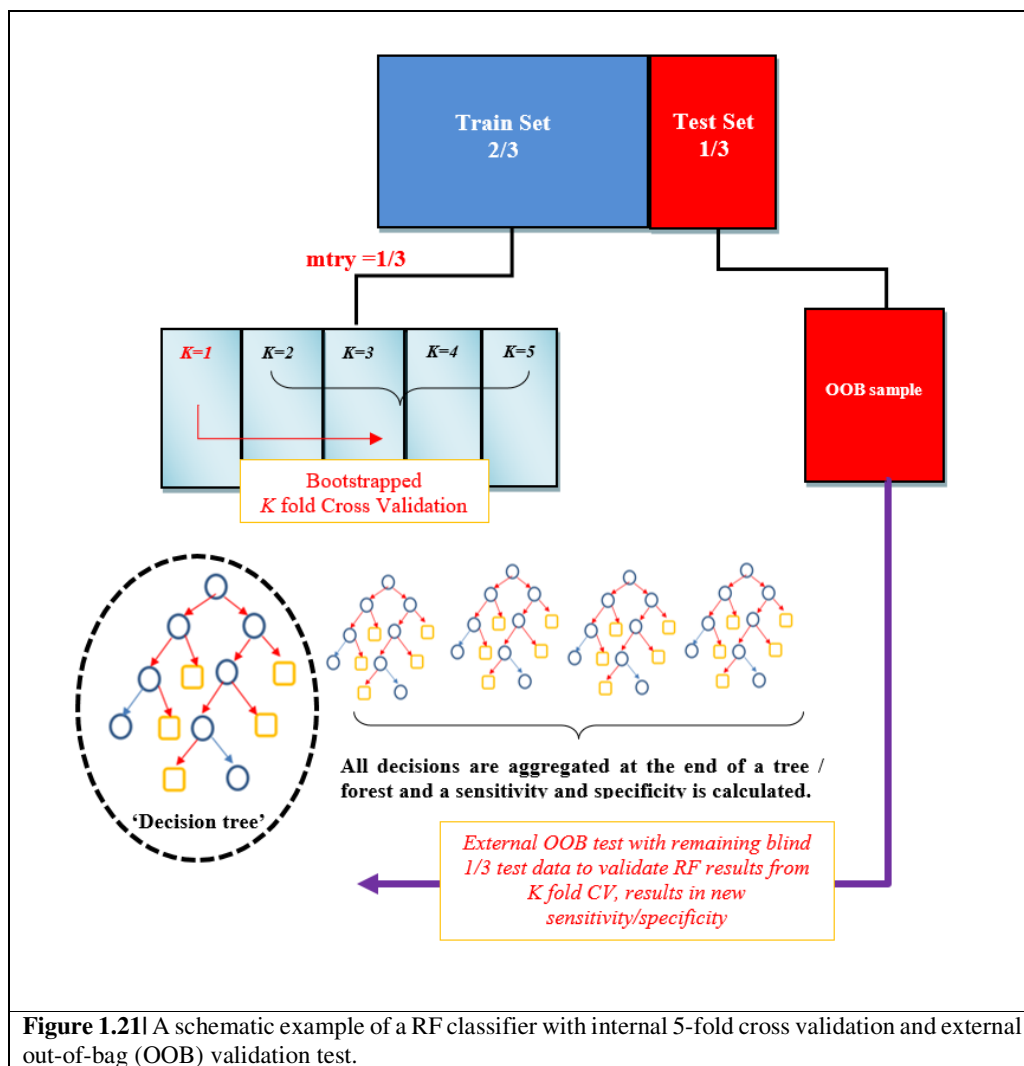
There are two additional features used with non-linear SVMs, which are beneficial; the parameters cost  $C$ , and gamma  $\gamma$ . The  $C$  parameter is a measure of the level of tolerance which a model should allow a misclassification, *i.e.*, a larger  $C$  value means a lower tolerance and the more complex boundaries. A high  $C$  is often seen with hard SVMs and results in a higher

misclassification rate [56]. The  $\gamma$  parameter is a measure or degree of flexibility and curvature of the hyperplane's boundary. This should be married well with the  $C$  function as to ascertain the best results for the classification. Ideally, what we want is for each of  $C$  parameter to be explored with all the  $\gamma$  values and *vice versa*, until the optimum tuning parameters are reached.

### 1.5.6 Random Forest Classifiers (RF)

Random Forest (RF) [57] is an ensemble machine learning algorithm of building a forest of uncorrelated decision trees or classification and regression trees (CART). A classification CART is of interest in this research.

RF builds many trees using a subset of data, i.e the training data set, of which a third of the data is chosen at random ( $m_{try} = 1/3$ ). From this it generates random features and variables for splitting the tree at the node level *i.e.*, it asks itself a question to find a binary split. For spectroscopic data, it may ask if datum  $x$  is greater in intensity/absorbance at specific wavenumber, *e.g.* at  $1000\text{ cm}^{-1}$  is an aspect of the training data greater than 0.2 absorbance? The node is then split into branches with a yes or no result. Each node then uses other randomised variables and features to keep splitting the branches of the tree until all variables are explored and eventually a decision tree based on classification is formed, *e.g.* what percentage of the starting diseased group is seen to be '*diseased*' based on spectral decision/variables. It does this by taking the decisions at the 'petals' or terminal ends of the trees/forest and aggregating a modal result. It continues to build  $\sim 500$  trees, until a forest is produced. Randomness is key to RF classifiers – each tree is trained using a random sample with replacement from the training set. Plus, when training individual trees, randomised variables and features subsets of features are used searching for splits. This reduces the correlation among trees in the forest, which improves predictive performance. Figure 1.21 demonstrates how the RF classifier works with a K fold cross validation with bootstrapping.



In this research, an RF classifier was used to find the most salient wavenumber aspects to take forward for an SVM analysis, using a Gini impurity importance index or Gini index [57]. As a classifier, RF performs a strong feature selection using only a small subset of strong variables for classification [57-58]. At each node within the binary split, the optimum split is found using the Gini index –a measure of the node split of the two classes per node, as a reference of impurity. The Gini index then aggregates all impurity measures of all trees/forest and produces a modal frequency, as to ascertain only the salient features within the data, *e.g.* the most discriminating wavenumbers.

## INTRODUCTION TO CLINICAL BIOSPECTROSCOPY

This section provides a review of current research in the field of clinical biospectroscopy and its use towards biofluid analysis and disease characterisation. A large proportion of this content was published in the Chemical Society Reviews, 2016, volume 45; 1803-1818, DOI:10.1039/C5CS00585J [6].

### 1.6. BIOMEDICAL VIBRATIONAL SPECTROSCOPY

IR and Raman spectroscopies are complementary as they both provide a ‘fingerprint’ or “signature” of the molecules within a sample depending on whether their bonds exhibit Raman or IR activities. Due to the unique molecular fingerprints obtained, Raman and infrared spectroscopies hold great promise in disease diagnostics.

The field has a rich history and the first disease-state diagnostic application was attempted by physicians in the mid-1800’s [59]. The late 1940’s saw work on nucleic acids and protein folding by [60-62] to present day research on tissues, cells and various other small molecules by pioneers, such as Mantsch, Naumann and Diem.

Vibrational biophotonic techniques are used widely in research and development of new areas of healthcare; with more than a decade dedicated to discerning snapshots of disease mechanisms probed in cells and tissues [62]. Meanwhile, a continuing effort for cell and tissue spectroscopy has established the fields of spectral cytology and spectral histology [6, 63-64]. However, there is a lack of standardisation, validation in large clinical trials and multicentre actions, combined with the limitations of ethical approval for large scale data trials. This means true clinical translation is hampered somewhat. Nonetheless, the quest for disease markers *via* ‘liquid biopsies’ is quickly becoming an emergent technology with untold potential.

It is common practice to screen blood for disease states and only a few studies have explored spectroscopic approaches. The coupling of Fourier transform to the spectrometer, affords gains in detector sensitivity, advances in data processing techniques, and to rapidly acquire data for signature of disease. Additionally, the field has the potential to perhaps embed into current clinical practice. Ultimately, this would bring more efficient public services, significant economic savings, improved patient outcomes and marked reduction in morbidity and mortality.

### 1.7. BIOFLUIDS AND DISEASE

Blood components like serum and plasma are routinely used in the clinics as they contain biomarkers that are useful for disease diagnostics [6]. In the field of cancer diagnosis, they are known to be a rich source of information and represent readouts of the ongoing cellular and extracellular events [65]. Furthermore, they are easily accessible and minimally invasive for

patients making large studies feasible. Recent trends indicate that the use of either a single or few biomarkers have fallen out of favour for multiple biomarkers for disease progression [66]. In this context, the role of vibrational spectroscopic methods can be determinant as the information provided contains pathophysiological readouts on biomolecular composition providing a chemical fingerprint or biofluid ‘signature’.

### **1.7.1 Biofluids and Disease Markers**

The ability to detect biochemical or morphological changes at the prodromal disease stage is paramount for the effective use of the therapeutic window. Moreover, the detection of biomarkers plays an important role in this exploration. The faster and earlier a disease can be detected the better treatment can take full advantage of therapeutic intervention. For cancer specifically, there is a broad range of such biochemical entities including proteins, nucleic acids, lipids, carbohydrates, small metabolites, and cytogenetic and cytokinetic parameters, as well as entire circulating tumour cells (CTCs) housed in biofluids. The search for disease markers is fast emerging in vibrational spectroscopy. The focus has been on serum and plasma, owing to the prevalence of these samples within current biobanks and that ethical approval is already well established for their collection and use of these biological samples in the detection of novel compounds associated with diseases.

## **1.8. CANCER**

### **1.8.1 Cancer Prevalence, Survival and Mortality**

Cancer prevalence has significantly changed within the last five years and is set to rise to 4 million people in the UK by 2030 [67]. Currently, within the UK there are 2.5 million people living with cancer, with England accounting for 80% of this statistic [68]. It is said that 1 in 2 people will be diagnosed with the disease at some point in their lives and that cancer survival is three times higher when diagnosed early [69]. Of the eight most common cancers (accounting for 40% of all cancer in the UK), about 25% of them are diagnosed late (at stage 3 or 4) and around 25% of patients survive for less than 10 years [70].

Global cancer rates are also on the increase, with Denmark having the highest incidence of cancers in females (325.3 per 100 000) and an overall cancer rate of 326.1 per 100 000. According to the World Cancer Research Foundation, France has the second highest incidence; having the highest incidence in males (360.6). This is 6th in the world (300.4), whereas the UK places at 22nd (266.9) globally [71]. Although cancer mortality rates have decreased in France over the last twenty years, it remains the biggest cause of death, with 148 000 deaths in 2012 [70].

### 1.8.2 Cancer Biology

Cancer is the unregulated growth of cells, occurring due to mutations in our normal cell renewal process. Errors at the DNA replication stage can lead to genetic instability and eventually physical changes within the body. Such changes affect the nucleotides. These nitrogenous-sugar molecules provide the building blocks of life and are often denoted as A (adenine), T (thymine), C (cytosine) and G (guanine) in DNA. A build-up of changes within these molecules can lead to the development of cancer, which is manifested in the cell cycle (see Figure 1.22). Hence, most cancer drugs target selective areas of the cell cycle to inhibit growth [72]. Our internal cellular machinery has developed '*checkpoints*' in which to apprehend such mutations both before and after genetic replication. These so-called G (gap/growth) phases are the cells signal to halt all processes if genetic damage is detected. At cellular renewal, it (cell cycle), undergoes the following phases G1, S, G2, collectively known as Interphase, followed by mitosis in eukaryotes. Before entering mitosis, these checkpoints routinely check for unfamiliar changes within the DNA architecture and provide corrective changes or cellular arrest (G0). If DNA damage is unobserved, the result is often abnormal DNA with the wrong number of chromosomes, and continued aberrant division leading to gene mutations, hence, tumour formation.

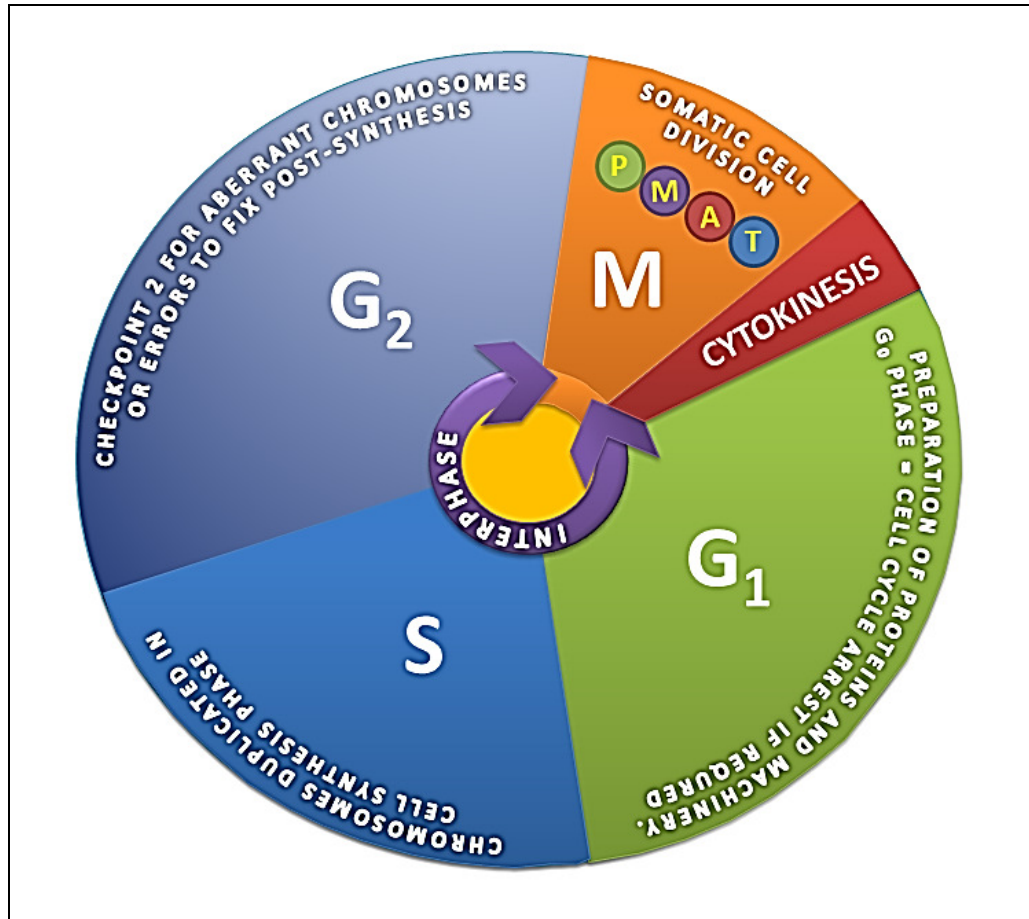


**Figure 1.22** A schematic showing the cell cyclic phases during somatic cell division. These include Interphase (G<sub>1</sub>, S and G<sub>2</sub>; if required G<sub>0</sub> or cellular arrest) and its automated genetic ‘checkpoints’ leading into cell division (Mitosis), which follows a series of known sequential steps; Prophase, Metaphase, Anaphase and Telophase, to generate two sets of daughter cells. Adapted from references [72-73].

### 1.8.3 Hallmarks of Cancer

Unregulated and uncontrolled cellular growth is due to the ‘molecular switch’ of two very important regulatory genes (proto-oncogenes and tumour suppressors). These genes play important roles in transcription and translation of genetic material. Oncogenes in their precursor stage (proto-oncogenes) are responsible for the smooth running of cell division and replication cycle, meaning the ‘switch’ is in normal operation, sending signals in the form of transcription factors (*myc*), including signal transduction molecules (*ras*) or growth factors such as (HER-2/neu) etc. This leads to an increase in cell proliferation, in a regulated way [73-74]. However, when one of the two pairs of proto-oncogenes become defective or mutated, then the molecular switch is left in the on-position. This means that the signals are sent from the oncogene to drive the cell renewal process (unregulated), leading to masses of defective genes, thus resulting in

tumorigenic cell growth. Tumour suppressor genes are the cells halting machinery. They function to stop aberrant cell division, and when a single gene of a pair is defective, it still copes with the task. However, when both pairs are defective by mutation or loss of gene function, then the molecular switch is left on. Examples of tumour suppressor genes and their prevalence in cancers are widely known, they include p53 (bladder, colorectal, breast, liver, brain tumours, *etc.*), BRCA1, BRCA2 (inherited breast and ovarian cancers) and APC (familial adenomatous and non-inherited colorectal carcinomas) [74].

Seminal works have indicated that cancer cells have six distinct capabilities [75].

1. Insensitive to inhibitory growth signals
2. Self-sufficient in growth signals
3. Avoids programmed cell death or apoptosis
4. Replication is indefinite
5. Induces angiogenesis/ vascularization spreading to adjoining tissues *via* metastasis
6. Deregulates of cellular metabolism and an innate ability to evade immune destruction [76]

## **1.9. LIVER DISEASE & PRIMARY LIVER CANCER**

The liver is a large complex organ capable of regeneration, which has around 500 different roles, such as blood cleansing and filtering, bile and amino acid production and toxin breakdown, including drugs and alcohol and a whole of host of other major integral functions.

### **1.9.1 Hepatic Fibrosis and Cirrhosis**

Hepatic fibrosis (HF or liver fibrosis, LF) is the result of the wound-healing response of the liver to repeated injury [77], such as viral hepatitis or non-alcoholic steatohepatitis (NASH) [78]. The body's natural defence initiates an inflammatory response, which leads to the decreasing amounts of extracellular matrix (ECM) proteins at the injury site, allowing necrotic/apoptotic cells to be replaced with new parenchymal cells of the liver. However, if injury is persistent liver regeneration eventually fails; the hepatocytes are substituted with an abundance of ECM, such as fibrillar collagen. HF advances from collagen bands to bridging fibrosis to end-stage cirrhosis [79].

Fibrosis is graded on a 5-point scale from F0 to F4. The activity, which is the amount of inflammation (specifically, the intensity of necroinflammatory lesions), is graded on a 4-point scale from A0 to A3 (Table 1.2).

**Table 1.2| METAVIR Score System.**

<b>Histological Activity:</b> <i>(Degree of Necrosis)</i>	<b>Fibrosis Stage</b> <i>(Degree of Inflammation/Scarring)</i>
A0 = no activity	F0 = no fibrosis
A1 = mild activity	F1 = expansion of portal zones
A2 = moderate activity	F2 = expansion of most portal zones and occasional bridging
A3 = severe activity	F3 = expansion of most portal zones, marked bridging and occasional nodules
	F4 = cirrhosis (end-stage irreversible scarring)

Chronic hepatitis C viral infection (cHCV) is the leading cause of liver cirrhosis and hepatocellular carcinoma (HCC) worldwide [79]. In cHCV, liver biopsies are considered the gold standard for diagnosing HF, however, it is an invasive diagnostic technique with associated morbidity, possible mortality, relatively high costs, and potential sampling error/interobserver variation [80-82].

The need for correct classification of LF is imperative as it is a precursor for more advanced liver disease, such as cirrhosis and liver cancer. Current screening regimes are still without a true gold standard [81] and warrant further development. Two techniques, Fibro Test and Fibro Scan are routine, and to date have shown good diagnostic accuracy at advanced fibrosis stages [82].

Cirrhosis is characterised by a thick enlarged hard-to-touch, richly scarred appearance of the liver, which is the necrosis of the liver functional units or hepatocytes. Because of liver damage, the hepatocytes form regenerative nodules (colonies of cells), which are surrounded by fibrotic tissue and excess collagen.

The cells responsible for this formation are the stellate cells, which in functioning tissue, are dormant vitamin A stores. Usually, the cells are housed in the perisinusoidal space (between the bile duct and the portal triad). Hepatocytes are situated around the bile duct and one side of the portal triad. The portal triad is the sinusoidal area where the portal vein, hepatic artery both converges towards the central vein, which is located at the centre of each hepatocyte [83].

Upon injury, however, the stellate cells become active and start to trigger a paracrine response for secreting TGF- $\beta$  into the perisinusoidal space, which induces the overproduction of collagen fibres and results in the formation of fibrotic networks. Eventually, with increased injury the perisinusoidal space becomes thicker with scar tissue and leads to further compression of the sinusoid, until pressure seeps out and causes fluid to build up in the peritoneal cavity. The response of which causes anti-diuretic hormone (ADH) and aldosterone to be overstimulated,

leading to various complication including ascites or swelling of the abdomen [84]. Ascites are very common in chronic alcoholic patients.

### **1.9.2 Hepatocellular Carcinoma (HCC)**

Hepatocellular carcinoma (HCC) is a primary cancer of the liver and is regarded as one of the most common cancers globally, and the third leading cause of cancer mortality [84]. In France, it is the second digestive cancer after colorectal. Over the last few decades, its incidence has increased in both sexes in France (4.8% in males and 3.4% in females, respectively) [85]. HCC is the biggest cause of mortality in cases of cirrhosis and is developed through stages from chronic hepatitis, fibrosis and cirrhosis, (approximately 80% of cases become cancerous) [84-86].

Its aetiology includes, viral inflammation from hepatitis B (HBV) and C (HCV), or aflatoxin B1 [87] (fungal epitope associated with peanuts stored for long periods), abuse of cigarette smoke and heavy alcohol consumption [88-89]. Genetic factors are attributed to an iron-overloading disease called haemochromatosis, Wilson's disease [90] and various porphyrias (rare metabolic abnormality of haemoglobin) [90-91].

#### *1.9.2.1 Hepatocarcinogenesis*

Known for its complex molecular pathogenesis, the hepatocarcinogenic lifespan is between 10 and 30 years [92-93] with primary initiation of external stimuli precluding genetic changes within the hepatocytes. It eventually causes cell suicide and up-regulation of the mitotic pathway at stages of fibrosis and cirrhosis [93]. From pre-neoplastic transformation to moderately differentiated HCC, the process is multi-stepped. It starts from focal hyperplasia (FH) due to some stimulus, like viral (HBV or HCV), alcohol or NAFLD (non-alcoholic fatty liver disease), etc., to low-grade and high-grade nodule dysplasia (LGDN and HGDN) [93-95]. Together, they result in moderately differentiated HCC, which has metastatic tendencies (see Figure 1.23).

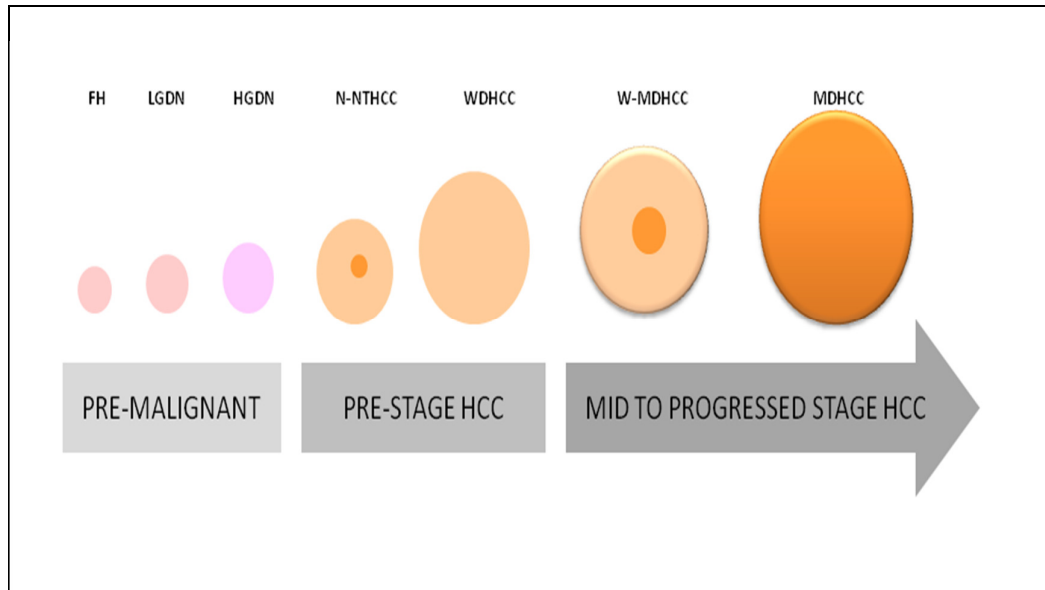


**Figure 1.23** The multi-stage process of human hepatocellular carcinogenesis from pre-neoplastic aspects to full malignancy, which would infer metastases. FH – Focal Hyperplasia, LGDN – Low Grade Dysplastic Nodule, HGDN – High Grade Dysplastic Nodule, N-NTHCC – Nodule-in-Nodule Type Hepatocellular Carcinoma, WDHCC – Well Differentiated HCC, W-MDHCC – Well to Moderate Differentiated HCC, MDHCC – Moderately Differentiated HCC. Adapted from [93-97].

### 1.9.2.2 HCC Tumour Staging

Early diagnosis of disease means a better therapeutic window and stronger prognosis of the disease course. There is an accepted protocol to grade or stage a tumour based on the size of a mass and histological appearance. However, HCC staging has further attributes to consider. According to recent EASL guidance [96], owing to its highly complex cancer progression and patients having insidious cirrhosis, four related aspects are proposed. These include tumour stage, severity of liver function impairment, patient wellbeing and treatment efficacy [97]. Whilst the traditional TNM classification system is employed to demonstrate prognostic relevance in hepatic cancers, it does not take it in to consideration the choice of therapy and specific staging of HCC. In addition, whilst most patients often have unresectable tumoural disease, then surgery is no longer an option. However, there is a collaboration of staging systems that are currently under practise, but with no consensus. Such systems aim to treat the disease based on the physiological status of the patient and the size of the growing tumour whilst incorporation of clinical features. One of them is the performance status [98]. Europe-wide is the Barcelona Clinic Liver Cancer system (BCLC) [98-99]. This system divides patients in to 5 stages of severity (0, A, B, C, D), with reliance from TNM, *I-IV* staging, and status of liver function with the CLIP (Cancer of the Liver Italian Programme), this includes the Child-Pugh's score, in combination with the WHO score, liver enzyme levels, and tumour morphology, denoting a performance status of the individual by assigning a number between 0-5 (0 is healthy

and 5 is death) [99-100]. With the derived algorithm, one can assign the best course of action at whichever stage the disease course presents. There is no all-encompassing staging algorithm to take in to consideration the umbrella aspects of liver function and tumour function (see Figure 1.24). Moreover, none of them take in to consideration the complex tumour biology.

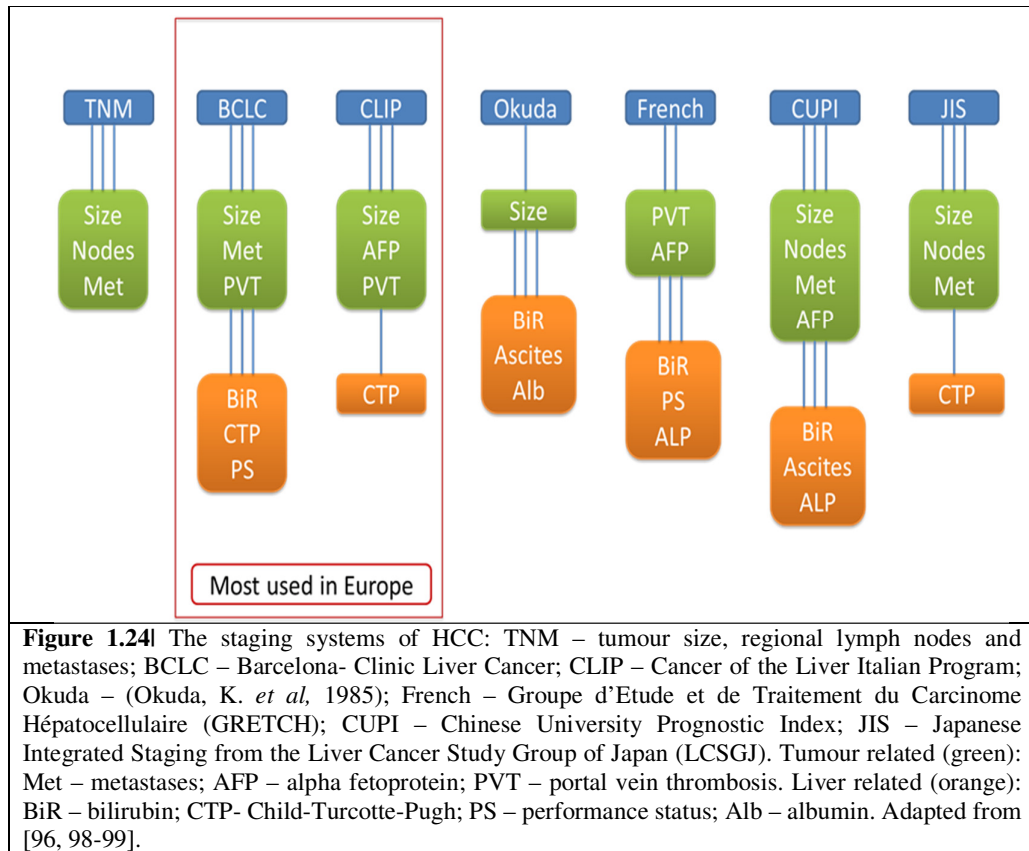


**Figure 1.24** The staging systems of HCC: TNM – tumour size, regional lymph nodes and metastases; BCLC – Barcelona- Clinic Liver Cancer; CLIP – Cancer of the Liver Italian Program; Okuda – (Okuda, K. *et al.*, 1985); French – Groupe d’Etude et de Traitement du Carcinome Hépatocellulaire (GRETCH); CUPI – Chinese University Prognostic Index; JIS – Japanese Integrated Staging from the Liver Cancer Study Group of Japan (LCSGJ). Tumour related (green): Met – metastases; AFP – alpha fetoprotein; PVT – portal vein thrombosis. Liver related (orange): BiR – bilirubin; CTP- Child-Turcotte-Pugh; PS – performance status; Alb – albumin. Adapted from [96, 98-99].

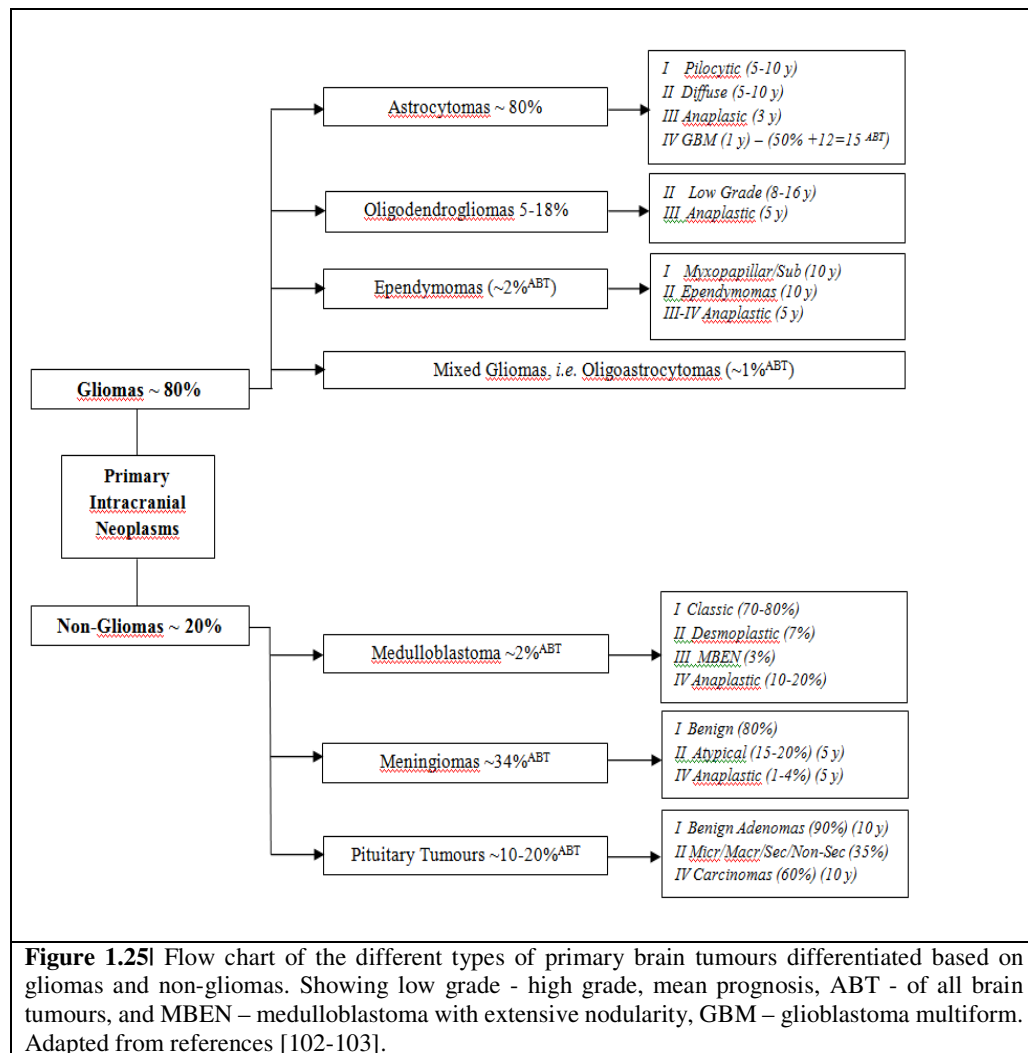
As shown above, in Figure 1.24, most staging classification systems focus on the tumour state itself, with the majority incorporating some aspect of the TNM staging criteria. Whilst each system has its merits as cited in the literature, there is none so well as described in a recent review [99]. Nevertheless, this brings to the forefront the serious drawback amongst the classifications.

### 1.10. PRIMARY BRAIN TUMOURS

There are about 130 different types of brain tumours, but the majority are benign, only a subset becoming malignant [100]. Primary intracranial neoplasms (ICN or brain tumours) are tumours whose origin is the brain, and glial tumours or gliomas account for 30-40% of all ICNs [101].

Gliomas are differentiated depending on where the glial tumours are located [102]. Figure 1.25 demonstrates a flowchart of the different types of primary brain tumours based glioma and non-glioma type.

In some cases, the tumour may originate outside of the brain, *i.e.*, in the lungs, this is known as a secondary metastatic ICN. The most common origins for secondary sites are the lungs, skin, colon, breast and kidney [68].



### 1.10.1 Tumour Classification and Grading

The WHO classification of ICNs is based on 4 main criteria. These include increased cellularity, nuclear atypia, endothelial proliferation and necrosis, they are generally defined as stage I, II, III and IV, respectively. Figure 1.26 shows a modified version of the stages.

	<u>Grade I</u>	<u>Grade II</u>	<u>Grade III</u>	<u>Grade IV</u>
<u>Cellularity</u>	Normal and slow-growing	Atypical and relatively slow-growing	Abnormal and actively reproducing	Abnormal-rapidly reproducing/growing
<u>Malignancy</u>	No	No	Infiltrate adjacent tissues	Most malignant
<u>Metastases</u>	No	Possibility of invading adjacent structures	Tumour spread to neighbouring tissues	Formation of new blood vessels and actively spreads
<u>Necrosis/Recur</u>	No/No	No/Possibility	No/Yes	Areas of dead cells in the center/N.A

**PROGNOSIS DETERIORATES**

**Figure 1.26f** Tumour grading in relation to visible observations according to the WHO (2007) for intracranial neoplasms. Graded I to IV (shaded to demonstrate prognosis is worse as grade increases). Adapted from reference [104].

Most cancers found in the brain are a result of the invasion of neighbouring tissues and distal metastases. These are approximately 10 times more common compared to primary brain tumours. Generally, ICNs are histologically quite different and are classified based on whether they are high-grade (aggressive and rapid growth/spread) or low-grade (controlled (*via* medication) slow growing). However, low-grade tumours can be uncharacteristic and may not respond effectively to treatment. Hence, the reason is that there is no clear line between benign and malignant when discerning ICNs. Low grade tumours account for the most numerate, such as pituitary tumours, acoustic neuromas, meningiomas and pineal tumours, whereas high-grade tumours are essentially gliomas and GBM, medulloblastomas and primary cerebral lymphomas, these are very aggressive growing tumours with associated very high mortalities [102-104].

Dependent upon early presentation of symptoms for any brain tumour, the patient is pushed through a series of treatment regimes. These include many blood tests, imaging techniques to visualize and aid diagnosis, such as MRI, CT scans, *etc.*, invasive surgery to perform biopsies or tumoural resection. These are often followed by a cocktail of drugs, radiation (sometimes proton beam therapy) and other adjuvant therapies such as photodynamic therapy. However, currently, it does not fall within the parameters set by other studies [105].

## 1.11. CURRENT CLINICAL VIBRATIONAL SPECTROSCOPY

### 1.11.1 Clinical Infrared Biofluid Spectroscopy

The use of IR and Raman spectroscopies to analyse and detect disease signatures from biofluids is a relatively new field. Recently, the use of transmission high-throughput-Fourier transform spectroscopy (HT-FTIR) has shown good diagnostic accuracy in disease classification. One study used linear discriminant analysis (LDA) and random forest (RF) classifiers to discriminate urinary bladder cancer from patients with UTIs with accuracy between 85% and 92% [106]. Backhaus *et al.* [107], using serum, successfully discriminated between breast cancer and controls with 93% sensitivity and 96% specificity. Cirrhotic patients either with or without hepatocellular carcinoma were successfully distinguished by combining support vector machine (SVM) and leave-one-out cross validation (LOOCV), achieving accuracy of between 85% and 87% [28]. Very high sensitivity (95.2%) and specificity (100%) values were achieved using FTIR serum analysis to discern differences in the degrees of liver fibrosis using only discriminant wavenumbers [29]. ATR-FTIR spectroscopy, coupled with classification machine, discriminated ovarian [107] and endometrial cancers [109] with diagnostic accuracies of 93.3% and 81.7%, respectively. Hands *et al.* [110] could differentiate between glioblastoma multiform (GBM) and low grade gliomas from controls of serum, demonstrating accuracies between 87.5% and 100%. They reported high percentage accuracies in the mid-90s for diagnosing low grade and high-grade gliomas (GBM) and non-cancer controls [111].

To date, IR analysis of serum has allowed for the identification of markers of bovine spongiform encephalopathy ante-mortem [112-114], rheumatoid arthritis [115], and beta-thalassemia [116]. In addition, it has been used as a prognostic tool to determine the severity of acute pancreatitis [117]. All these studies have achieved diagnostic accuracies between 74% and 100%. More recently, interest has also been reported for the determination of protein in the serum [118] and the distinction of patients with a leukaemia from blood samples [119].

A range of samples of biomedical interest have been reported in recent times. Peuchant *et al.* [120] used the FTIR spectroscopy analysis of plasma from patients with Alzheimer's syndrome to demonstrate the possibility of delineating the disease from normal ageing subjects used as controls. Hierarchical classification in the mid-IR region showed very good separation between controls and Alzheimer's, with spectral discrimination owed to biochemical nuances in lipid and nucleic acid structures. This is indicative in oxidative stress mechanisms of Alzheimer's. A more recent study could grade severities of the disease using plasma, with high accuracies being reported [121]. Griebe *et al.* [122] were able, using FTIR spectroscopy, to distinguish patients

with Alzheimer's disease from healthy controls using cerebrospinal fluid, with sensitivity and specificity of 99% and 86%, respectively.

Most recently, a study showed good sensitivities (87%) and specificities (96%) for the detection of neonatal galactosemia and diabetes from healthy controls using HT-FTIR combined with SVM-LOOCV machine learning [123]. Thus far, the focus for biofluid work has been on plasma and serum, but some studies have shown efficacy using bile, urine, tears, synovial fluid, and amniotic fluid. Combining HT-FTIR with SVM-LOOCV, a study completed on bile samples achieved sensitivities of 82% and 95% and specificities between 85% and 100% for discriminating patients with and without malignant biliary strictures [124]. Work on synovial fluid could differentiate samples from arthritic joints affected by rheumatoid arthritis, osteoarthritis, spondyloarthropathies and meniscal injuries using FTIR spectroscopy coupled with LDA-LOOCV, which demonstrated 96.5% correct classification [125].

FTIR spectroscopy associated with LDA on saliva, correctly classified diabetic patients from healthy controls with 100% overall accuracy for the training set and 88.2% for the test set [126]. Additionally, an exploratory study demonstrated FTIR spectroscopy analysis of sputum could be a useful approach for the diagnosis of chronic obstructive pulmonary disease (COPD), based on slight alterations in the spectral regions of amide I and II plus the glycogen rich aspects [127].

Investigating the potential of human tears for the diagnosis of ocular diseases, Travo *et al.* [128] have shown discrimination of patients with keratoconus from healthy controls. This is a degenerative disorder affecting the cornea. They also discriminated between patients at an early or advanced stage of disease by using HT-FTIR and PCA, with a statistical significance ( $p < 0.0001$ ), owing to the lipid and carbohydrate regions.

Prenatal disorders from amniotic fluids have also been investigated by ATR-FTIR spectroscopy revealing spectral profile changes between amniotic fluids from pregnancies with foetal malformations, preterm delivery and healthy term pregnancies [129]. In other work, Liu *et al.* [130] investigated the amniotic fluid potential for foetal lung development assessments by IR spectroscopy. They reported by way of a multivariate technique of PLS regression and calibration models, good outcomes for two components (glucose and lactate).

Whilst there has been some considerable work in the field, unfortunately, only a few large studies have been reported. A study by Petrich *et al.* [131], demonstrated the potential of mid-IR spectroscopy for the triage of patients with acute chest pains from two hospitals in the United States. The study included 1429 serum samples from 389 patients from the hospitals. The samples comprised of 104 patients with acute myocardial infarction (AMI), 136 patients with unstable angina pectoris and the remaining from patients with chest pains from different

aetiologies. FTIR spectroscopy performed in transflection mode, combined with a threshold value generated from a robust linear discriminant analysis, achieved high sensitivity and specificity enabling successful triage of patients with AMI, (the most serious complication), compared to the other sources of chest pain. They stated such discriminant features were due to the presence of glycation and the appearance of carbohydrates. Interestingly, their results were comparable to the performance of routine cardiac laboratory markers within the same study population. They concluded that FTIR analysis had the potential to aid the diagnostic procedure as early as within the first 6 hours after the onset of chest pain [131].

### **1.11.2 Clinical Raman Biofluid Spectroscopy**

Few studies have evaluated the potential of Raman spectroscopy applied to serum for cancer diagnosis. Pichardo-Molina *et al.* [132] demonstrated Raman serum spectroscopy combined with PCA and LDA, could discriminate between controls and patients with breast cancer with sensitivity 97% and a specificity of 78%. Similarly, Harris *et al.* [133] have shown the potential of this technique for the detection of head and neck cancer with sensitivity and specificity of 75%. Additionally, serum work by Sahu *et al.* [134] showed differentiation of oral cancer patients from controls, demonstrating moderate to good results (81% correctly classified). More recently, Raman spectroscopy has been used to predict the probability of cancer recurrence. The study showed that samples before surgery were ill-classified, but samples after classification were approximately 78% [135].

In other work, Gonzalez-Solis *et al.* [136] showed the potential of Raman spectroscopy and its capability in differentiating normal subjects from patients with cervical cancers. They found that there were discrete differences in glutathione, tryptophan,  $\beta$  carotene, and amide III with relation to cancer samples and controls using PCA. A recent proof-of-concept study showed a viable alternative method for discriminating liver cancer patients and cirrhotic patients using Raman spectroscopy. In this study, PCA failed to show discrimination but SVM-LOOCV could correctly classify. The results showed accuracies of 84.5% to 90.2% for serum sessile drop dried depositions, and 86% to 91.5% for freeze-dried serum [137].

In other work, Neugebauer *et al.* [138] analysed dried drops of plasma using Raman spectroscopy for the differentiation of samples of non-infectious systemic inflammatory response syndrome (SIRS) and sepsis using PCA-LDA with a sensitivity of 100% and a specificity of 82% and confirmed on an independent dataset with a prediction accuracy of 80%. This work highlights the importance of stratification of at-risk patients for better advantage of therapy.

Differences in types of dementia, including Alzheimer's was achieved using serum Raman spectroscopy. This study demonstrated sensitivities and specificities exceeding 95% for near-IR Raman spectroscopy [139].

Raman spectroscopies (RS) have also been applied on synovial fluid samples for disease estimation. The study combined RS with a k-means analysis using band intensity ratios from two regions ( $1080\text{ cm}^{-1}/1002\text{ cm}^{-1}$  and  $1670\text{ cm}^{-1}/1655\text{ cm}^{-1}$ ). Both of which correspond to the changes in the proteins. Such changes were attributed to severities of synovial joint ailments. They could show discrimination between patients with osteoarthritis of low or high severity with a sensitivity and specificity 74% and 71%, respectively [140]. Quantitative work by Rohleder *et al.* [38] on serum and ultra-filtrate serum from 247 blood donors showed RS enhanced discrimination between metabolites of serum components. Furthermore, this study could discern between high density and low density lipoprotein for the first time using serum-based Raman micro-spectroscopy. Moreover, RS analysis of urine combined with PCA and quadratic discriminant analysis (QDA), allowed the discrimination of patients suffering from diabetes mellitus and hypertension with low, high risk or with kidney failure. The results revealed differentiation in the content of urea, creatinine, and glucose. They showed that the amounts of urea and creatinine decreased in disease evolution, whilst glucose increased. Overall, they presented a classification accuracy of 70% [141]. Likewise, analysis of several metabolites in biological fluids such as tears [142] and bile acids [143] have been conducted. Such studies have shown the efficacy of vibrational spectroscopy for the detection of important discerning biological molecules for prospective disease detection.

Inherently, RS suffers sensitivity and fluorescence issues and to overcome these fundamental drawbacks, enhancement of the Raman signal is an area of promising research. Surface enhanced Raman spectroscopy (SERS) has been developed. This takes advantage of the benefits of advances in nanotechnology. The potential applications of this technique have been demonstrated for the detection of gastric cancer [144], colorectal [145] and nasopharyngeal [146]. Interestingly, SERS of saliva showed the ability to predict lung cancer by monitoring the decrease of proteins and nucleic acids with 80%, 78%, and 83% accuracy, sensitivity, and specificity respectively [147]. Using silver and gold colloids as SERS substrates, Bonifacio *et al.* [148] had shown that repeatable spectra could be obtained from protein-free blood serum and plasma. Other investigations report on adenoviral conjunctivitis from tears [149] and prostate cancer detection in urine [150]. Thus far, the development of biofluid SERS can represent a potential for sensitive diagnosis. However, these technologies do not provide label-free detection; which is seen in non-enhanced RS.

## **1.12. SUMMARY, WORKING HYPOTHESIS AND MAIN AIMS/ OBJECTIVES**

### **1.12.1 Summary**

In summary, the introduction in the thesis has outlined and described comprehensively the basic theory of vibrational spectroscopy, the governing molecular vibrational spectroscopy techniques and their applications within the clinical environment and how it fits within the clinical world. The introduction has now set the scene for the studies to be done on serum investigation *via* both FTIR and Raman spectroscopies, with a range of modalities/applications.

The field remains a largely niche area with huge clinical and economic impact for the disease and cancer diagnostic/screening world.

### **1.12.2 Working Hypothesis**

Vibrational spectroscopy combined with advanced chemometrics can be used as a powerful rapid screening tool for disease diagnostics for cancer from biofluids, such as serum, towards a possible POC requirement.

### **1.12.3 Main Aim**

To develop a spectroscopic methodology which can rapidly screen or diagnose a cancerous disease state from biofluids, towards a point-of-care (POC) diagnostic test.

### **1.12.4 Specific Aims and Objectives**

1. To conduct a thorough literature search in the proposed area of study of biospectroscopy of biofluids
2. To investigate and analyse the effects of preanalytical variation by way of pooled human serum freeze-thaw cycles and environmental air drying *via* both Raman and FTIR microspectroscopy
3. To investigate and develop a rapid methodology towards dried and liquid testing *via* Raman and FTIR spectroscopy to focus on patient cases (hepatitis with liver fibrosis and cirrhosis, brain tumour patients with varying degrees of primary low-grade and high-grade gliomas and metastatic cancers)
4. To down-select the optimum developed liquid spectroscopy technique and employ on a large cohort of cirrhotic patients who had complications with primary liver cancer/HCC for differentiation *via* liquid spectroscopy of disease states and severity
5. To analyse the data and write up the doctoral thesis

**| CHAPTER 2 |**

**INSTRUMENTATION  
AND EXPERIMENTAL  
METHODS**

---

**| CHAPITRE II |**

**METHODES  
EXPERIMENTALES  
ET INSTRUMENTATION**

## II.1 RÉSUMÉ

Le chapitre 2 détaille les approches expérimentales et l'instrumentation spectroscopique utilisées dans le cadre de cette thèse. Plusieurs modalités spectroscopiques IRTF et Raman ont été utilisées pour d'étudier le sérum pour la partie pré-analytique et pour les applications cliniques. La variation pré-analytique décrit l'effet de cycles répétés de congélation / décongélation et de séchage à l'air ambiant sur l'intégralité du pool de sérum humain. Pour la spectroscopie IRTF les modalités suivantes ont été utilisées : méthode ATR (Réflexion Totale Atténuée), en transmission *via* une analyse à haut débit (HTS-IRTF) de la goutte séchée et imagerie de la goutte séchée. Pour la spectroscopie Raman, deux modalités en mode micro-spectroscopie et mode macro-spectroscopie ont été envisagées sur la goutte séchée et la goutte liquide respectivement.

### 2.1. CHAPTER OVERVIEW

Chapter 2 details the experimental approaches employed within this research project and the spectroscopic instrumentation used. A range of modalities have been used for the both FTIR and Raman spectroscopy to investigate serum for pre-analytical variation, followed by disease applications.

The pre-analytical variation described the effect of repeated freeze-thaw cycles (FTC) and environmental drying (ED) on the integrity of human pooled serum. FTIR spectroscopy of the following modalities was employed: ATR and transmission *via* high throughput analysis (HT-FTIR) and mapping/imaging both in the dried serum state. However, using Raman spectroscopy, the serum was investigated in the dried and liquid phases with microscopic and macroscopic analyses.

For the disease applications, a protocol was developed for a macro liquid Raman approach and was used to investigate retrospective patient databanks (Reims, France –University of Reims hospital centre, Reims, France) containing samples of hepatic fibrosis, cirrhotic and primary liver cancer patients. An HT-FTIR approach was used to investigate two patient datasets involving hepatic fibrosis patient's biobank located in Reims in France. This study was approved by the Comité de Protection des Personnes Est– agreement #2008/09 and by the Agence Française de Sécurité Sanitaire des Produits de Santé (AFSSAPS – agreement #2008-A00023-52). The second series of experiments was from brain tumour patients from the Brain Tumour Northwest biobank (BTNW) and Walton Centre, located in Preston, England; with ethical approval (application #1108).

## 2.2. SPECTRAL METHOD DEVELOPMENT & SERUM ANALYSIS

In the first instance, to investigate serum freeze-thaw (FTC) and environmental drying (ED) FTIR spectroscopy was employed, followed by Raman spectroscopy. A range of modalities were tried and tested, and parameters were developed for the analysis and subsequent data analysis. A suite of FTIR and Raman spectrometers were utilised across the two laboratories throughout the Ph.D project.

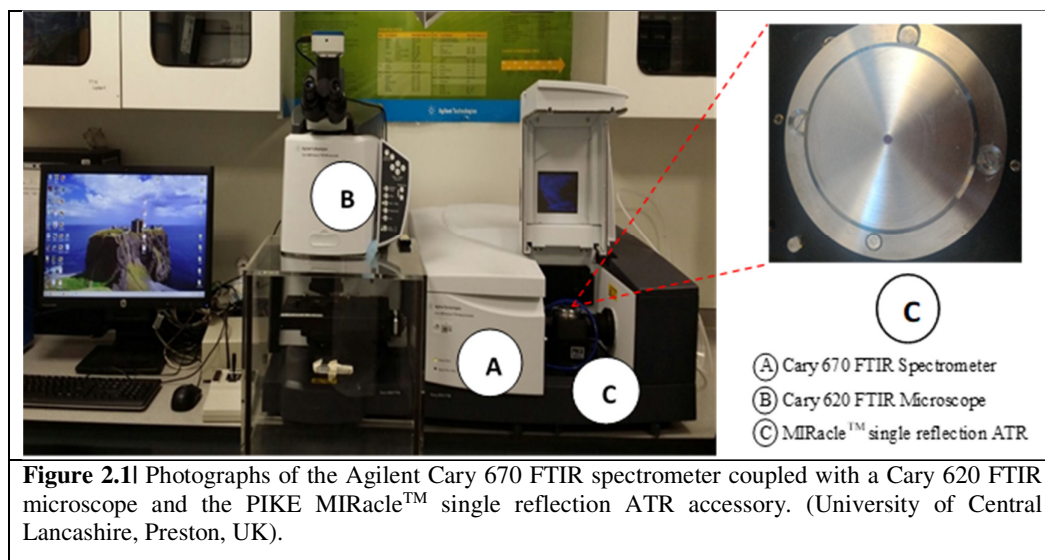
### 2.2.1 FTIR Spectrometers

#### 2.2.1.1 Agilent Cary 670 FTIR Spectrometer

The Agilent Cary 670 FTIR spectrometer (Agilent Technologies, USA) (Figure 2.1) is equipped with a Global<sup>(TM)</sup> source, which emits light in the mid-IR frequency region ( $2.5$  to  $25\mu\text{m}$  or  $40$  to  $4000\text{ cm}^{-1}$ ), a KBr beam splitter, which is a thin Ge film encased by two IR-transparent KBr windows; providing a working transparency over a wide spectral window ( $400\text{ cm}^{-1}$  - NIR), and a deuterated triglycine sulphate (DTGS) detector, which is the basic detector used in macroscopic mode. This instrument was used for both ATR and transmission data collection.

##### 2.2.1.1.1 ATR-FTIR Serum Approach

ATR data collection was carried out by coupling the spectrometer with a single reflection PIKE MIRacle<sup>TM</sup> ATR accessory (see Figure 2.1). The ATR accessory comprises a Ge IRE, which allows a transmission range of  $\sim 5500\text{-}780\text{ cm}^{-1}$ [151].



Normal human mixed pooled serum ( $0.2\ \mu\text{L}$  sterile filtered, CS100-100 (TCS Biosciences, UK) arrived frozen and was used for the FTC and ED analysis. It was allowed to thaw at room

temperature (RT). This was recorded at an average of ~23 °C. The serum was then aliquoted (100 µL) and stored at -80 °C. From this 1 sample was left out and tested for the first freeze-thaw (FTC1). Following spectroscopic testing, the remainder (FTC1) was returned to cryogenic storage at -80 °C.

For spectral analysis, a volume of 1 µL of serum was deposited directly on the ATR crystal and allowed to air-dry for ~ 8 mins. at RT [111]. General room humidity was noted to be around 40% within the controlled lab environment. Spectra were collected in triplicate from each spot deposited (n=10) and for each FTC (n=15). Background spectra were collected before every spot and analysed by a ratio method. Due to the intimate contact required between the biofluid sample and IRE, between spots the serum biofilm debris was removed, and the crystal was cleaned with a series of detergent and ethanol washes. Virkon disinfectant (Thermo Fisher Scientific, UK) was used to remove the biofilm, followed by 70% ethanol solution (Thermo Fisher Scientific, UK). The following parameters were used for ATR spectral collection using the ProResolutions software, V2.1:

- *Spectral range:* 4000-400 cm<sup>-1</sup>
- *Number of scans:* 32 co-added
- *Spectral Resolution:* 4 cm<sup>-1</sup>
- *Sampling:* pooled human serum (1 µL)

#### 2.2.1.1.2 Transmission FTIR Serum Approach

Environmental drying (ED) effects were investigated *via* transmission FTIR by coupling the Cary 620 FTIR microscope (Figure 2.2). A liquid nitrogen cooled mercury cadmium telluride (MCT) detector was used to capture the photons.

Whilst investigating the FTC effect, the same normal mixed pooled serum was used to observe ED changes. This study was performed to monitor dry drop heterogeneity over a 24 hour period. Half a microliter of serum was deposited on to an IR-transparent calcium fluoride substrate (CaF<sub>2</sub> – Ø = 13 x 2 mm polished window, Crystran, Ltd., UK). The window was positioned under the microscope objective (60 x NA = 0.75) of the 620 FTIR microscope. Spectra were taken at random acquiring data from the centre and periphery of the drying serum spot. Spectral collection was taken firstly at 10 mins after drying, followed by consecutive 30 minute intervals until 3.5 hours had elapsed. The remaining spectra were collected at 7 hour, 14 hour, and 24 hour from spot deposition. All spectra were acquired in triplicate and a background spectrum was taken prior to each time interval. The following parameters were used:

- *Spectral range:* 4000-600 cm<sup>-1</sup>

- *Number of scans:* 32 co-added
- *Aperture size:* 120  $\mu\text{m}^2$
- *Microscope objective:* x 60 (NA 0.75, LUMPlan FLN)
- *Spectral Resolution:* 6  $\text{cm}^{-1}$
- *Sampling:* pooled human serum (0.2  $\mu\text{L}$ )

### 2.2.1.2 Bruker HT-FTIR Tensor 27 Spectrometer

The Bruker FTIR Tensor 27 spectrometer coupled with a high throughput screening XTension (HT-XT or HT) module was employed in transmission mode (Bruker Optics GmbH, Ettlingen, Germany) (Figure 2.2). The spectrometer is equipped with a Globar<sup>TM</sup> source, KBr beam splitter and a DTGS detector covering the spectral ranges 400-7200  $\text{cm}^{-1}$ . Spectral collection was carried out using the OPUS v6.5 software (Bruker Optics, GmbH, Ettlingen, Germany). For spectral acquisition, a 384 multiwell silicon plate was used to house the sample for HT-FTIR spectroscopy (see Figure 2.2).

#### 2.2.1.2.1 High Throughput Transmission (HT) FTIR Serum Approach

Following serum thawing at RT, all samples were diluted 3-fold using physiological water (0.9% injectable Sodium Chloride, PROAMP<sup>®</sup>, Aguettant, France). Then, a volume of 5  $\mu\text{L}$  of each preparation were deposited on to a 384-well ( $\text{Ø} = 4 \text{ mm}$ ) silicon plate and allowed  $\sim 1 \text{ h}$  to air-dry [152] in a controlled laboratory environment ( $\sim 40\%$  humidity).

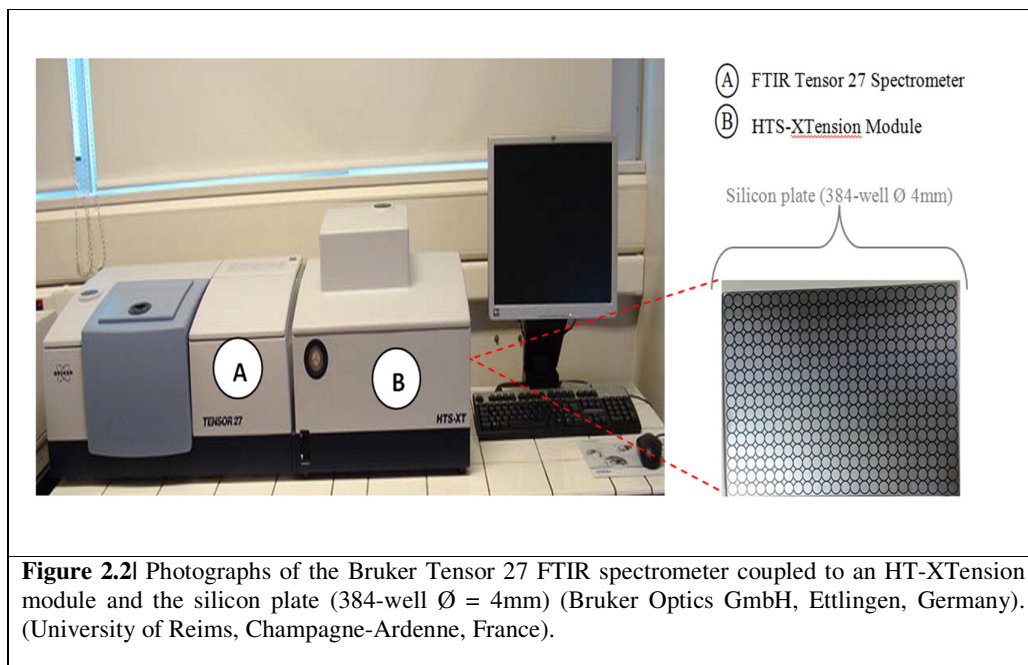


**Figure 2.2|** Photographs of the Bruker Tensor 27 FTIR spectrometer coupled to an HT-XTension module and the silicon plate (384-well  $\text{Ø} = 4 \text{ mm}$ ) (Bruker Optics GmbH, Ettlingen, Germany). (University of Reims, Champagne-Ardenne, France).

Spectra were collected with 1 spectrum per well and 8 replicates per sample. A total of two plates were prepared to repeat the results ( $15 \times 8 \times 2 = 240$  spectra in total). A background spectrum was acquired prior to sample acquisition before each well was tested and automatically corrected by the software (OPUS v6.5 Bruker GmbH).

- *Spectral range:* 4000-400  $\text{cm}^{-1}$
- *Number of scans:* 32 co-added
- *Spectral resolution:* 4  $\text{cm}^{-1}$
- *Sampling:* pooled human serum diluted (5  $\mu\text{L}$ )

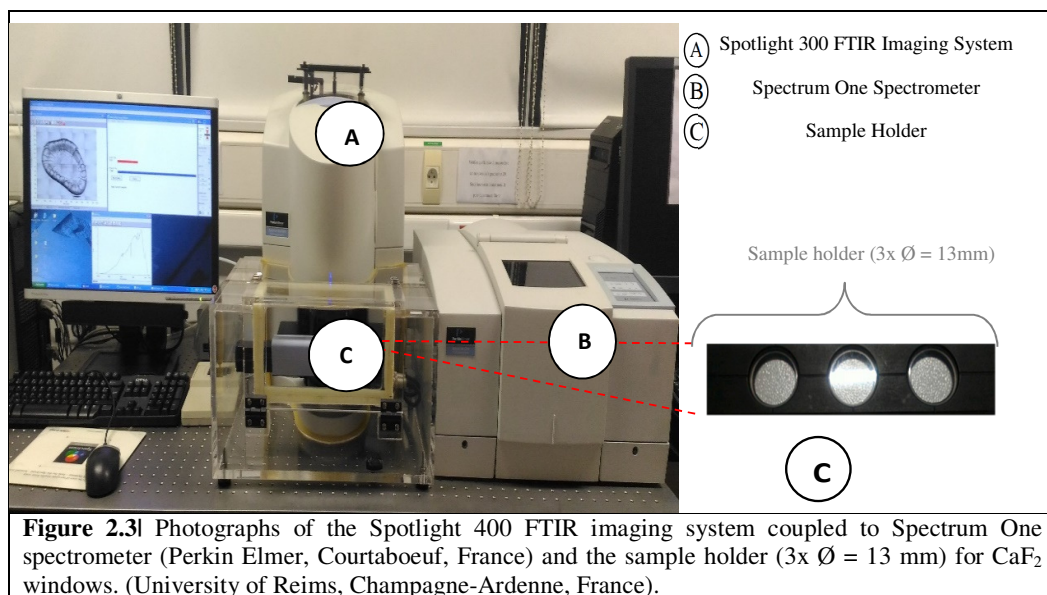
### 2.2.1.3 Perkin Elmer Spotlight 400 FTIR Spectroscopic Imaging System

The Spotlight 400 FTIR imaging system (Perkin Elmer, Courtaboeuf, France) consists of the Spectrum One FTIR spectrometer coupled with the Spotlight 400 FTIR microscope (see Figure 2.3). Spectrum One has a DTGS detector and operates in transmission and reflectance modes. The Spotlight 400 FTIR imaging system is equipped with a single-element detector for point mode analysis and a multi-element MCT line detector with 16 pixels capable of operating at a spatial resolution of either 6.25  $\mu\text{m}/\text{pixel}$  or 25  $\mu\text{m}/\text{pixel}$ .

#### 2.2.1.3.1 FTIR Microspectroscopy of Dried Serum Drops

To study serum drop heterogeneity throughout drying of a serum sample, a 24 hour kinetics study was carried out using the Spotlight 400 FTIR imaging system. Human pooled serum was left to thaw at RT and  $\sim 0.2 \mu\text{L}$  was deposited on to a  $\text{CaF}_2$  window (see Figure 2.3). A total of 198 spectra were recorded from 11 line scans. A background spectrum was collected and by a ratio method prior to each of the 11 line scans. The following parameters were used:

- *Spectral range:* 4000-750  $\text{cm}^{-1}$
- *Number of scans (sample):* 32 coadded
- *Aperture size:* 100  $\mu\text{m}^2$
- *Modality:* point mode transmission (line scan)
- *Spectral resolution:* 4  $\text{cm}^{-1}$
- *Sampling:* pooled human serum (0.2  $\mu\text{L}$ )



#### 2.2.1.3.2 FTIR Imaging of Dried Serum Drops

In a second experiment, the MCT 16-pixel multi-element detector was used to collect images from the serum drying drop in line with the kinetics study. Both the point mode line scan and imaging of the same area were carried out (at same time). The Spectrum Image software v1.6 (Perkin Elmer) collected an image in the same geometry of the diameter of the drying serum drop (~0.2 µL). A single image was taken at each of the 11 time points over the course of 24 hour, after a background spectrum was collected from an area free of the serum on the substrate. This was subsequently corrected by the software. The image size was ~ 1400 x 65 µm<sup>2</sup>. The image experiment was repeated in triplicate to check the reproducibility of the data. A total of 2178 spectra were recorded from 11 images. The following parameters were used:

- *Spectral range:* 4000-750 cm<sup>-1</sup>
- *Number of scans (sample):* 16 coadded
- *Aperture size:* 100 µm<sup>2</sup>
- *Modality:* Imaging
- *Spectral resolution:* 6 cm<sup>-1</sup>
- *Spatial resolution:* 25 µm/pixel
- *Sampling:* pooled human serum (0.2 µL)

## 2.2.2 Raman Spectrometers

### 2.2.2.1 Horiba Jobin-Yvon LabRAM HR800 Microspectrometer

The Horiba Jobin-Yvon LabRAM HR800 (HR800) is a dispersive spectrometer with integrated confocal microscope (see Figure 2.4). The spectrometer has a focal length of ~800 mm and the confocal microscope is equipped with a range of short-working and long-working distance objectives (SWD and LWD). An Andor electromagnetic CCD (EMCCD) detector is used to capture the photons for the signal. The HR is coupled with two laser excitations from an air-cooled 3 W Toptica Photonics source (532 nm – Nd:YAG and 785 nm NIR diode). There are a range of dispersive holographic diffraction gratings (300, 600, 1200 and 1800 lines/mm). The HR system has customizable confocal hole, slit size and laser power options.

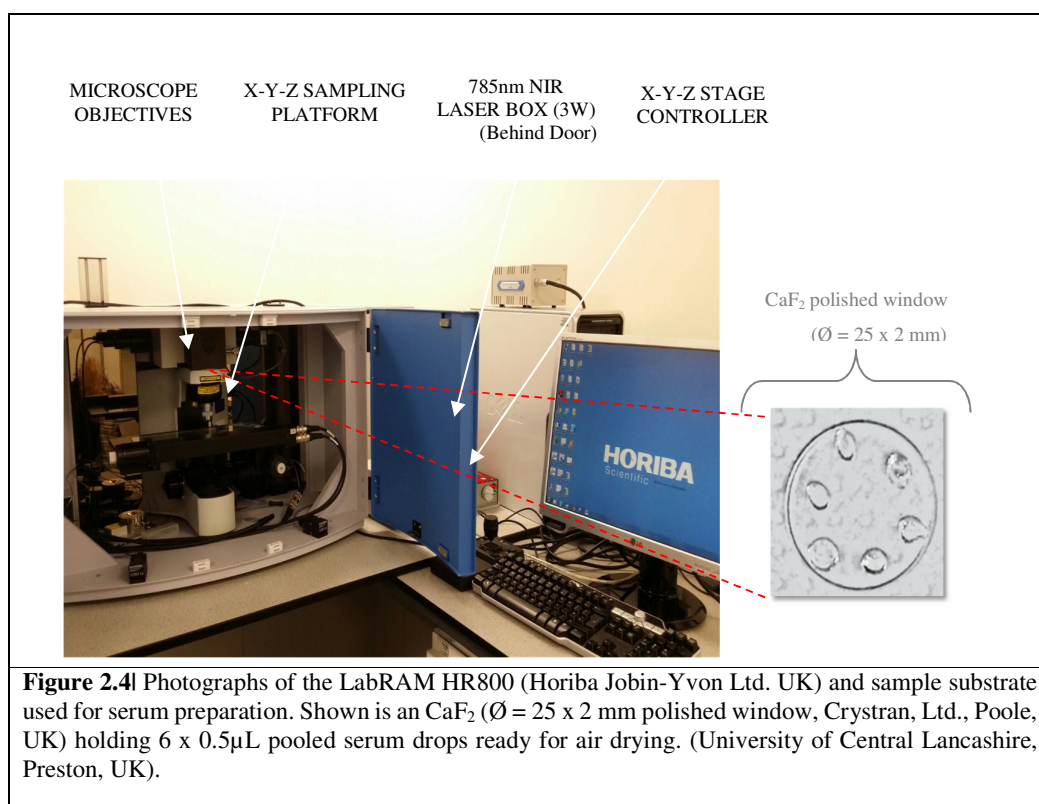


**Figure 2.4|** Photographs of the LabRAM HR800 (Horiba Jobin-Yvon Ltd. UK) and sample substrate used for serum preparation. Shown is an CaF<sub>2</sub> (Ø = 25 x 2 mm polished window, Crystran, Ltd., Poole, UK) holding 6 x 0.5µL pooled serum drops ready for air drying. (University of Central Lancashire, Preston, UK).

#### 2.2.2.1.1 Raman Microspectroscopy for Dried Serum

Human pooled serum was subjected to spectroscopic measurements *via* Raman confocal microspectroscopy for further comparisons of serum FTC and ED effects. Every effort was made to run the analysis in tandem with the FTIR assessment, so identical serum preparations were made and to limit the potential for aberrant results across the systems.

First, the serum was thawed at RT and then deposited on to a CaF<sub>2</sub> window (see Figure 2.5). For the FTC, the measurements were taken from dried spots (drying time of 10 mins.) in a controlled lab environment. For ED measurements, spectra were collected at 11 time points over a 24 h period, with triplicate spectra carried out at each point. A total of n=450 spectra and n=33 spectra for FTC and ED, respectively. Spectral acquisition was taken from random areas across each of the drying/dried serum spots. The following parameters were used:

- *Spectral range:* 2000-500 cm<sup>-1</sup>
- *Excitation laser:* air-cooled 30 W 785 nm diode
- *Laser power:* ~30 mW (at sample)
- *Diffraction grating:* 1800 lines/mm
- *Spectral resolution:* 3 cm<sup>-1</sup>.
- *Confocal hole:* 400 μm
- *Slit size:* 100 μm
- *Integrations:* 2 x 15 seconds
- *Modality:* microspectroscopy -single point mode
- *Microscope objective:* x 50 LWD (NA 0.50, LUMPlan FLN)
- *Substrate:* CaF<sub>2</sub> window
- *Sampling:* dried pooled serum (0.5 μL)

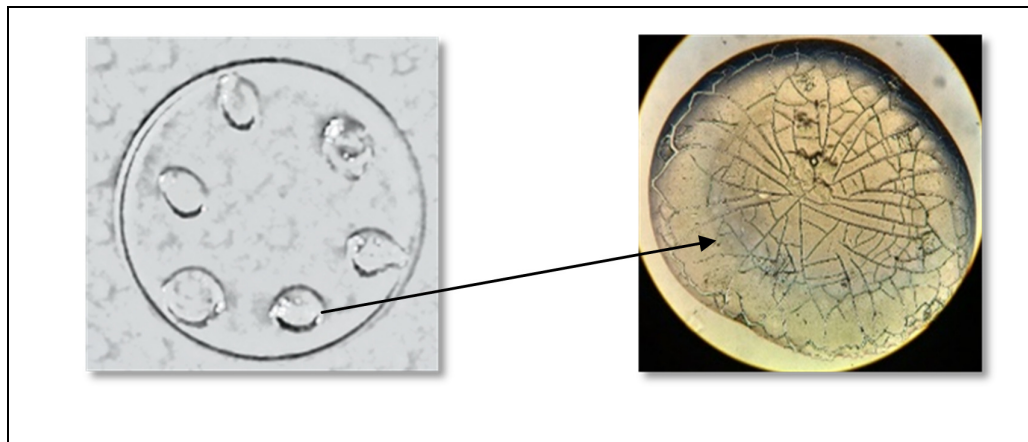


**Figure 2.5|** Photographs of a CaF<sub>2</sub> window deposited with 0.5 μL spots of thawed liquid serum (image before dried on the left). Image on the right is x 40 magnification of 1 0.5 μL dried drop (arrow identifies drop). The dried drop image demonstrates fern-like patterns radiating from the centre to the peripheral aspects, the so-called ‘coffee-ring phenomena’.

Depositing liquid serum to dry on a substrate is called drop coating dried deposition (DCDD). This method is one of the most used within spectroscopic biofluid analyses. This is due to the negative or very little contributions of mid-IR transparent substrates [153, 20]. Figure 2.5 shows the formation of serum drops on to the substrate prior to spectral collection.

### 2.2.2.2 Horiba Jobin-Yvon LabRAM ARAMIS Microspectrometer

The Horiba Jobin-Yvon LabRAM ARAMIS (Aramis) is a dispersive spectrometer with integrated confocal microscope (see Figure 2.6). The confocal microscope is equipped with both SWD and LWD objectives. Spectra are captured on to a Horiba Synapse<sup>®</sup> CCD 1024 x 256 pixels thermoelectric (TE) detector. The Aramis system is coupled with two laser excitations from an Toptica Photonics air-cooled 3 W source (532 nm – Nd:YAG and 785 nm NIR diode). There are a range of dispersive holographic diffraction gratings (300, 600, 1200 and 1800 lines/mm). The HR system has a customizable confocal hole, slit size and laser power options.

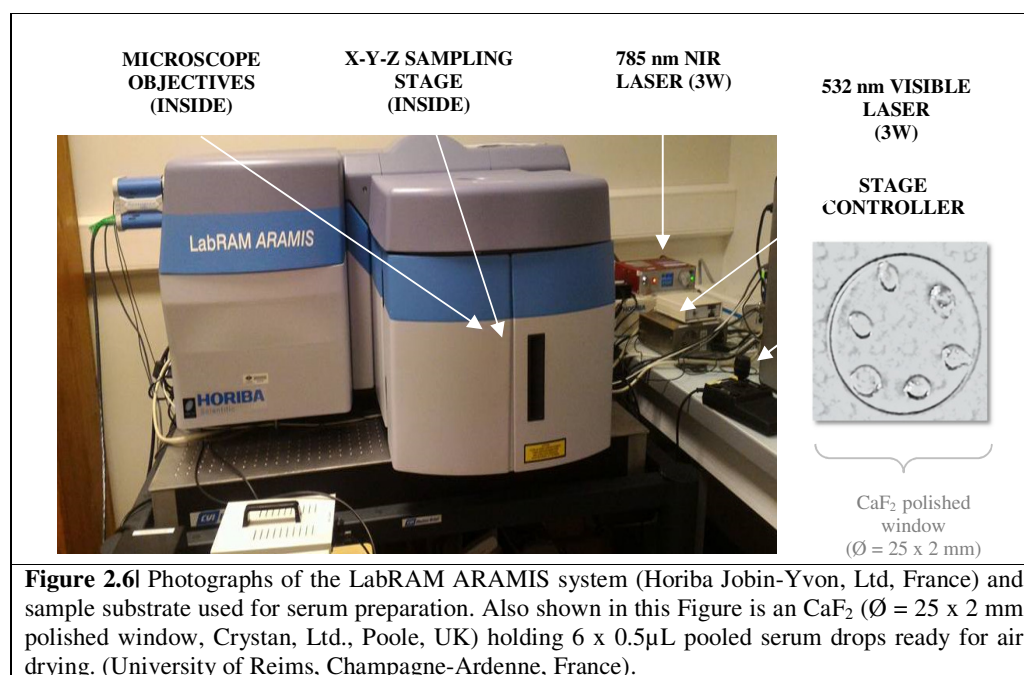


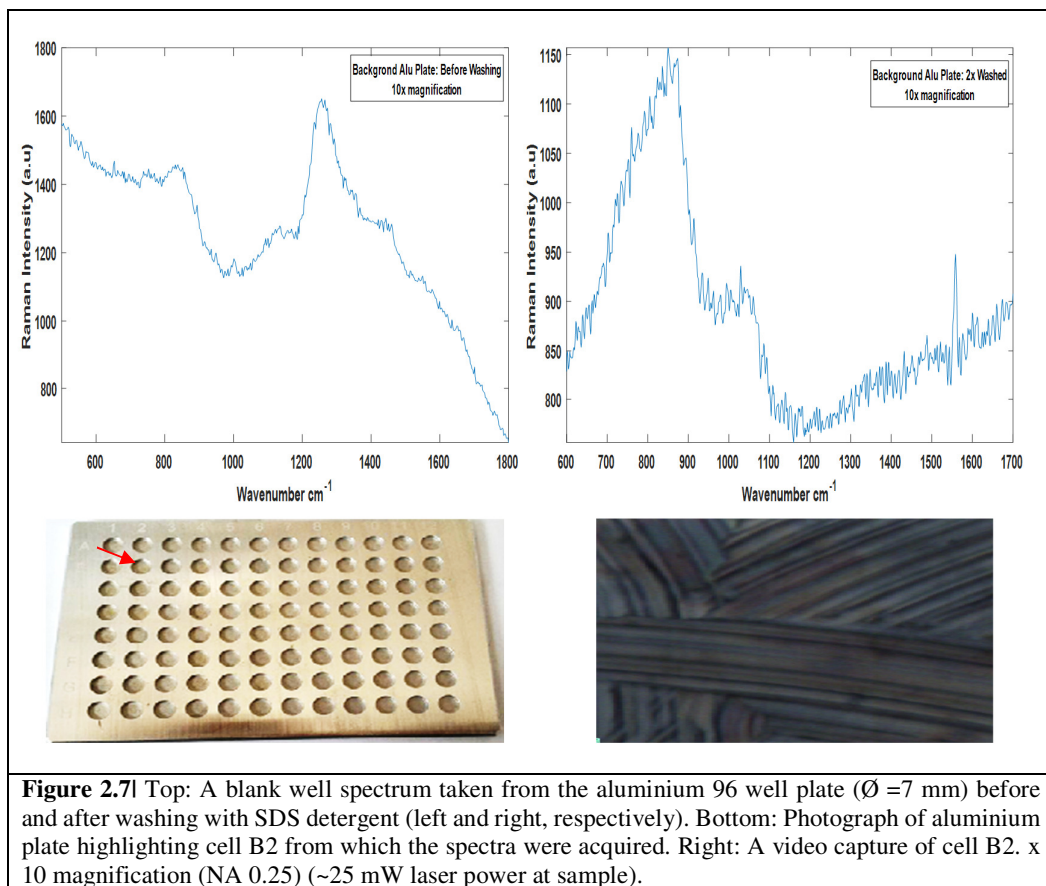
**Figure 2.6** Photographs of the LabRAM ARAMIS system (Horiba Jobin-Yvon, Ltd, France) and sample substrate used for serum preparation. Also shown in this Figure is a CaF<sub>2</sub> (Ø = 25 x 2 mm) polished window, Crystan, Ltd., Poole, UK) holding 6 x 0.5µL pooled serum drops ready for air drying. (University of Reims, Champagne-Ardenne, France).

#### 2.2.2.2.1 Raman Microspectroscopy for Liquid & Dried Serum

Using the ARAMIS system, further comparative investigations with FTC and ED effects were conducted. Prior to spectral collection, the background of each of the aluminium wells were checked for contamination with a spectral signature, before and after washing with biological detergent. Figure 2.7 shows the spectra before and after for checking the wells, and the video capture of the well B2 of the aluminium plate.

The following parameters were used with two substrates (CaF<sub>2</sub> and aluminium multiwell aluminium plate). For dried analysis, 10 mins. air-drying was allowed before spectral acquisition. For liquid analysis, optimisation of the volume of biofluid, plus depth of focusing was tested to ensure the spectra was taken from the spot and not just the surface of the drop. A total of n=450 spectra were taken from the FTC measurements and n=33 from the ED measurements. The following parameters were used:

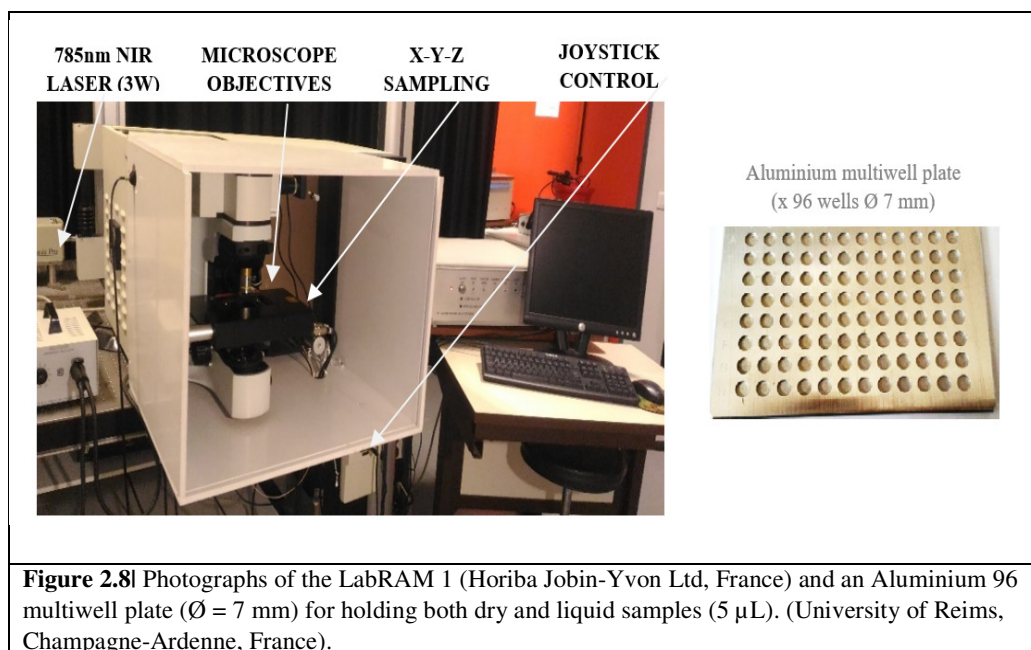
- *Spectral range:* 1800-500 cm<sup>-1</sup>
- *Excitation laser:* 532 nm (Nd:YAG), 785 nm diode
- *Laser power:* ~25 mW
- *Diffraction grating:* 600 lines/mm
- *Spectral resolution:* 3 cm<sup>-1</sup>.
- *Confocal hole:* 500 μm
- *Slit size:* 150 μm
- *Integrations:* 2 x 15 s.
- *Modality:* single point mode
- *Microscope objective:* 100x LWD (NA 0.25, LUMPlan FLN)
- *Substrate:* CaF<sub>2</sub> window & a 96 well aluminium plate
- *Sampling:* pooled dried and liquid serum (0.5 - 5 μL)



### 2.2.2.3 Horiba Jobin-Yvon LabRAM 1 Microspectrometer

To circumvent the coffee-ring phenomena of the dried serum drop, investigations of the dry-liquid phase were conducted. Sampling parameters were optimised using different volumes of the liquid serum, as well as instrumental optimisations of grating choice, slit and confocal hole size and integration times, plus Z-profiling depth of sampling.

The Horiba Jobin-Yvon LabRAM 1 (Horiba Scientific, Villeneuve d'Ascq, France) (LabRAM 1) is a dispersive spectrometer with integrated confocal microscope (Figure 2.8). The confocal microscope is equipped with both SWD and LWD objectives. Spectra are captured on to a Horiba Synapse<sup>®</sup> CCD 1024 x 256 pixels thermoelectric (TE) detector. The LabRAM 1 system is coupled with two laser excitations from an air-cooled 3 W source (532 nm – Nd:YAG and 785 nm Ti:Sa). There are a range of dispersive holographic diffraction gratings (600, 950, and 1200 lines/mm). The LabRAM 1 system has a customizable confocal hole, slit size and laser power options.



#### 2.2.2.3.1 Dried Centre vs. Periphery Measurements and Liquid Analysis

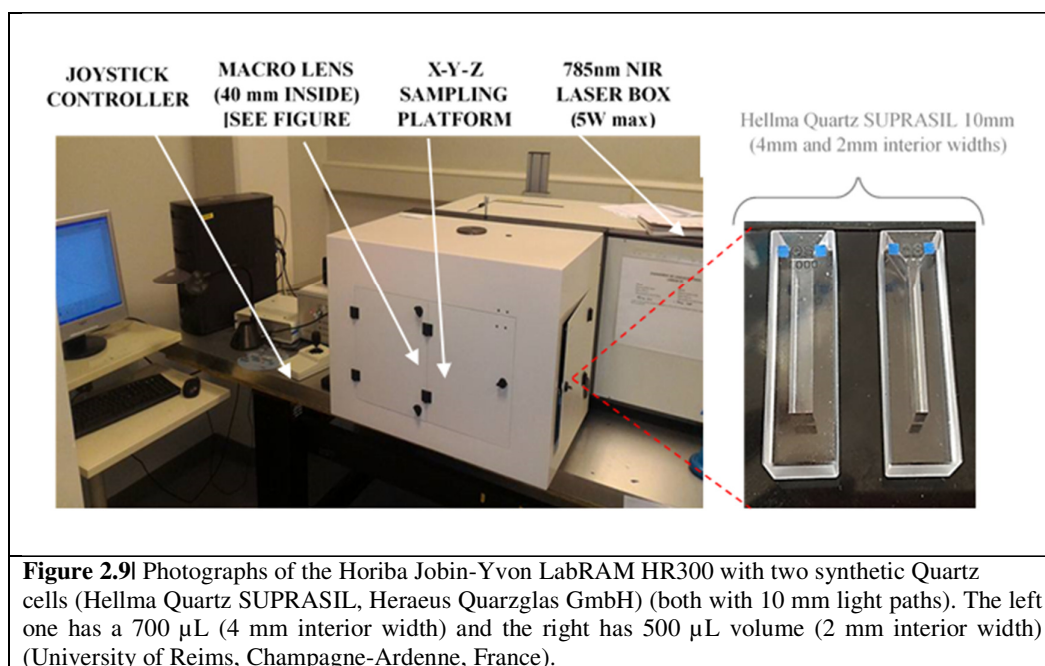
Using the LabRAM 1 system, FTC measurement were conducted in two phases, both liquid and dried (centre vs. periphery measurements). Initially, serum was deposited, and spectra were acquired within 10 mins to ensure a liquid phase was taken only. Following this, upon drying, random spectra were collected in triplicate from the periphery of the drop and the centre aspect to observe differences in chemistry and heterogeneity across the dried drop. The following

optimised parameters were used with both substrates (CaF<sub>2</sub> and aluminium plate). A total of n=450 liquid serum measurements were made and n=135 dried centre and periphery measurements. The following parameters were employed:

- *Spectral acquisition*: 1800-500 cm<sup>-1</sup>
- *Excitation laser*: 785 nm diode (Ti: Sa)
- *Laser power*: 3 W and ~90 mW
- *Laser exposure*: 100% (75% for centre vs. periphery measurements)
- *Diffraction grating*: 950 lines/mm
- *Spectral resolution*: 3 cm<sup>-1</sup>.
- *Confocal hole*: 1000 µm
- *Slit size*: 150 µm
- *Integrations*: 3 x 45 s.
- *Collection*: single point mode
- *Microscope objective*: x 50 SWD (NA 0.75)
- *Substrate*: 96 well aluminium plate
- *Serum Sampling*: pooled dried and liquid serum (5 µL)

#### 2.2.2.4 Horiba Jobin-Yvon LabRAM HR300 Spectrometer

The Horiba Jobin-Yvon LabRAM HR300 (HR300) (Horiba Scientific, Villeneuve d'Ascq, France) (Figure 2.9) is high resolution (focal length ~300 mm) dispersive microspectrometer that employs an Andor EMCCD detector. It is capable of two laser excitations (632.8 nm – He:Ne and 785 nm diode). There are a range of dispersive holographic diffraction gratings available (300, 600, 900, 1200 and 1800 lines/mm) with customizable confocal hole and slit and laser power options.

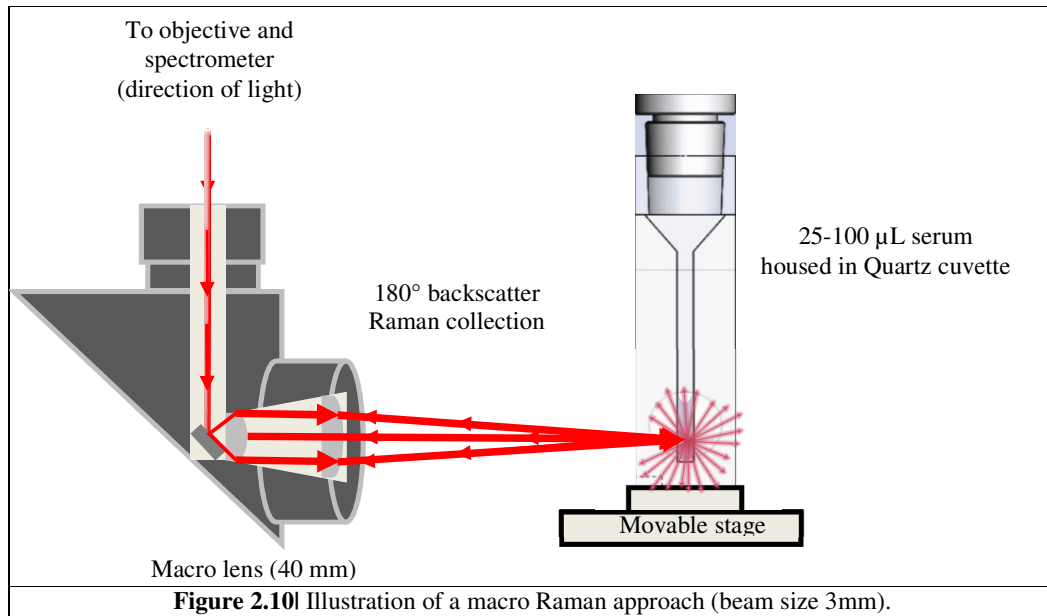


#### 2.2.2.4.1 Macro Liquid Raman Serum Measurements

Using the LabRAM HR300 spectrometer combined with a 40 mm macro lens adaptor (Figure 2.10), the following optimised parameters were used with different volumes of serum (25-100  $\mu\text{L}$ ) and integrations tested (optimization testing: 1-6 accumulations and 15, 30, 60, 90, 120, 180 and 240 seconds). The spectral collection parameters are noted below:

- *Spectral acquisition:* 1800-500  $\text{cm}^{-1}$
- *Excitation laser:* 3 W 785 nm diode
- *Laser power:*  $\sim 75$  mW
- *Diffraction grating:* 950 lines/mm
- *Spectral resolution:*  $\sim 1-2$   $\text{cm}^{-1}$
- *Confocal slit/hole:* 1000  $\mu\text{m}$
- *Slit size:* 150  $\mu\text{m}$
- *Integrations:* 5 x 120 s.
- *Collection:* - single point macro mode
- *Substrate:* - Quartz cuvettes (seen Figure 9)
- *Sampling:* - pooled liquid and patient serum

Figure 2.10 demonstrates a schematic of the horizontal setup. Employing a 40 mm macro lens adaptor, the light path (NIR 785 nm) was guided through internal lenses housed within the adaptor and the  $180^\circ$  backscattered Raman signal was collected from the light interaction with the serum and recorded with the HR300's CCD detector.



#### 2.2.2.5 Horiba Jobin-Yvon HE Raman Spectrograph & Fiberoptic Raman Probe

A spectrograph is an industrial robust instrument which separates incoming light by its wavelength or frequency and records the spectrum in a multichannel detector [154]. The Horiba Jobin-Yvon high efficiency (HE) spectrograph was used coupled to the InPhotonics Raman Probe™ for spectral data collection with non-moving optics (Figure 2.11). The basic components to the HE spectrograph are:

- *Entrance slit*: eliminates unwanted light and fix spectral resolution
- *Collimator*: a lens/mirror converts a diverging beam to a parallel one
- *Disperser*: a holographic grating to cause the interference of light
- *Camera*: a lens/mirror focuses image of slit entrance on detector surface
- *Detector*: an electronic device to capture the spectrogram image

Figure 2.11 demonstrates a schematic of the internal components of the InPhotonic Raman Probe. In its most basic design it comprises the following components [155]:

- *1<sup>st</sup> Lens*: blocks unwanted laser light from excitation
- *Band-pass filter*: blocks silica Raman bands and transmits pure signal
- *Dichroic filter*: transmits the laser line focused by 2<sup>nd</sup> lens to the sample
- *2<sup>nd</sup> Lens*: gathers backscattered light from sample *via* the dichroic filter
- *Long-pass filter*: removes Rayleigh & anti-Stokes, allows Stokes only
- *3<sup>rd</sup> lens*: focuses Raman light to the HE spectrograph for detection

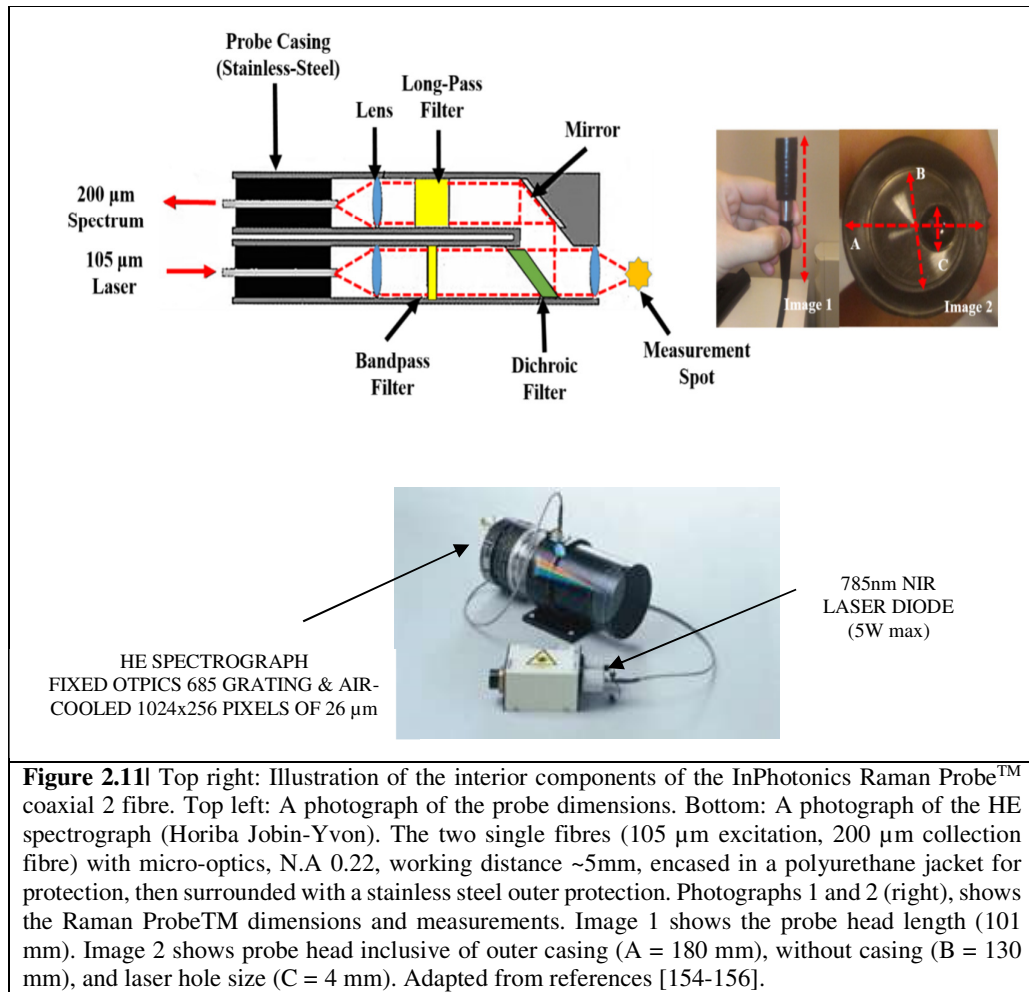


**Figure 2.11** Top right: Illustration of the interior components of the InPhotonics Raman Probe™ coaxial 2 fibre. Top left: A photograph of the probe dimensions. Bottom: A photograph of the HE spectrograph (Horiba Jobin-Yvon). The two single fibres (105 µm excitation, 200 µm collection fibre) with micro-optics, N.A 0.22, working distance ~5mm, encased in a polyurethane jacket for protection, then surrounded with a stainless steel outer protection. Photographs 1 and 2 (right), shows the Raman Probe™ dimensions and measurements. Image 1 shows the probe head length (101 mm). Image 2 shows probe head inclusive of outer casing (A = 180 mm), without casing (B = 130 mm), and laser hole size (C = 4 mm). Adapted from references [154-156].

#### 2.2.2.5.1 Fiberoptic Raman Serum Measurements

Employing the Raman Probe™ in a top-down orientation, the following parameters were used:

- Spectral acquisition: 3200-200  $\text{cm}^{-1}$
- Excitation laser: 2.5 W 785 nm diode
- Laser power: ~60 mW
- Diffraction grating: 685 lines/mm (fixed optics)
- Spectral resolution: ~5  $\text{cm}^{-1}$
- Confocal slit/hole: fixed optics
- Integrations: 10, 15, 20 and 30 s, accumulated x 1 or x 2
- Collection: single point fibre mode
- Substrate: Quartz cuvettes
- Serum Sampling: pooled liquid serum

### 2.3. SPECTRAL QUALITY & VARIANCE ASSESSMENTS

Aforementioned in the introduction (Chapter 1), with Raman data specifically, there are some fundamental steps required to ‘clean’ the signal prior to any analysis. Figure 2.12 demonstrates the three signals used for correcting the dark current (A), optics (B) and NIST standards for the 785 nm excitation line (C). The corrected serum signal is shown as (D).

The standard reference materials (SRM) used in this project were #2241, #2243 for 785 and 532 nm excitations, respectively (SRM NIST, Gaithersburg, MD, USA). All pre-calibration and

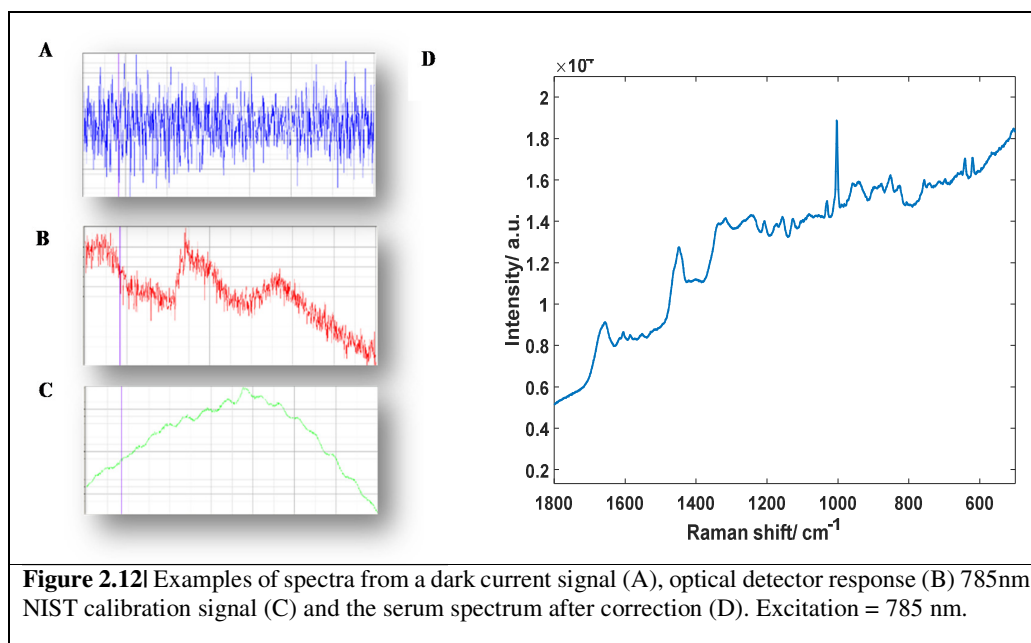


**Figure 2.12|** Examples of spectra from a dark current signal (A), optical detector response (B) 785nm NIST calibration signal (C) and the serum spectrum after correction (D). Excitation = 785 nm.

calibration checks were later averaged for correction of the Raman signal in the pre-processing phase (see Figure 2.13).

#### 2.3.1 Spectral Quality Testing

As alluded to in Chapter 1, the spectral data from FTIR and Raman experiments were subjected to a quality threshold. Spectral quality and variance analysis was conducted prior to pre-processing the spectral data. Figure 2.14 demonstrates the serum spectrum and the important quality bands highlighted to demonstrate how the in-house SNR algorithm works.

Additionally, to compare with other methods used by the instrument manufacturers, a second method was used as a quality check. This method is in line with the manufacturer’s guidance (OPUS v6.5 Software, Bruker Optics GmbH, Ettlingen, Germany). Equation 7a was employed for calculating of the root mean square (RMS) SNR.

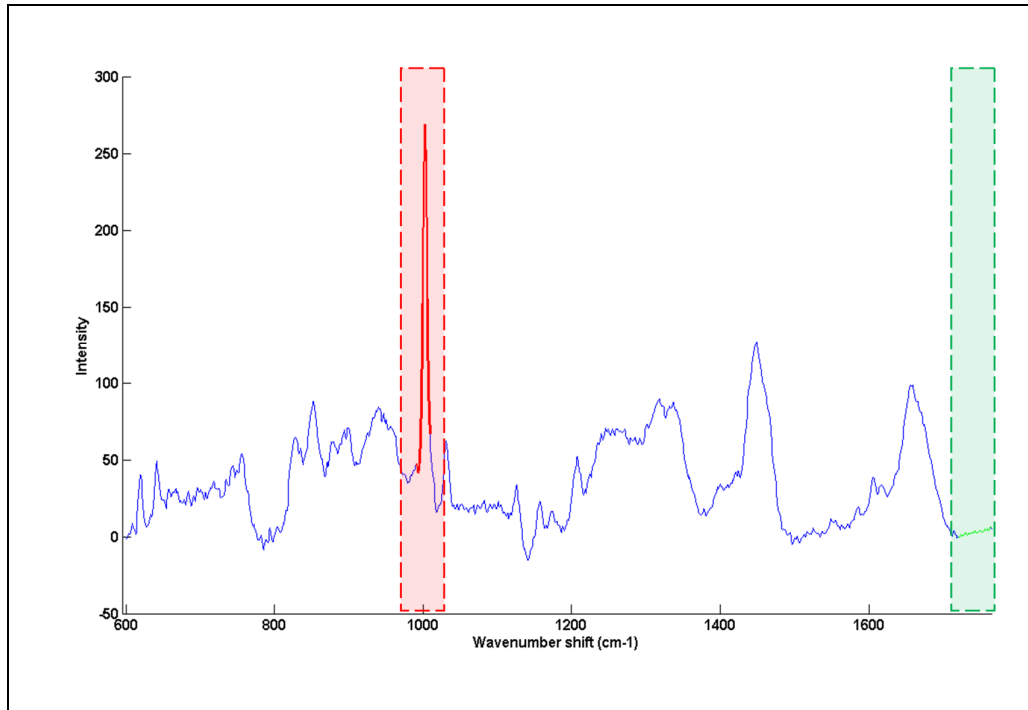


**Figure 2.13** Normalised Raman serum spectrum indicating the (red) signal and (green) noise region used for calculation of SNR within the QT. Spectra passed the QT when the SNR exceeded 30 [27].

$$RMS = \sqrt{\frac{\sum(x_i - y_i \text{ Range})^2}{N}}$$

**Eq. 7a**

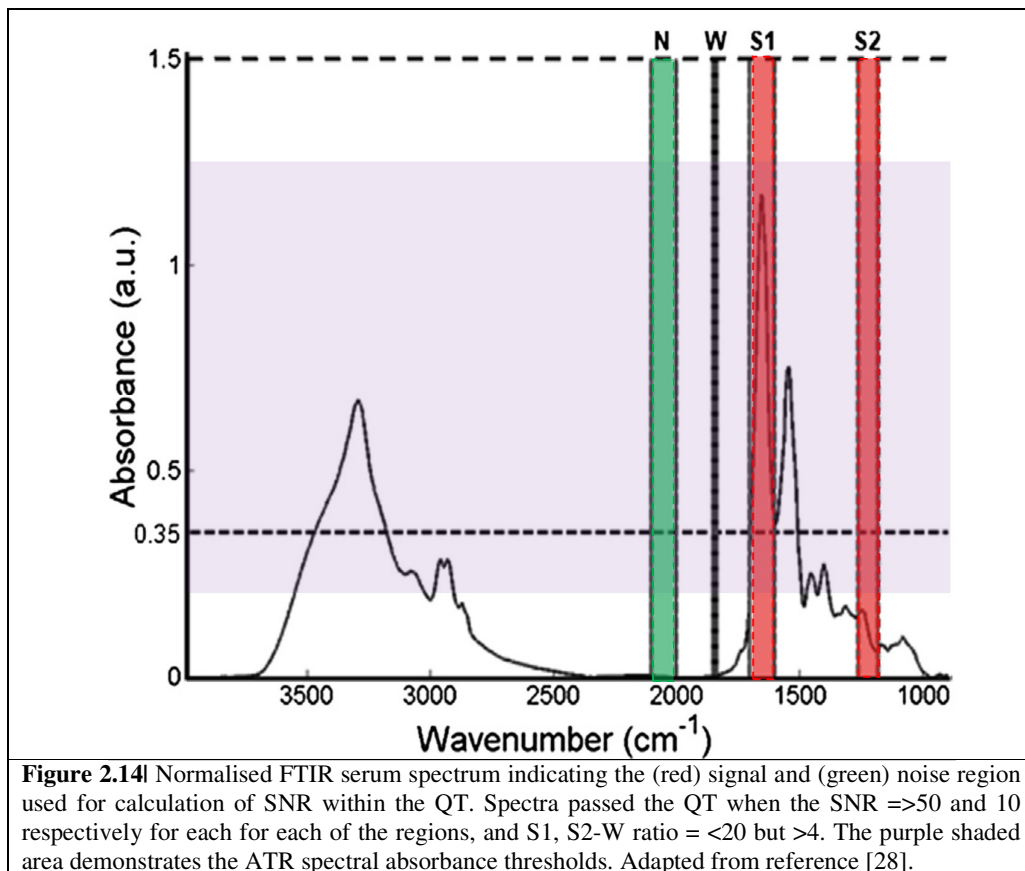
This function calculates the SNR of a spectrum’s intensities over a given spectral range, i.e, any flat or low value region, taken as molecularly silent. As the Raman shift is in the MIR region, Bruker states that the SNR is calculated in the range 2100-1900  $\text{cm}^{-1}$  but may be adjusted based on visual appearance of the spectra. RMS is calculated as the root of the mean square of deviations (*i.e.*, the STD). Then a quadratic function is fitted to the spectrum, defining the (nominal) signal. The mean of which is divided by the newly calculated noise values and yields the SNR (Eq.7b).

$$(\text{RMS}) \text{ SNR} = \frac{S}{\text{RMS}}$$

Eq. 7b

These values were compared the same method for deionized water. Thus, the lower threshold limit for samples had to be higher than that of the SNR of water. Further, a comparison with the SNR profiling function on Lab Spec 4 was carried out, as the values were easily interpretable. For our data, a threshold > 2.5-3 times the noise was acceptable for good spectral quality. There are three SNR tests to be employed for the Raman spectral QT in this project, if necessary; all is dependent on the instrument used and spectral signal recorded.

In contrast, using the FTIR spectral quality test, as stated previously, only minor adjustments to the an already published quality parameter was necessary to differentiate HT-FTIR and ATR-FTIR datasets. Figure 2.14 shows the specific regions for calculation of the QT used on the OPUS software (v.6.5).



### 2.3.2 Variance Analysis

From the spectra that were successful in passing the quality test, the variability between spots of the same sample were assessed by calculating descriptive statistics, such as mean and standard deviations (average and median values). Examples of values attained are shown in Table 2.1 below.

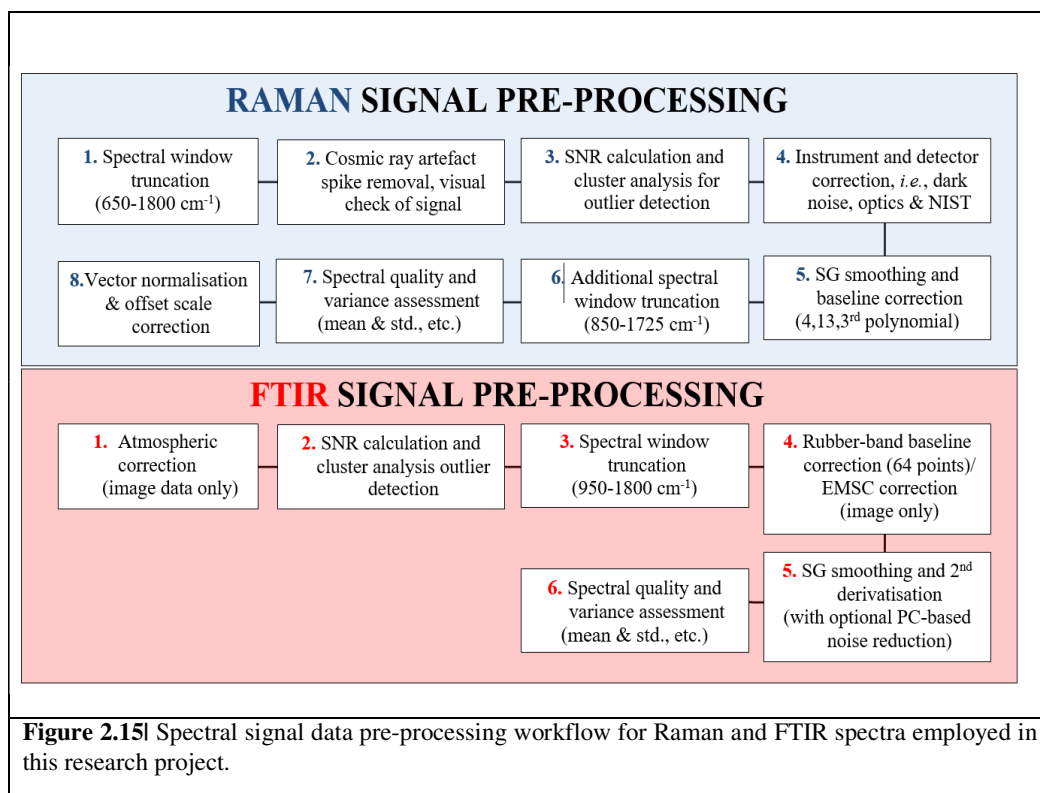
**Table 2.1|** An example of some descriptive statistical values for raw Raman spectral data from dried serum drops, including the number of spectra passing quality testing and SNRs.

DCDD FTC_#	C/P QT	mS/N	MIN STD	MAX STD	MEAN STD	MEDIAN STD
1	C/9	41.79	3806.7	6830.7	5934.7	6223.3
	P/9	31.01	3807.4	5540.3	4996.6	5087.7
2	C/9	34.51	2534.7	5030.2	4081.7	4418.8
	P/9	29.67	6174.1	7339.0	6902.9	6952.5
3	C/9	30.01	2705.0	5955.7	4858.8	5185.9
	P/8	21.02	2096.9	7728.1	5358.3	5624.0
4	C/9	42.68	4725.3	9418.9	7783.8	8159.2
	P/9	28.88	1785.5	6846.4	4328.7	4314.2
5	C/9	34.92	2600.6	4639.1	3852.6	3932.3
	P/9	24.08	2022.6	4982.6	3678.4	3894.1
6	C/9	31.55	5159.5	7714.8	7045.7	7287.4
	P/9	26.51	2134.9	4446.2	3498.3	3631.5
7	C/9	19.18	926.21	3666.1	2372.2	2429.5
	P/9	40.77	3834.3	5729.7	4684.6	4743.3
8	C/8	38.90	2014.8	5057.3	3936.0	4118.6
	P/8	30.29	2170.0	5153.2	4134.6	4368.5
9	C/9	31.58	1816.9	3212.6	2602.7	2679.0
	P/9	45.22	1851.4	3407.5	3005.9	3125.4
10	C/9	67.98	460.6	1640.0	1107.3	1203.7
	P/9	36.87	445.8	1819.7	1149.6	1174.7
11	C/9	35.61	1886.2	5257.2	3731.4	3877.0
	P/9	20.27	1092.5	1616.8	1473.2	1517.1
12	C/9	34.90	1875.9	2533.0	2316.7	2356.9
	P/9	14.31	491.5	1938.4	1189.0	1220.5
13	C/9	18.61	403.33	2356.4	1300.8	1257.2
	P/8	36.67	2620.4	4331.9	3595.4	4152.6
14	C/9	27.08	3934.2	6009.2	5454.9	5621.1
	P/9	15.97	1068.9	2897.5	2083.4	2175.4
15	C/9	17.96	199.5	803.1	517.08	531.35
	P/9	72.80	1516.8	4271.2	3295.7	3595.8

#: number; DCDD: drop coated dried deposition; C/P acquired spectra from physical spot (centre or periphery);  
STD: standard deviation; mSNR: mean signal-noise-ratio *via* RMS calculation

The variance values plus the individual results for the quality assessments are carried out on all spectroscopic data in all experiments but is shown here for purposes of not repeating tables for every aspect in the results and discussion later.

Following both spectral quality and variance testing, the data is submitted to either a FTIR or Raman pre-processing workflow. Figure 2.15 demonstrates the preprocessing regimes used for analysis of the data within this thesis.



### 2.3.3 Statistical Data Analysis

All the data were processed using the SPSS statistical programme. Test and control data were compared and analysed. All the data were expressed as mean  $\pm$  the standard error of the mean (SEM) or Standard Deviation (SD). A value of  $p < 0.05$  was taken as significant.

## 2.4. FTIR & RAMAN SERUM DIAGNOSTIC APPLICATIONS

Selected FTIR and Raman approaches were employed as a screening application for disease diagnostics. The following section will detail the methodologies employed for FTIR and Raman diagnostics within this research project.

### 2.4.1 FTIR Serum Diagnostics

Two proof-of-concept studies using the HT-FTIR approach developed previously, were carried out for two different clinical contexts:

*Study 1: Hepatic fibrosis patients stages I-IV (n= 43)*

*Study 2: Brain tumour patients (BTNW) (n=70)*

#### 2.4.1.1 Patient Sera for HT-FTIR Spectroscopy

Following the HT-FTIR protocol for a 3-fold serum dilution described previously, both patient groups were prepared for analysis and 5  $\mu$ L of the preparations were deposited on to a 384-well ( $\varnothing$ = 4 mm silicon plate). Following air-drying in a controlled laboratory environment the following parameters were employed for spectral collection:

- *Spectral range:* 4000-400  $\text{cm}^{-1}$
- *Number of scans:* 32 co-added
- *Spectral resolution:* 4  $\text{cm}^{-1}$

Prior to data collection from the sample, a background spectrum was acquired and corrected by the instruments' software (automatically). For each patient, approximately 8-10 individual technical repeats were produced. A total of n= 430 spectra was collected from the fibrotic patient set, and n= 700 spectra for the BTNW patient set.

##### 2.4.1.1.1 Hepatic Fibrosis Patient Biobank

The study was conducted with a bank of serum samples stored at  $-80\text{ }^{\circ}\text{C}$ , originally taken for a FibroTest in patients with chronic hepatitis C (cHCV). Informed consent was obtained from all patients for performing the diagnostic test as part of routine medical care. Following biochemical analysis, the remaining serum was stored at  $-80\text{ }^{\circ}\text{C}$ . The study was carried out according to the principles of the Declaration of Helsinki (DoH).

A total of n= 400 spectra was acquired from 40 patients using the HT-FTIR spectroscopic analysis of fibrosis stages (F0-FIV); where 0 indicates no presence of fibrosis or very early stages, FI-FII (minimal fibrotic formation), and FIII-FIV (advanced fibrosis).

It should be noted that these samples were used for both FTIR and Raman analyses.

##### 2.4.1.1.2 BTNW Patient Biobank

The brain tumour samples were obtained from the Walton Research Tissue Bank and Brain Tumour North West (BTNW); all patients had given research consent. Only newly diagnosed

patients with a histopathological diagnosis of GBM (WHO grade IV) were included. All blood samples were taken preoperatively. The serum tubes were left to clot at room temperature for a minimum of 30 minutes and a maximum of 2 h from venepuncture to centrifugation. Clot separation *via* centrifugation was achieved at 1200×g for 10 mins. and 500 µL aliquots of serum was dispensed into pre-labelled cryovials. Serum samples were snap frozen using liquid nitrogen and stored at –80 °C.

Demographic data for each patient was also stored on the tissue bank database and could be unblinded by a member of the clinical team caring for the patient. The research described here was performed with full ethical approval (BTNW and Walton Research Tissue Bank Application number 1108).

For spectroscopic investigation, 70 patients' blood serum was analysed with the HT-FTIR spectroscopy. The gliomas and the severity of brain tumours were derived from patients with a mix of normal, clinically confirmed GBM brain tumours and metastatic patients. A total of n=700 spectra were acquired.

#### **2.4.2 Raman Serum Diagnostics**

To investigate the diagnostic potential of the macro Raman technique using the 40 mm lens adaptor and cuvette approach developed, the HR300 was used in single point macro mode, as previously described.

Two proof-of-concept studies were carried out for two different clinical contexts:

*Study 3: Hepatic fibrosis patients (stages I-IV) (n=43)*

*Study 4: Cirrhotic patients with/without HCC (CiRCE) (n=250)*

##### **2.4.2.1 Patient Sera for Liquid Macro Raman Spectroscopy**

For liquid macro Raman analysis 50 µL samples per patient were prepared and deposited in to a Quartz cuvette with the interior width (4 mm) and subjected to the horizontal macro Raman approach (Figure 11). The following parameters used for both studies are described (2.2.2.4.1). This largescale patient population (n=250) were derived from clinically confirmed cirrhotic patients with and without HCC. The aim of the study was to employ macro Raman serum spectroscopy for classification of cancer from cirrhosis. Each patient sample was repeated 5 times and a total of n=1250 spectra were acquired.

Patient serum samples from both HCC and cirrhotic cases were taken from a wider study called CiRCE (Cirrhose et Risque de Cancer dans le Grand-Est), which is a case-control north-eastern France study; ongoing for around 8 years, aiming to analyse many factors involved in hepatocarcinogenesis amongst cirrhotic patients. In a wider aspect, environmental, nutritional and metabolic factors have been investigated and interrogated using a suite of biochemical, molecular biology and metabolomic tools, elsewhere by other researchers. This study was approved by the Comité de Protection des Personnes Est; under the agreement: 2008/09, and by the Agence Française de Sécurité Sanitaire des Produits de Santé (agreement no: 2008-A00023-52), and patients gave their written consent for participation. All patient samples were taken from 6 north-eastern France hospitals (Besancon, Dijon, Metz, Nancy, Reims and Strasbourg). Besancon was later excluded from spectroscopic testing as the contributing centre revealed incorrect protocol from sample inclusion. Sample provenance was from 24 hour fast-orientated patients and immediately post venepuncture; the blood samples were processed, and the serum was stored frozen at -80°C.

Clinical diagnosis of cirrhosis was made either by histology of a liver biopsy or by a combination of clinic-biological signs of hepatic portal hypertension, and/ or endoscopy of portal hypertension or imaging of cirrhosis. Cirrhotic patients were assessed for characteristics of HCC at inclusion *via* ultrasonography (US) and/or computed tomography (CT) and/or magnetic resonance imaging (MRI), plus clinical biochemistry, *i.e.*, AFP levels < 100 ng/mL, and subjected to routine follow-up regimes of up to 1 year revealed none of the cirrhotic patients were suspected with HCC, *i.e.*, 6-month hepatic ultrasonography and levels of AFP.

Confirmed diagnosis of HCC by the pathologists relied on the EASL guidelines [157], and patients younger than 35 years were not included, nor were patients with HIV infection, extrahepatic carcinoma, and unconsented patients (*e.g.* not been able to give written consent). A full list of antecedent medical information was collected for the samples, including age, sex, cirrhotic/HCC severity and grading, aetiology (alcohol/HVB, HVC), diabetes, plus levels of bilirubin and AFP.

**| CHAPTER 3 |**

**FTIR SERUM  
SPECTROSCOPY SAMPLE  
STABILITY AND  
DAGNOSTIC  
APPLICATIONS**

---

**| CHAPITRE III |**

**SPECTROSCOPIE IRTF DU  
SÉRUM: STABILITÉ DE  
L'ECHANTILLON ET  
APPLICATIONS  
DIAGNOSTIQUES**

### III.1 RÉSUMÉ

Les résultats présentés dans ce chapitre concernent les études menées sur la stabilité du sérum et le potentiel diagnostique à travers les différentes approches IRTF. Un des paramètres pré-analytiques suivi était la répétition des cycles de congélation / décongélation du sérum et le séchage du sérum à l'air ambiant. Ensuite, les applications sont portées sur deux études diagnostiques. Le but de cette recherche est double. Le premier objectif était de comprendre les variations pré-analytiques du pool de sérum humain, en comparant une approche en réflexion ATR-IRTF et une approche en mode transmission HTS-IRTF en observant l'effet des cycles de congélation et décongélation répétitifs et du séchage à l'air ambiant sur des sérums humains congelés. Le second objectif était d'appliquer ces connaissances à l'analyse de cas diagnostiques (fibrose hépatique et gliomes), pour une application potentielle au dépistage/diagnostic à haut débit, associée à une analyse de données multivariée avancée.

### III.2 CONCLUSION

En résumé, cette étude en deux parties a analysé par différentes technologies IRTF le pool humain de sérums pour évaluer la variabilité pré-analytique. Les profils spectraux ont été analysés pour analyser l'effet des cycles répétés de congélation et de décongélation du pool de sérum et pour déterminer sur les mêmes échantillons les effets de séchage du sérum à l'air ambiant. L'analyse de données par ACP a montré très peu de changements dans le profil spectral sérique suite aux cycles de congélation/décongélation. Globalement, les cycles semblent mixtes, sans véritable clustering logique ou pouvant être décrits expérimentalement via des modifications pré-analytiques. L'ensemble de données obtenu par méthode haut-débit HTS-IRTF pour les cycles decongélation/décongélation a également montré un résultat similaire, quelque soit le type de technique IRTF utilisée. Ici, la collection spectrale était hautement automatisée, ce qui en fait une bonne application à haut débit. L'analyse par ACP a montré une autre combinaison complète de cycles de congélation et de décongélation, ce qui conforte que cet aspect pré-analytique n'aurait pas d'incidence sur les profils spectraux. Pour les deux techniques, des pics communs ont été montrés pour les sérums, les protéines ayant la plus grande influence dans la région des bandes amide. Cette région reflète généralement deux contributions principales: les bandes amide I à 1580-1680  $\text{cm}^{-1}$  amide II à 1500-1580  $\text{cm}^{-1}$ .

Afin d'étudier plus en profondeur les effets du séchage ambiant, l'ACP a également été appliquée aux données de séchage (prises sur 11 temps sur une période de 24 heures). La déshydratation du sérum induit l'effet « coffee-ring » (anneau de café), l'épinglage des lignes de contact de la goutte séchant entraînant la formation d'un gradient de concentration entre le sel, les ions, les protéines et autres biomolécules. Cette étude a montré qu'un tel effet est observé avec l'ACP, car les mesures en fonction du temps semblent suivre un schéma séquentiel allant du point  $t=0\text{h}$

(sérum liquide en gouttes fraîches) au point  $t=24h$  suivant le séchage. Ceci est visible dans les changements dans la région spectrale de vibration des liaisons  $C = O \sim 1655 \text{ cm}^{-1}$ , à la déformation des  $N-H \sim 1540 \text{ cm}^{-1}$  et la vibration des  $C = C \sim 1615 \text{ cm}^{-1}$ .

Comme il est de pratique courante de travailler rarement sur des échantillons non frais compte tenu de la nécessité de stockage cryogénique, nous avons effectué dans cette étude préliminaire une évaluation spectroscopique IR des variations potentielles dues aux cycles de congélation / décongélation et au temps laissé à l'air ambiant ou au séchage de d'un pool de sérums humains, explorant les différences potentielles intra-échantillon de la stabilité des échantillons de sérum, sans la phase fraîche. Les facteurs importants, tels que les exigences de stockage, les aspects de dilution et toutes les phases préparatoires clés au sein d'un laboratoire doivent être pleinement pris en compte. En règle générale, quelle que soit l'analyse de la variabilité, qu'elle soit pré-, intra- ou post-analytique, le biofluide de choix doit respecter le processus analytique permettant de suivre les erreurs.

La deuxième partie de cette étude consistait à tester ces méthodologies éprouvées pour leur potentiel diagnostique. Deux banques de sérum de patients ont été interrogées (fibrose et gliome). Les sérums de patients atteints d'une fibrose ont été mesurés à l'aide de la méthodologie haut débit HTS-IRTF et analysés à l'aide de deux approches chimiométriques, l'ACP et l'AFD. Pour la fibrose, les résultats révèlent un groupe divisé par spectres de patients, par stade de fibrose et par un mélange de fibrose pour représenter les caractéristiques de la maladie de bas et haut grades.

L'ACP n'a pas été en mesure de classer les groupes de patients. Les « loadings positifs » observées sur DF1 ont démontré une légère séparation entre les patients F2 et F4 (fibrose légère vs fibrose avancée, telle que la cirrhose). DF2 a en outre montré une légère différence entre les fibroses modéré et élevé, comme l'expliquent les loadings négatifs et positifs, respectivement. Les pics présents sur les loadings négatifs de DF2 montrent des intensités accrues dans les régions de  $1530 \text{ cm}^{-1}$ ,  $1635 \text{ cm}^{-1}$  et  $1748 \text{ cm}^{-1}$ . Ces pics sont identifiables à des liaisons amide II, amide I (hélices alpha) et esters lipidiques, qui pourraient représenter un ensemble de bandes « marqueur ». D'autres modifications pourraient être associées à des bandes de protéines à environ  $1220 \text{ cm}^{-1}$ , à environ  $1550 \text{ cm}^{-1}$  et à des feuilles plissées / structures protéiques agrégées [177].

Ces résultats démontrent que l'ACP et l'AFD peuvent faire ressortir certaines différences biochimiques entre certains stades de la fibrose. Bien qu'une tentative de validation par PC-DFA ait été tentée, cela n'ajoute rien au résultat. À l'avenir, il serait avantageux d'utiliser davantage

les techniques MVA, telles que SVM, ANN ou PLS-DA pour tenter de mieux classer les données, suivi d'un test à l'aveugle sur le modèle retenu.

Les sérums de patients atteints de gliome ont été mesurés à l'aide de la méthodologie HTS-IRTF et analysés à l'aide d'une validation croisée ACP, AFD et RBF-SVM. Tout d'abord, une analyse bidirectionnelle des données a été effectuée à l'aide d'ACP et l'AFD ; une première séparation par patient, et en second lieu par catégories normale, métastases et glioblastome multiforme (le plus avancé et agressif). Ici, il a été démontré que l'ACP et l'AFD peuvent montrer certaines distinctions entre les états normal et pathologique, en combinant les deux stades de cancer.

Le facteur DF1 permet clairement une bonne séparation entre les patients sains (NORM) et malades (MET) via des bandes de discrimination attribuées à la bande de la déformation -CH<sub>3</sub> des lipides à 1348 cm<sup>-1</sup> et de l'élongation C=O de la bande peptidique associée à la bande amide I des structures protéiques alpha-hélicoïdales à 1640 cm<sup>-1</sup>.

Les loadings positifs de DF1 permettant la séparation NORM/MET mettent en avant trois pics, la déformation -CH<sub>2</sub> des groupes méthylène et des lipides à 1440-1462 cm<sup>-1</sup>, l'amide I des structures protéiques  $\alpha$ -hélicoïdales à 1640 cm<sup>-1</sup>, et l'étirement CO des acides nucléiques, ADN / ARN dans la gamme 1075-1088 cm<sup>-1</sup>. Les loadings négatifs de DF1 font ressortir deux pics à 1348 cm<sup>-1</sup> et 1640 cm<sup>-1</sup>, qui impliquent la déformation lipidique de CH<sub>3</sub> et la structure protéique en hélice alpha de l'amide I, permettant la séparation entre les patients sains et malades. Le facteur DF2 permet un début de séparation entre MET et GBM. Les loadings positifs peuvent être attribués à la majorité des patients atteints de GBM et les loadings négatifs à la plupart des patients atteints de MET ; les deux groupes étant influencés par la présence de patients sains. DF2 n'est donc pas aussi discriminant que DF1.

Dans l'ensemble, cette étude démontre que la variance globale de l'analyse IRTF à haut débit est moins grande lorsque l'on compare la RSD des approches méthodologiques ATR et HTS-IRTF. En résumé, la présente étude montre que les variations précliniques peuvent être minimisées avec de bonnes pratiques de laboratoire, ne dépassant pas une quantité importante de congélations / décongélations répétitives, et que ces variances possibles, si bien prises en compte, ont une influence minimale sur la capacité de diagnostic de la technologie IRTF en tant qu'outil de classification / diagnostic des maladies lorsqu'elle est utilisée avec l'analyse multivariée des données.

### 3.1 INTRODUCTION

Biofluid diagnostics or ‘liquid-biopsies’ is emerging as an interesting alternative to cell and tissue analysis. The extraction of bio-fluids are minimally invasive to the patient and have great ease of access at routine procedures, such as general screenings, blood donations or diabetic glucose monitoring. Blood components such as serum and plasma are said to present a high degree of diagnostic-rich information for the clinician [65]. Within the bloodstream alone, there are over 20,000 different proteins and many proteomes. This information-rich liquid presents extracellular biochemical information for spectroscopists. Such an approach enables the acquisition of a biochemical fingerprint towards a global molecular biomarker screening regime, surpassing the quest for single biomarkers of disease. To date, serum, plasma, saliva and bile have demonstrated significant diagnostic and prognostic potentials within bio-fluid spectroscopy [6, 27, 110-111, 131, 137, 152]. Some studies have demonstrated the efficacy for its use in disease screening. Petrich *et al.* [131] analysed 1429 serum samples from 389 patients to demonstrate the ability of IR spectroscopy to discriminate myocardial infarction from other ailments pertaining to generic chest pain (sensitivity and specificity of 88.5% and 85.1%, respectively we obtained). Backhaus *et al.* [107] used sera from breast cancer and healthy patients and demonstrated a diagnostic accuracy of >95%. With this same analysis, they also demonstrated close to 100% diagnostic ability of IR to differentiate between hepatitis C, Alzheimer’s disease, and coronary heart disease. Hands *et al.* [27] demonstrated diagnosis of gliomas from whole patient serum, resulting in 96% and 100% sensitivity and specificity, respectively.

To fully realise biofluid FTIR spectroscopy however, some of its potential drawbacks warrant further clarity. IR is a strong absorber of water, so the most common protocol for bio-fluid analysis using FTIR vibrational spectroscopy is to collect spectral data from a drop-dried bio-fluid. This technique is very simple but does suffer some minor drawbacks. Upon drying, an evident chemical gradient occurs across the drying drop, the so-called ‘coffee-ring’ phenomenon [158,-161], meaning a heterogeneous sample deposition results as the internal molecules migrate to the periphery of the drop. Few studies have tried to circumvent this, but Esmonde-White *et al.* [161] showed there is no substrate effect on the chemical content of the periphery ring but evidence of spatial distribution of the intrinsic protein components. To develop further understanding on this matter, more recently a HT-FTIR transmission serum study was able to show that with increased dilutions, the ‘coffee-ring’ effect is more pronounced, suggesting lipids, nucleic acids and proteins as the migrating components [152]. To date, a variety of sample preparation techniques have surfaced to combat. Ollesch *et al.* [162] employed a vacuum-controlled drying, demonstrating picolitre drop-drying with an automated

transmission IR process. They reported significantly increased spectral resolution (comparative to a non-automated approach) [162]. Ultimately, within the field, such studies have driven efforts to develop disease pattern recognition. Currently research is underway towards a digital assessment of the water content in ATR spectroscopy for the calculation and subsequent removal from the IR signal in the pre-processing (un-published).

Pre-clinical or pre-analytical variability refers to the sample preparation/processing stages, whereby differences could be derived from any aspect of the timeline from sample collection, processing to final storage. This aspect seems to stand out as the critical point severely hampering large-scale, multi-centric studies from having good quality data. Overall, it seems there is a need for robust standardisation and to diminish sample-related factors prior to distinguishing diagnostic prowess. It is generally understood that most analytical errors often originate at the pre-analytical level [163-165], which could influence any aspect of data pre- and post-treatment. A recent small bio-fluid study employing HT-FTIR transmission spectroscopy examined sample-related variation. They found sample collection modality, choice of substrate, volume, dilution and manner of deposition, and freeze-thaw and drying conditions all are sample-related factors that affect data quality and reproducibility [165].

### **3.1.2 Introduction to Hepatic Fibrosis**

Hepatic fibrosis results from the constant formation of dead and regenerated liver cells, which causes the liver to become inflamed and leads to the formation of scar tissue. The body's natural defence initiates an inflammatory response which leads to decreasing amounts of extracellular matrix proteins at the injury site, allowing the necrotic/apoptotic cells to be replaced with new parenchymal cells of the liver. With persistent/ chronic injury, liver regeneration eventually fails, so the hepatocytes are substituted with an abundance of matrix proteins, *i.e.*, fibrillar collagen, leading to bridging fibrosis to end-stage irreversible cirrhosis. The grades of fibrosis are shown in Table 3.1.

**Table 3.1** METAVIR F score system for assessing the extent of inflammation and fibrosis by histopathological evaluation in liver biopsy of patients with hepatitis C. The grade indicates the activity or degree of inflammation. The stage depicts the degree of scarring/fibrosis [82, 166].

<b>Histological Activity: (Degree of Inflammation)</b>	<b>Fibrosis Stage (Degree of Scarring / Fibrosis)</b>
A0 = no activity	F0 = no fibrosis
A1 = mild activity	F1 = expansion of portal zones
A2 = moderate activity	F2 = expansion of most portal zones and occasional bridging
A3 = severe activity	F3 = expansion of most portal zones, marked bridging and occasional nodules
	F4 = cirrhosis (end-stage irreversible scarring)

Chronic hepatitis (types B and C), heavy alcohol consumption, trauma, toxins or other factors can all lead to hepatic fibrosis. Generally, fibrosis is seen as a precursor for more advanced liver disease, such as cirrhosis and primary liver cancer or hepatocellular carcinoma. Therefore, it is essential for correct staging and early classification. The liver does not contain any nerves, meaning liver diseases and liver cancer can be asymptomatic. Meanwhile, current diagnostic methods and screening techniques are still without a true gold standard [167] and are at their core, time-intensive methods which are unfit for large screening programs. Additionally, they are highly dependent on accurate interpretation by medical professionals and still are subject to interpretable variances in opinion from clinician to clinician. Recently, a blood serum biomarker test (Fibrotest) and an elasto-graphic technique akin to ultrasound, termed Fibroscan, has shown a potential for good diagnostic accuracy; specifically, at advanced fibrosis (93% and 70% sensitivity and specificity, respectively) [82].

### 3.1.3 Introduction to Gliomas

Gliomas account for ~ 2% of all diagnosed cancers per annum within the UK and represents 20 years of lives lost on average (breast cancer is 13.5 years) [168]. It is one of the deadliest human diseases and has an appalling prognosis, e.g. 32% of 7000 people diagnosed with primary brain cancer in the UK will be still alive at the end of the first year following diagnosis [168]. Moving forward 5 years, this statistic drops to 14% [169]. Overall, the health burden that results from diagnosis of the tumour of the brain is important, not only because of the diagnosis of cancer, but because of the progressive neurological disease that accompanies it [170]. According to the WHO, malignant gliomas are glioblastomas and are characterised at grade IV, anaplastic astrocytomas, oligoastrocytomas and anaplastic oligodendrogliomas are all grade III [104, 171-172]. The early diagnosis of glioma can be difficult. After a clinical suspicion the diagnosis is

made by imaging technologies, such as magnetic resonance imaging (MRI) and computer tomography (CT) scanning, and when a patient is symptomatic, the diagnosis is obvious by CT [172]. Confirmation of the diagnosis is made by histological examination of the part surgically obtained. A biopsy of the brain involves a very painful drilling through the skull to sample under microscopic examination. At this stage, there is no indication as to the nature of the tumour, *i.e.*, benign or malignant. Histological gradation is not able to provide a precise prognosis and therapeutic information for the individual treatment of patients [172]. Patho-diagnosis is to some extent subjective. A study found disagreement between original and review data for clinical diagnostic for 43% of cases [173]. Previous intraoperative spectroscopic glioma grading research has shown the ability of FTIR for *in situ* classification of tumour margins and was able to detect high-grade tumours with 100% and 97% sensitivity and specificity, respectively [28]. Additionally, Hands *et al.* [111] used ATR-FTIR to demonstrate the diagnosis of low-grade and high-grade gliomas from non-cancer with 94% and 97% sensitivity and specificity, respectively. More recently, they were able to show the power of differentiation between cancer vs. non-cancer, cancer severity and the metastatic origin from serum with high diagnostic accuracy, using feature extraction to improve overall diagnostic ability *via* discriminant features from a stratified clinical approach [28].

The aim of this research is two-fold, the first aim was understanding of pre-clinical variations on pooled human serum, using ATR-FTIR, HT-FTIR and a FTIR transmission by observing the action of repetitive freezing and thawing cycles and environmental drying on non-fresh human sera will be developed. The second aim was to apply this knowledge to the analysis of diagnostic cases (hepatic fibrosis and gliomas), for a potential high-throughput screening application, combined with advanced multivariate data analysis.

### **3.2 MATERIALS AND METHODS (for details see 2.2.1.1)**

#### **3.2.1 Serum Samples**

Two sets of studies were conducted for this research chapter, a set for pre-analytical variation and another set for high-throughput screening of disease biomarkers.

#### **3.2.2 Pre-analytical Variation Studies**

The pre-analytical variation set of studies was further subdivided into two studies: the freeze-thaw cycle (FTC) analysis of pooled human serum, and the subsequent environmental air drying of the serum (ED). In a first instance, research-grade mixed pooled ‘off the clot’ human serum (TCS Biosciences, Buckingham, UK) was used to study preclinical variation. Following passive thawing at room temperature (RT), the serum samples (n=15) underwent repetitive FTC. The samples were stored at -80° C until spectral acquisition, with a 24-hour period between each

FTC. Prior to spectral collection, each of the FTC vials were manually inverted and vortexed to ensure thorough mixing of all serum components. Secondly, the same samples were monitored for air-drying effects on serum stability *via* an ED study.

A total of n=450 spectra were collected for FTC analysis (n=15 cycles, 10 spots and 3 spectra per spot), and n=33 spectra across 11-time points throughout 24 hours serum drying (3 spectra per time point).

#### 3.2.2.1 ATR-FTIR Serum Analysis

ATR-FTIR spectral acquisition was carried out on the Cary 600 series FTIR spectrometer (Agilent Technologies, USA), equipped with a single reflection diamond ATR accessory (PIKE MIRacle™, UK) (see 2.2.1.1.1 for full details). One microlitre of sera was deposited on to a diamond internal reflection element (IRE) and dried for ~ 8 minutes at RT. Spectra were collected over the 4000-600 cm<sup>-1</sup> wavenumber range, a spectral resolution of 4 cm<sup>-1</sup> with 32 co-added scans. Prior to spectral collection the ATR platform was wiped clean using Virkon disinfectant (Fisher Scientific, UK) and 70% ethanol solution (Thermo Scientific, UK). This was repeated prior to each spot and a background spectrum was acquired and automatically subtracted prior to each spot deposition (Pro-Resolutions Software, Agilent Technologies, USA).

#### 3.2.2.2 HT-FTIR Serum Analysis

HT-FTIR spectral acquisition was carried out on the Bruker high-throughput screening (HT-XT) extension coupled to a Tensor 27 spectrometer (Bruker Optics GmbH, Ettlingen, Germany) (see 2.2.1.2.1 for full details). FTC serum samples were diluted 3-fold [165] with physiological water (0.9% injectable sodium chloride, PROAMP<sup>(R)</sup>, Aguetant, France) and 5 μL was deposited on to a 384-well silicon plate of 4 mm diameter per well, before leaving to dry at RT for ~ 1 h. Spectral collection was carried out in the transmission mode *via* the OPUS v6.5 software (Bruker Optics GmbH, Ettlingen, Germany), with a spectral resolution of 4 cm<sup>-1</sup> over the range of 4000-400 cm<sup>-1</sup> with 32 co-added scans. A background spectrum was acquired and subtracted prior to each sample measurement. One spectrum was obtained per well, and the experiment was repeated (n= 240). A zero-filling factor was applied, and a Blackman-Harris 3-term function was employed for Fourier transformation. Between each of the experiments the silicon plate was cleaned using distilled water, 40% SDS solution and 70% ethanol.

#### 3.2.2.3 FTIR Transmission Micro-spectroscopy Serum Analysis

To investigate the kinetics of environmental ageing of the drop-dried serum the Cary 620 microscope FTIR spectrometer was employed. The 128 x 128-pixel liquid nitrogen-cooled focal plane array (FPA) detector (Agilent Technologies, USA) was used (see 2.2.1.1.2 for full details).

A small drop (0.2  $\mu\text{L}$ ) of undiluted serum was deposited on an IR-grade  $\text{CaF}_2$  substrate and dried at RT for 10 minutes. Serum kinetics was carried out by using point mode spectral collection of specific time points over a 24-hour period. Spectral collection was carried out using the 4000-600  $\text{cm}^{-1}$  range, a spectral resolution of 6  $\text{cm}^{-1}$ , a background absorption spectrum acquired and subtracted automatically and 32 co-added scans (Pro-Resolutions Software, Agilent Technologies, USA). Spectra were collected after 10 mins, 30 mins, 1 h, 1.5 h, 2 h, 2.5 h, 3 h, 3.5 h, and at 7 h 14 h, and 24 h (n=33).

### 3.2.3 Diagnostic Screening Studies

These diagnostic studies that evaluated patient sera from two diseased populations were acquired from retrospective UK and France biobanks. Firstly, a bank of serum samples stored at  $-80^\circ\text{C}$ , originally taken for a Fibrotest procedure in patients with chronic hepatitis C were subjected to spectroscopic analysis. Informed consent was obtained from all patients for performing the diagnostic test as part of routine medical care. Following biochemical analysis by the bio-pathology team at Reims hospital CHU, the remaining serum was stored at  $-80^\circ\text{C}$ . The study was carried out according to the principles of the Declaration of Helsinki (DoH). Secondly, brain tumour patient samples obtained from the Walton Research Tissue Bank and Brain Tumour North West (BTNW) were investigated. The gliomas and the severity of brain tumours were derived from patients with a mix of normal (*NORM*), clinically confirmed glioblastoma multiforme brain tumours (*GBM*) and metastatic patients (*MET*). All patients had given research consent for the study. Only newly diagnosed patients with a histopathological diagnosis of GBM (WHO grade IV) were included for the GBM cohort. For the MET population, the cancer sources were from origins of breast, lung, melanoma, and renal (BLMR). Full ethical approval from the BTNW and Walton Research Tissue Bank was granted (Application number 1108). Tables 3.2a and 3.2b present the demographic clinical data for both screening studies (fibrosis and gliomas).

**Table 3.2a** Brain tumour patient demographics, including tumour grade, number of patients, age range/mean ages and gender.

<b>Tumour Grading</b>	<b>Patients</b>	<b>Age Range / years</b>	<b>Mean Age/ years</b>	<b>Gender M; F</b>
NORM	23	16-58	42.9	M12; F11
MET	24 (BLMR)	35-84	62.5	M9; F15
GBM	23	43-79	63.4	M19; F4

**Table 3.2b** Fibrosis patient demographics, including disease stage (METAVIR F score), number of patients, age range/mean ages and gender.

<b>METAVIR F</b>	<b>Patients</b>	<b>Age Range / years</b>	<b>Mean Age/ years</b>	<b>Gender M; F</b>
F0	12	18-57	39.6	M5; F7
F1	9	43-60	54.2	M3; F6
F2	19	44-73	59.9	M8; F11
F3	4	50-69	59.8	M2; F2
F4	5	51-66	58.8	M3; F2

All blood samples for the diagnostic studies were stored in tubes and left to clot at RT for a minimum of 30 minutes and a maximum of 2 h from venepuncture to centrifugation. Clot separation *via* centrifugation was achieved at  $1200 \times g$  for 10 minutes and 500  $\mu\text{L}$  and 1000  $\mu\text{L}$  aliquots of serum was dispensed into pre-labelled cryovials. Serum samples were snap frozen using liquid nitrogen and stored at  $-80\text{ }^\circ\text{C}$  until spectroscopic analysis. For the serum fibrosis study, a total of  $n=410$  spectra were acquired from 49 patients using the HT-FTIR spectroscopic analysis of fibrosis stages (F0-F4); where 0 indicates no presence of fibrosis or very early stages, F1-F2 (minimal fibrotic formation), and F3-F4 (advanced fibrosis/cirrhosis) (refer to Table 3.1 for more details). It should be noted that these samples were used for both FTIR and Raman Spectroscopy analyses (Raman Spectroscopy analyses are covered in Chapter 4). For the serum glioma study, a total of  $n=700$  spectra were acquired from 70 patients using the same HT-FTIR approach.

### 3.2.3.1 Diagnostic HT-FTIR Spectroscopy

The patient serum samples were analysed for high-throughput screening with FTIR, following preclinical observations with normal pooled sera. Both patient groups were processed in the same manner and employed the same HT-FTIR methodology with a 3-fold dilution. In brief, the 5  $\mu\text{L}$  preparation was loaded on a silicon plate, air-dried and subjected to transmission point mode spectroscopy from each well; collecting 1 spectrum per well, with 10 technical repeats per patient.

### 3.2.4 Spectral Quality Testing and Variance Analysis

Raw spectra from spectroscopic studies were submitted to a spectral quality test for the both ATR and transmission FTIR, to check SNR, control absorbance intensity, observe water vapour (OPUS v6.5 Software, Bruker Optics GmbH, Ettlingen, Germany). The quality test documented previously [27, 28], discarded spectra from future analysis if the spectral absorbance was less than 0.35 and more than 1.8 arbitrary units (a.u). To account for the low intensity of the ATR-

FTIR data, a parameter change using 0.02 a.u as the lowest threshold and 1 a.u as the highest was adopted. For calculating of SNR of the maximum absorbance of two characteristics bands are chosen *i.e.*, amide I ( $\sim 1700\text{-}1600\text{ cm}^{-1}$ ), and a sugar-ring vibration ( $\sim 1260\text{-}1170\text{ cm}^{-1}$ ) followed by a derivation to assign the maximum values. Noise is evaluated at  $\sim 2100\text{-}2000\text{ cm}^{-1}$  and is calculated based on its maximum value of the first derivative. Furthermore, the water vapour content is evaluated on the spectral range which indicates strong water vapour absorbance *i.e.*,  $\sim 1847\text{-}1837\text{ cm}^{-1}$ . Spectra submitted passed the test if the SNR ratio was greater than 50 and 10, respectively for each of the regions, and the signal to water ratio was less than 20 but greater than 4. (see Figure 2.14 from 2.3.1 for full details). The spectra that passed the threshold test were analysed for the variability between spots of the same sample by calculating basic statistics, such as mean and RSD.

### 3.2.5 Spectral Pre-processing & MVA Strategies

#### 3.2.5.1 Pre-processing Strategies

The spectra were pre-processed using a MATLAB platform R2015b (The Math-Works, Inc., USA). Starting with a noise reduction *via* a principal component (PC)-based noise reduction algorithm for non-linear iterative partial least squares (NIPALS), the spectra were deconstructed using the first 30 PCs of the signal to improve the SNR of the dataset. Essentially, the data is deconstructed into orthogonally (uncorrelated) latent variables called PCs and then reconstructed again negating the higher noisier PCs. After de-noising, the baseline was corrected using the Rubber-band method and smoothed using a Savitzky-Golay process, followed by vector normalisation to account for sample thickness variation.

It is noteworthy to state that all datasets were observed for principal component analysis (PCA) *via* scores and loading differences using different manipulations of combinations of the following processes: full spectrum, fingerprint only spectrum, non-derivatives and 2<sup>nd</sup> derivative functions prior to moving forward with subsequent analysis.

#### 3.2.5.2 MVA Strategies

All datasets were then submitted to PCA and then canonical variates analyses termed discriminant function analysis (DFA).

PCA was originally developed as an invaluable unsupervised dimension reduction data analysis technique that helped to find latent data patterns within a data matrix of  $m \times n$  ( $m$  is the variables (columns) *i.e.*, wavenumbers, and  $n$  are the observations (rows), *i.e.*, the associated absorbance. Decomposition of the data matrix could find its pure components of the spectrum, *e.g.* wavenumbers, spectrum of interest plus noise [47]. PCA transformed the data in to uncorrelated variables that were orthogonal linear combinations arranged in the descending order of PCs, *i.e.*,

most variation and in turn the greatest data separation was determined *via* the 1<sup>st</sup> PC. In ascending order, each successive PC explains less and less of the data variation.

DFA was originally developed as supervised data reduction analysis technique, which used linear combinations inherent within the data matrix to help determine the greatest data separation, whilst accounting for *a priori* information, such as class, disease state, or sample differences due to freeze-thaw and drying *etc.* The orientation of the combinations was visualised as increases in class membership and reductions in class variation, *i.e.*, the algorithm maximises between and minimises within the data groups.

### 3.3 RESULTS & DISCUSSION

#### 3.3.1 Freeze-Thaw Cycle Study

##### 3.3.1.1 ATR-FTIR Spectral Variance

To investigate the pre-clinical variation seen within a serum sample, whether it is analytical, 'human' or biological differences, two series of experiments were designed to observe changes in the freezing and thawing of human pooled serum and the ambient environmental drying of serum. The spectroscopic data were collected and pre-processed for the removal and reduction of extraneous background effects. The data were firstly de-noised using NIPALS algorithm for PC-based noise reduction, using 30 PCs. The data were then vector normalised to account for differences in path-length and variations within the sample that could be attributed to the analytical operation of the instrument.

Table 3.3 demonstrates the freeze-thaw cycle data for the fingerprint region of the spectrum. From each freeze-thaw cycle (n=15), 30 spectra were collected (n=450), the mean of each cycle (n=10) showed a smaller overall variance. The variation between the freeze-thaw cycles is shown by the relative standard deviation (RSD). The values displayed show the range of the RSD, plus the overall mean and median RSD values per cycle. The analysed data represent the mean values for each of the freeze-thaws across the spot deposited (n=150). A spectral quality test (see 2.3.1 for details) was completed, which demonstrated a 100% of the mean spectra succeeded (n=150).

From the whole of the biological spectrum analysed, the highest and lowest aspects of the region in relation to RSD% were the 1799 cm<sup>-1</sup> region (316%), and 1534 cm<sup>-1</sup> region (0.31%), respectively. The lowest region can be assigned to the amide II region, specifically the  $\beta$ -pleated sheet structures,  $\delta(\text{N-H})$  and  $\nu(\text{C-N})$  174-175], whereas the most varied region is suggestive of a noise region, a somewhat molecularly silent area on the spectrum. The overall variation here can be attributed to noise. The row highlighted in red in Table 3.3 shows the overall highest

values of mean/median RSD values (17.43% and 13.6%), respectively. Noticeably, the lowest variance region across all the freeze-thaw cycles was ~ 1520 – 1645 cm<sup>-1</sup>, indicative of protein bands.

**Table 3.3** Statistical values for variance analysis, demonstrating the relative standard deviation between cycles of freeze-thaw using ATR-FTIR spectroscopy.

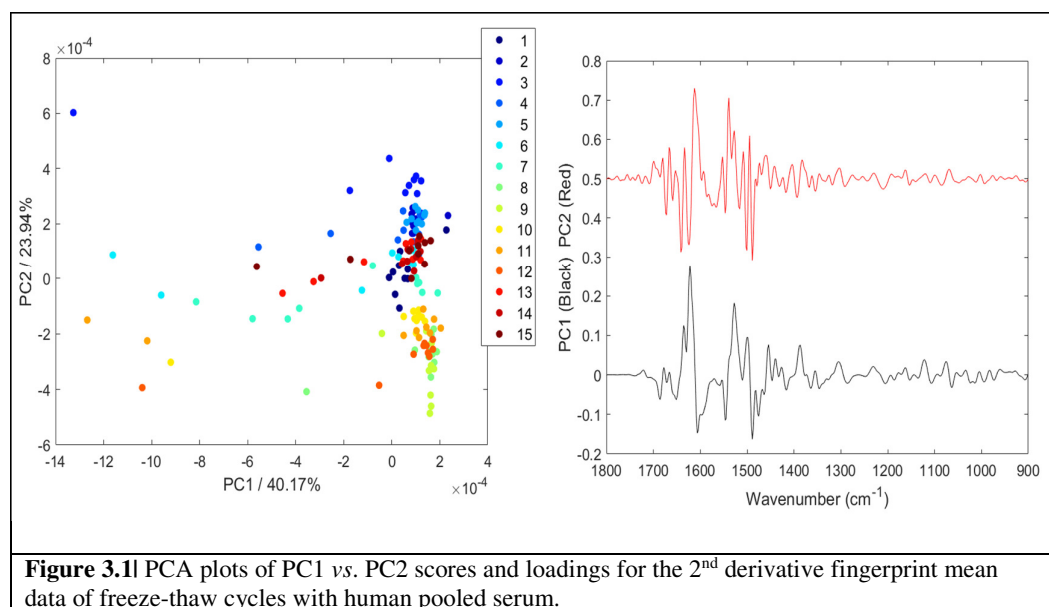
ATR-FTIR FTC	Spectral QT passed	RSD% min	$\tilde{\nu}$ / cm <sup>-1</sup>	RSD% max/	$\tilde{\nu}$ / cm <sup>-1</sup>	Av. RSD %	Med. RSD %
1	10	0.44	1635	316	1797	9.44	2.43
2	10	0.13	1534	187	1799	6.49	1.70
3	10	0.39	1631	316	1799	12.74	7.55
4	10	0.46	1531	316	1799	11.64	6.37
5	10	0.31	1577	316	1798	8.40	1.59
6	10	0.28	1635	210	1794	13.40	10.15
7	10	0.87	1535	316	1795	15.86	8.99
8	10	0.32	1541	247	907	9.97	4.75
9	10	0.28	1535	316	1795	8.99	2.18
10	10	0.67 /	1543	316	1799	13.63	7.55
11	10	0.58	1645	316	1799	17.43	13.56
12	10	0.37	1633	259	1799	13.33	8.36
13	10	0.77	1526	316	1798	14.52	6.55
14	10	0.42	1632	316	1793	8.32	3.62
15	10	0.49	1711	257	1794	10.86	5.50

As can be seen from Table 3.3, most of the cycles have a very low overall RSD value, the green highlights all the cycles that have a mean RSD value of < 10 and <5 for mean and median, respectively. From this, it can be asserted that there is very good reproducibility across the data set for freeze-thaws and infer that any major variance shown in subsequent analysis could only be owed to the composition of the sample itself.

### 3.3.1.2 ATR-FTIR Principal Component Analysis

Following variance analysis, the data were submitted for explorative clustering by PCA. Various combinations of the pre-processing of the data were tried following the necessary noise reduction, normalisation and offset to the baseline. The data were observed by PCA scores/loadings for the full spectrum (1800-600 cm<sup>-1</sup>), the fingerprint region (1800-900 cm<sup>-1</sup>), both with and without 2<sup>nd</sup> differentiation of the signal. All methods showed very little difference in terms of the scores/loadings on PCs 1-5, so it was decided that subsequent analysis would be carried out on the 2<sup>nd</sup> derivative fingerprint region going forward. Additionally, for clarity and the fact that no difference was seen between the data points of the mean data spots and full data, mean analysis was chosen for clarity of visualisation. Figure 3.1 demonstrates PCA results. The scores (left) and loadings (right) for PC1 and PC2, show ~ 64% of the explained data variance

overall. PC1 and PC2 loadings are respectively shown in black and red on the plot. As can be seen here, explorative analysis with PCA was unable to show significant and logical separation of the freeze-thaw cycles. One can see that PC2 is separating a few groups slightly away from the central cluster. Cycles 9-12 are visible on the lower aspect of PC2, explained by the positive loadings on the lower frequency region of the spectrum (red). Additionally, there are stray/outliers within the data that appear to be very spread across the biplot. The tentatively assigned component loadings are shown in Table 3.4 to the serum bio-profile. The loadings for both PCs are seen clearly in Figure 3.2.



Although it appears that some clustering is shown, one could argue this is quite insignificant when we observe the clustering plot is shown in a space of  $\times 10^{-4}$ . Overall, the cycles appear mixed, with no real logical clustering seen, or that can be understood experimentally. One could argue that such an observation is due to the inherent intra-sample variability, and perhaps differences in spotting technique, and not related to the FTC effect, based on the illogical sequence seen amongst the cycles. This also aligns well with previous research, whereby only the fresh sera found complete separation from 5 repetitive FTC [165]. Based on these observations, any further multivariate analysis would only highlight potential artefacts within the data, so PCA was the endpoint for analysis.

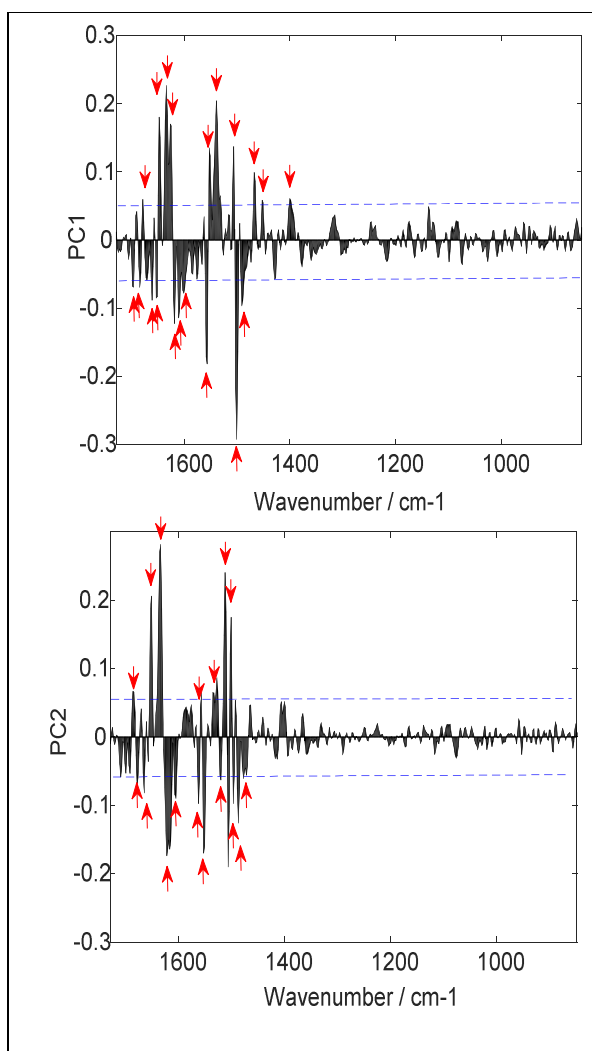


**Figure 3.2l** PC1 (top) and PC2 (bottom) component loadings from PCA, showing minimum threshold (dotted blue line) and applicable peak positions (red arrows). Data is from 2<sup>nd</sup> derivative fingerprint region of freeze-thaw cycle analysis using the mean data points per spot.

**Table 3.4** Tentatively assigned FTIR serum biological peak assignments based on the PC loadings (Figure 3.2), PC1 and PC2 from mean spot data in the 2<sup>nd</sup> derivative.

$\tilde{\nu}/\text{cm}^{-1}$	Tentatively assigned FTIR serum peaks	PC1	PC2
1398	$\delta(\text{CH})$ (lipids), $\nu(\text{CO})$	+	-
1452	$\delta(\text{CH}_2) / \delta(\text{CH}_3)$	+	-
1468	$\delta(\text{CH}_3)$ antisym. (protein)	+	-
1487			-
1496	$\delta(\text{CH}_2) / (\text{CH}_3)$		-
1500	Amide II (proteins) ( $\beta$ -pleated sheets) $\delta(\text{N-H})$ (60%), $\nu(\text{C-N})$ (40%)	-	+
1506		+	-
1512	Tyr		+
1522	Amide II (proteins) ( $\beta$ -pleated sheets) $\delta(\text{N-H})$ (60%), $\nu(\text{C-N})$ (40%)		-
1527	Amide II (proteins) $\delta(\text{N-H})$ (40-60%) / $\nu(\text{C-N})$ (18-40%)	-	+
1539		+	
1552		+	-
1556		-	+
1562			-
1603	Amide I (proteins) ( $\beta$ -pleated sheets) $\nu(\text{C-O})$ (80%), $\nu(\text{C-N})$ (10%), $\delta(\text{N-H})$ (10%)	-	
1606			-
1610		-	
1618		-	
1620	Amide I (proteins) $\nu(\text{C-O})$ (70-85%) / $\nu(\text{C-N})$ , $\delta(\text{N-H})$		-
1626		+	
1633		+	+
1647	Amide I of antiparallel $\beta$ -sheet/aggregated strand protein structures $\nu(\text{C-O})$ (76%), $\nu(\text{C-N})$ (14%), $\delta(\text{C-N})$ (10%) $\nu(\text{C-O})$ (76%), $\nu(\text{C-N})$ (14%), $\delta(\text{C-N})$ (10%)	+	
1651		-	+
1660		-	
1664			-
1676	Amide I (proteins) antiparallel $\beta$ -pleated sheets and turns		-
1678		+	
1684	$\nu(\text{C-O})$ in nucleic acids, carbonic acid/ esters	-	+
1698		-	+

Figure 3.2 shows the major peaks responsible for the observation seen in PCA (scores – Figure 3.1). It is worth noting, the region around 1500-1700  $\text{cm}^{-1}$  is generally dominated by amide bands and the strong characteristic absorption band at  $\sim 1655 \text{ cm}^{-1}$  is formed from the stretching vibration of  $\nu(\text{C-O})$  of the amide I, whilst  $\delta(\text{N-H})$  bending vibrations, coupled to  $\nu(\text{C-N})$  stretching, appear around 1550  $\text{cm}^{-1}$  [175].

### 3.3.1.3 HT-FTIR Spectral Variance

To further investigate the preclinical variation seen within a sample, a high throughput study was devised, to see if one method was more able to see differences in freeze-thaw cycles, than another. Using HT-FTIR spectroscopic data were collected in an automated way, pre-processed and submitted to the same analysis as above. To keep in line with the previous experiment, the data were submitted for PC-based noise reduction, using 30 PCs, and vector normalised prior to any multivariate analysis.

Table 3.5 shows the HT-FTIR freeze-thaw cycle data for the fingerprint region of the spectrum. From each freeze-thaw cycle (n=15), 2 lots of 8 spectra per well were collected (n=240), the mean of each cycle (n=8) showed a smaller overall variance, as can be seen in the Table 3.3. As before, the relative standard deviation (RSD) was used to assess overall variance. When observing the fingerprint biological spectrum of the serum, the minimum RSD value (0.52%) at 1631 cm<sup>-1</sup>, and the maximum (281%) at 1799 cm<sup>-1</sup>. The lowest regions can be attributed to the amide I band, specifically the  $\nu(\text{C-O})$ , with some attributes from  $\nu(\text{C-N})$  and the  $\delta(\text{N-H})$  [27,47] experiment. The largest mean and median RSD value is highlighted in orange in Table 3.5 (18.51% and 12.67%). In comparison to the values seen in Table 3.3, these appear overall higher, but the maximum RSD values appear to be generally less *i.e.*, an RSD mean/median range difference between the studies are 10.98% and 11.86% (ATR), and 8.23% and 9.04% (HT), respectively mean and median. Therefore, the data acquired from the automated HT-FTIR seems to be more reproducible, suggesting less effects with this method. Alongside of this, a HT spectral quality test (described in 2.3.1) was carried out and resulted in a 100% of the mean spectra succeeding the test.

**Table 3.5|** Statistical values for variance analysis, demonstrating the relative standard deviation between freeze-thaw cycles using HT-FTIR spectroscopy.

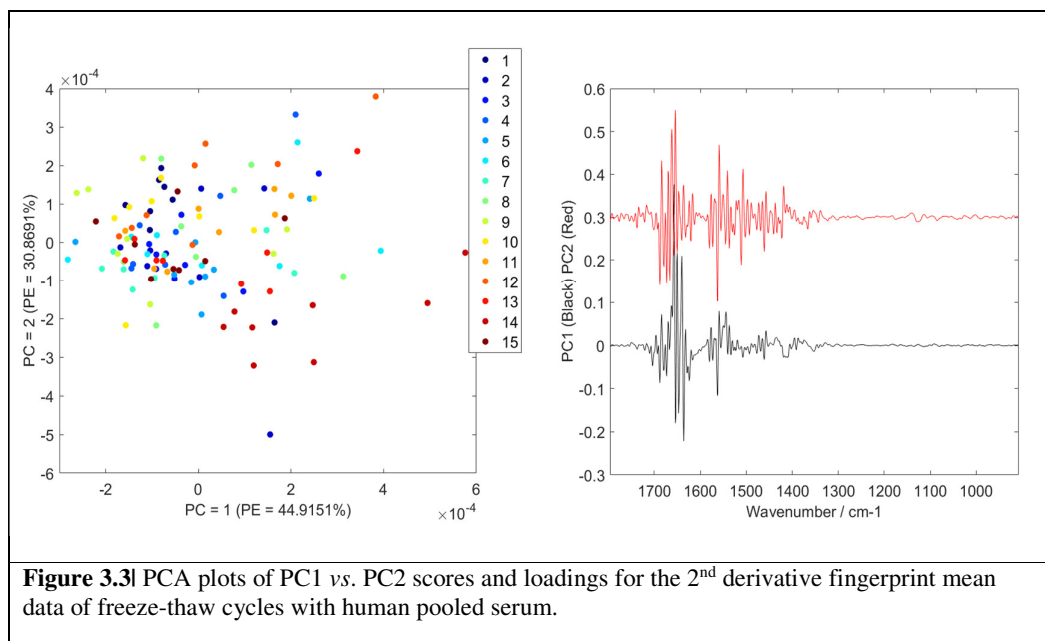
HT-FTIR FTC	Spectral QT passed	RSD% min/ $\tilde{\nu}$ /cm	RSD% max/ $\tilde{\nu}$ /cm	Av. RSD %	Med. RSD %
1	8	1.54 /1626	106 / 1799	15.75	10.61
2	8	1.40 /1554	187 / 1799	17.50	10.67
3	8	0.92 /1562	92 / 1799	14.30	9.02
4	8	0.89 /1628	106 / 1800	12.54	7.20
5	8	0.52 / 1631	149 / 1799	13.00	5.90
6	8	1.28 / 1638	92 / 1791	10.28	10.19
7	8	1.24 / 1631	110 / 1796	15.05	11.10
8	8	1.58 / 1560	101 / 1798	17.34	13.29
9	8	1.36 / 1457	200 / 1798	12.26	3.63
10	8	1.18 / 1748	96 / 1790	18.51	12.67
11	8	1.41/ 1357	99 / 1790	16.01	11.26
12	8	0.56 / 1104	112 / 1791	14.16	6.12
13	8	1.08 / 1387	103 / 1798	15.74	8.98
14	8	0.97 / 1631	281 / 1799	10.55	8.32
15	8	1.40 / 1733	105 / 1799	17.59	12.11

As can be seen (Table 3.5), most of the cycles have a very low overall RSD value, the green highlights all the cycles that have a mean RSD value of < 15 and <10 for mean and median, respectively.

#### 3.3.1.4 HT-FTIR Principal Component Analysis

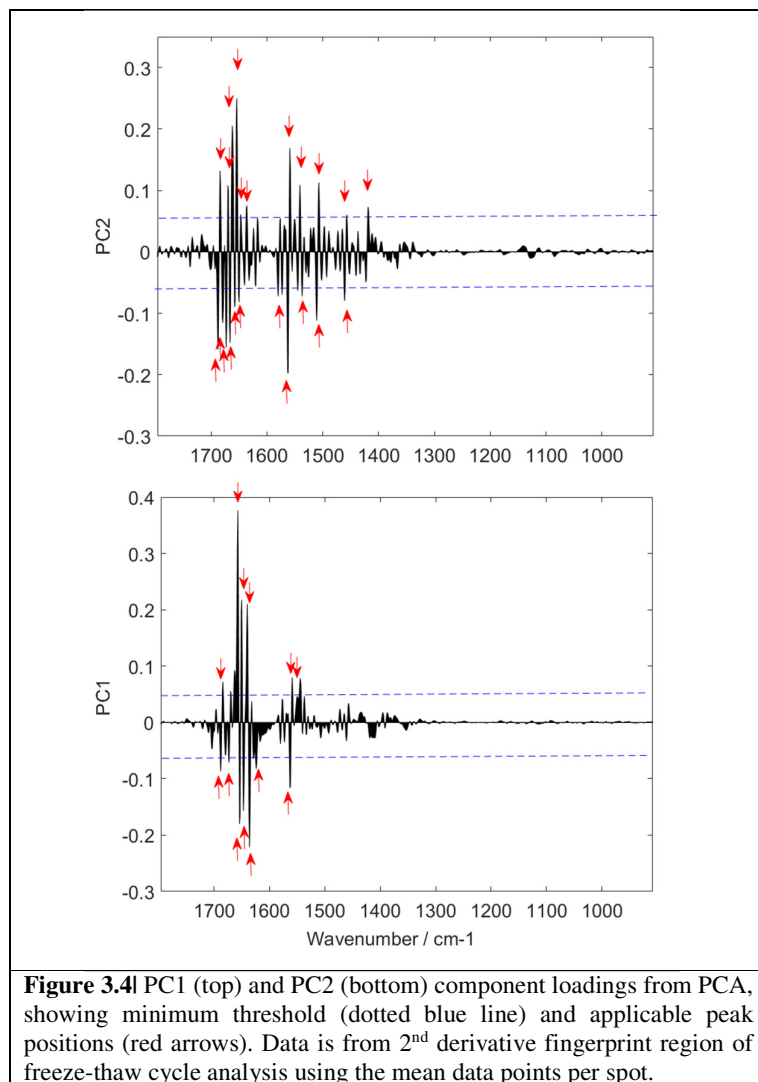
Explorative clustering *via* PCA was carried out in comparison with the ATR-FTIR study earlier (3.3.1.2). Again, various combinations of the pre-processing of the data were tried following the necessary noise reduction, normalisation and offset to the baseline, and revealed that the mean data 2<sup>nd</sup> derivative region would be moved forward for further PCA analysis.

Figure 3.3 shows the PCA results. The scores (left) and loadings (right) for PC1 and PC2, show ~ 75% of the explained data variance overall. PC1 loadings are shown in black and PC2 is visible in red on the plot. Explorative PCA was unable to show significant and logical separation of the freeze-thaw cycles as seen with the ATR results previously (Figure 3.2). Here, there appears to a general mix of all freeze-thaws with no clear clustering, *i.e.*, no cycles appear to be segregated *etc.* The tentatively assigned component loadings are shown in Table 3.6. The loadings for both PCs are displayed in Figure 3.4.



As before, the PCA space is shown to be very small and insignificant ( $\times 10^{-4}$ ). Although this technique is automated for spectral data collection, it does require at this stage an operator to spot the diluted serum samples in to the wells of the microtiter plate. This could indeed be a source of variabilities. However, when we analyse the result obtained here, we can infer that complete mix of the cycles suggests that freeze-thaw, albeit intra-sample differences, and different FTIR modalities tried, there is very little distinction between the samples themselves in terms of pre-clinical variation. Again, this result corroborates well with previous research, aforementioned [165]. As with previous analysis, PCA was the endpoint to this analysis.

Figure 3.4 shows that the major peaks responsible for the observation seen in PCA (scores – Figure 3.3). As can be seen the biggest influences within the loadings appear to be suggestive of a high protein influence. The region around  $1500-1700\text{ cm}^{-1}$  is generally dominated by amide bands. At the mid region of around  $1500-1580\text{ cm}^{-1}$  the amide II proteins  $\beta$ -pleated sheets are seen in both PC1 and PC2 loadings. The region stretching  $1580-1680\text{ cm}^{-1}$  is showing a very large indication from the antiparallel  $\beta$ -sheets and turns from aggregated proteins structures influences from amide I band stretches and deformations. There is very little influence of the scores from the low fingerprint region, which is characteristic of DNA/RNA and glycosylation linkages [175]. Overall, it appears that PC2 shows the most peaks around the amide II region, and PC1 demonstrates the largest peaks at the amide I bands.



**Table 3.6|** Tentatively assigned FTIR serum biological peak assignments based on the PC loadings (Figure 3.4), PC1 and PC2 from mean spot data in the 2<sup>nd</sup> derivative fingerprint region using HT-FTIR [28, 47, 174-176].

$\tilde{\nu}/\text{cm}^{-1}$	Tentatively assigned FTIR peaks	PC1	PC2
1418	$\nu(\text{C-O})$ $\nu(\text{COO}^-)$		+
1457	$\delta(\text{CH}_2) / (\text{CH}_3)$		+
1461			-
1507	Tyr, amide II (proteins) ( $\beta$ -pleated sheets) $\delta(\text{N-H})$ (60%), $\nu(\text{C-N})$ (40%)		+
1512			-
1538			-
1541	Amide II (proteins) ( $\beta$ -pleated sheets) $\delta$ (N-H) (60%), $\nu(\text{C-N})$ (40%)		+
1544		+	
1559	Amide II ( $\delta$ (N-H) (43%), $\nu(\text{C-N})$ (29%), $\delta$ (C-O) (15%), $\nu(\text{C-C})$ (9%), $\nu(\text{N-C})$ (8%))	+	+
1563		-	-
1581			-
1623		-	
1636		-	+
1640	Amide I of antiparallel $\beta$ -pleated sheets/aggregated protein structures / $\alpha$ -helical protein structures ( $\nu(\text{C-O})$ (76%), $\nu(\text{C-N})$ (14%), $\delta(\text{C-N})$ (10%))	+	
1647			+
1650		+	
1651			-
1653		-	
1654		-	+
1657		+	-
1662			+
1666			-
1667			-
1670	Amide I of antiparallel $\beta$ -pleated sheets and turns /aggregated protein structures		+
1673		-	
1679			-
1684		+	+
1688	$\nu(\text{C-O})$ nucleic acids	-	-

### 3.3.2 Environmental Drying Study

#### 3.3.2.1 FTIR Spectral Variance

A 24 h timed serum drying study was evaluated for changes in the serum profile throughout drying and to ascertain whether such changes could affect the pre-clinical variation. The spectroscopic data was collected following spotting (<1  $\mu\text{L}$ ) on  $\text{CaF}_2$  IR transparent substrate and pre-processed for the removal and reduction of extraneous background effects. Following the standard FTIR pre-processing adopted (de-noised using NIPALS algorithm for PC-based noise reduction, using 30 PCs and vector normalised), the data was offset. Figure 3.5 shows the full spectrum data with the  $\text{CO}_2$  region omitted for the full drying study, starting from time 0 –

10 mins at the bottom of the figure, culminating with the last time point (24 h after spotting) at the top of the figure. As can be seen most the variance observed is within the fingerprint region (right side of Figure 3.5), *i.e.*,  $1800 - 900 \text{ cm}^{-1}$ . It was previously [27] noticed that the higher frequency region is masking the lipid region ( $\nu(\text{CH}_3)$  antisymmetric stretch of fatty acids at  $\sim 2955 \text{ cm}^{-1}$ ) and the N-H stretch of proteins at  $\sim 3200 \text{ cm}^{-1}$ . Usually, when the biological sample is drying these regions are observed as a large broadband from  $\sim 3600 - 3000 \text{ cm}^{-1}$  due to strong water absorption. It is only as the sample dehydrates that these bands become apparent. Hands *et al.* [28] showed a similar drying study but with smaller increments of time points. They dried a sample from 0 – 32 mins taking spectra at shorter intervals within the 10 mins of dehydration, showing the characteristic large band broadening at the earlier stages of drying. Other works also shows the similar result of the biological spectrum [107, 158].

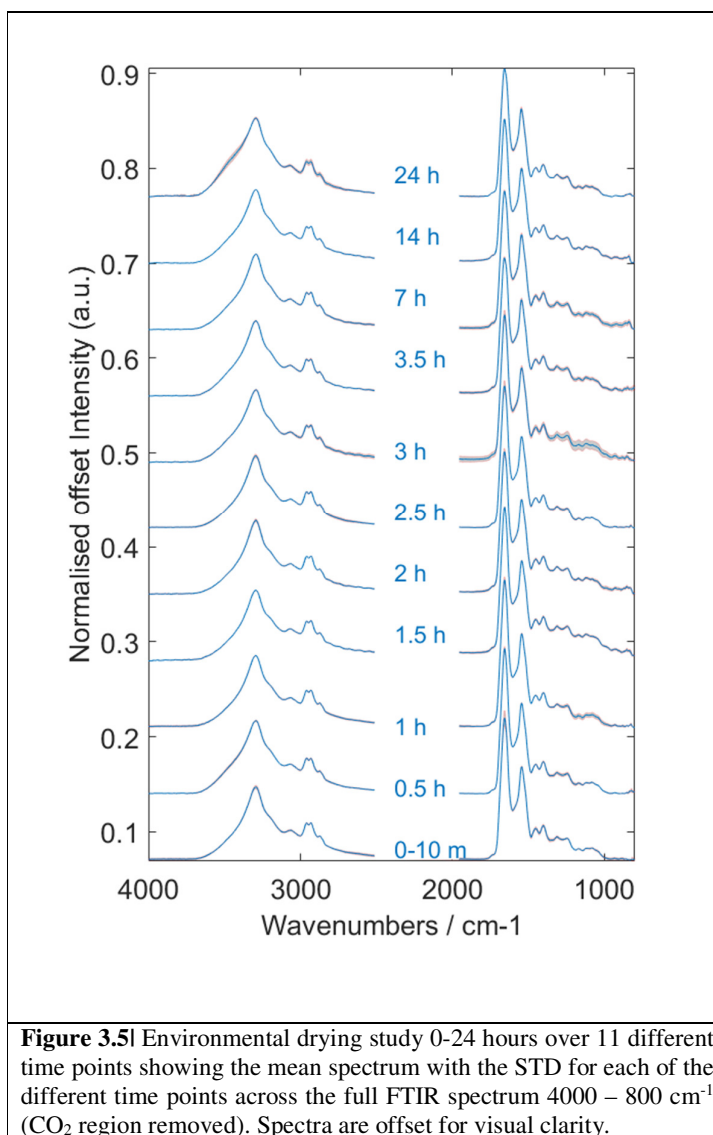


Table 3.7 shows the environmental drying data for the fingerprint region of the spectrum. From each drying stage time point ( $n=11$ ), 3 spectra were collected ( $n=33$ ). The RSD values were calculated to observe the overall variance. Given the small number of spectra collected per time point, as to ensure that spectra at a point  $x$  was only taken at that point, 3 spectra were only collected. A 100% of the spectra passed the quality test. The highest value was found on the ends of spectrum ( $1800$  and  $900 \text{ cm}^{-1}$ ) accounting for  $\sim 70 - 100\%$  RSD. The lowest relative varied region demonstrating a very low RSD of  $0.1\%$  was the amide I band region ( $\sim 1660 \text{ cm}^{-1}$ ). It can be noted here that the overall values for RSD % were very low, suggesting very good reproducibility of the experiment. The ends of the spectrum demonstrate the highest values are

due to the possibility of the noise area or a slight artefact from the data truncation to the fingerprint region. The row highlighted in orange on Table 3.7 demonstrates the overall highest values of mean/median RSD values (15.47% and 7.79%), respectively.

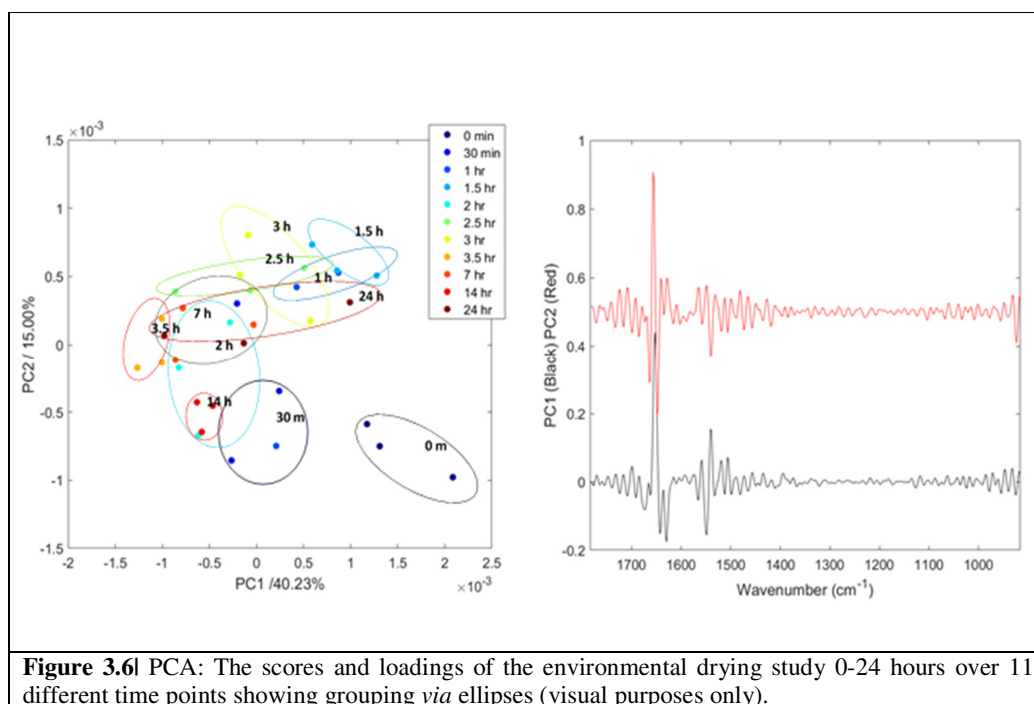
**Table 3.7** Statistical values for variance analysis, demonstrating the relative standard deviation between cycles of serum drying using transmission FTIR spectroscopy.

Transmission FTIR Drying	Spectral QT passed	RSD% min / $\bar{\nu}/\text{cm}^{-1}$	RSD% max / $\bar{\nu}/\text{cm}^{-1}$	Av. RSD %	Med. RSD %
0 – 10 mins	3	0.67 / 1631	81 / 912	14.02	4.94
30 mins	3	0.20 / 1635	87 / 945	10.80	5.67
1 hr	3	0.12 / 1485	73 / 955	15.07	7.21
1.5 hrs	3	0.1 / 1664	12 / 903	4.01	3.65
2 hrs	3	0.43 / 1635	32 / 960	8.70	4.48
2.5 hrs	3	0.23 / 1541	88 / 1800	11.87	4.39
3 hrs	3	2.11 / 1550	101 / 1799	12.05	11.21
3.5 hrs	3	0.19 / 1672	25 / 1799	8.45	6.59
7 hrs	3	0.58 / 1650	74 / 1799	15.47	7.79
14 hrs	3	0.16 / 1660	19 / 1800	5.81	3.22
24 hrs	3	0.12 / 1662	100 / 951	10.15	4.99

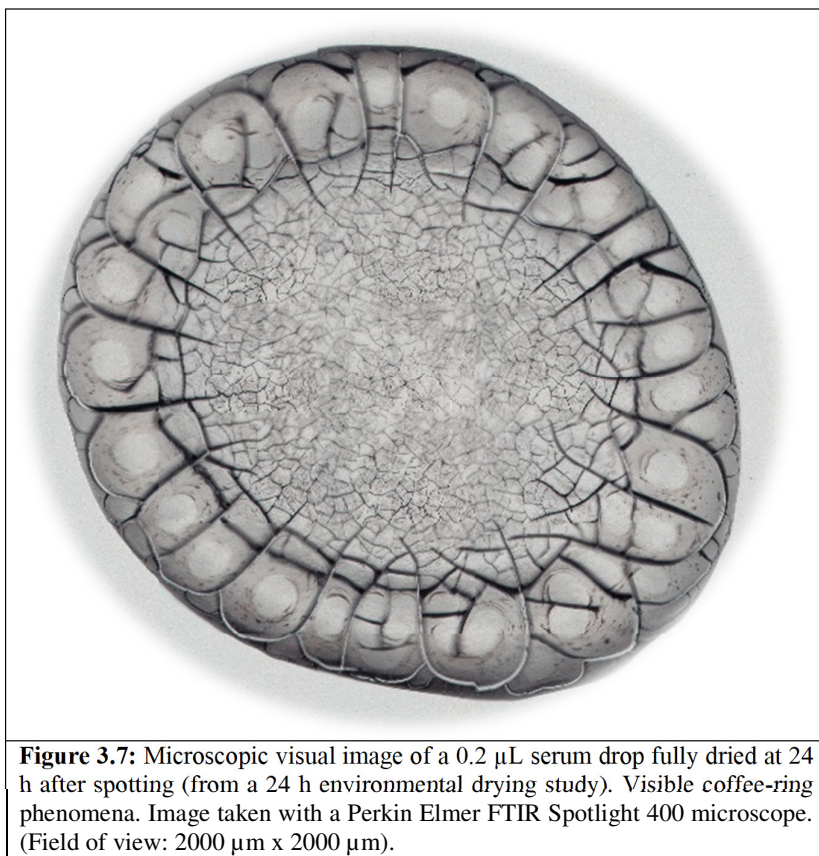
### 3.3.2.2 FTIR Principal Component Analysis

Figure 3.6 shows the PCA results with the scores (left) and loadings (right) for PC1 and PC2 that accounts for ~ 55% of the explained data variance overall. PC1 loadings are shown in black and PC2 is in red on the plot. The time points have been highlighted graphically by ellipses for better visibility and to demonstrate the variance shown intra-sample time point. As can be seen the 24 h time point data is the most varied. At this point in serum dehydration, one can fully assert that such a small amount deposited would have fully dried, so this variability could be due to the water reabsorption from the 14 hours to 24 hour window. The so-called coffee-ring phenomena states that upon drying, the salts and ions stay within the centre of the drops, as well as the heavy molecular components and the lighter molecules, such as proteins migrate towards the periphery of the drop. Figure 3.7 shows an image of the coffee-ring formation on one of the dried drops after 24 hours.

The component loadings are shown in Table 3.8. The loadings for both PCs are seen clearly in Figures 3.6 and 3.8. The loadings on PC1 seem to show peaks assigned to the C=O stretch  $\sim 1655\text{ cm}^{-1}$ , the N-H deformation  $\sim 1540\text{ cm}^{-1}$  and the C=C stretch  $\sim 1615\text{ cm}^{-1}$ . PC2's loadings show the same attributes, with increased intensity on the protein  $\beta$ -sheet  $\sim 1640\text{ cm}^{-1}$ , and C=O  $\sim 1655\text{ cm}^{-1}$  for amide I. Notably, here PCA shows that the early time points (0-10 mins) data appear to be clustered away from the rest of the data, suggesting that the internal chemistry shows differences in the molecules. This is to be expected and given the coffee-ring effect taking place has the molecule fully dehydrates, the physical presence of the centre and ring formation starts to show a chemical gradient.



**Figure 3.6** PCA: The scores and loadings of the environmental drying study 0-24 hours over 11 different time points showing grouping *via* ellipses (visual purposes only).



**Figure 3.7:** Microscopic visual image of a 0.2  $\mu\text{L}$  serum drop fully dried at 24 h after spotting (from a 24 h environmental drying study). Visible coffee-ring phenomena. Image taken with a Perkin Elmer FTIR Spotlight 400 microscope. (Field of view: 2000  $\mu\text{m}$  x 2000  $\mu\text{m}$ ).

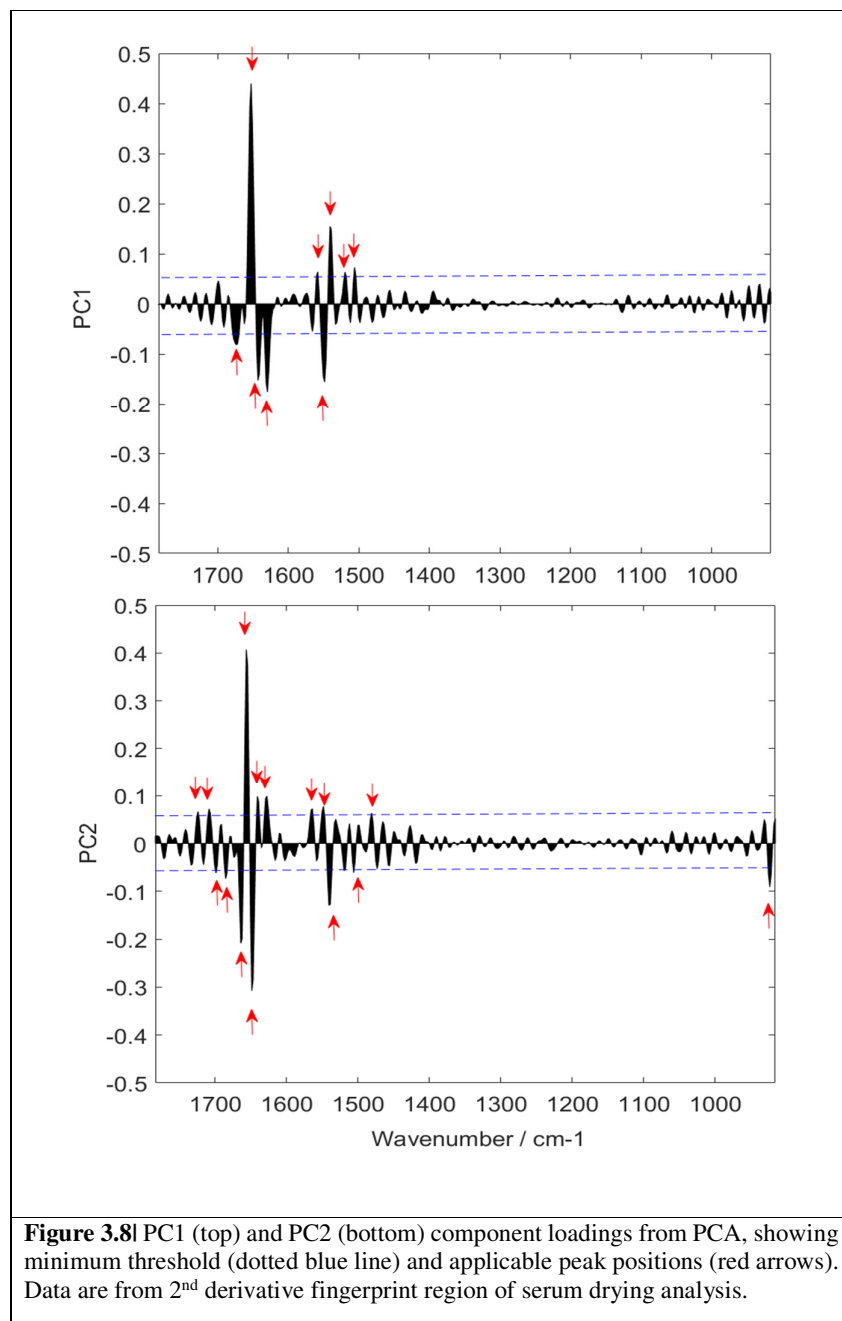


**Table 3.8|** Tentatively assigned FTIR serum biological peak assignments based on the PC loadings (Figure 7), PC1 and PC2 from the 2<sup>nd</sup> derivative fingerprint region using transmission-FTIR for serum drying [27-28, 174-176].

$\tilde{\nu}/\text{cm}^{-1}$	Tentatively assigned FTIR peaks	PC1	PC2
923	$\delta(\text{C-O-C})$ carbohydrates, $\nu(\text{C-C})$ residue $\alpha$ -helix		+
1506	$\nu(\text{C-C})$ , Tyr	+	-
1520	$\nu(\text{C-C})$ , amide II	+	
1539			-
1541	Amide II of proteins ( $\beta$ -pleated sheet structures) $\delta$ (N-H) (60%), $\nu(\text{C-N})$ (40%)	+	
1549		-	
1550			+
1558	Amide II ( $\delta(\text{N-H})$ (43%), $\nu(\text{C-N})$ (29%), $\delta(\text{C-O})$ (15%), $\nu(\text{C-C})$ (9%), $\nu(\text{C-N})$ (8%))	+	
1564			+
1628	Amide I of antiparallel $\beta$ -pleated sheets/aggregated protein structures / $\alpha$ -helical protein structures ( $\nu(\text{C-O})$ (76%), $\nu(\text{C-N})$ (14%), $\delta(\text{C-N})$ (10%))		+
1630		-	
1641			+
1643		-	
1649			-
1653		-	
1657			
1662	Amide I of antiparallel $\beta$ -pleated sheets and turns /aggregated protein structures		-
1674		-	
1684			-
1697			-
1709	$\nu(\text{C-O})$ of carbonic acid/nucleic acids		+
1724	$\nu(\text{C-O})$ esters		+

### 3.3.3 Diagnostic Serum Fibrosis Study

#### 3.3.3.1 Fibrosis Spectral Variance

Table 3.9 depicts the results for the variance analysis for the fibrosis study conducted with HT-FTIR spectroscopy. The fibrosis stage (0, 1, 2, 3, 4) is indicated for each patient. The results presented are from the mean analysis of the RSD, demonstrating the minimum, maximum, average and median values across the patient spectra. Additionally, the results of the FTIR spectral quality test are shown with a maximum of 11 spectra taken at collection for each patient. Overall, 94.25% of the spectra passed the quality test. The spectra that did not meet the absorbance threshold were discarded. This was also visualised using cluster analysis with explorative HCA (data not shown).

**Table 3.9|** Statistical values for variance analysis, demonstrating the relative standard deviation between mean patients of the fibrosis study using HT-FTIR spectroscopy.

HT-FTIR/ Fibrosis Study	Fibrosis Stage	Spectral QT passed	RSD% min / $\bar{\nu}/\text{cm}^{-1}$	RSD% max / $\bar{\nu}/\text{cm}^{-1}$	Av. RSD %	Med. RSD %
1	0	10	0.17 / 1558	316 / 957	6.56	4.88
2	0	8	0.54 / 1556	105 / 957	6.25	3.73
3	3	9	0.00 / 1550	47 / 958	4.47	4.01
4	0	10	0.34 / 1562	131 / 958	9.66	8.12
5	0	11	0.47 / 1562	155 / 958	13.58	10.31
6	0	11	0.25 / 1562	260 / 957	6.98	5.12
7	0	9	0.22 / 1560	243 / 959	9.48	7.70
8	3	10	0.13 / 1566	225 / 959	8.29	5.79
9	3	11	0.28 / 1560	229 / 957	6.41	5.11
10	3	11	0.27 / 1620	228 / 958	7.44	4.85
13	0	11	0.27 / 1620	138 / 957	8.26	6.33
14	0	10	0.46 / 1690	204 / 957	8.24	6.66
15	1	10	0.17 / 1562	316 / 957	7.05	5.60
16	1	10	0.33 / 1556	70 / 957	7.30	5.63
17	0	10	0.70 / 1620	82 / 957	13.53	11.73
18	1	10	0.46 / 1624	157 / 957	8.26	6.33
19	1	10	0.49 / 1690	202 / 957	7.97	6.13
20	2	10	0.74 / 1666	188 / 957	8.99	6.33
21	4	10	0.21 / 1563	110 / 958	11.81	6.84
22	4	11	0.27 / 1663	192 / 957	9.26	4.26
23	4	11	0.31 / 1620	120 / 958	8.26	4.13
24	4	11	0.30 / 1560	101 / 958	7.27	5.53
25	4	10	0.26 / 1566	75 / 957	8.26	6.23
26	2	11	0.40 / 1558	78 / 957	8.11	5.13
27	2	10	0.41 / 1621	98 / 958	8.02	4.33
28	2	11	0.41 / 1622	108 / 957	8.26	6.33
29	2	10	0.24 / 1620	100 / 957	8.16	7.03
30	2	11	0.27 / 1656	138 / 957	10.26	6.83
33	0	11	0.24 / 1655	124 / 957	8.26	6.22
39	2	11	0.26 / 1621	122 / 957	9.26	5.43
40	2	11	0.17 / 1623	158 / 957	10.20	7.13
41	2	11	0.33 / 1556	70 / 957	7.30	5.63
42	2	10	0.20 / 1620	82 / 958	8.53	6.73
43	1	10	0.56 / 1634	157 / 958	8.26	6.33
44	2	11	0.39 / 1680	202 / 958	10.97	6.43
45	2	10	0.42 / 1666	188 / 957	8.22	6.73
46	2	11	0.71 / 1563	110 / 958	9.01	7.04
47	2	10	0.22 / 1663	192 / 957	9.16	5.26
48	2	11	0.38 / 1625	120 / 958	8.36	4.13
49	2	11	0.39 / 1566	101 / 958	7.17	6.53
50	2	10	0.33 / 1556	99 / 957	7.22	4.13

As seen from Table 3.9, the minimum RSD value (0.00%) is at  $1550\text{ cm}^{-1}$  and the maximum (316%) is at  $957\text{ cm}^{-1}$ . The  $1550\text{ cm}^{-1}$  region is attributed to the amide II band, specifically the  $\nu(\text{C=O})$ ,  $\nu(\text{C-N})$  and the  $\delta(\text{N-H})$  [27, 175]. The region appears to be the least varied overall throughout the spectra. The most varied region is found at the low end of the spectrum, close to the cut off mark for spectrum truncation. This region is usually associated with  $\nu(\text{C-C})$  residue alpha-helix [27]. The largest mean and median RSD value is highlighted in orange (13.51% and 11.51%). The green highlight represents the sample that is below 5% on both mean and median RSD. Overall, the basic statistics results highlight very good reproducibility of the dataset.

### 3.3.3.2 HT-FTIR Principal Component Analysis

Data were observed in three ways, by patient ( $n=425$ ), by fibrosis disease stage (5 groups – (F0, F1, F2, F3 and F4) and finally by a melange of fibrosis disease (3 groups – A, B and C). For information, the melange was composed of all the patients from stage 0 and 1 in group A, stage 2 in group B, and the remaining stage 3 and 4 in group C (Figure 3.9). As shown here, PCA does not show any discernible differences between the fibrosis groups nor the mix of the groups. The loadings highlight significant protein and lipid influences, but it is not possible to detect any real separation.

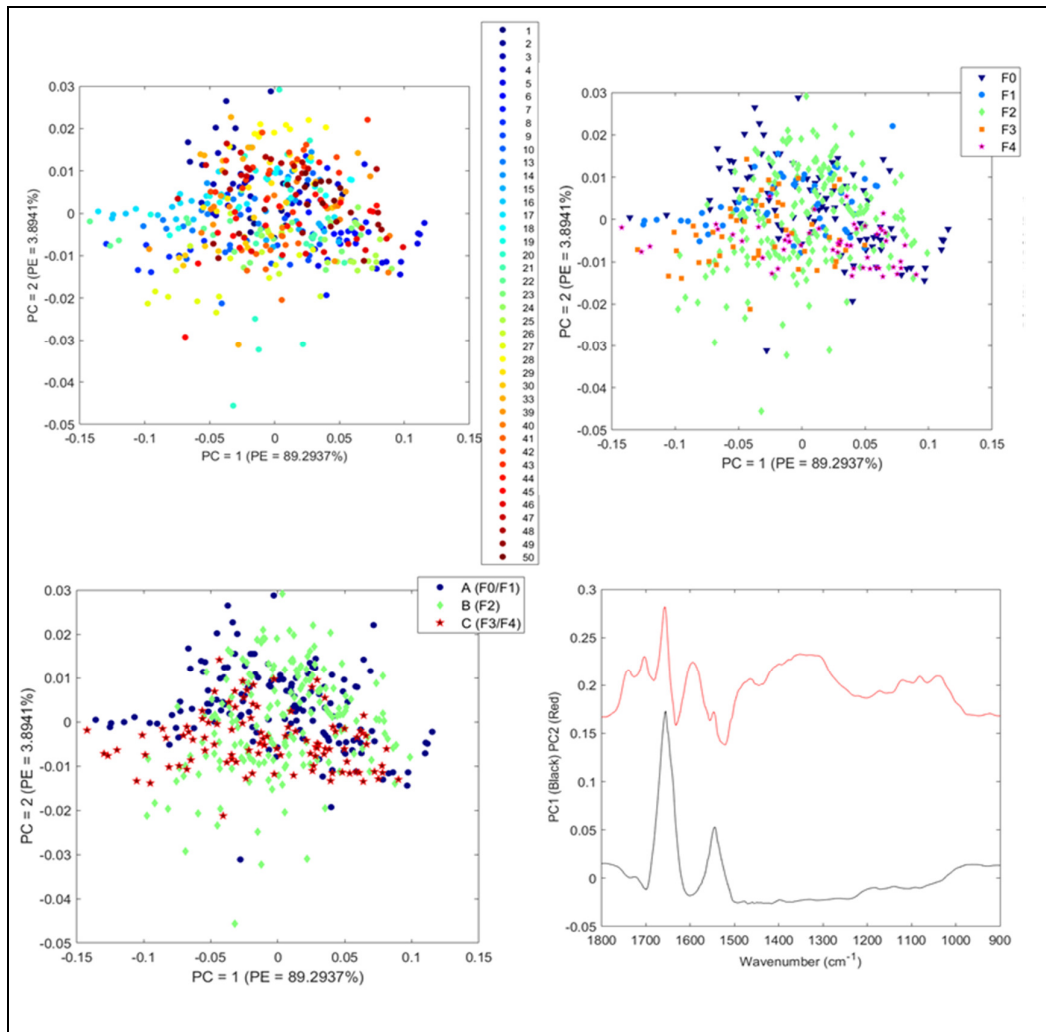


**Figure 3.9|** PCA: PC1 vs. PC2 for 3-way explorative observation analysis. Scores: top left (fibrosis patient-wise), top right (fibrosis METAVIR F score-wise), bottom left (combined METAVIR F score disease) Loadings: PC1 and PC2 (bottom right).

### 3.3.3.3 Discriminant Function Analysis

Figure 3.10 shows the DFA results. Two-way analysis was carried out; differentiation of fibrosis stages as according to the METAVIR F score, followed by grouped fibrosis stages to represent low-grade, mid-grade and high-grade patients. When one views the first DF plot (top), it appears to show some degree of grouping or class membership. The positive loadings seen on DF1 show the F2 patient spectra to be positioned away from F4 (the advanced fibrotic disease, such as cirrhosis). Whereas DF2 more clearly shows; on the second plot (bottom), the slight split in membership between low-grade and high-grade diseases, as explained by the negative and positive loadings, respectively. The peaks situated on the negative loading of DF2 show increased band intensities at  $\sim 1530\text{ cm}^{-1}$ ,  $1635\text{ cm}^{-1}$  region and  $1748\text{ cm}^{-1}$ .

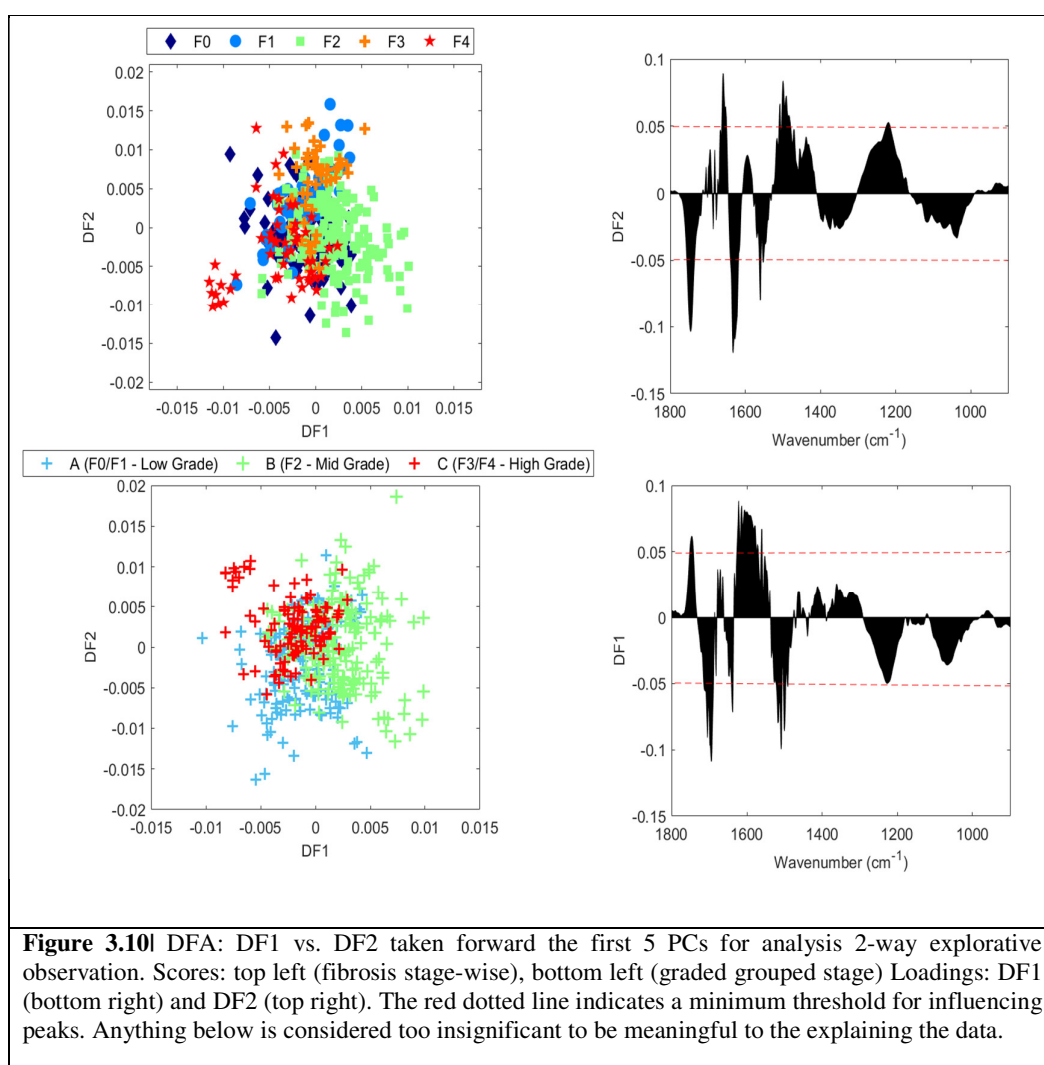


**Figure 3.10** DFA: DF1 vs. DF2 taken forward the first 5 PCs for analysis 2-way explorative observation. Scores: top left (fibrosis stage-wise), bottom left (graded grouped stage) Loadings: DF1 (bottom right) and DF2 (top right). The red dotted line indicates a minimum threshold for influencing peaks. Anything below is considered too insignificant to be meaningful to the explaining the data.

This is indicative of amide II, amide II ( $\alpha$ - helices), and carbonyl bonds of lipids [33-35]. The positive loadings are associated with a weak presence of amide III bands ( $\sim 1220\text{ cm}^{-1}$ ), a significant intensity increase in amide II ( $\beta$ -pleated sheet structures) ( $\sim 1550\text{ cm}^{-1}$ ), and amide I of antiparallel  $\beta$ -pleated sheets/aggregated protein structures [177]. Table 3.10 contains the DF loadings for the fibrosis dataset.

**Table 3.10** Tentatively assigned FTIR serum fibrosis biological peak assignments based on the DF loadings (Figure 3.10), DF1 and DF2 from the fingerprint region using HT-FTIR [29-35].

$\tilde{\nu}/\text{cm}^{-1}$	Tentatively assigned FTIR Serum Fibrosis peaks	DF1	DF2
1221	Amide III (weak)		+
1231		-	
1501	Amide II	-	+
1516		-	+
1530		-	-
1551			-
1560		+	
1614		+	
1622	Amide I of $\alpha$ -helical protein structures	+	
1633			-
1639	Amide I band ( $\beta$ -pleated shift)	-	
1660	Amide I of antiparallel $\beta$ -pleated sheets/aggregated protein structures		+
1697	$\nu(\text{C-O})$ , fatty acids, lipids	-	
1748		+	-

### 3.3.4 Diagnostic Serum Glioma Study

#### 3.3.4.1 Spectral Variance Analysis of Serum Glioma

Table 3.11 shows the results for the variance analysis for the glioma serum study conducted with HT-FTIR spectroscopy. The results presented are from the fingerprint region analysis of the RSD, demonstrating the minimum, maximum, average and median values across the patient spectra. Additionally, the results of the FTIR spectral quality test are shown. A total of 8 spectra were taken per patient (n=70). Overall, 85.3% of the spectra passed the quality test (n=588). The spectra that didn't meet the absorbance threshold were discarded. This was visualised using cluster analysis with explorative HCA. Both the highest and lowest RSD% is seen in the MET patient group (high – 24.3%, low – 0.00%). The highest values were found at  $1119\text{ cm}^{-1}$ , which is attributed to the C-O stretch (antisymmetric), C-O-H bend of lipids [27]. The lowest relative varied region is due to amide II of proteins ( $\beta$ -pleated sheet structures)  $\delta(\text{N-H})$  (60%),  $\nu(\text{C-N})$  (40%). It can be noted here that the overall values for RSD % were very low, suggesting very good reproducibility of the data. The row highlighted in orange on Table 3.11 demonstrates the

overall highest values of mean/median RSD values (10.53% and 9.33%), respectively. The green highlights refer to the patients with the values lower than 5% RSD.

**Table 3.11I** Statistical values for variance analysis, demonstrating the relative standard deviation between mean patients of the glioma study using HT-FTIR spectroscopy.

HT-FTIR/ Glioma Study	Disease Stage	Spectral QT passed	RSD% min / $\bar{\nu}/\text{cm}^{-1}$	RSD% max / $\bar{\nu}/\text{cm}^{-1}$	Av. RSD %	Med. RSD %
1	GBM	10	0.40 / 1568	9.25 / 903	4.79	4.75
2	GBM	6	0.41 / 1510	10.04 / 1137	3.05	2.67
3	GBM	10	0.07 / 1540	8.99 / 1141	3.02	2.99
4	GBM	10	0.14 / 1533	11.02 / 904	5.12	4.55
5	GBM	10	0.40 / 1566	15 / 904	6.00	5.75
6	GBM	10	0.36 / 1562	20 / 905	6.98	5.12
7	MET	10	0.20 / 1566	24.3 / 1119	6.48	5.71
8	GBM	9	0.26 / 1533	12.5 / 1123	5.29	5.11
9	GBM	10	0.42 / 1543	22.9 / 1124	5.31	4.51
10	GBM	10	0.41 / 1543	19 / 1021	4.41	4.11
11	GBM	10	0.39 / 1561	21.9 / 1141	6.31	4.81
12	GBM	10	0.29 / 1555	22.8 / 1132	5.54	4.85
13	MET	9	0.33 / 1562	13.8 / 1127	8.26	4.33
14	MET	10	0.46 / 1569	20.4 / 1157	8.24	5.66
15	GBM	10	0.42 / 1558	9.16 / 907	8.15	4.60
16	GBM	8	0.40 / 1556	9.50 / 917	9.30	6.63
17	GBM	10	0.41 / 1510	7.2 / 920	5.53	4.73
18	MET	9	0.45 / 1512	15.7 / 1123	5.26	4.33
19	GBM	8	0.48 / 1551	21.2 / 1142	7.97	6.13
20	MET	10	0.50 / 1562	18.8 / 1125	6.99	5.33
21	GBM	10	0.36 / 1556	11 / 1111	8.81	6.84
22	GBM	10	0.38 / 1536	12 / 1142	9.26	4.26
23	GBM	10	0.42 / 1526	12.1 / 1132	8.26	4.13
24	GBM	10	0.39 / 1533	10.1 / 1131	7.27	5.53
25	GBM	10	0.29 / 1536	9.75 / 1099	8.26	6.23
26	MET	7	0.25 / 1548	7.8 / 1044	8.11	5.13
27	GBM	10	0.18 / 1558	9.88 / 1102	8.02	4.33
28	GBM	9	0.12 / 1522	10.8 / 1125	5.26	6.33
29	MET	10	0.29 / 1512	10.01 / 1125	5.16	7.13
30	MET	10	0.39 / 1566	13.8 / 1125	4.26	4.23
31	MET	10	0.41 / 1556	9.50 / 1124	5.30	4.13
32	MET	7	0.28 / 1510	7.21 / 1175	5.53	3.93
33	MET	7	0.02 / 1512	15.7 / 1145	4.96	3.99
34	MET	10	0.00 / 1551	21.2 / 1146	5.97	5.85
35	MET	8	0.25 / 1562	18.8 / 1147	5.97	5.39
36	MET	9	0.16 / 1556	11.10 / 1145	4.81	4.14
37	MET	6	0.14 / 1556	9.50 / 1123	8.38	6.83
38	MET	10	0.11 / 1510	7.2 / 1147	8.11	8.03
39	MET	10	0.38 / 1512	15.7 / 1114	7.26	6.23
40	MET	9	0.29 / 1536	24.3 / 1119	3.05	2.67
41	MET	8	0.25 / 1548	12.5 / 1123	3.02	2.99

42	NORM	6	0.18 / 1558	22.9 / 1124	5.12	4.55
43	NORM	9	0.12 / 1522	24.3 / 1119	6.00	4.75
44	NORM	10	0.29 / 1512	13.8 / 1125	3.05	2.67
45	NORM	9	0.39 / 1566	9.50 / 1124	4.96	3.99
46	NORM	4	0.41 / 1556	7.21 / 1175	5.97	3.85
47	NORM	10	0.29 / 1536	13.8 / 1125	4.97	4.39
48	NORM	10	0.18 / 1558	7.2 / 1147	5.96	3.99
49	NORM	10	0.12 / 1522	15.7 / 1014	5.97	5.85
50	NORM	9	0.29 / 1512	11.02 / 904	3.94	2.39
51	NORM	8	0.17 / 1548	15 / 904	8.26	6.33
52	NORM	10	0.14 / 1533	20 / 905	8.24	6.66
53	NORM	9	0.40 / 1566	12.1 / 1132	7.05	5.60
54	NORM	6	0.39 / 1566	10.1 / 1131	7.30	5.63
55	NORM	10	0.41 / 1556	9.75 / 1099	10.53	9.33
56	NORM	10	0.28 / 1510	13.01 / 1152	8.26	6.33
57	NORM	10	0.42 / 1543	9.75 / 1099	7.97	6.13
58	NORM	10	0.41 / 1543	7.8 / 1044	5.12	4.55
59	NORM	10	0.14 / 1533	9.88 / 1102	6.00	4.75
60	NORM	10	0.40 / 1566	11.02 / 904	3.05	2.67
61	NORM	10	0.29 / 1512	15 / 904	5.12	4.55
62	NORM	10	0.17 / 1548	20 / 905	4.25	4.02
63	NORM	8	0.42 / 1543	9.75 / 1099	5.02	4.89
64	NORM	10	0.41 / 1543	7.8 / 1044	3.05	2.55

#### 3.3.4.2 Serum Glioma Principal Component Analysis

Figure 3.11 shows the PCA results. The scores (left) and loadings (right) for PC1 and PC2, account for 89.3% of the explained data variance overall. The data was investigated using a two-way explorative analysis, *i.e.*, patient-wise and disease-wise observations, top and bottom plots on the figure respectively. The bi-plots show the spread of the data across the patients (top) and disease-stage (bottom). As can be seen, the latter shows better visualisation for discerning different clusters within the data. It is apparent that the NORM group, *i.e.*, no disease within the serum samples analysed, show tight clustering as explained by PC2 component loadings. The diseased groups (MET and GBM) represent two different staging grades within the classification of gliomas (generally a medium and high-grade staging). On the figure, these two groups seem to be represented by a mix of both, with no clear separation shown. The MET group appears slightly more tightly clustered compared to the GBM patients, overall. The loadings for PC2 show the most influenced peaks are at  $1657\text{ cm}^{-1}(+)$ ,  $1595\text{ cm}^{-1}(+)$ ,  $1080\text{ cm}^{-1}(+)$  and  $1040\text{ cm}^{-1}(+)$ , which are assigned on a positive loading and as amide I, amide II and C-O stretch (DNA/RNA). Although PC1 explains ~80% of the data, it fails to show separation between the classes of data. Overall with PCA alone, it appears to present a general mix of MET patients with GBM patients, however, it does separate from NORM and cancer datasets, interestingly.

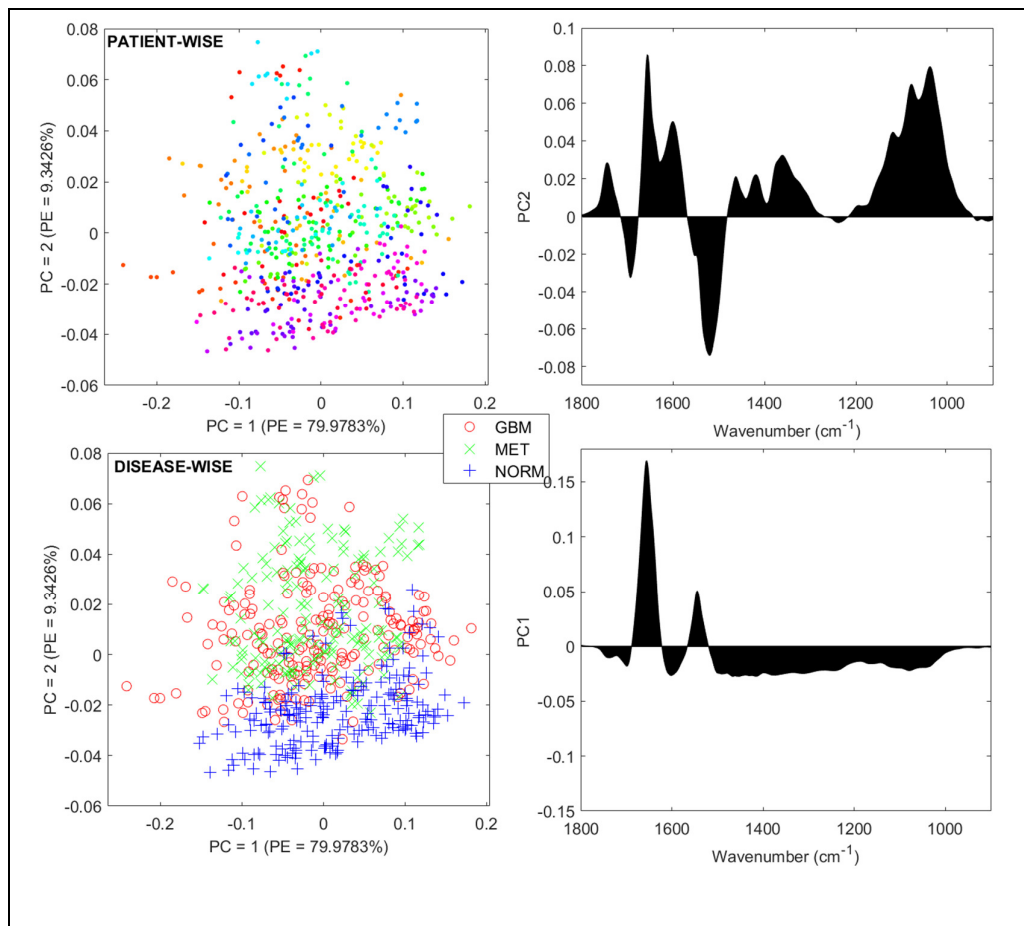
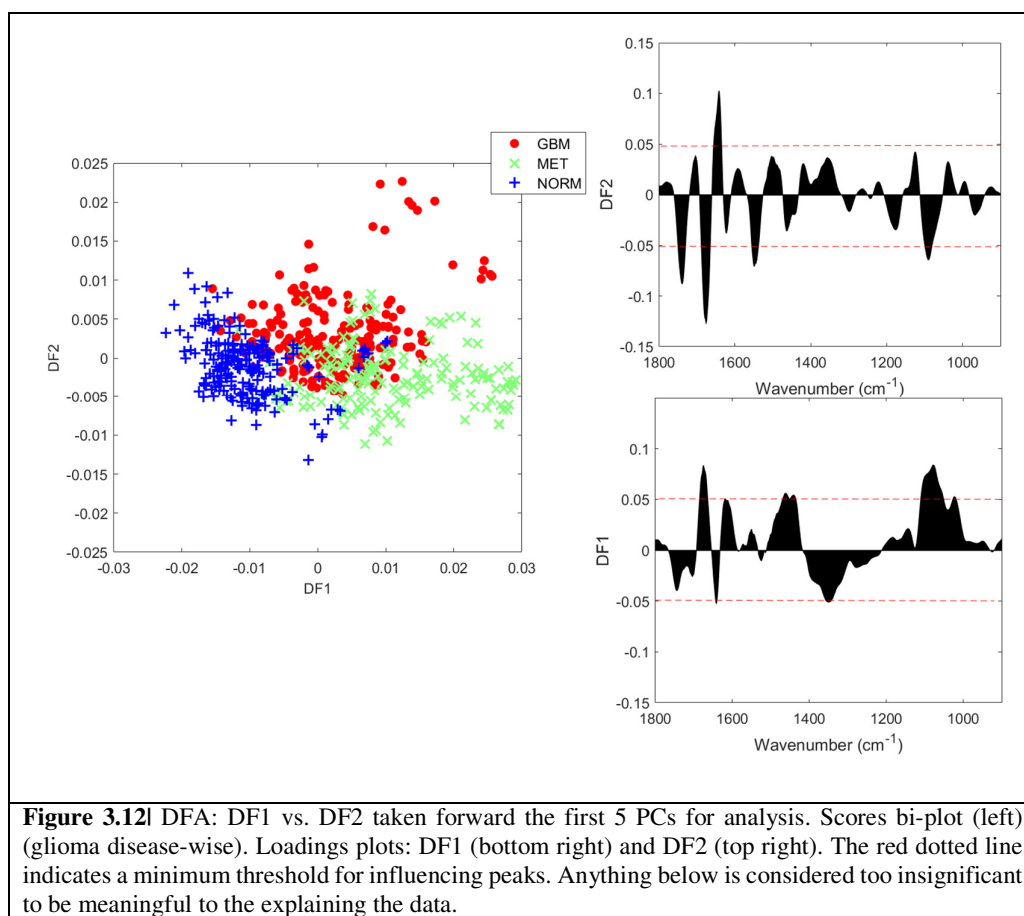


**Figure 3.11** PC1 vs. PC2 taken forward the first 10 PCs for analysis for a two-way explorative observation. Top left (patient-wise (n=64)), bottom left (disease-wise (3 groups)) PC scores. Top right demonstrates the component weight for PC2, whilst PC1 is shown on the bottom right. Data is from the fingerprint region of the spectra and collected *via* HT-FTIR for the BTNW Glioma study.

### 3.3.4.3 Serum Glioma Discriminant Function Analysis

Figure 3.12 shows the results of the DFA. Following PCA, the data was subjected to DFA with the first 5 PCs that explains the biggest variance within the data, and the first three DFs were observed. The data showed DF1 and DF2 to be the most discriminant. As can be seen here, the three classes of data have shown increased tight clusters and overall demonstrates some discerning groups between NORM patients as shown by DF1, plus DF2 is starting to show some initial clustering amongst the MET vs. GBM patients. This result is interesting as it suggests that the intrinsic biochemical differences between the two disease stages, plus the healthy and disease are detectable using spectroscopy. Whilst this is not a perfect clustering separation, it tends to suggest that DFA can discriminate between these three classes of patients.



DF1 clearly finds a good separation between NORM and MET patients. NORM patients are attributed to the negative loadings of DF1, which is the broad peak of -CH<sub>3</sub> deformation of lipids at 1348 cm<sup>-1</sup> and amide I of  $\alpha$ -helical protein structures at 1640 cm<sup>-1</sup>. The positive loadings of DF1 demonstrate the MET from NORM separation and are due to three peaks, the -CH<sub>2</sub> deformation of methylene groups and lipids at 1440-1462 cm<sup>-1</sup>, amide I of  $\alpha$ -helical protein structures at 1640 cm<sup>-1</sup>, and C-O stretch of DNA/RNA at 1075-1088 cm<sup>-1</sup>. The negative loadings of DF1 are on two peaks, 1348 cm<sup>-1</sup> and 1640 cm<sup>-1</sup>, which demonstrate the -CH<sub>3</sub> lipid deformation and the  $\alpha$ -helix protein structure of amide I, finding separation between healthy and diseased (MET). In addition, DF2 finds some separation between MET and GBM. The positive loadings can be attributed to the majority of GBM patients, and the negative ones to most of the MET patients; both with an influence from NORM patients, unfortunately. DF2 in result is not as discriminatory as DF1. Table 3.12 shows the tentatively assigned loadings for both DF directions. To validate this result, PC-DFA was attempted but the data result did not add anything to the current observation, so was not progressed further (data not shown).

**Table 3.12** Tentatively assigned FTIR serum glioma biological peak assignments based on the DF loadings (Figure 3.12), DF1 and DF2 from the fingerprint region using HT-FTIR [27-28-176].

$\tilde{\nu}/\text{cm}^{-1}$	Tentatively assigned FTIR serum Glioma peaks	DF1	DF2
1024	$\nu(\text{C-O})$ RNA, ribose/glucose vibration	+	
1075	$\nu(\text{C-O})$ deoxyribose/ribose, DNA, RNA	+	
1088			-
1348	$\delta(\text{CH}_3)$ lipids	-	
1440	$\delta(\text{CH}_2)$ methylene group, lipids	+	
1462		+	
1550	Amide II ( $\beta$ -pleated sheet structures) $\delta(\text{N-H})$ (60%), $\nu(\text{C-N})$ (40%)		-
1640	Amide I of $\alpha$ -helical protein structures ( $\nu(\text{C-O})$ (76%), $\nu(\text{C-N})$ (14%), $\delta(\text{C-N})$ (10%))	-	+
1674	Amide I of antiparallel $\beta$ -pleated sheets/aggregated protein structures ( $\nu(\text{C-O})$ (76%), $\nu(\text{C-N})$ (14%), $\delta(\text{C-N})$ (10%))	+	-
1740	$\nu(\text{C-O})$ , fatty acids, lipids, proteins		-

### 3.4 CONCLUSION

In summary, this two-part study sought to analyse human pooled sera with a suite of FTIR technologies, including ATR-FTIR, transmission (both traditional and high-throughput), for preclinical variability. This was investigated by repetitive cycles of freezing and thawing, to ascertain whether there is an effect on the data due to such procedures, and then to analyse the same samples for environmental drying effects on the serum profile. Combining spectroscopy with PCA demonstrated very little changes within the freeze-thaw serum profile; any changes in the bi-plots were deemed to insignificant as the subspace has highly magnified. Overall, the cycles appear mixed, with no real logical clustering or that could be described experimentally *via* preclinical changes. PCA was the endpoint analysis for this dataset. The HT-FTIR dataset for FTC also showed a similar result, irrespective of type of FTIR technique employed. Here the spectral collection was highly automated, which makes it a good high-throughput application. Subsequent PCA showed another complete mix of cycles of freezing and thawing, which is reassuring to understand that moving forward to diagnostic capabilities of the technique's automation presents no extraneous data effect. Here again, PCA was the endpoint analysis. For both techniques common spectral peaks were shown for the sera, as protein being the biggest influence at the amide bands region. This region is generally due to two main contributions, the amide II bands at 1500-1580  $\text{cm}^{-1}$ , and the amide I band at 1580-1680  $\text{cm}^{-1}$ .

To further investigate the effects of ambient drying, PCA was also applied on the environmental drying data (taken across 11-time points throughout 24 hours). Serum dehydration induces the coffee-ring effect, whereby the pinning of the contact lines of the drying drop causes the salt, ions and proteins to form a concentration gradient. This study showed that such an effect is seen using PCA, as the time points seem to follow a sequential pattern starting from point 0 (fresh drop liquid sera) towards 24 h post drying. This is seen within the loadings owed to the C=O stretch  $\sim 1655 \text{ cm}^{-1}$ , the N-H deformation  $\sim 1540 \text{ cm}^{-1}$  and the C=C stretch  $\sim 1615 \text{ cm}^{-1}$ .

As it is routine practice, to seldom work on non-fresh samples given the requirement of cryogenic storage, in this preliminary study we have carried out IR spectroscopic assessment of potential variations owing to cycles of freeze-thaw and to the environmental ageing or drying of a sample of human pooled sera, exploring potential intra-sample differences of serum sample stability, without the fresh phase. Important factors, such as storage requirements, dilution aspects, and all key preparatory phases within a laboratory setting need to be fully considered. Generally, for any analysis of variability, whether it is intra-, pre- or post-analytical, the biofluid of choice must dictate the analytical process for error-tracking.

The second part of this study was to use the tried and tested methodologies for diagnostic capabilities. Two patient serum banks were interrogated (fibrosis and glioma). The fibrosis patient sera were measured using the HT-FTIR methodology and analysed using PCA and DFA. A three-way split of the fibrosis data revealed, a group split by patient spectra, by fibrosis disease stage and by a mix of fibrosis disease to represent low and high-grade disease characteristics. PCA was unable to classify the patient groups.

The positive loadings seen on DF1 demonstrated a slight separation between F2 and F4 (the advanced fibrotic disease, such as cirrhosis) patients. DF2 further showed a slight difference between low-grade and high-grade diseases, as explained by the negative and positive loadings, respectively. The peaks situated on the negative loading of DF2 show increased intensities in the 1530  $\text{cm}^{-1}$  region, the 1635  $\text{cm}^{-1}$  region and 1748  $\text{cm}^{-1}$  profiles. This pinpointed amide II, amide II ( $\alpha$ -helices), and carbonyl bonds of lipids as marker bands. Such positive loadings could be associated protein bands at  $\sim 1220 \text{ cm}^{-1}$ ,  $\sim 1550 \text{ cm}^{-1}$  and pleated sheets/aggregated protein structures [177-188]. This study demonstrated the both PCA and DFA were able to show biochemical differences between some of the patient disease stages. Although a PC-DFA validation was tried, it did not add anything to the outcome. Moving forward with this, it would be advantageous to further use MVA techniques, such as SVM, ANN or PLSDA to try to classify the data further, followed by a blind test.

The glioma patient sera were measured using the HT-FTIR methodology and analysed using PCA, DFA and RBF-SVM cross validation. Firstly, a two-way split of the data was analysed using PCA and DFA; first split by patient, and second by normal, metastases and glioblastoma multiforme (the most advanced and aggressive). Here, it was demonstrated that both PCA and DFA can show some distinctions between normal *vs.* disease states, when combining the two cancer stages together. DF1 clearly finds a good separation between NORM and MET patients *via* marker bands attributed to the broadband peak of  $-\text{CH}_3$  deformation of lipids at 1348  $\text{cm}^{-1}$  and amide I of  $\alpha$ -helical protein structures at 1640  $\text{cm}^{-1}$ . The positive loadings of DF1 demonstrate the MET from NORM separation and are due to three peaks, the  $-\text{CH}_2$  deformation of methylene groups and lipids at 1440-1462  $\text{cm}^{-1}$ , amide I of  $\alpha$ -helical protein structures at 1640  $\text{cm}^{-1}$ , and C-O stretch of DNA/RNA at 1075-1088  $\text{cm}^{-1}$ . The negative loadings of DF1 are on two peaks, 1348  $\text{cm}^{-1}$  and 1640  $\text{cm}^{-1}$ , which implicates the  $\text{CH}_3$  lipid deformation and the alpha-helix protein structure of amide I, finding separation between healthy and diseased (MET) states. DF2 started to separate between MET and GBM. The positive loadings can be attributed to the majority of GBM patients, and the negative ones to most of the MET patients; both with an influence from NORM patients. DF2 in found to be not as discriminatory as DF1.

Overall, this study has demonstrated that high-throughput analysis has less overall variance when comparing the RSD of ATR and HT-FTIR methodological approaches.

In summary, the present study has shown that preclinical variation can be minimised with good laboratory procedures, not-exceeding a significant amount of repetitive freeze-thaw, and that such possible variances, when well taken into account, have minimal influences in diagnostic capability of FTIR technology as a disease classification/screening tool when employed with MVA.

## **| CHAPTER 4 |**

### **RAMAN SERUM SPECTROSCOPY : SAMPLE STABILITY AND LIQUID DIAGNOSTIC APPLICATION**

---

## **| CHAPITRE IV |**

### **SPECTROSCOPIE RAMAN DU SERUM : STABILITE DE L'ECHANTILLON ET APPLICATION DIAGNOSTIQUE DU SERUM LIQUIDE**

#### **IV.1 RÉSUMÉ**

Suite aux travaux précédents sur l'IRTF du sérum, il était nécessaire de faire sécher les sérums avant de les analyser. La technique IRTF l'avantage d'être à haut débit, ce qui est intéressant pour une approche clinique. Dans ce chapitre, le travail est focalisé sur le développement de la spectroscopie Raman appliquée à l'analyse séchée ou en phase liquide. Dans un premier temps, l'approche spectroscopie Raman est appliquée sur le même pool de sérums humains traité dans le chapitre précédent, pour étudier les effets de la variation pré-analytique. Deuxièmement, la méthode Raman choisie est utilisée sur des sérums de patients pour évaluer, comme pour l'IRTF son potentiel de diagnostic / dépistage. Cette recherche a un double objectif. Premièrement, ces travaux ont permis de mieux comprendre les variations pré-analytiques du sérum humain sur des échantillons séchés et liquides et en observant l'effet des cycles répétitifs de congélation / décongélation et de séchage ambiant sur des sérums humains non frais. Enfin, la technique est évaluée dans le cas de la fibrose hépatique en utilisant un protocole d'analyse des sérums à l'état liquide par macroscopie Raman. Cette nouvelle approche, récemment mis au point pour une application potentielle de criblage Raman, a été associée à une analyse multivariée de données.

#### **IV.2 CONCLUSION**

En résumé, cette étude en deux parties visait à analyser un pool de sérums humains en phase sèche et en phase liquide avec différentes approches en spectroscopie Raman, afin d'évaluer la variabilité pré-analytique. Comme pour l'analyse IRTF, des cycles répétés de congélation et de décongélation ont été suivis afin de déterminer leurs effets sur l'échantillon, puis d'analyser ces mêmes échantillons pour déterminer les effets du séchage ambiant sur le profil sérique. En combinant la spectroscopie Raman avec des analyses chimiométriques exploratoires telles que l'ACP et le CHA, les valeurs aberrantes suivant les évaluations de variance et de qualité des données ont pu être mises en évidence pour une suppression ultérieure. Dans l'ensemble, l'ACP a montré très peu de changements dans le profil sérique suivant les cycles de congélation-décongélation. Tous les changements ont été jugés insignifiants et aucun schéma spécifique des données n'a été observé. Globalement, les données provenant des cycles de congélation/décongélation semblent en général assez mélangées, sans véritable clustering logique ou pouvant être décrit expérimentalement *via* des modifications pré-analytiques. Les données acquises à la fois pour les cycles de congélation/décongélation et séchage à l'air ambiant sur différents instruments ne montrent aucun effet sur les spectres. Nous concluons que cette variation pré-analytique a très peu d'effet sur les données spectrales.

Comme il est de pratique clinique courante de ne travailler que rarement sur des échantillons non frais compte tenu de la nécessité d'un stockage cryogénique, les facteurs importants, tels que les exigences de stockage, les aspects de dilution et toutes les phases préparatoires clés dans

un laboratoire, doivent être pleinement pris en compte. De manière générale, pour toute analyse de variabilité, qu'elle soit pré-, intra- ou post-analytique, le biofluide de choix doit respecter le processus analytique permettant de suivre les erreurs.

Le dernier aspect de ce travail était d'évaluer le potentiel diagnostique de la méthodologie de spectroscopie Raman sur des échantillons liquide de sérum de patients à différents stades de fibrose. Les données ont été analysées à l'aide de l'ACP et l'AFD. L'analyse a révélé un groupe divisé par spectres de patients, par stade de fibrose et par un mélange de fibrose pour représenter les caractéristiques de la maladie de bas et de haut grade. L'ACP n'a pas pu faire ressortir des différences.

Les loadings positifs observés sur DF1 démontrent une légère séparation entre les spectres des patients sains et ceux des patients avec une fibrose au stade F4. Les différences sont attribuées à la région 900-1300  $\text{cm}^{-1}$ , qui englobe les acides aminés et la région amide III. Cette étude a démontré que les deux AFD pouvaient montrer certaines différences biochimiques entre certains stades de la fibrose (sain ou avancé). Bien qu'une tentative de validation CP-AFD ait été tentée, cela n'ajoute rien aux résultats déjà obtenus. Les données ont ensuite été soumises aux classifieurs RF et LDA pour une analyse supplémentaire. Les meilleures sensibilités et spécificités obtenues représentaient des résultats modérés et il est donc conclu qu'aucun des algorithmes utilisés n'a été capable de fournir une discrimination claire de la maladie.

En conclusion, les résultats de cette étude montrent que l'exploitation des données Raman en phase liquide par une analyse multivariée avancée en tant qu'outil de classification ne suffisait parfois pas pour établir une discrimination si l'évolution de la maladie est extrêmement complexe. Bien que les effets des cycles de congélation/décongélation et du séchage à l'air ambiant semblent avoir des effets négligeables sur les résultats des données, il est toujours important de ne pas sur-traiter les échantillons et il faut rester prudent pour limiter les effets physiques sur les échantillons, comme avec tout échantillon biologique, il pourrait être sensible et se dégrader éventuellement. Les présents résultats ont clairement montré que l'on pouvait minimiser les variations précliniques avec de bonnes procédures de laboratoire, en ne dépassant pas des quantités élevées de gel-dégel répétitif, et que de telles variances éventuelles ne jouent aucun rôle significatif dans la capacité de diagnostic de la spectroscopie Raman, qui est une classification de la maladie / outil de dépistage lorsqu'il est utilisé avec diverses stratégies MVA. De plus, il repose uniquement sur la complexité de la maladie.

#### **4.1 INTRODUCTION**

Serum-based spectroscopic diagnostics is an interesting and emerging adjunct to the cellular-histology arena for biomedical spectroscopy. It has gained specific diagnostic interest owing to

its strengths; non-destructive testing, readiness and ease of sample availability, capability of rapid testing and re-testing, and simple and minimally invasive acquisition making it an ideal technique for routine testing/screening [108]. The biochemistry of human serum is known to comprise a highly complex ‘peptidome’ composed of low molecular weight serum markers amongst other macromolecules [65]. Serum accounts for approximately 55% w/v of blood when combined with plasma and houses ~20, 000 proteins, from albumin to troponin, making it information rich for disease processes [179-181]. This primary carrier of small molecules serves as a ‘liquid information highway’ that bathes the tissues, and its metabolomics variation can be attributed to a subject’s life-style and regime, inclusive of gender, stress levels and body mass index (BMI). A recent study [182] demonstrated the richness of such chemical information *via* molecular phenotypic profiles of 1200 UK respondents, for the serum metabolome. Such a study provides a quantitative assessment of molecular activities that govern cellular processes [182], which could shed new light on disease mechanisms. Ultimately, the use of biofluids such as serum, semen, plasma, saliva and bile have demonstrated significant prognostic and diagnostic potential within bio-spectroscopy, as recently reviewed by [6].

In a conscientious effort to lessen the research gap from bench to bedside, strict adherences to good laboratory practice (GLP) and appropriate standard operating procedures (SOP), in line with an effort to circumvent analytical errors, are necessary to see an increase in large clinical trials or multicentre studies. However, there is a major challenge to ensure that all participating hospitals must strictly follow pre-analytical procedures to ensure the best and most discriminating outcome from testing. It is understood that clinical samples are often subject to repeat testing and undergo potentially complex preparatory phases, so to limit such phases could be problematic. Accordingly, understanding pre-analytical phases and their effects on serum samples could actively control sample-related variation, which could be derived from dilutions, serial sampling, repeated freezing/ thawing cycles and air-drying, amongst many others. Overall, it seems there is a need to provide robust and standardised protocols, which seek to diminish sample-related factors before any indication of diagnostic application can be made. A factor of key importance to this study is that most analytical errors originate at the pre-analytical stage which could then influence any aspect of data pre- and post-treatment [163-164].

Spectroscopic techniques are excellent analytical methods for an expanding range of materials and provide an objective approach to classification on a molecular level [183]. Raman spectroscopy (RS) analyses molecular excitations of biomolecules when irradiated with monochromatic laser light. Biomolecules exhibit responses to differing wavelengths of light, meaning the resultant spectra present a unique ‘fingerprint’ of the sample’s global biochemistry. However, its major drawbacks are that it can be hampered by the high content of fluorophores

in biofluids, and a whole host of non-chemical artefacts, such as Mie scattering, stray light and cosmic ray artefacts (CRA) [20]. However, RS can also offer distinct advantages when dealing with biofluids. Due to the low absorption coefficient across the visible spectrum, water obscuring is not an issue, as is inherent with infrared spectroscopy (IR). Although, one of the most common methods for biofluid analysis is the use of drop-coating dried deposition (DCDD) on spectroscopically neutral substrates, such as CaF<sub>2</sub> [38, 184], RS makes analysis in the liquid state still possible. Owing to the low concentration of serum analytes, and poorer signal-noise (SN) with RS liquid analysis [185], when sample drying, a chemical gradient across the drop is derived from the pinning of the contact line. Essentially, during this rheological process, the centre zone of the drop feeds the peripheral zone, until full evaporation is achieved following Marangoni flow [158-159], documented more recently, as the “coffee-ring” phenomenon [140, 159-160]. A heterogeneous sample deposition can result as the internal molecules migrate to the periphery of the drop. Incidentally, there is no substrate effect on the chemistry of the periphery but there is evidence of spatial distribution of the internal protein components [152]. There have been some developments to improve this with the use of FTIR spectroscopy in recent times [137]. However, any state analysis with RS means that liquid samples can be employed directly, without the need for dilution and some work using immersion RS [185], as well as some work on freeze-drying, has been conducted. They reported no differences between the methods when applied on a diagnostic model [186]. Recently, there has been an effort to develop tear rheological understanding on this matter also [128, 142, 165, 187].

Ultimately, within the field, such studies have driven forward the development of disease pattern recognition (DPR). However, it should be noted that more studies are necessary to improve pre-clinical findings, first. It is in this specific effort a recent study has been conducted [188]. As mentioned in Chapter 3, this FTIR study aimed to provide an understanding of biofluid sample-related factors. The authors of the study found sample collection modalities, substrate choice, volume, dilution and drop deposition manner, plus consecutive freeze-thaw (with fresh *versus* frozen) and drying conditions, all affect data quality and reproducibility. With that in mind, a series of RS investigations on freezing and thawing cycles (FTC), and environmental drying (ED) of normal pooled human serum have been conducted to aid the understanding of pre-clinical variations, from the perspective of micro dried, liquid RS protocols. Further developmental work has also been conducted to find the optimum Raman sampling methodology, to take forward for future diagnostic works (see Chapter 5).

In a second series of experiments, the same samples from hepatic fibrosis patients described previously, were analysed using a developed RS approach. The patient group details are found in chapter 2. Generally, fibrosis is seen as a precursor for more advanced liver disease, such as

cirrhosis and primary liver carcinoma. Therefore, the need to correctly stage and classify earlier is vital in the effective treatment of complex diseases. These patients are all derived from a voluntary group who underwent a 'Fibrotest' and 'Fibroscan' examination. Fibrotest is a blood serum biomarker test and Fibroscan is an elastographic technique like ultrasound, and both have previously shown a potential for good diagnostic accuracy; specifically, at advanced fibrosis stages (93% and 70% sensitivity and specificity, respectively) [137]. The reference method here is the Fibrotest and not METAVIR, however, the stages have been determined by a conversion made from the Fibrotest results into a METAVIR score by a senior gastrohepatologist at the Reims University hospital for the purposes of this research.

This research has a dual aim. Firstly, this work developed further understanding of pre-clinical variations on pooled human serum through the use of RS on both dried samples and liquid samples and by observing the action of repetitive freeze-thaw cycles and environmental drying on non-fresh human sera. Secondly, this work interrogated hepatic fibrosis using a newly developed macro Raman liquid sample protocol for a potential high-throughput Raman screening application, combined with advanced multivariate data analysis.

## **4.2 MATERIALS & METHODS (for 2.2.2 for details)**

### **4.2.1 Serum Samples**

Two series of experiments were conducted, involving preanalytical variation and a set for a development macro Raman liquid sample approach.

### **4.2.2 Preanalytical Variation Studies**

The pre-analytical variation study was further subdivided into two studies: the freeze-thaw cycle (FTC) analysis of pooled human serum, and the subsequent environmental air drying of the serum (ED).

#### *4.2.2.1 Freeze-Thaw Cycles (FTC)*

Mixed pooled 'off the clot' human serum (TCS Biosciences, Buckingham, UK) was used to investigate preclinical variation. Following passive thawing at room temperature (RT), the serum samples (n=15) underwent repetitive FTC. The samples were stored at -80° C until spectral acquisition, with a 24-hour period between each FTC. Prior to spectral collection, each of the FTC vials were manually inverted and vortexed to ensure thorough mixing of all serum components. Three spectra were collected from arbitrary positions from the 10 dried serum spots per FTC (n=15). A total of n=450 spectra FTC measurements were acquired per experiment across the three different instruments.

#### 4.2.2.2 Environmental Air-Drying (ED)

Secondly, the same samples were monitored for air-drying environmental effects on serum stability *via* the ED study. Sample storage and handling were conducted in a sterile environment to minimise contamination. Prior to spectroscopic assessment all samples were thawed at room temperature (RT) and relative humidity ~ 40%. Three spectra were collected after leaving to fully air-dry, from a random area located on the spot on the serum sample at 11-time intervals throughout 24 h. Spectra were collected after 10 min, 30 min, 1 h, 1.5 h, 2 h, 2.5 h, 3 h, 3.5 h, 7 h, 14 h, and 24 h (n=33). A total of n=33 ED measurements were taken per experiment

#### **4.2.3 Raman Microscopic DCDD Serum Analysis**

A series of drop coated dried deposition (DCDD) and liquid phase (LP) analyses were carried out. Table 4.1 shows the overview of instrumentation and parameters employed for micro Raman analysis for FTC and ED studies. All DCDD work was done at the microscopic level (~ a few microns), whereas the liquid analysis was done with larger sample volumes and with macro or semi-macro setups (~ a few millimetres).

Prior to use, all instrumentation was properly calibrated and checked according to laboratory user guidelines and SOPs for each of the respective laboratories in the UK and France. It was routine practice to perform a standardised laser power check of the source, and at the sample *via* the microscope objectives. With this, the spectrometer was checked for the zero position (Rayleigh line) and calibrated daily to check for spectral line drift. Spectrometer linearity was checked using a warmed neon lamp before all pre-calibration checks, and later averaged for subtraction and correction of the Raman signal in the pre-processing phase. Prior to any sampling, there is always an assessment of dark current made by collecting spectra in the absence of laser power. Dark current is the residual noise from the spectrometer and components when no photons are present; often left over from the CCD detector. To verify the optical detector response, spectra were then taken with laser power but in the absence of sample.

Additionally, spectra were calibrated in relative intensity with NIST calibration standards for 785 nm and 532 nm (standard reference material #2241, #2243; NIST, Gaithersburg, MD, USA). Finally, the instrument was calibrated daily using a silicon (Si) sample (~ 520.8 cm<sup>-1</sup>) to verify the instrument's performance and check for any band-shifting. All spectral acquisitions were recorded using a suite of Horiba Jobin-Yvon LabRAM instruments and Lab Spec proprietary software (v5/6) (Horiba Scientific Jobin-Yvon, Lille, France).

**Table 4.1|** Overview of instrumentation and parameters employed for micro Raman development and analysis for FTC and ED.

Horiba LABRAM	Grating (lines/mm)	Objective	Laser (nm) Power (mW)	Slit/ Confocal ( $\mu\text{m}/\mu\text{m}$ )	Sampling ( $\mu\text{L}$ )	Substrate
Instrument 1 HR800	1200	50x LWD, NA 0.25	785~30	100/0	0.5	CaF <sub>2</sub>
		Integration: 15 s x 2 Range: 1800 – 500 cm <sup>-1</sup> Spectral Res: 4 cm <sup>-1</sup> FTC Phase: DCDD (n=450) ED Phase: DCDD (n=33)				
Instrument 2 ARAMIS	300, 600, 1200, 1800	100x LWD, NA 0.75	532/785~25	10000	0.5, 1-10	CaF <sub>2</sub> , Alu
		Integration: 15 s x 2 Range: 1800 -500 cm <sup>-1</sup> Spectral Res: 4 cm <sup>-1</sup> FTC Phase: DCDD (n=450) / LP785 (n=450) / LP532 (n=450) ED Phase: DCDD (n=33)				
Instrument 3 One (1)	950	50x LWD, NA 0.25	~90	1000/150	5	Alu
		Integration: 15 s x 2 Range: 1800 – 500 cm <sup>-1</sup> Spectral Res: 4 cm <sup>-1</sup> FTC Phase: LP (n=450) / DCDD (Centre vs. Periphery) (n=270)				

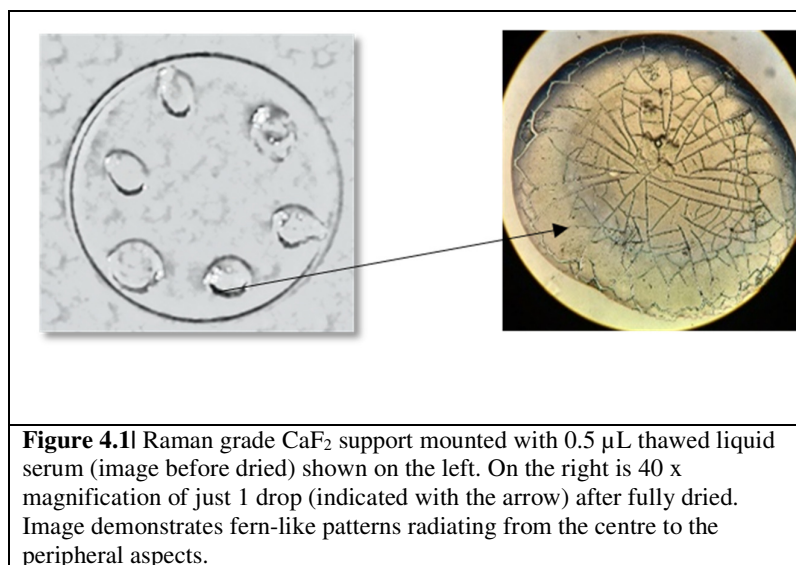
NA – numerical aperture; LWD – long working distance; Res – resolution.

WD – long working distance; Res – resolution.

#### 4.2.3.1 Instrument 1: LabRAM HR800

This instrument was used for both FTC and ED measurements. Transmission spectral acquisition was carried out on the Horiba Jobin-Yvon LabRAM HR800 microspectrometer HR800 (Horiba Scientific, UK). An air-cooled CLDS 300 mW 785 nm NIR excitation laser was guided to the sample using a 50x LWD objective (NA 0.50).

The normal pooled serum sample (0.5  $\mu\text{L}$ ) was deposited on a Raman grade CaF<sub>2</sub> substrate and dried for ~ 10 minutes at RT. Following preliminary optimisation work, spectral acquisition was targeted to the spectral region (1800-500 cm<sup>-1</sup>) with 1800 lines mm<sup>-1</sup> diffraction grating and a spectral resolution of 4 cm<sup>-1</sup>. A confocal slit/hole of 100/400  $\mu\text{m}$  and 2 x 15 s integrations were used to collect in point mode with 100% laser exposure. The power at sample was ~30 mW. The Lab Spec software was used to navigate and capture the data. Figure 4.1 shows a nominal amount of serum drying down the lens of a microscope. The so-called ‘fern-like’ formation is clearly visible.



#### 4.2.3.2 Instrument 2: LabRAM ARAMIS

Further collections of FTC and ED measurements were repeated on a Horiba Jobin-Yvon LabRAM ARAMIS micro-spectrometer with a Synapse thermoelectric (TE) CCD 1024 x 256 detector. Following the same procedure of depositing serum on to the substrate, and drying for ~ 10 minutes at RT, various preliminary optimisations were made by adjusting a whole host of parameters seen in Table 4.1 above. Following preliminary optimisation work, spectral acquisition was targeted to the spectral region (1800-500 cm<sup>-1</sup>) with 600 lines mm<sup>-1</sup> diffraction grating and a spectral resolution of 5 cm<sup>-1</sup>. The 785 nm laser light was focused with 100 x LWD objective (NA 0.75), and hole/slit confocal combination of 500/150 μm. The Lab Spec (v6.5) software was used to navigate and capture the data. Spectra were collected using a 2 x 15 s, over the same 11 time points (for ED measurements), and arbitrarily across the spot 10 times with 30 spectra per collection for FTC measurements. Additionally, an aluminium plated (Al) well was used for the FTC measurements which also resulted in n=450 spectra. The 7 mm diameter plate was used for both liquid and dried state analysis of the serum. A 532nm and 785nm excitation source was used for repeat FTC measurements. (n= 450 for each wavelength). To ensure the aluminium substrate was contaminant and debris-free prior to use, blank spectra were taken from all 96 wells, followed by continuous wash cycles with a mix of 0.5% SDS detergent, distilled water and 40% ethanol. Repeat blank spectra of all wells and additional washes were taken to ensure no trace material was left behind prior to any testing.

#### 4.2.3.3 Instrument 3: LabRAM 1

Spectral collection was also carried out using a Horiba Jobin-Yvon LabRAM One (1) micro-spectrometer with a Synapse thermoelectric (TE) CCD 1024 x 256, collecting spectra over the

1800-500  $\text{cm}^{-1}$  mid-IR spectral region, employing a 50x LWD objective (NA 0.25). A NIR 785 nm laser excitation, 950 lines  $\text{mm}^{-1}$  diffraction grating and slit/hole combination of 150/1000  $\mu\text{m}$ , were used. The Lab Spec software was used to navigate and capture the data. Approximately 5  $\mu\text{L}$  of thawed liquid sample was deposited on to selected wells of 96 well aluminium plate and spectra were collected immediately to ensure the spectra were only representative of a purely liquid phase). A total of  $n=450$  spectra were acquired from the liquid phase.

#### *4.2.3.3.1 Dried Drop Spatial Distribution: Centre versus Periphery*

Upon spot drying, the analyst can perform spectral acquisition with the use of the online video camera mode and pinpoint data collection on the serum drop. Spectra were obtained after the sample (5  $\mu\text{L}$  serum spots) had dried, taking arbitrary triplicate spots from the centre and peripheral zones, to observe any significant difference in the spatial chemistry. A total of  $n=135$  for each centre and ring aspects were acquired. Figure 4.1 (above) shows dried result of serum when observed down a microscope lens (highlighting the physical differences between centre and peripheral zones).

#### *4.2.3.3.2 Macroscopic Liquid Serum Development*

The focus of this study was to develop a macro Raman liquid analysis protocol for future diagnostic works. Given some of the widely understood drawbacks with DCDD, it was decided to investigate liquid analysis at the macro level. Overall, a liquid macro Raman method was developed bypassing the microscope objective for sample acquisition.

#### *4.2.3.4 Instrument 4: LabRAM HR300*

The Horiba Jobin-Yvon LabRAM HR300 was employed for this work. Liquid serum was housed within quartz cells. The cells were composed of a synthetic quartz derived from silicon (Hellema, Quartz SUPRASIL from Heraeus Quarzglas GmbH), which gives transmission values of more than 80 % over a spectral range of between 200 nm and 2500 nm for an empty cell, as advised by the manufacturer. Each cell had slightly different dimensions, one with a narrow internal well, and the other without, meaning a difference in internal holding volume.

Employing a macro lens adaptor, the laser light-path (NIR 785 nm) was guided through lenses and the  $180^\circ$  backscattered Raman signal was collected from the light interaction with the serum using 600 lines  $\text{mm}^{-1}$  diffraction grating. The feasibility of this method (Figure 2.1) was observed by taking 20 spectra from the first cuvette, per different volumes, *i.e.*, 25, 50, 75 and 100  $\mu\text{L}$ , employing a range of integration times (60, 120, 180, 240, 300 s x 1, 2, 3, 4, 5

accumulations). Finally, using both cuvettes spectra were collected (n=200). The data were analysed to see which of the cuvette-sample spectra gave the best reproducibility and SNR).

#### 4.2.4 Macroscopic Diagnostic Liquid Raman

From the development work carried out a diagnostic approach was taken to employ the new macro liquid Raman methodology. The patient sera were derived from a bank of serum samples stored at  $-80^{\circ}\text{C}$ , originally taken for a Fibrotest procedure in patients with chronic hepatitis C, in France. Informed consent was obtained from all patients for performing the diagnostic test as part of routine medical care. Following biochemical analysis by the bio-pathology team at Reims hospital CHU, the remaining serum was stored at  $-80^{\circ}\text{C}$ . The study was carried out according to the principles of the Declaration of Helsinki (DoH). Table 4.2 shows the demographic clinical data for the screening study (hepatic fibrosis).

**Table 4.2** Table showing fibrosis patient demographics, including disease stage (METAVIR F score), number of patients, age range/mean ages and gender.

METAVIR F	Patients	Age Range / Mean Age (years)	Gender M; F
F0	12	18-57 / 39.58	M5; F7
F1	9	43-60 / 54.22	M3; F6
F2	19	44-73 / 59.89	M8; F11
F3	4	50-69 / 59.75	M2; F2
F4	5	51-66 / 58.80	M3; F2

All blood samples for the diagnostic studies were stored in tubes and left to clot at RT for a minimum of 30 minutes and a maximum of 2 h from venepuncture to centrifugation. Clot separation *via* centrifugation was achieved at  $1200 \times g$  for 10 minutes and 500  $\mu\text{L}$  and 1000  $\mu\text{L}$  aliquots of serum was dispensed into pre-labelled cryovials. Serum samples were snap frozen using liquid nitrogen and stored at  $-80^{\circ}\text{C}$  until spectroscopic analyses. In brief, the 50  $\mu\text{L}$  patient sera was placed in the quartz cuvette and subjected to transmission point mode Raman spectroscopy on the fully thawed liquid; collecting 5 acquisitions per patient. Forty-one patients were investigated using the liquid approach. It should be noted that these samples were used for both FTIR and Raman analyses.

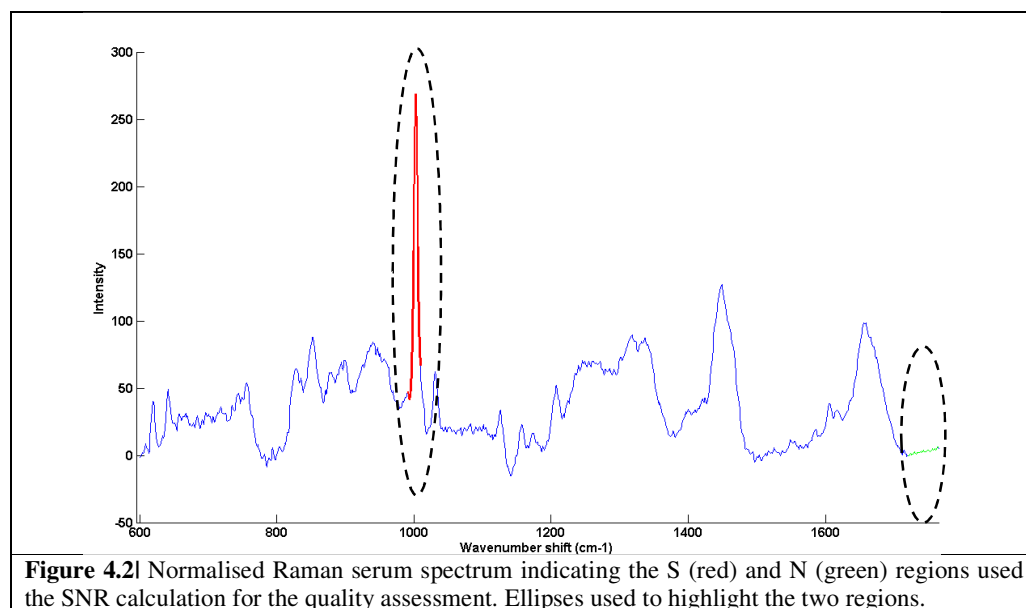
##### 4.2.4.1 Spectral Quality Testing and Variance Analysis

Raw spectra were subjected to a spectral quality test using MATLAB software (version 2015b, The MathWorks, Inc., USA). The test looked at two spectral regions ( $\sim 990\text{-}1010\text{ cm}^{-1}$  and  $1720\text{-}$

1780  $\text{cm}^{-1}$ ), as these were chosen to represent the spectral aspects for signal (S) and noise (N). Spectra passed the QT if the SNR exceeded a value of 30, which is used in biological spectra and is in line with previous work [137]. The S was defined as one of the most bio-characteristic intense peaks found within a Raman spectrum; *i.e.*, the ring breathing mode of Phenylalanine at region  $\sim 990\text{-}1010 \text{ cm}^{-1}$  (such a range was chosen to allow for potential minor peak shifts). Figure 4.2 demonstrates the two regions on a normalised Raman bio-spectrum used for calculation of the SNR.

Alternatively, a second non-programmed method was used, which is in line with the manufacturer's guidance (OPUS v6.5 Software (Bruker Optics GmbH, Ettlingen, Germany)). This method was employed for calculation of the RMS SNR value. This function calculates the SNR of a spectrum's intensities over a given spectral range, *i.e.*, any flat or low value region. As the range is in the mid infrared, Bruker state that the SNR is calculated in the range 2100-1900  $\text{cm}^{-1}$  but can be optimised based on visual appearance of the spectra. RMS is calculated as the root of the mean square of deviations (*i.e.*, the STD). Then a quadratic parabola is fitted to the spectrum in the region of interest, defining the (nominal) signal. The mean of which is divided by the newly calculated noise values and yields the SNR. This is shown in Chapter 2. The results of which were compared with same method for deionised water, meaning that the lower limit threshold for samples had to be higher than that of the SNR of water.

Finally, the spectra that passed the threshold test was observed for the variability between spots of the same sample by calculating basic statistics, such as mean and RSD (see Table 4.3).



## 4.2.5 Spectral Pre-processing and MVA Strategies

### 4.2.5.1 Pre-processing Strategies

The spectra were pre-processed using a MATLAB platform R2015b (The MathWorks, Inc., USA). After quality and variance assessment, a baseline subtraction was carried out using polynomial fit along with a (3, 9) Savitzky-Golay smoothing model [42]. The data were then vector normalised and finally offset-corrected to realign all spectra to a scale from 0 a.u.

It is noteworthy to state that all datasets were observed for principal component analysis (PCA) *via* scores and loading differences using different manipulations of combinations of the following processes: full spectrum, fingerprint only spectrum, non-derivatives and 1<sup>st</sup> derivative functions prior to moving forward with subsequent analysis.

### 4.2.5.2 MVA Strategies

All datasets were then submitted to cluster analyses *via* HCA and PCA in the first instance for outlier detection and sample removal prior to more advanced chemometric assessments. DFA was used to ascertain clusters in to groups following PCA and then PC-DFA if necessary. Following this, for the diagnostic study only, more advanced machine learning algorithms were employed to find classification of the data groups, such as random forest classifiers (RF) and Gini-SVM (Full explanations of all MVA techniques and details of statistical analyses are given throughout Chapter 2).

## 4.3 RESULTS & DISCUSSION

### 4.3.1 Serum Sampling Observations

When working with human bodily fluids it is important to ensure that the integrity of the sample is intact and that salient characteristics, whether used to highlight disease or not, are free from extraneous sample-related contaminants. To ensure the correct usage of normal pooled serum, upon correct thawing at RT and relative humidity, all serum aliquots were manually inverted several times and subjected to automated vortex prior to analysis, to align with clinical protocols. This is due to the sample's physical appearance, *i.e.* sometimes visible with flocculent material. Routine clinical SOPs state that such appearance is normal and is caused by remaining fibrin-fibrinogen complexes [189], following repeated freezing and thawing cycles. It is already known that the action of repeated freeze-thawing usually causes denaturation and cryo-precipitation of serum components and the turbid appearance is more noticeable with increased FTCs [189]. It is important to note that such turbidity of the serum was generally seen after numerous FTCs and was free from precipitates in the first 2-4 FTCs. However, equally important is that the presence of such precipitates does not negate the serum performance, and it is stated that the removal of such precipitates could remove key nutrients and salts if filtered [190].

### 4.3.2 Raman Spectral Variance

The data from both the FTC on CaF<sub>2</sub>, using the 785 nm excitation wavelength were compared between two Horiba instruments (HR800 (I) vs. ARAMIS (II)). In a first instance, the datasets were looked at in detail separately, before being compared using PCA and HCA clustering. An overview of all values for both datasets is shown in Table 4.1. The results for the variance test after pre-processing, along with the result of the QT and SNR are evident. For ease of comparison later, the data is ordered so that the results from one dataset (II) are above the other dataset (I). As can be seen below, approximately, more of the HR800 dataset passed the quality testing (n=441), compared to the other (n=317). Additionally, the SNR values were slightly better for the HR800 data (16.54 vs 8.71). This could perhaps be attributed to the 100% laser power at 30 mW compared to the 25 mW with the ARAMIS. Over 90% (I) of the spectra collected for each FTC passed; 27/30 being the lowest. In comparison, approximately 60% of the spectra per FTC for the ARAMIS dataset passed quality testing; 18/30 being the lowest value. The highest SNR values per FTC were seen to be with FTC 2 for the ARAMIS (10.58) and FTC 13 for the HR800 (19.16). The median RSD range was larger for ARAMIS (10.45-5.99 = 4.46), with an average median point across all FTC of 8.59 whereas, the values for HR800 were 5.74 and 7.47, respectively.

**Table 4.3|** Statistical values for variance analysis, demonstrating the relative standard deviation between cycles of freeze-thaw using DCDD Raman microspectroscopy.

Raman FTC# (Aramis / HR800)	SNR	Spectral QT passed	RSD% min/ $\tilde{\nu}/\text{cm}^{-1}$	RSD% max/ $\tilde{\nu}/\text{cm}^{-1}$	Av. RSD %	Med. RSD %
1 Aramis	9.12	18	0.22 / 1590	222 / 1497	10.12	8.01
1 HR800	14.72	29	0.12 / 1590	202 / 1447	9.03	7.85
2 Aramis	10.58	20	0.23 / 1591	188 / 1499	9.44	7.77
2 HR800	15.23	30	0.12 / 1580	218 / 1444	8.11	6.50
3 Aramis	10.11	20	0.23 / 1600	216 / 1499	12.34	9.12
3 HR800	14.97	30	0.17 / 1590	118 / 1447	10.22	8.75
4 Aramis	6.33	21	0.24 / 1555	108 / 1499	11.55	9.03
4 HR800	18.10	28	0.14 / 1588	178 / 1447	11.21	9.58
5 Aramis	6.90	19	0.30 / 1575	300 / 1498	9.85	9.12
5 HR800	15.97	30	0.12 / 1590	222 / 1489	9.12	8.58
6 Aramis	8.72	30	0.30 / 1565	210 / 1494	12.40	10.45
6 HR800	15.00	30	0.12 / 1568	113 / 1447	11.33	8.99
7 Aramis	10.44	20	0.38 / 1575	214 / 1495	13.36	10.26
7 HR800	14.08	29	0.19 / 1573	188 / 1457	12.04	10.99
8 Aramis	8.95	19	0.37 / 1581	147 / 1444	10.97	7.23
8 HR800	18.59	30	0.14 / 1575	150 / 1447	8.08	5.25
9 Aramis	8.90	20	0.48 / 1588	200 / 1495	8.99	6.12
9 HR800	15.67	29	0.11 / 1573	212 / 1447	8.91	4.82
10 Aramis	9.65	20	0.68 / 1548	116 / 1479	11.54	9.48
10 HR800	15.27	29	0.18 / 1575	112 / 1447	10.30	7.03
11 Aramis	8.64	20	0.49 / 1601	306 / 1499	11.43	8.99
11 HR800	16.35	30	0.13 / 1590	123 / 1485	9.09	6.12
12 Aramis	8.46	20	0.31 / 1595	259 / 1499	9.33	5.99
12 HR800	18.97	30	0.17 / 1575	299 / 1477	9.58	5.89
13 Aramis	7.68	20	0.24 / 1590	306 / 1498	10.45	8.56
13 HR800	19.16	27	0.39 / 1575	108 / 1448	9.85	5.68
14 Aramis	7.33	20	0.41 / 1590	304 / 1443	9.32	8.56
14 HR800	19.08	30	0.18 / 1575	112 / 1447	9.00	8.45
15 Aramis	8.79	30	0.45 / 1590	307 / 1444	10.16	9.12
15 HR800	16.99	30	0.28 / 1565	222 / 1447	8.89	7.77

RSD: relative standard deviation; SNR: mean signal-noise-ratio *via* RMS calculation

Before any calculation of the variance, the data was submitted to routine detector optics correction as mentioned, plus truncation to the wavenumber region of interest, followed by Savitzky-Golay smoothing with 3-point smoothing to increase spectral feature contrast, a 5<sup>th</sup> degree polynomial background adjustment and normalised with vector

### 4.3.3 Instrument 1 Results

#### 4.3.3.1 Principal Component Analysis

Figure 4.3 shows the results for the DCDD method for each of the FTCs carried out on the CaF<sub>2</sub> support for the HR800 data. The spectra were pre-processed and cut to the fingerprint region (1800-600 cm<sup>-1</sup>). The PC scores plot for all individual spectra from all FTCs (1a) and the component loadings (1c) offer a clear visualisation of the datasets in n-dimensional space. An offset of all mean spectra for FTCs, demonstrating the major bands seen within the spectra are shown (1b). The HCA dendrogram (hierarchical cluster analysis) (c), demonstrates the degree of dissimilarity as a measure of heterogeneity between each of the FTCs using the Euclidean distance parameter with Ward's algorithm [48]. There is very little clear separation between the FTCs, except for FTC 5; which is shown to be away from the remainder of the FTCs in both the PC scores and HCA plot. This could have arisen from slight changes in the environment at the time of testing, or human error. Of the perceived variance, PC 2 is showing ~21% variance and is responsible for the appearance of FTC 5. As seen within (14b) and the loadings (14c), the significant peaks within the dried serum appear to be from the ring breathing mode of phenylalanine (Phe) at ~1004 cm<sup>-1</sup> and 1033 cm<sup>-1</sup>, the protein backbone structures amide I at ~1655 cm<sup>-1</sup>, and amide III at ~1240-1278 cm<sup>-1</sup> (shaded for clarity). One can also observe smaller intensities of Tyr/Phe bands (~640/643 cm<sup>-1</sup>) and ring breathing mode of Tyr (~852 cm<sup>-1</sup>). As seen from the HCA plot, FTC 1 and 15 share a close degree of similarity. An expected result would be that from FTC 1 and above, there would be some degree of variance, owing to the natural ageing of the sample and the fact that the same sample has been subject to repeat passes of freezing and thawing. This result is interesting as we can perhaps attribute it to the heterogeneity of the drying process, meaning very little if any contribution is coming from the action of freezing and thawing, it seems.

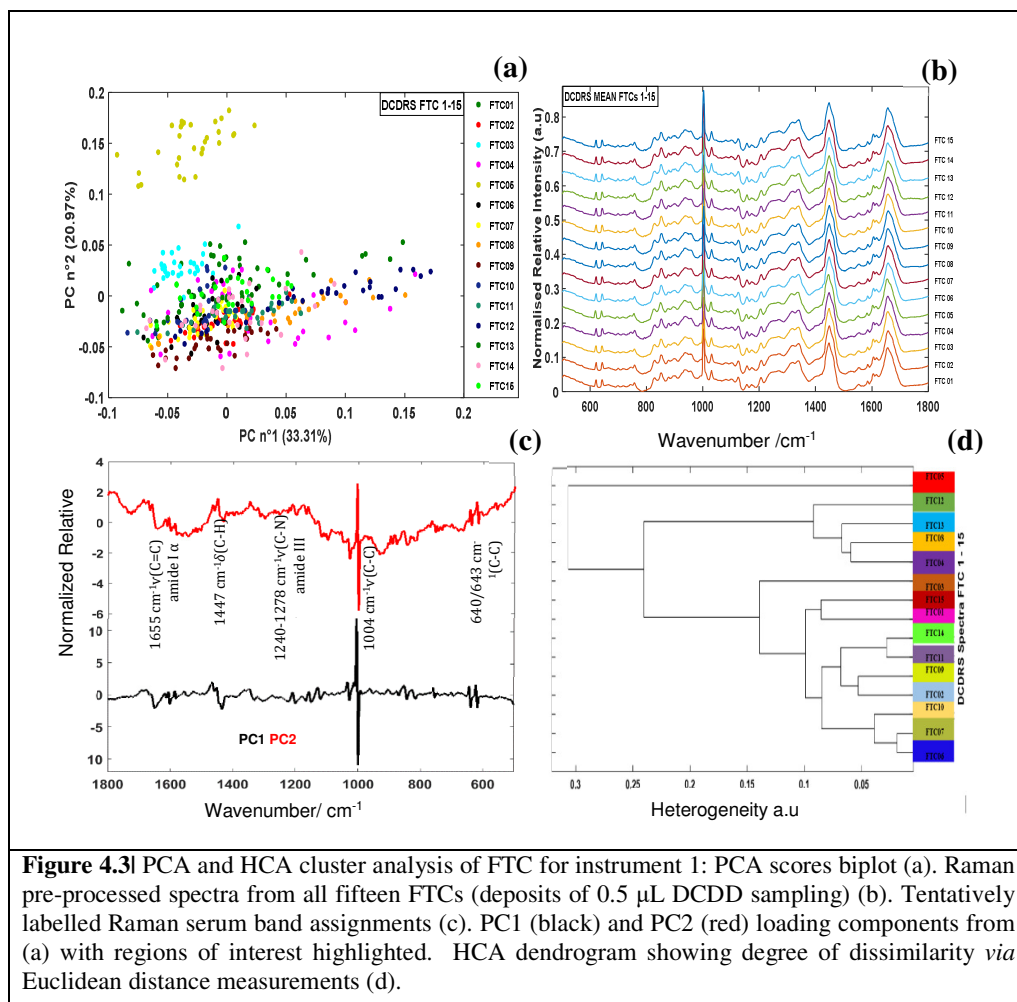


**Figure 4.3|** PCA and HCA cluster analysis of FTC for instrument 1: PCA scores biplot (a). Raman pre-processed spectra from all fifteen FTCs (deposits of 0.5  $\mu$ L DCDD sampling) (b). Tentatively labelled Raman serum band assignments (c). PC1 (black) and PC2 (red) loading components from (a) with regions of interest highlighted. HCA dendrogram showing degree of dissimilarity *via* Euclidean distance measurements (d).

Generally, PCA results did not reveal anything. DFA was carried out on the data to further observe potential group membership amongst separation of the data in DF-space. However, the data did not identify any differences so no further analysis was undertaken. The DF and PCA loadings showed the same information. Table 4.4 shows the loadings.

**Table 4.4** Most salient spectral bands and Raman bio-molecular assignments of DF (1 & 2) loadings, after DFA [27, 132, 137, 191-194]

$\tilde{\nu}/\text{cm}^{-1}$	Tentatively assigned Raman peaks
620	Phe
640	Tyr
650-667	DNA (G)
714	Polysaccharides
757	Proteins
780-792	DNA/RNA (C, U, T)
829, 852-854	Tyr
877-897	$\nu(\text{C-O-C})$ Glycoside ring
938	Protein ( $\alpha$ helix)
1003	Phe
1032	Phe ( $\delta(\text{CH})$ in plane)
1061	$\nu(\text{C-N})$ , $\nu(\text{C-C})$ in proteins
1155	$\nu(\text{C-N})$ , $\nu(\text{C-C})$ proteins
1176	Tyr ( $\delta(\text{C-H})$ bend)
1236	Amide III (protein)
1311	DNA (A)
1340	Trp, (A), phospholipids
1369-1375	DNA (A, T, G)
1446	Proteins, phospholipids
1557	Amide II (protein)
1609	Tyr, Phe
1658	Amide I (protein)

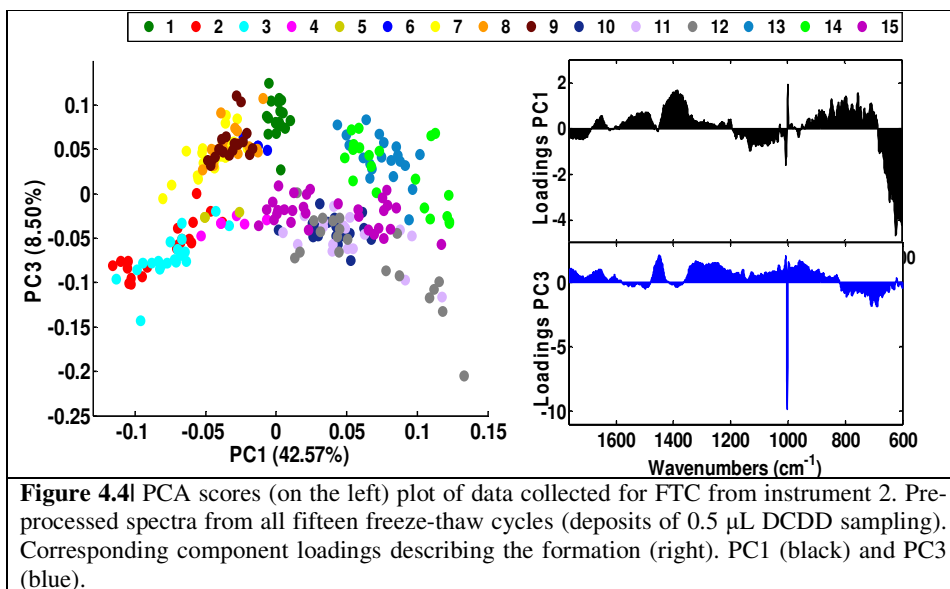
NS: Not Seen/Significant; A: Adenine; G: Guanine; C: Cytosine;  
T: Thymine; U: Uracil; Trp: Tryptophan; Tyr: Tyrosine; Phe: Phenylalanine

#### 4.3.4 Instrument 2 Results

##### 4.3.4.1 Principal Component Analysis

Further analysis *via* PCA with all data points ( $n=317$ ), seen in Figure 4.4 demonstrates the spread in the data, along with the component weights or magnitudes (right) for the variation observed across the new subspace direction (scores). There is some clustering of the FTC groups based on the direction of PC1, which shows splitting of FTCs 1-3 and 7-9 (explained by PC3). The rest of the higher number cycles, such as 10-15 appear to be more spread and mixed amongst each other. It appears that both PCs are demonstrating some pattern separation of the data overall, but with no clear distinction between all the groups. Notably, the results seen previously with FTCs 5 and 9 completely separating is absent here, which could mean that such a result was incongruent with the action of other FTCs. The magnitudes for each of the scores (PC1 and PC3) (Figure 4.4, left), demonstrates that the pattern seen could be attributed mainly to the positive loadings on both, whereas the negative ones show that contributions from Phe ( $1003 \text{ cm}^{-1}$ ), Tyr/ DNA/ proteins and polysaccharides ( $620-890 \text{ cm}^{-1}$ , plus minor contributions from

$\nu(\text{C-N})$ ,  $\nu(\text{C-C})$  in proteins and amide III ( $1061 - 1236 \text{ cm}^{-1}$ ), which could explain what is shown in PC1 negative and PC1 positive (Figure 4.4, left). Additionally, PC3 positive shows that FTCs 7-9's separation could be owed to any of the major contributions PC1's negative domain and PC3's positive aspects. Overall, there are little distinct features in the data from the PCA. Further, DFA was carried out, but this did not add anything to understanding the data. From herein, DFA wasn't used for this study.



The results from the PCA and DFA loadings plot are shown below in Table 4.5. The DFA scores demonstrated the same orientation and information as the PCA above (Figure 4.4), so the data was not shown; only the loadings values.

**Table 4.5!** Most salient spectral bands and Raman bio-molecular assignments of DF (1 & 3) loadings, after DFA validation [27, 132, 137, 191-194]

DF1	$\bar{\nu}/\text{cm}^{-1}$	Tentatively assigned Raman peaks	DF3	$\bar{\nu}/\text{cm}^{-1}$	Tentatively assigned Raman peaks
+	1033	Phe	+	1003	Phe
+	1311	DNA (A)	+	1236	Amide II
+	1447	Protein/ phospholipids	+	1447	Protein/ phospholipids
+	1609	Tyr, Phe			
-	890	$\nu(\text{C-O-C})$ Glycoside ring	-	890	$\nu(\text{C-O-C})$ Glycoside ring
-	1003	Phe	-	1035	$\nu(\text{C-N})$ (protein)
-	1155	$\nu(\text{C-N})$ , $\nu(\text{C-C})$ (proteins)	-	1420	Protein/ phospholipids
-	1557	Amide II	-	1610	Tyr, Phe
-	1658	Amide I		1658	Amide I

Tyr: Tyrosine; Phe: Phenylalanine

It should be noted that the differences to the two datasets above across two instruments could be human error in testing, or from a change in the chemical contributions of the molecules responsible for such a separation. However, when the datasets are considered individually, there is no real pattern to discern the FTCs with the HR800 dataset, whilst there are some patterns forming in the dataset from ARAMIS. Overall, it can be said that here, the differences observed here, presented no additional meaning within the data. The data could not demonstrate if the variations were from the variability within the cycles or not.

#### 4.3.5 Instrument 3 Results

##### 4.3.5.1 Centre vs. Periphery Study

Table 4.6 shows the results for the variance test after pre-processing the data, along with the result of the QT. More than 98.5% of the data for each of the regions tested passed the quality testing, with only FTC 7 from the centre dataset having 8/9, and FTC 3 and 13 from the periphery (8/9). The power at the sample here was ~90 mW, which meant that overall the SNR was greater when compared to the HR800 and ARAMIS instruments (above). This also resulted in better resolved peaks. The RMS calculated SNR values show that overall the centre aspect of the dried serum spot had a marginally better signal to noise ratio (39.89: 31.61 mean ratio), with actual values of 10 (C) versus 5 (P) having the highest values. Although the highest value (72.80) did come from FTC 15 from the peripheral aspect, so did the lowest (14.31, FTC 13). Additionally, the average SNR values for centre and periphery were 33.82 and 29.70,

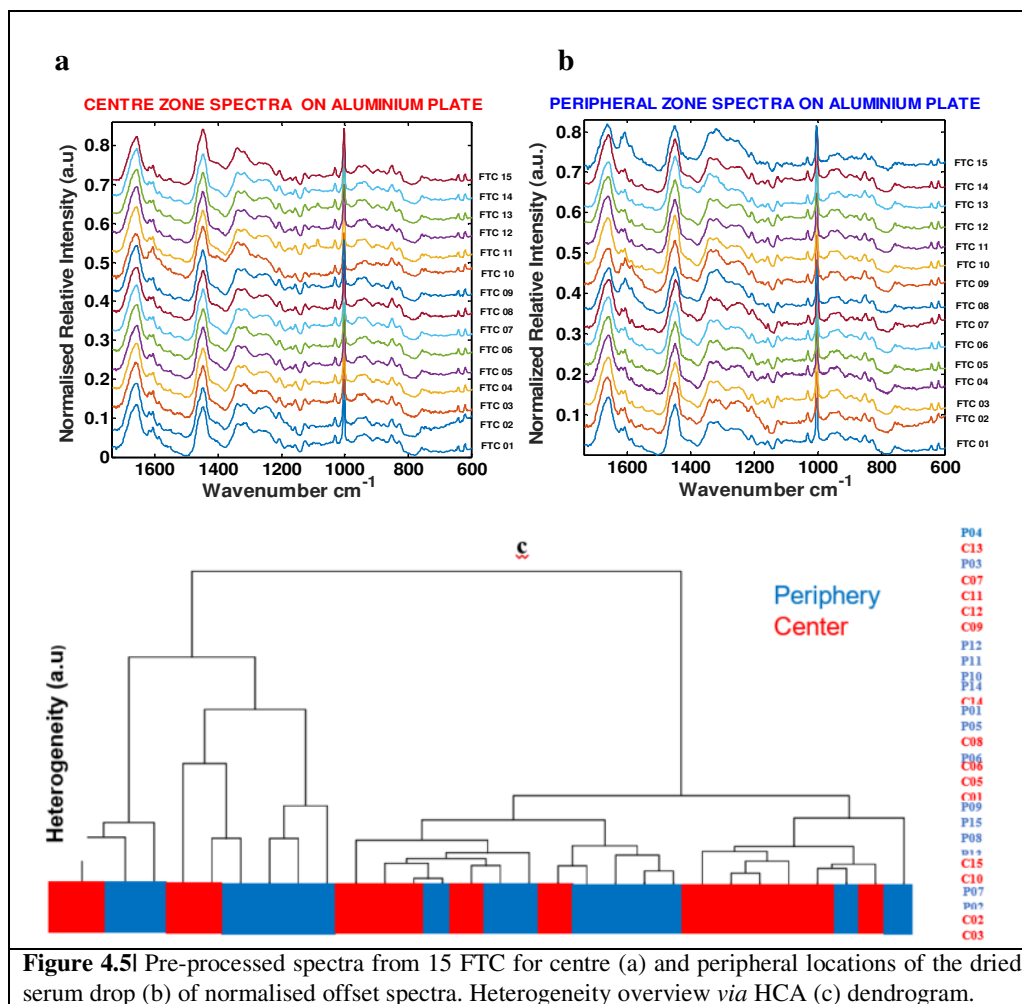
respectively. Furthermore, as seen (from Table 4.6), the median RSD standard deviation range was larger for the centre region (10.03), with an average median point of 5.23. Whereas, the values for the periphery region were 7.6 and 4.03, respectively. We can see that the data is highly reproducible and ultimately, the centre region gives the best spectra signal, but has the most amount of variability across the FTCs, demonstrating that the periphery region gave less overall variation. The centre aspects give the overall highest RSD value (328, 1440  $\text{cm}^{-1}$ ), whilst the same value was 321, 1477  $\text{cm}^{-1}$  for the peripheral aspect.

**Table 4.6** Statistical values for variance analysis, demonstrating the relative standard deviation between cycles of freeze-thaw using DCDD Raman micro-spectroscopy for centre vs. periphery investigations

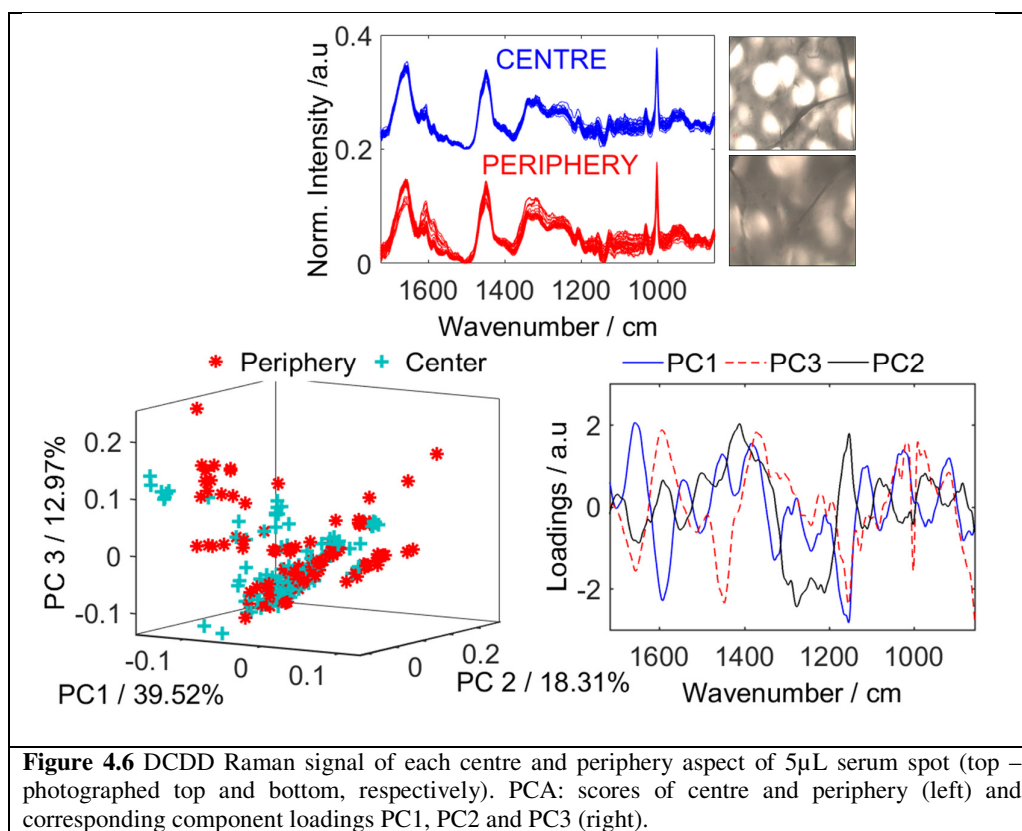
DCDD 5 $\mu\text{L}$ FTC	SNR	Centre / Periphery	Spectral QT passed	RSD% min / $\bar{\nu}$ / $\text{cm}^{-1}$	RSD% max / $\bar{\nu}$ / $\text{cm}^{-1}$	Av. RSD %	Med. RSD %
1	41.79	Centre	9	0.89 / 1502	328/1440	13.85	8.11
	31.01	Periphery	9	0.43 / 1501	321/1447	19.88	12.85
2	34.51	Centre	9	0.53 / 1504	187 / 1449	11.05	7.84
	29.67	Periphery	9	0.68 / 1500	208 / 1447	18.11	14.50
3	30.01	Centre	9	0.59 / 1501	316 / 1459	12.34	9.12
	21.02	Periphery	8	0.68 / 1499	198 / 1447	10.22	8.75
4	42.68	Centre	9	0.46 / 1499	316 / 1449	11.55	9.03
	28.88	Periphery	9	0.41 / 1505	258 / 1444	10.75	6.45
5	34.92	Centre	9	0.23 / 1500	289 / 147	10.85	8.25
	24.08	Periphery	9	0.29 / 1504	212 / 1447	11.14	9.00
6	31.55	Centre	9	0.12 / 1502	200 / 1440	10.99	9.85
	26.51	Periphery	9	0.17 / 1499	114 / 1447	15.45	12.00
7	19.18	Centre	9	0.85 / 1499	289 / 1447	12.58	8.99
	40.77	Periphery	9	0.89 / 1505	147 / 1444	14.52	10.25
8	38.90	Centre	8	0.57 / 1500	312 / 1447	9.85	7.88
	30.29	Periphery	8	0.74 / 1506	132 / 1443	13.12	9.99
9	31.58	Centre	9	0.69 / 1500	320 / 1445	9.99	6.89
	45.22	Periphery	9	0.71 / 1498	145 / 1448	12.12	10.44
10	67.98	Centre	9	0.89 / 1500	210 / 1447	13.45	10.00
	36.87	Periphery	9	0.58 / 1500	178 / 1445	12.47	8.79
11	35.61	Centre	9	0.74 / 1501	147 / 1447	17.45	12.12
	20.27	Periphery	9	0.42 / 1500	300 / 1447	9.85	6.45
12	34.90	Centre	9	0.74 / 1500	189 / 1447	14.47	11.10
	14.31	Periphery	9	0.41 / 1499	289 / 1447	10.00	8.99
13	18.61	Centre	9	0.46 / 1499	158 / 1447	14.52	9.87
	36.67	Periphery	8	0.47 / 1502	246 / 1447	14.45	11.00
14	27.08	Centre	9	0.54 / 1500	149 / 1446	11.25	10.47
	15.97	Periphery	9	0.49 / 1499	234 / 1448	13.23	10.85
15	17.96	Centre	9	0.46 / 1498	289 / 1447	10.85	8.87
	72.80	Periphery	9	0.23 / 1502	128 / 1458	12.32	11.10

RSD: relative standard deviation; SNR: mean signal-noise-ratio *via* RMS calculation

Figure 4.5 shows results from the centre and periphery study on dried serum drops on an Al multi-well. The spectra per region are presented as an offset to visualise all 15 FTCs (8a and 8b, for centre and periphery aspects, respectively). As a method of comparison and the relationship between each of the FTCs from both regions, there is an HCA dendrogram (8c). It is clear to see that there is a general mix of the data from both regions, as denoted by the red and blue blocks (HCA dendrogram). The relatedness between the datasets/ and sample repeats can be distinguished from the two large clusters plus individually between the regions from the key (left of HCA dendrogram). Additionally, as can be seen, there is a slight difference to the peak at  $\sim 610\text{ cm}^{-1}$  (Tyr/Phe) for the peripheral aspect. It appears that it is more pronounced and at some points reaches close to the intensity of the amide I peak. Further, there is a slight intensity decrease on the Phe ring breathing mode at  $1003\text{ cm}^{-1}$ . This could be a movement of protein components under migration towards the contact line. These observations are consistent with previous studies, using protein solutions and tear fluid [142, 194-195]. Some research suggests that the periphery demonstrates a homogenous protein distribution [27, 137, 142, 195] whereas, the central aspect retains minor protein contributions, urea components and some electrolytes [194]. However, with the analysis of the mean of the periphery and centre aspects from the dried spot [137], concluded that there was very little visual distinction between the two aspects.



The data were then subjected to PCA to try to observe further patterns in the data by reducing the overall dimensions of the data from n-dimensions to a select few. Figure 4.6 shows the results from PCA scores and loadings for the periphery dataset. As seen, there is some minor separation seen in the periphery dataset; PC1 providing the best response with differences between 8 groups on the negative scores space and 7 groups on the positive. Such as FTC 1-2, 6-9, 13 and 15, compared with 3-5, 10-12 and 14. PC2 only finds very minor further distinction, with less clear split of FTC 1, 13 and 14 vs. 2, 4, 9 and all but two reads of 15. The two could be possible outliers. Overall, there is a similar pattern seen with the centre dataset, whereby FTC 2, 10, 15 on the negative domain of PC1, and 7 and 13 on the positive. PC2 also finds less overall separation, 14 on the negative, and 2, 4 and 12 on the positive.



Additionally, a white light image was acquired from each of the respective physical positions from which the spectra were collected. This shows the physical appearance and hence differences owed to the process of drying a bio-fluid drop. The drops themselves were measured post accumulation in the liquid phase. It is known that the refractive index changes as a sample shifts from a liquid-phase to solid, as is the case in serum drying and we see the coffee-ring effect [152, 187]. As the drop dries the process is incremental. The periphery starts to dry first, followed by a growing fern-like pattern from the outer-edge to the centre of the drop, finishing with the extremities of the ferns [187], (seen in Figure 4.1). Essentially, a concentration gradient forms, whereby the heavier serum protein components migrate to the periphery, causing a ring like formation and an overall sample heterogeneity [137, 191]. Furthermore, it has been reported that spectral distortions occur within the drying cracks of the drop, attributed to differences in baseline and the amide I and II regions [192]. Accordingly, it appears that the macromolecular concentration has an impact on the spatial distribution of proteins [140]. This phenomenon increases as a consequence of dilution [152]. When we observe the loadings on Figure 4.6, we can see that there are a few contributing components ( $1375$ ,  $1609$  and  $1655\text{ cm}^{-1}$ , which could be ascribed to the  $\text{CH}_2$  and  $\text{COO}^-$  region, the Tyr/Phe band and amide I. Some suggest that the band at  $\sim 1375\text{ cm}^{-1}$  could be attributed specifically to minute changes in the microenvironment,

which has effect on the side aspects of COO<sup>-</sup> and CH<sub>2</sub> containing glutamic and aspartic acids [153].

#### **4.3.6 Environmental Drying**

The data from both ED studies on CaF<sub>2</sub>, using the 785 nm wavelength were compared between two Horiba instruments (HR800 (I) vs. ARAMIS (II)). As mentioned previously, the ED study was conducted to see if the action of air drying affected the serum sample components. An overview of all values for both datasets is shown in Table 4.5, which demonstrates the results for the variance test after pre-processing, along with the result of the QT and SNR enumerations. The data are ordered so that the results from one dataset (II) are above the other dataset (I). Both datasets fully passed the spectral quality testing (100% of data), although, the SNR values were slightly better for the HR800 data (average value being 16.72 vs. 10.90). This could be attributable to the slight differences in laser power. The highest SNR values were seen to be with the 2 h time point for the HR800 (17.77) and 3 h for the ARAMIS (11.2). The median standard deviation range was larger for instrument 2 (0.0019–0.0008 = 0.0011), with an average median point across all ED points of 0.0011, whereas, the values for instrument 1 were 0.0019 and 0.0025, respectively. This indicates the high reproducibility between each of the datasets. From this, one can deduce that the method is transferable.

Calculation of the variance was done after routine instrument correction and data pre-processing (CRA removal, 3-point SG smoothing, a 3<sup>rd</sup> degree polynomial background correction and vector normalisation and offset). The data were then submitted to PCA, HCA and DFA.

**Table 4.7|** Statistical values for variance analysis, demonstrating the relative standard deviation between cycles of two investigations (Aramis and HR800) using DCDD Raman microspectroscopy for ED investigations

DCDD 0.5 $\mu$ L ED	SNR	HR800 / Aramis	Spectral QT passed	RSD% min / $\bar{\nu}$ / $\text{cm}^{-1}$	RSD% max / $\bar{\nu}$ / $\text{cm}^{-1}$	Av. RSD %	Med. RSD %
10 min	10.16	Aramis	3	0.19 / 1504	222 / 1440	15.12	14.45
	15.66	HR800	3	0.13 / 1504	174 / 1447	9.21	6.85
30 min	10.96	Aramis	3	0.17 / 1501	200 / 1449	16.78	14.20
	16.51	HR800	3	0.16 / 1501	178 / 1447	10.77	8.75
1 h	10.81	Aramis	3	0.19 / 1500	200 / 1459	12.27	8.75
	17.55	HR800	3	0.17 / 1501	188 / 1447	10.66	7.89
1.5 h	10.98	Aramis	3	0.13 / 1501	258 / 1449	21.05	16.45
	16.71	HR800	3	0.11 / 1500	147 / 1444	10.05	9.15
2 h	10.89	Aramis	3	0.13 / 1501	202 / 1447	11.46	13.47
	17.77	HR800	3	0.11 / 1502	178 / 1447	10.85	9.23
2.5 h	10.99	Aramis	3	0.13 / 1501	274 / 1440	18.45	14.00
	16.51	HR800	3	0.09 / 1502	199 / 1447	10.06	8.85
3 h	11.2	Aramis	3	0.18 / 1502	178 / 1447	18.00	14.25
	18.25	HR800	3	0.11 / 1501	199 / 1444	10.58	7.05
3.5 h	10.96	Aramis	3	0.17 / 1501	285 / 1447	13.88	11.85
	17.3	HR800	3	0.12 / 1500	142 / 1443	8.75	6.07
7 h	10.96	Aramis	3	0.19 / 1500	220 / 1445	13.89	12.17
	15.3	HR800	3	0.13 / 1501	175 / 1448	9.78	7.47
14 h	10.98	Aramis	3	0.19 / 1501	208 / 1447	16.44	14.79
	16.35	HR800	3	0.13 / 1504	138 / 1445	11.41	9.80
24 h	11.03	Aramis	3	0.14 / 1504	220 / 1447	10.45	10.12
	16.03	HR800	3	0.12 / 1504	158 / 1447	8.35	6.45

QT: spectra passing quality testing; SNR: mean signal-to-noise-ratio; STD: RSD standard deviation;  
Pre-processed: detector optics, background corrected, smoothed and normalised

Figure 4.7 shows the results for the environmental drying DCDD method for each of the 11 time points tested across both instruments over 24 hours. The spectra were pre-processed and cropped to the fingerprint region ( $1765\text{-}600\text{ cm}^{-1}$ ) and offset for visualisation of all the data. This way, it is possible to see specific differences in the spectra. The data are presented as a side-by-side comparison of the datasets (instrument 1 and instrument 2) by all the 11 time points spectrally assessed ( $n=33$ , respectively). Comparing instrument 1 and 2 (left and right respectively), there is more variation visible at each of the time slots, which is most apparent at 30 mins and 1 hr. In contrast, the only variance seen in with the 2<sup>nd</sup> instrument is at 10 min drying time; especially around the amide I band ( $\sim 1655\text{ cm}^{-1}$ ). Given that water is a polyatomic molecule, the allowed vibrations in Raman are usually only seen shifted at the high wavenumber region ( $\sim 3600\text{ cm}^{-1}$ ), plus sometimes, a smaller contribution of the H-O-H bend at  $\sim 1600\text{ cm}^{-1}$ , which could be seen if the intensity of the laser is strong enough. However, here it is possible to assign the variation to slight intensity differences between replicates.

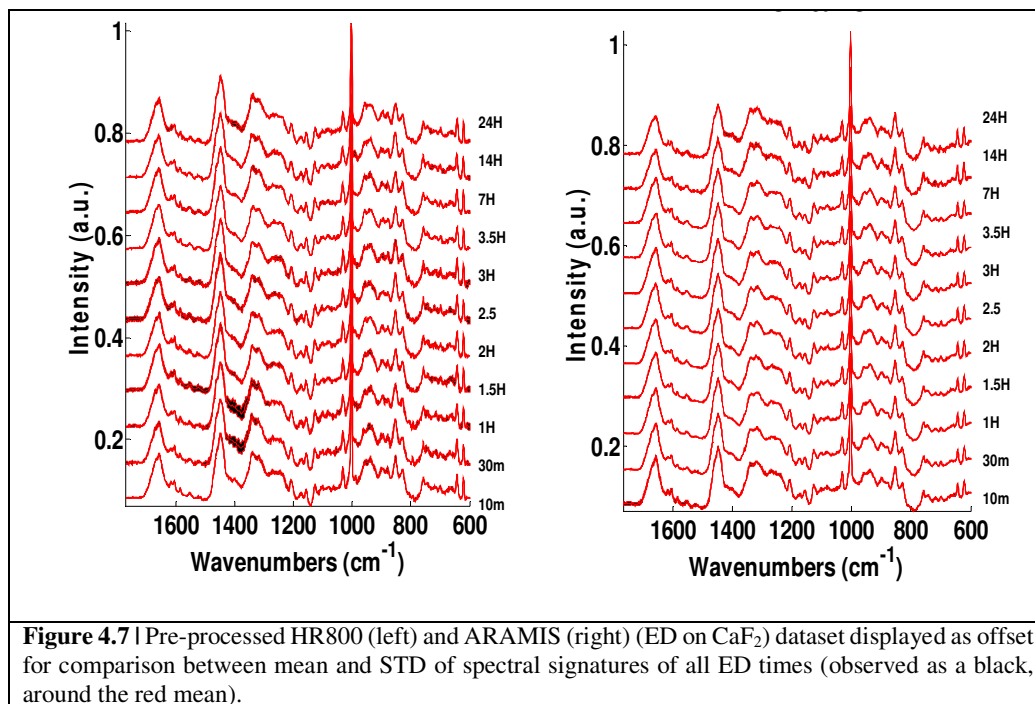
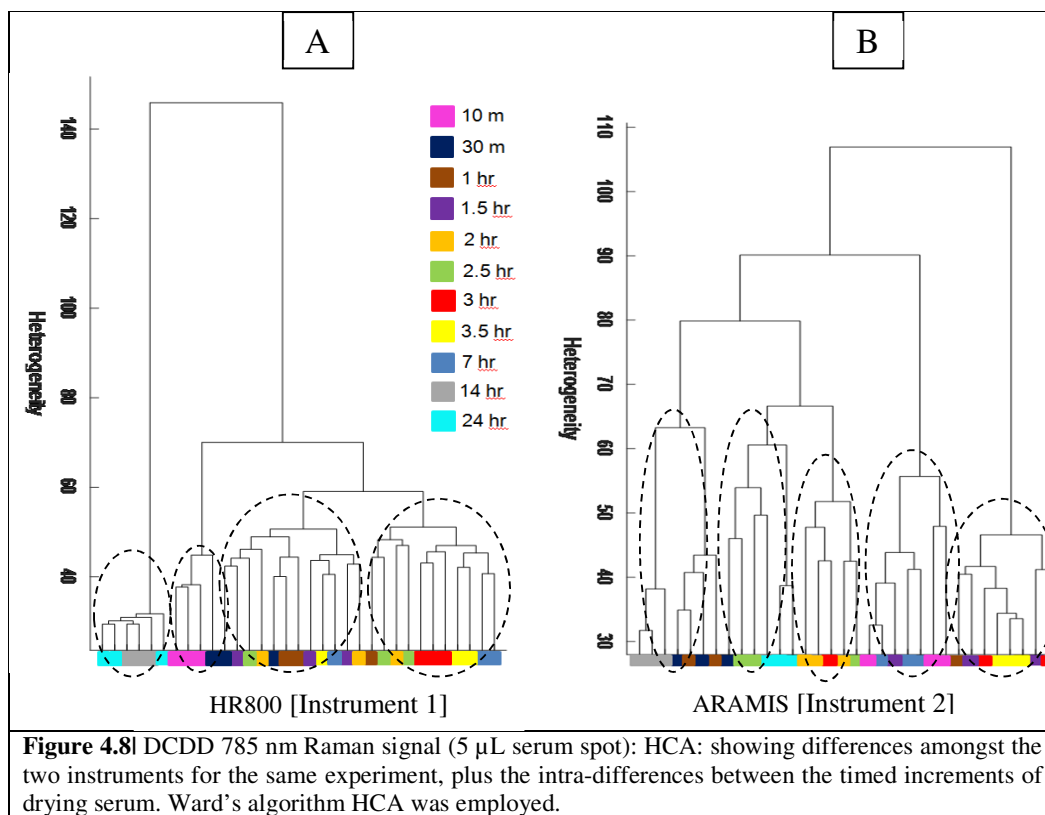
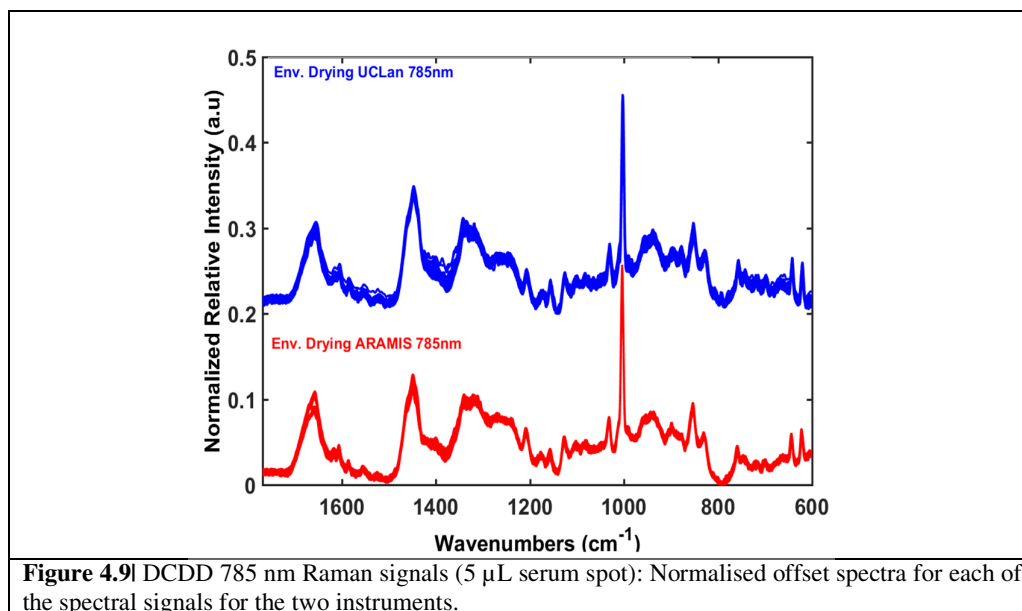


Figure 4.8 displays the relatedness (how comparable it is) of the spectra per time point as a comparison between instruments on an HCA dendrogram. As a function of heterogeneity between the individual data collected throughout the 24-hour testing period, Ward's algorithm was used to present the Euclidean distance between the samples and as such presents a visualisation of the relationship. The dataset from instrument 1 is displayed on the left and instrument 2 on the right. As it can be seen, there are three data points per time, which is indicated by colour, and generally the best observation would be to see all three of the colours aligned with each other. When comparing the two datasets such a pattern is absent. However, there are 4 and 5 cluster formations (as depicted by the ellipses) seen between the I (A) and II (B), respectively.



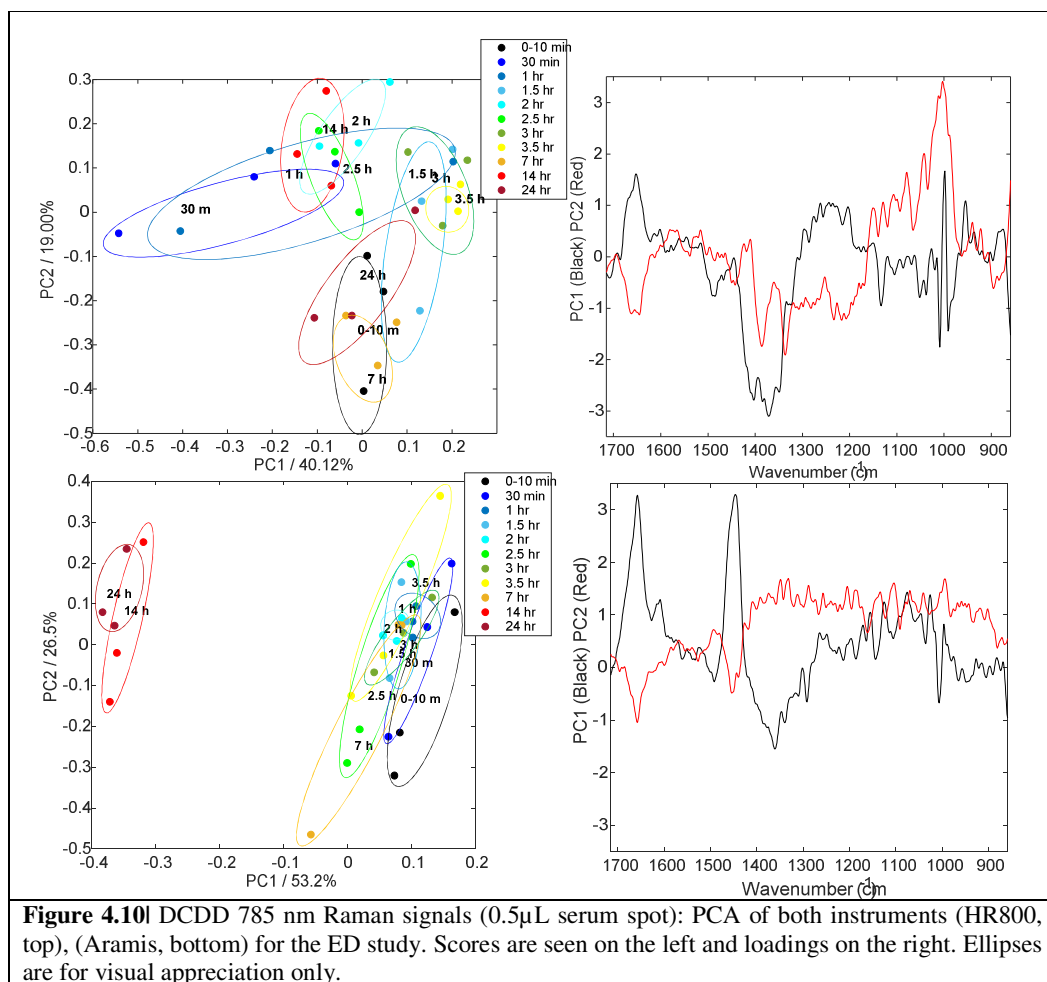
Generally, the data points from 10 and 30 min are similar as are the data from the last two time measurements (14 h and 24 h). Overall, the greatest Euclidean value provided separation of 14 h and 24 h from all the other time points for the HR800 dataset. It can be seen that the remaining 'middle' time points are clustered together and are generally mixed, whereas, the biggest difference in the ARAMIS was one cluster of 1 h - 3.5 h versus the rest. Additionally, the data points (30 mins and 1 h (on the ARAMIS), appear to be more related than 10, 30 mins. Essentially, the samples appear to be less uniform than first thought, according the differences in times tested and the relatedness of the samples. It would be expected that with the action of drying, there are spatial differences of the intrinsic molecules, which at the point of complete evaporation and drying, would occupy fixed positions, and in turn the protein molecules migrate to the periphery, seeing the ions and salts remain centre-wise. This supports previous literature, that throughout serum drying, heavier components, such as proteins and nucleic acids, migrate to the periphery [111, 152, 196]. Figure 4.9 shows both datasets after pre-processing offset to one another for ease of comparison.



#### 4.3.6.1 Principal Component Analysis

Figure 4.10 shows the results of the PCA for the ED study. The scores (left) and loadings (right) for PC1 and PC2, accounts for  $\sim 59\%$  and  $80\%$  of the explained variance overall for each data from the instruments, instrument 1 and 2, respectively. PC1 loadings are shown in black and PC2 is visible in red on the plots. The time points have been highlighted in graphic ellipses for visual ease. As can be seen, the larger the ellipses per group, the greater the degree of variance within the data repeats. For instrument 1, there is no real pattern seen between the time points, with 0-10 mins being separate from 30 mins and 1 hr in a triangle formation, plus the remaining time points are all lying about the mixture of the triangle. For instrument 2, samples taken from two time points (14 h and 24 h) have found some separation from the remaining groups. Here, according to the loadings, it appears that the amide I and II bands seem to be responsible for this formation, as highlighted by PC1 (bottom right). Whereas, PC2 on instrument 1 shows some marginal separation of three data groups from the remainders (0-10 mins, 7 h and 24 h). This formation is described by the red loading (top right). Here, the phenylalanine band ( $\sim 1004 \text{ cm}^{-1}$ ) and amide III ( $1320\text{-}95 \text{ cm}^{-1}$ ) appears to show some influence. Overall however, there is no real formation and sequence shown between the timings *via* PCA. It was concluded that with

DCDD Raman spectroscopy and the methodology employed here, there is no discerning differences between the spectra across a drying drop of 24 h.



### 4.3.7 Preanalytical Variation Discussion

Combining light microscopy with a Raman Spectroscopy system enables micrometre analysis of the sample of interest. Here, a series of experiments were devised to observe the pre-analytical variability of freezing, thawing and drying of normal pooled human serum. FTCs are common in clinical laboratory settings, as often it cannot be avoided given some initial sample volumes taken from the patient. Additionally, clinically, samples are often in the non-raw phase when they arrive for testing; that is, they have undergone some element of freezing to preserve the sample's biology. Furthermore, investigations to the pre-analytical variation from FTCs are few and far between within the field of bio-analytical spectroscopy, compared to other fields of mass

spectroscopy [43-46, 48]. Such a subject is important to ensure that pre-analytical variabilities does not mask the clinical details, downstream. To conclude with regard to preclinical variation, standardisation protocols go some way to actively control sample-bias and allow for a better discovery of prognostic and diagnostic signature markers. Further still, it is known that protein stability is problematic in bio-fluids and studies suggests that speeding up the freezing process and slowing down the thawing, leads to severe protein damage [201]. Whereas, slow freezing and fast thawing prevents such protein denaturation [202]. Some research studies have suggested that negating repetitive freeze-thaw cycles and storing for long periods in frozen conditions are advised [188]. That said, in the present study, careful attention was made to allow freezing and thawing without any external catalyst (i.e., non-passive thawing), in the controlled laboratory environment with relative humidity levels. The results were achieved using a suite of research-grade benchtop spectrometers and devised protocols meant that such results were easily reproducible, if necessary. However, although a non-destructive method, the very small amounts of samples analysed, once dried were occupying sample space in the AI wells and substrates, so would eventually have to be removed. The limitations of this study are that no evaluation of the pH of the samples were taken to look for possible microbial growths within the specimen, which may cause anomalous results. Additionally, the results are based on 15 different freeze-thaws but from one stock sample. Future work could look to compare freeze-thaws of different research-grade normal serum and human diseased samples and maybe even looked to automate the whole process for the clinical need. Overall, this work shows that liquid samples demonstrate the same amount of variance when compared to dried sample analyses. With this mind, it is more advisable to work only on liquid biofluid samples for micro-Raman spectroscopy analysis in the future, to ensure that pre-analytical variations are kept to a minimum and be safe in the knowledge that possible disease signatures are not overwhelmed with analytical sample related consequences. Furthermore, not drying the sample means that issues of the physical effects of separation and spacing of molecules and the coffee-ring effect can be completely circumvented. Taken from the promising results for liquid macro testing; especially with the macro adapter and cuvettes, it was deemed appropriate to proceed with the batch of clinical samples in this approach. The benefits here would be twofold. The prolonged drying times seen with biofluid samples, within spectroscopy, would be negated as well as the physical separation effects of the analytes under investigation. This combined with having an efficient SOP would go a long way to limit any preanalytical variation.

### 4.3.8 Liquid Serum Fibrosis Raman Study

#### 4.3.8.1 Spectral Variance Analysis

Table 4.8 shows the results for the variance analysis for the fibrosis study conducted with the developed macro liquid Raman spectroscopy for the patients passing the spectral quality test. The degree of fibrosis (0, 1, 2, 3, 4) is indicated for each patient. The results presented are from the mean analysis of the RSD, demonstrating the minimum, maximum, average and median values across the patient spectra. Additionally, the results of a Raman spectral quality test are shown (a maximum of 5 spectra per patient was done). Overall, 94.25% of the spectra passed. The spectra that did not meet the absorbance threshold were discarded. This was visualised using cluster analysis with explorative HCA (data not shown).

Overall, there were more fibrosis patient samples included than revealed below. In total 80 patient samples were interrogated by Raman spectroscopy but due to bias linked to transplantation issues as agreed by medial consultation, plus some patients were revealed to be linked with hepatitis B and NASH, so were removed from the study for data analysis. In summation, 49 patients were only taken forward (n=225).

**Table 4.8|** Statistical values for variance analysis, demonstrating the relative standard deviation between mean patients of the fibrosis study using macro liquid Raman spectroscopy

Raman Fibrosis Study	Fibrosis Staging	Spectral QT passed	RSD% min/ $\bar{v}$ / $\text{cm}^{-1}$	RSD% max/ $\bar{v}$ / $\text{cm}^{-1}$	Av. RSD %	Med. RSD %
1	0	5	0.17 / 1552	128 / 1060	8.18	7.12
2	0	5	0.13 / 1555	222 / 1055	9.22	7.11
3	3	5	0.10 / 1565	124 / 1090	9.45	6.99
4	0	5	0.12 / 1562	131 / 1090	9.56	8.46
5	0	5	0.17 / 1562	155 / 1090	10.12	9.47
6	0	5	0.15 / 1562	260 / 1100	8.25	8.11
7	0	5	0.12 / 1560	243 / 1090	8.14	8.04
8	3	5	0.13 / 1566	225 / 1089	8.47	8.00
9	3	5	0.18 / 1560	229 / 1089	6.54	6.01
10	3	5	0.17 / 1670	228 / 1058	7.87	7.08
13	0	5	0.17 / 1670	138 / 1091	9.45	9.33
14	0	5	0.16 / 1670	204 / 1080	8.89	8.74
15	1	5	0.27 / 1572	289 / 1091	7.41	7.14
16	1	5	0.23 / 1557	70 / 1082	7.14	7.08
17	0	5	0.40 / 1566	82 / 1092	10.12	8.88
18	1	5	0.16 / 1621	157 / 1090	8.24	7.12
19	1	5	0.39 / 1691	202 / 1091	7.14	6.99
20	2	5	0.34 / 1661	188 / 1088	8.11	6.87
21	4	5	0.31 / 1560	110 / 1089	10.11	9.12
22	4	5	0.37 / 1660	192 / 1089	9.17	9.08
23	4	3	0.21 / 1622	120 / 1098	8.77	7.89
24	4	5	0.20 / 1562	101 / 1090	7.99	7.02

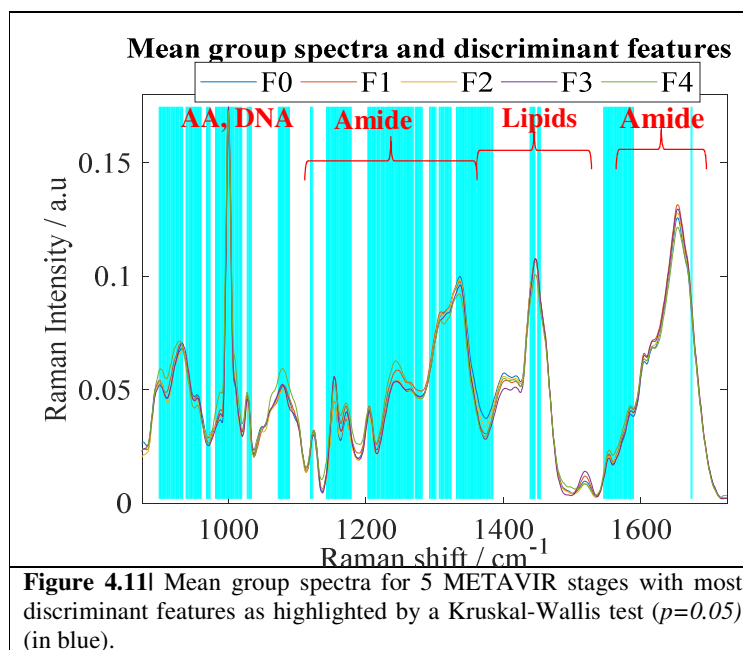
25	4	5	0.16 / 1567	75 / 1100	8.12	7.89
26	2	5	0.10 / 1557	78 / 1097	8.11	7.51
27	2	5	0.31 / 1627	98 / 1088	8.97	7.84
28	2	5	0.08 / 1625	108 / 1087	8.99	8.14
29	2	5	0.25 / 1625	100 / 1098	8.19	7.56
30	2	5	0.16 / 1655	138 / 1090	9.32	8.47
33	0	5	0.23 / 1654	124 / 1097	8.27	8.00
39	2	5	0.21 / 1652	122 / 1080	9.27	8.99
40	2	5	0.01 / 1655	158 / 1090	9.99	8.55
41	2	5	0.31 / 1526	70 / 1090	7.45	7.02
42	2	5	0.21 / 1526	82 / 1090	8.88	8.45
43	1	5	0.51 / 1634	157 / 1091	8.28	8.22
44	2	5	0.38 / 1526	202 / 1089	10.78	10.09
45	2	5	0.22 / 1523	188 / 1088	8.85	8.15
46	2	5	0.28 / 1525	110 / 1092	9.88	9.51
47	2	5	0.28 / 1528	192 / 1080	9.18	9.11
48	2	5	0.04 / 1675	120 / 1090	7.02	7.00
49	2	5	0.45 / 1577	101 / 1090	7.89	7.06
50	2	5	0.47 / 1547	99 / 1091	7.01	6.20
106	0	3	0.38 / 1680	111 / 1097	11.12	10.44
109	0	3	0.08 / 1666	197 / 1080	11.93	10.42
112	1	3	0.38 / 1563	221 / 1090	10.01	9.25
118	2	3	0.28 / 1663	121 / 1099	11.91	11.12
127	1	3	0.25 / 1625	129 / 1100	11.02	11.00
134	1	3	0.24 / 1566	130 / 1101	10.55	9.99
136	0	3	0.14 / 1556	178 / 1099	10.02	9.21
140	2	3	0.14 / 1680	101 / 1098	10.09	9.88
141	1	3	0.19 / 1666	99 / 1090	9.55	8.89

From all patients with a patient number below 100, a maximum of 5 spectra were collected. With patients with a patient number over 100, a maximum of 3 spectra were collected, due to timing. As seen from Table 4.9, 99.08% of the spectra included for analysis passed the quality testing. Only 2 spectra from patient 23 did not meet the quality threshold. The spectra from patients not entering the quality testing due to issues linked to medical conditions (n=93 spectra) were disregarded.

The minimum RSD value (0.01%) at 1655 cm<sup>-1</sup> and the maximum (289%) is at 1090 cm<sup>-1</sup>. The 1655 cm<sup>-1</sup> region is attributed to the amide I band, specifically the  $\nu(\text{C-O})$  (proteins),  $\nu(\text{C-C})$  (lipids) [193]. The region appears to be the least varied overall throughout the spectrum. The most varied region is found around 1090 cm<sup>-1</sup>, which is the  $\nu(\text{C-N})$  of proteins [132]. The largest mean and median RSD value are 11.93% and 10.44% respectively. Approximately, 81% of the median values were all lower than 10.00, demonstrating a very good reproducibility.

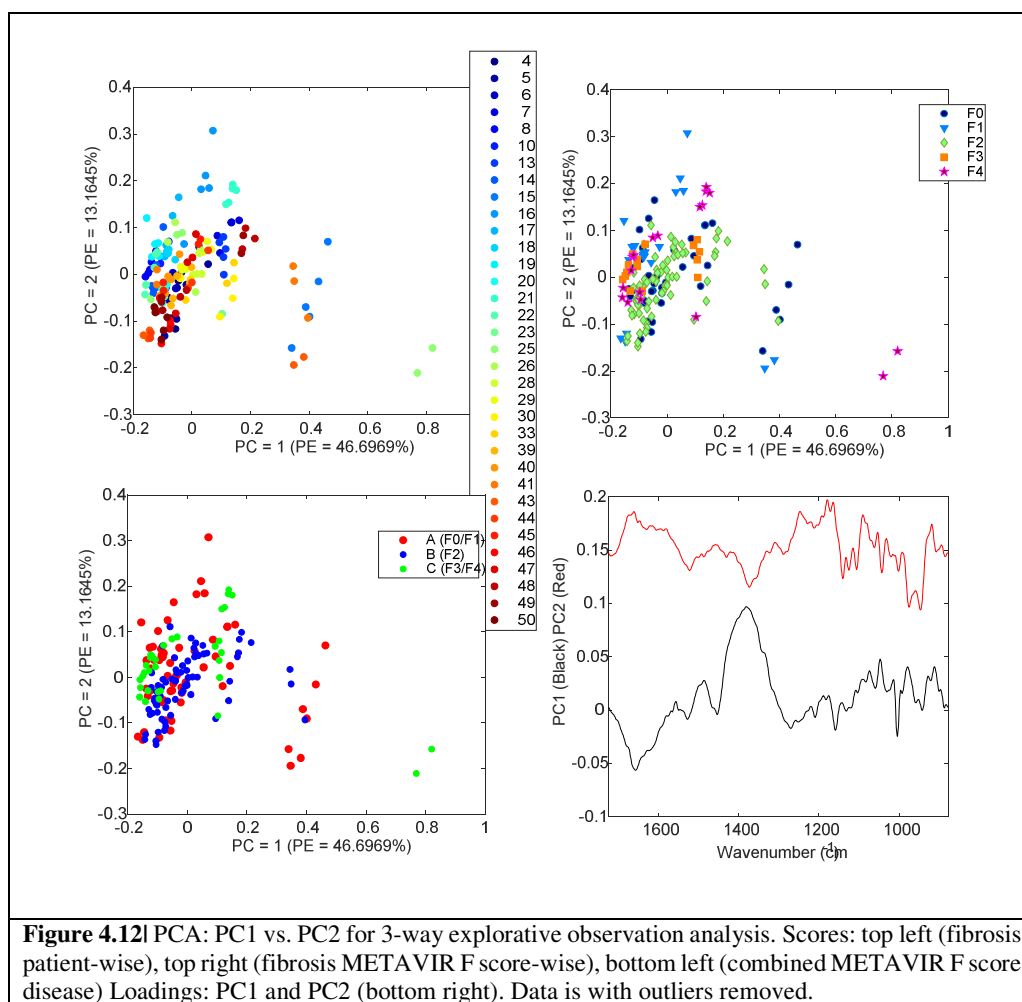
#### 4.3.8.2 Principal Component Analysis

Prior to PCA a Kruskal-Wallis discrimination test ( $p=0.05$ ) was carried to look for the regions of the mean of each F group (F0, F1, F2, F3 and F4) spectrum which were considered the most discriminant. Figure 4.11 demonstrates such regions in blue. As can be seen most of the bands are shown to be most of the bio-spectrum, with most of them concentrated around the amide I, II and III and lipid regions, plus the amino acids and DNA region (highlighted on Figure 4.11).



Moving forward, preliminary PCA clustering revealed some patients' spectra to be still quite noisy compared to the others. When looking closer to the spectra from these patients, it appeared that these were outliers (based on their differences in spectral shape from the remaining), and so a decision was made to remove them for further analysis. A total of 180 spectra were analysed *via* PCA and subsequent data analysis.

With PCA, data were analysed firstly in three ways (Figure 4.12), by patient, by fibrosis disease stage (5 groups – (F0, F1, F2, F3 and F4) and finally by a mix of fibrosis disease (3 groups – A, B and C). For information, such a mix was composed of all the patients from stage 0 and 1 in group A, stage 2 in group B, and the remaining stage 3 and 4 in group C. As shown here, PCA does not fully show any discernible differences between the fibrosis groups nor the mix of the groups. The loadings highlight significant protein and lipid influences, but we are unable to see any real separation. Due to the divide of A, B and C groups, it was thought that a separation of three groups would be shown. This was not the case, implying that the biology of these disease cases is too complex to show differences at this stage of the testing.



#### 4.3.8.3 Discriminant Function Analysis

Figure 4.13 contains the DFA results. As can be seen, two-way analysis was carried out; differentiation of fibrosis staging as according the METAVIR F score, followed by grouped fibrotic stages to represent low-grade, mid-grade and high-grade patients. The first DF plot (top) generally appears to present some degree of grouping or class membership. DF1 separates a 100% of the F4 spectra based on the positive loadings. These are attributed to  $\sim 930$ ,  $1033$ ,  $1130$  and  $1265\text{ cm}^{-1}$ , which could be tentatively assigned to a collagen skeletal backbone ( $\nu(\text{C-C})$ ), proteins ( $\nu(\text{C-N})$ ), carbohydrates and skeletal lipids, plus  $\nu(\text{C-N})/\nu(\text{N-H})$  stretch of amide III (see Table 4.9 for details). F4 and F0 is separate based on the negative loadings (DF1). Hence, what is shown is separation between healthy (F0) and cirrhosis (F4). F2 and F3 appear to be spread throughout the middle of the plot, meaning that the influence of their chemistry is somewhat low in the scale. Whilst, descriptive, DF2 loadings do not greatly add anything to the result. The second plot in Figure 4.14 does not show any further separation between the

orientated groups. Due to the results found here, DFA was the end stage of analysis for this data, meaning no PC-DFA is shown. The data were checked however, but not shown here.

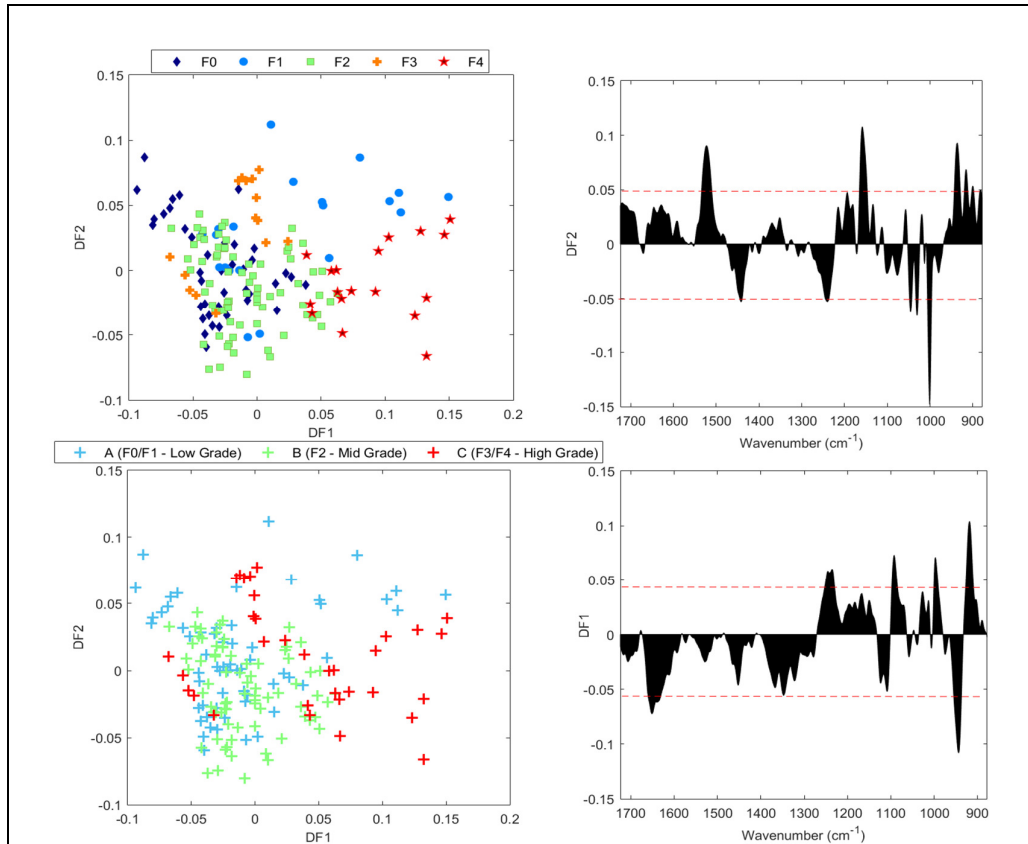


**Figure 4.13** DFA: DF1 vs. DF2 taken forward the first 5 PCs for analysis 2-way explorative observation. Scores: top left (fibrosis disease-wise), bottom left (graded grouped disease). Loadings: DF1 (bottom right) and DF2 (top right). The red dotted line indicates a minimum threshold for influencing peaks. Anything below is considered too insignificant to be meaningful to the explaining data.

**Table 4.9|** Tentatively assigned Raman peaks with DF 1 and DF 2 loadings for most discriminate wavenumber regions only as revealed by Kruskal-Wallis discriminant testing [27, 132, 137, 191-194]

DF1	$\bar{\nu}/\text{cm}^{-1}$	Tentatively assigned Raman peaks
+	932-57	$\nu(\text{C-C})$ skeletal of collagen backbone (proline, hydroxyproline)
+	1078-96	$\nu(\text{C-N})$ proteins
+	1114-71	$\nu(\text{C-N})$ (proteins); $\nu(\text{C-O})$ (carbohydrates); $\nu(\text{C-C})$ skeletal (lipids).
+	1155	$\beta$ -carotene ( $\nu(\text{C-C})$ ); $\nu(\text{C-C})/\nu(\text{C-N})$ proteins
+	1245	Amide III ( $\text{C-N/N-H}$ ), $\nu(\text{C-C})/\delta(\text{C-N})$ (lipids/phospholipids)
-	851	Tyr, Pro and polysaccharides
-	1003, 1030	Phe ring breathing mode (mainly collagen); Carotenoids, Phe
-	1155	$\nu(\text{C-N})$ , $\nu(\text{C-C})$ (proteins)
-	1447	$\delta(\text{CH}_2)$ (lipids and proteins), fatty acids
-	1688	Amide I ( $\nu(\text{C-O})$ ) – proteins. $\nu(\text{C-C})$ (lipids)

DF2	$\bar{\nu}/\text{cm}^{-1}$	Tentatively assigned Raman peaks
+	1078-96	$\nu(\text{C-N})$ proteins
+	1114-71	$\nu(\text{C-N})$ (proteins); $\nu(\text{C-O})$ (carbohydrates); $\nu(\text{C-C})$ skeletal (lipids).
+	1447	Protein/ Phospholipids
+	1310, 1355	Triglycerides (fatty acids), $\delta(\text{C-H})$ , $\delta(\text{CH}_2)$ $\delta(\text{CH}_2/\text{CH}_3)$ twisting, wagging, collagen, nucleic acids
+	1554, 1581	Carotenoid $\nu(\text{C-aC})$ / conjugated $\nu(\text{C-C})$ ; $\nu(\text{C-C})$ - porphyrins, Phe, hydroxyproline
-	1078-96	$\nu(\text{CN})$ proteins
-	1114-71	$\nu(\text{C-N})$ (proteins); $\nu(\text{C-O})$ (carbohydrates); $\nu(\text{C-C})$ skeletal (lipids).
-	1554, 1581	Carotenoid $\nu(\text{C-C})$ / conjugated $\nu(\text{CC})$ ; $\nu(\text{CC})$ - porphyrins, Phe, hydroxyproline

#### 4.3.8.4 Random Forest Classifiers & RBF-SVM

Due to the complexity within the data being easily undiscernible with PCA and DFA, a random forest test for classifiers (RF) was sought. This was shortly followed by a Gini-SVM using an RBF kernelisation.

The RF classifier was built in a 4-way analysis with a 1 vs all approach, then 2 vs rest, followed by 3 vs remaining, until it was seen as each vs each class membership. The data orientation, along with the wave numbers need to go forward for further testing are shown in Figure 4.14. The results are shown in Table 4.10 below. As can be seen, the strongest sensitivity and specificity taken together was 85% and 47%, respectively. This result was seen from a F012 vs F34 orientation; that is a low-grade disease vs high-grade.

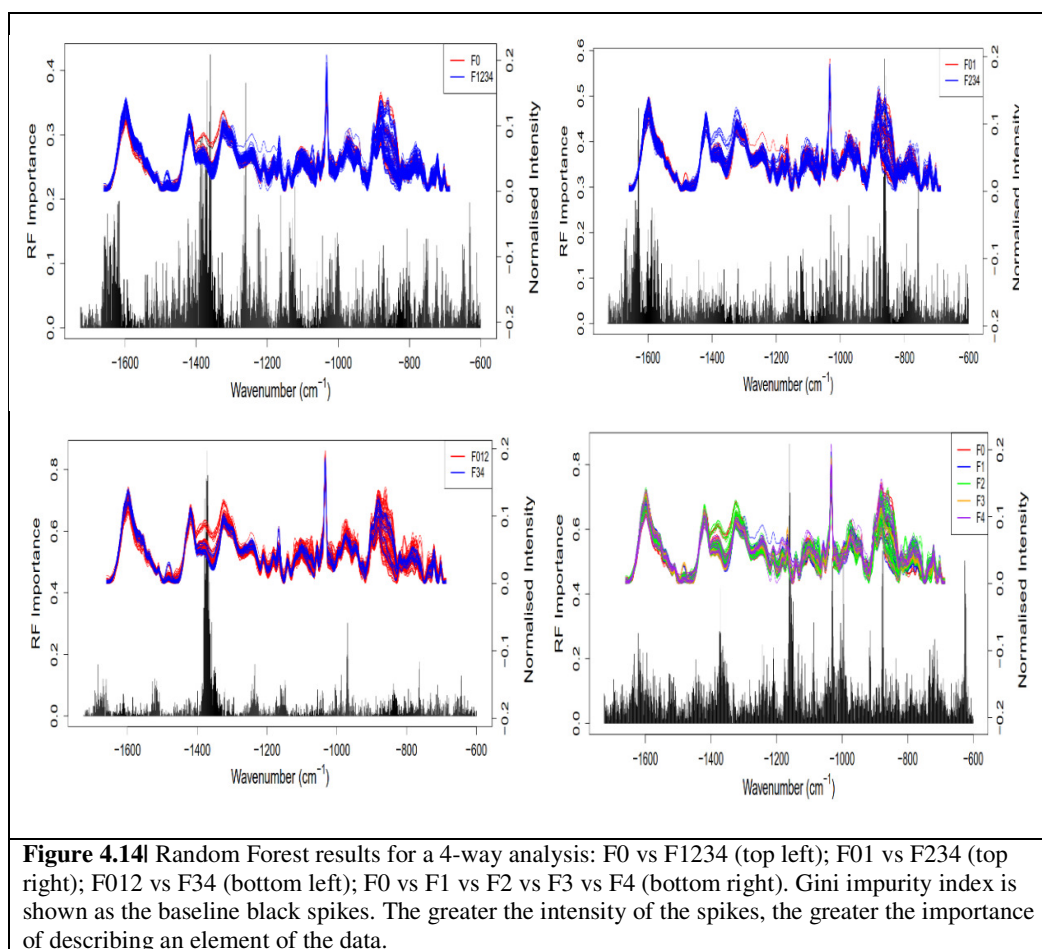


**Table 4.10** Random forest results: Sensitivities and specificities for fibrosis sera study on a patient and spectral level for all 4 stages of disease progression in four dataset orientations.

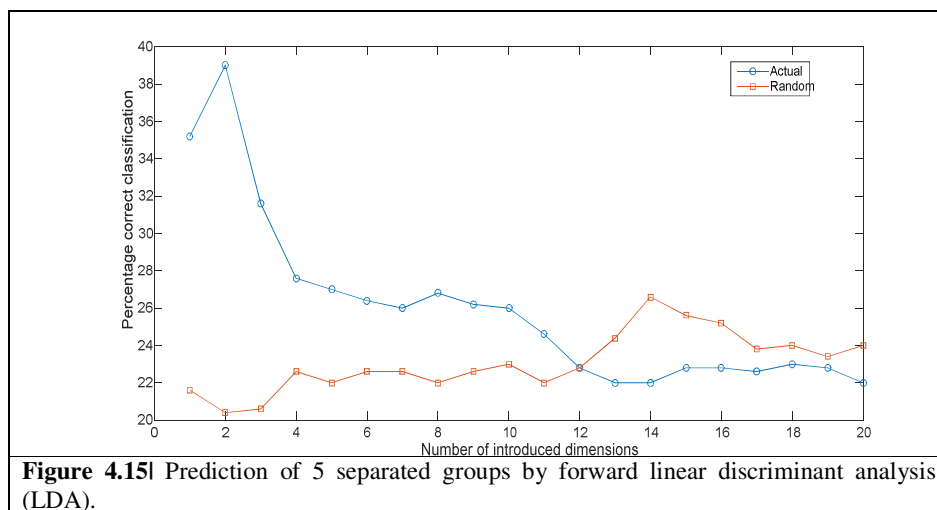
Datasets	RF	RF	SVM	SVM
	Sens %	Spec %	Sens %	Spec %
F0 vs F1234	36	75	42	75
F01 vs F234	43	59	32	53
F012 vs F34	85	47	79	53
F0 vs	24	73	18	70
F1 vs	10	80	13	78
F2 vs	5.8	49	7	53
F3 vs	3.8	93	2	90
F4	2	91	0	72

The RBF-SVM kernel analysis was done by taking the top Gini-impurity index for the top 30 wavenumbers as highlighted with RF. This information was then fed in to the SVM algorithm. An automatic 3-fold cross validation was performed with the training data to ascertain the best

values for test for cost and gamma parameters. These values were utilised to train the SVM in a one-vs rest mode firstly, followed by the same data pattern orientation used within RF classifiers. The arbitrary selected training dataset consisted of two-thirds of the patient data. The remaining data comprised the blind test set which was eventually projected in to the model. The SVM results are also shown in Table 4.10.

#### 4.3.8.5 Forward Linear Discriminant Analysis

The data were finally submitted to another chemometric algorithm; LDA. Firstly, a PLS-DA was attempted but the results did not work correctly, due to the possibility of limited useful information across the fibrosis groupings. Further to this, a forward LDA was attempted. This method attempts to introduce select wavenumbers (from Kruskal-Wallis testing) in to the algorithm, step-by-step, for discrimination. The second derivative averaged spectra proved to be the best choice for moving forward for this analysis. The data were divided in 38 test spectra and 5 validation steps. The validation spectra were randomly chosen in order to have the 5 classes represented. The test was repeated 100 times. Figure 4.15 shows the proportion of correctly classified samples as a function of the number of introduced variables. The results are compared with the one obtained with random allocation of the groups.



Here, it is possible to see that with two variables the proportion of correct classifications of the validation set is ~ 38%, whereas a random allocation gives only 20% correct classification.

From the same experiment, it is possible to look at the confusion matrices (still on the same 100 validation procedures). Figure 4.16 demonstrates the confusion matrices for the actual vs. randomised results. The rows indicate the real classes and the columns are the result of the test *i.e.*, on the ‘actual’ test result 39 observations among 100 of the group F0 were correctly

identified. The same kind of results from the random allocations ‘randomised’ of the samples. The difference in correct identification *i.e.*, 205 among 107 demonstrates that the results are not random.

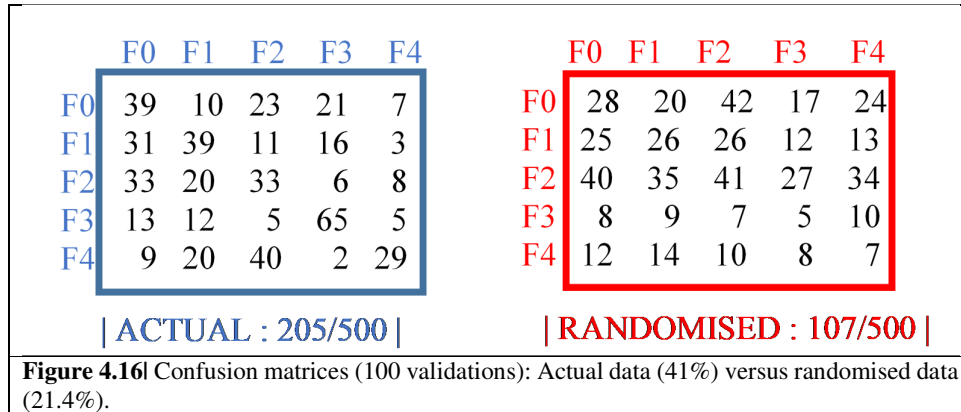
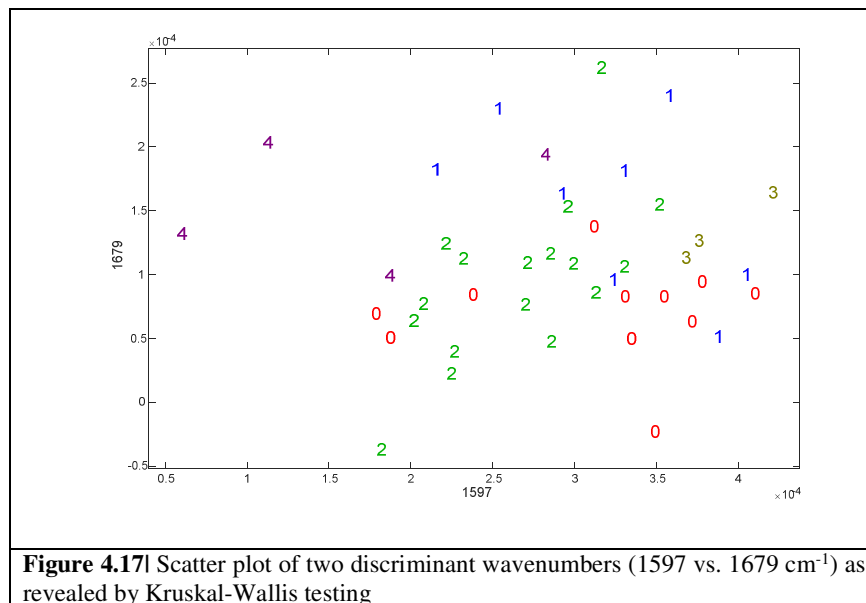
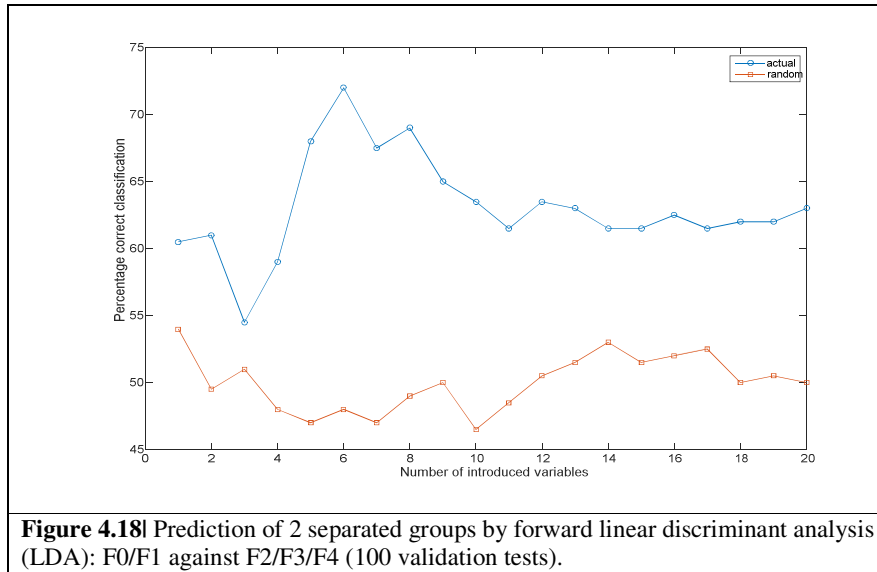


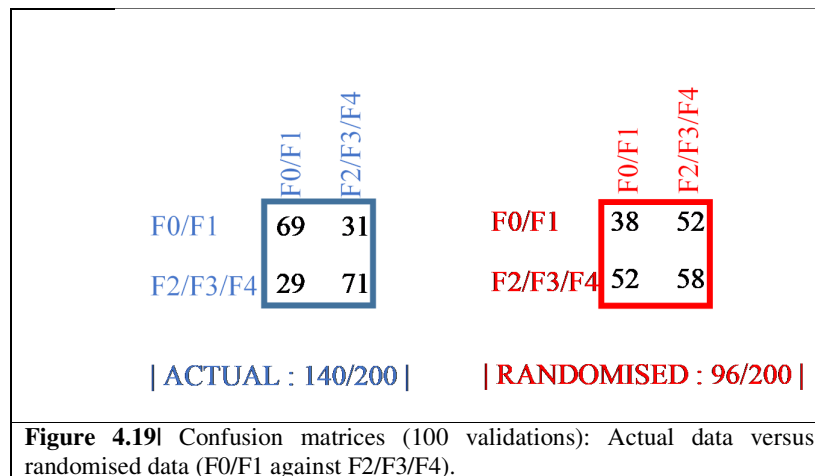
Figure 4.17 shows a scatter plot of two discriminating wavenumbers (1597 and 1679  $\text{cm}^{-1}$ ) [amide 1 band assignment]. It is possible to see a slight tendency here to separate the F4 class from the F0. F2 is rather in the middle.



When using the same procedure with only two groups, *i.e.*, F0/F1 separated from F2/F3/F4, here we achieve 6 best variables, giving more than 70% correct classification. When compared with the random test we see a 50% correct classification. This is shown with Figure 4.18.



From this, it is possible to look at the confusion matrices (still on the same 100 validation procedures). Figure 4.19 demonstrates the confusion matrices for the actual vs. randomised results. In the 'actual' result, 140/200 (70%) were correctly identified, whilst in the 'random' result 48% was seen.



Overall, forward LDA was able show minimal separation between some of the groups. It appears that the information contained within these data is increasingly difficult to find. The two groups noted above appeared to have given the best results possible amongst these data.

#### 4.4 CONCLUSION

In summary, this two-part study sought to analyse human pooled sera in both the dried and liquid phase with a suite of Raman spectroscopy methodologies, to assess preclinical variability. This was investigated by repetitive cycles of freezing and thawing, to ascertain whether there is an effect on the sample, and then to analyse the same samples for environmental drying effects to the serum profile. Combining spectroscopy with cluster analysis such as PCA and HCA, the outliers following the variance and quality assessments of the data were able to highlight for subsequent removal. Overall, PCA demonstrated very little changes within the freeze-thaw serum profile; any changes in the biplots were deemed to insignificant and no specific data pattern was seen. Overall, the cycles appear generally quite mixed, with no real logical clustering or that could be described experimentally *via* preclinical changes. The data acquired for both FTC and ED across different instruments did not show any effect on the spectra, even after freezing and thawing and drying a few times. It is concluded that such pre-analytical variation has very little effect on the data.

As it is routine clinical practice, to seldom work on non-fresh samples given the requirement of cryogenic storage, this preliminary study carried out IR spectroscopic assessment of potential variations owing to cycles of freeze-thaw and to the environmental ageing or drying of a sample of human pooled sera, exploring potential intra-sample differences of serum sample stability, without the fresh phase. Important factors, such as storage requirements, dilution aspects, and all key preparatory phases within a laboratory setting, need to be fully considered. Generally, for any analysis of variability, whether it is intra-, pre- or post-analytical, the bio-fluid of choice must confer the analytical process for error-tracking.

The latter diagnostic aspect of this study was the investigation of fibrosis serum samples using the developed liquid macro Raman spectroscopy methodology. The fibrosis patient sera were analysed using PCA, DFA. A three-way split of the fibrosis data revealed, a group split by patient spectra, by fibrosis disease stage and by a mix of fibrosis disease to represent low and high-grade disease characteristics. PCA was unable show differences.

The positive loadings seen on DF1 demonstrated a slight separation between healthy *vs.* cirrhotic patient spectra from F4 and F0. Such a result was attributed by peaks from 900-1300  $\text{cm}^{-1}$ , which encompasses the amino acids, amide III region. This study demonstrated the both DFA was able to show some biochemical differences between some the patient disease stages (healthy *vs.* advanced disease). Although a PC-DFA validation was tried, it did not add anything more to the data already.

Moving forward with this, the data were submitted to both RF classifiers and forward LDA for further interrogation. The highest sensitivity and specificity were a moderate result and so it is concluded that neither of the algorithms employed were able to provide a disease discrimination, overall.

In conclusion, the results of this study have shown that combining advanced multivariate analysis as classification tools, is sometimes not enough to find discrimination if the disease course is highly complex and analysed in liquid phase. Although, freeze, thaw and drying appear to have negligible effects on the data outcome, it is still important to not over-process samples and caution is needed to limit the physical effects to the samples, as with any biological sample, it could be susceptible to degradation eventually. The present results have clearly shown that preclinical variation can be minimised with good laboratory procedures, not-exceeding high amounts of repetitive freeze-thaw, and that such possible variances play no significant role in the diagnostic capability of Raman spectroscopy which is a disease classification/screening tool when employed with various MVA strategies. Moreover, it is based solely on the disease complexity overall.

## **| CHAPTER 5 |**

**LIQUID SERUM RAMAN  
SPECTROSCOPY :  
SCREENING OF  
HEPATOCELLULAR  
CARCINOMA FROM  
CIRRHOTIC PATIENTS**

---

## **| CHAPITRE V |**

**ANALYSE MACRO-RAMAN  
DU SERUM LIQUIDE :  
DIAGNOSTIC  
DE PATIENTS  
CIRRHOTIQUES AVEC ET  
SANS CHC DE PATIENT**

## V.1 RÉSUMÉ

Ce chapitre concerne l'approche macro-Raman développée précédemment pour l'analyse du sérum liquide, appliquée à l'étude des patients cirrhotiques atteints ou non d'un cancer primitif du foie, le cancer hépatocellulaire (CHC) pour évaluer les capacités de dépistage de la maladie. L'analyse directe du sérum liquide permet de contourner le temps de séchage et surtout l'hétérogénéité chimique observée avec le phénomène de « coffee-ring ». Une séparation spatiale de molécules à haut et faible poids moléculaires apparaît dans la goutte de sérum lorsqu'elle est laissée à sécher, régie par l'effet Vroman [207], et fournit par la suite un paramètre physique supplémentaire dans la prise des données spectrales.

## V.2 CONCLUSION

L'analyse du sérum par spectroscopie présente plusieurs avantages : elle est non invasive, facilement réalisable à faible coût et offre des capacités de surveillance, bénéfique à long terme pour le patient. En raison de sa nature même en tant que flux complexe de produits sanguins extrêmement intéressants, il peut être un bon reflet du milieu interne du corps avec des lectures biochimiques ou des « empreintes digitales » lors de l'exploitation spectroscopique. En cas de maladies telles que la fibrose, la cirrhose et l'invasion tumorale, l'analyse du sang donne un compte rendu du microenvironnement, qui héberge des biomarqueurs de la maladie. Ici, cette étude a utilisé une nouvelle approche macro-Raman pour interroger le profil sérique des échantillons de sérum de patients cirrhotiques avec ou sans CHC. L'approche est effectuée en phase liquide du sérum, afin de développer un outil spectroscopique de diagnostic / dépistage pour le bien-être du patient. La spectroscopie Raman peut fournir une empreinte spectrale de toutes les molécules présentes dans le sérum. À partir de là, plusieurs milliers de variables spectrales ont ensuite été soumises à une analyse statistique multivariée par le biais d'algorithmes d'apprentissage automatisés afin de déterminer les principales caractéristiques des données. Suivant une procédure interne de prétraitement, des algorithmes de classification tels que l'ACP et l'HCA ont été utilisés dans un premier temps pour cibler des valeurs aberrantes au sein des données. Lors de l'avancement des spectres du patient viable, l'ACP n'a montré que les différences entre les patients F0 en bonne santé et les patients malades (cancer + cirrhose). Dans l'ensemble, aucune différence significative n'est observée lors de la comparaison d'un ensemble de données binaires (cancer vs cirrhose) *via* ACP. La DFA montre des informations similaires pour la classification binaire, mais avec une multiclass (toutes les données), une séparation plus grande entre maladie et normale a été exprimée. En revanche, DF1 montre une bonne discrimination entre le cancer et la normale ( $p < 0.001$ ) et de manière similaire, DF2 a montré certaines différences entre le cancer et la cirrhose *via* le test post-hoc de Tukey. La CP-DFA démontre une sensibilité et une spécificité de 100% (ellipses de confiance à 99%) pour les

maladies par rapport à la normale, mais une classification médiocre pour le cancer de la cirrhose. Enfin, les méthodes RF et Gini-SVM présentent des résultats modérément bons pour cette classification multiclassée dans les groupes de patients (55%, 62% (cancer), 54%, 55% (cirrhose) et 99%, 100% (F0).

En résumé, il est très difficile cliniquement et biologiquement de faire la distinction entre le CHC et la cirrhose quand environ 80% de tous les cas de cirrhoses se transforment en CHC. Ceci est également montré dans les résultats de cette étude, des différences distinctes dans le profil sérique sont observables par spectroscopie Raman du sérum liquide. Cependant, discerner le cancer d'une population malade atteinte d'une cirrhose est révélé difficile. Ici, cette étude a démontré la possibilité de l'utilisation de la spectroscopie macro-Raman sur des échantillons liquides sans l'utilisation d'un module de microscope à des fins de dépistage de maladies.

## 5.1 INTRODUCTION

Primary liver cell cancer or hepatocellular carcinoma (HCC) accounts for 65,000 mortalities per annum and it is the third leading cause of cancer deaths worldwide. After colorectal cancer, it is the second most prevalent digestive cancer with over two-thirds of patients being male [84-85]. In cases of hepatic cirrhosis, it is the biggest cause of mortality and it is developed through stages from chronic hepatitis. Under normal physiological condition, the liver is capable of self-regeneration. However, through cycles of repair and injury, the liver becomes inflamed and scarred due to a build-up of regenerative nodules (colonies of cells), which are surrounded by fibrotic tissue and excess collagen. Fibrosis or scarring of the liver tissue precedes end-stage/irreversible liver damage (cirrhosis) [86]. HCC aetiology includes, viral inflammation from hepatitis B (HBV) and C (HCV), or aflatoxin B1 [87] (a fungal epitope), abuse of cigarette smoke and heavy alcohol consumption [86-87]. Moreover, the main problem faced by patients today, is understanding the interface of when one disease stops and when another one is initiated in complex disease cases with cirrhosis. Also, it is difficult to determine when the cirrhosis-HCC margin begins, and ends is problematic. Whilst the biggest cause of HCC is metastases, persons with cirrhosis have an increased risk of developing the cancer, as there is a strong positive relationship with fibrotic stage. Moreover, it is said that ~80% of cirrhotic livers will transform [88-89].

Hepato-carcinogenesis is a complex process and overall knowledge remains nebulous. However, it is known to span ~10 to 30 years [90-91] with primary initiation of external stimuli precluding genetic changes within the liver cells. Eventually, it induces cell suicide and up-

regulation of the mitotic pathway with the continuation of fibrosis and cirrhosis [92]. This complex disease pathway is a multistep process, starting with stimuli-induced focal hyperplasia. Such stimulus could be viral (HBV or HCV), alcohol or non-alcoholic steatosis hepatitis (NASH) including others. The process graduates from low-grade to high-grade nodule dysplasia [92-93]. The result is moderately differentiated-HCC, which has metastatic tendencies. Other genetic factors are attributed to an iron-overloading disease called haemochromatosis, Wilson's disease [89],  $\alpha$ -1-antitrypsin deficiency, glycogen storage disease and various porphyrias (rare metabolic abnormality of haemoglobin) [90].

To date, there has been a cohort of clinical guidelines that all advocate surveillance programs in cases of patients with cirrhosis, for positive remedial curative treatments at early stages of disease onset [98, 203]. Technological advances of physical methods of employing light at the interface of medicine is not uncommon, as such clinical guidelines advocate ultrasound (US) screening of cirrhotic patients at 6-month intervals. This is due to tumour doubling time of 6-12 months, plus blood biochemistry assays to detect the changes in serological biomarkers, such as  $\alpha$ -faeto-protein (AFP) and des- $\gamma$ -carboxy-prothrombin (DCP), and others *i.e.*, glypican-3/ $\alpha$ -1-fucosidase. However, all are not without limitations as demonstrated by a 14 year-long study monitoring AFP levels in cases of liver damage [204]. In the study the authors found that ~ 90% of biomarker elevations were not associated with cancer, and only ~15% of patients with elevated AFP were seen over the full duration [204]. Additionally, the DCP protein or abnormal levels owed to a defect in the posttranslational carboxylation of the prothrombin precursor in malignant cells, can confer some utility as a marker of advanced HCC [99]. Although, given the known downfall, it is still widely used in Japan for diagnosis and surveillance. Additionally, there is some knowledge to suggest the combination of the two biomarkers could provide further evidence for such screening but the sensitivities and specificities for such testing, remain low, or that the testing populations are regarded as too small/insignificant to warrant incorporation to the tumour-node-metastases (TNM) staging system. This is the case with other HCC potential biomarkers [205].

Above and beyond serum biomarkers, radiographic regimes, such as right upper quadrant (RUQ) ultrasound assessment have been reported to have a sensitivity of 65-80% and specificity of 87-94% and is currently one of the strongest screening regimes available for cirrhotic and HCC surveillance [94-95, 206]. Nevertheless, the assessment is still operator-dependant and does suffer difficulties with interpretation in persons who are obese or who have underlying nodular cirrhosis. Moreover, whilst computed tomography (CT) and liver-magnetic resonance imaging (L-MRI) can be employed, there is still no current evidence that routine screening with

such assessments are viable and hence, they are still absent from recommended guidelines. That said, they can be used to confirm tumoural nodes greater than 1 cm post-ultrasound. In consideration of the above, it remains that there are no set biomarkers for HCC detection from cirrhosis. According to the most up to-date clinical practice guidelines, accurate tumour biomarkers for early detection still need to be developed [95, 98, 206]. Given that current routine procedures are not fully adequate [6], other efforts have started to emerge within the bio-spectroscopy field, specifically.

Biofluids are an attractive medium for disease diagnostics due to the ease of accessibility and routine analysis of blood biochemistry, which means bio-fluid banks are well resourced [132]. Bio-fluidic vibrational spectroscopy is emerging as a potential candidate for disease screening for point-of-care (POC) diagnostics. Raman spectroscopy (RS) is an analytical technique based on the change of wavelength of light that occurs when a light beam interacts with certain molecules. Fundamentally, RS has been exploited for structural and biochemical information for diseased tissues, cells and bio-fluids within biomedicine to date. RS is rapid, non-destructive, label-free and amenable to any state analysis, due to the very minimal effects from water or aqueous environments. Moreover, liquid analysis is achievable without the drying stage of bio-fluids on to mid-IR transparent substrates, such as  $\text{CaF}_2$ . Hence, the well-known coffee-ring phenomena are circumvented entirely. An early study demonstrated the utility for serum Raman micro-spectroscopy for HCC diagnosis from cirrhotic patients [137]. This study employed drop coating dried deposition (DCDD) of serum combined with support vector machine – leave-one-out cross validation (SVM-LOOCV), for global biochemical disease fingerprinting, demonstrating a diagnostic accuracy of 85-92% [137]. However, in a bid to develop the diagnostic potential, here this study proposes a macro-Raman liquid analysis directly on the wet serum. This negates drying times and most importantly the chemical heterogeneity seen with the coffee-ring phenomena. A spatial separation of dense and non-dense molecules appears across the serum drop when left to dry as governed by the Vroman effect [207], and subsequently provides an additional physical effect in spectroscopic data management.

In this chapter of the study, a RS approach was developed for wet analysis at the macro scale. This proof-of-concept approach was used to analyse patients of cirrhosis with and without primary liver cancer (HCC), and compared to a normal dataset, for disease screening capabilities of Raman spectroscopy.

## 5.2 EXPERIMENTAL METHODOLOGY (For details, see 2.4.2)

### 5.2.1 Serum Biobank

This work was part of the Pro-Spec study, which aimed to identify biomarkers of HCC in blood samples taken from cirrhotic patients. The Pro-Spec study was an ancillary project to the CiRCE (Cirrhose et Risque de Cancer dans le Grand-Est) study; an 8-year ongoing case-control assignment in the North East region of France; six centres inclusive of Besancon, Dijon, Metz, Nancy, Reims and Strasbourg. Cirrhotic and primary liver carcinoma serum samples were collected from all centres for the analysis of factors pertaining to hepato-carcinogenesis in cirrhotic circumstances. Due to subsequent findings of an incorrect study protocol from sample inclusion, one centre was fully omitted from spectroscopic analysis. All patients gave consent in writing for the inclusion of their samples to the study. For each patient, the following clinic-biological data were collected, and they included age, sex, cause of cirrhosis, staging of cirrhosis, serum AFP measurement, and staging of the tumour in the case of HCC; (see Table 5.1 for pertinent information). The study was approved by the Comité de Protection des Personnes Est; under the agreement: 2008/09 and by the Agence Française de Sécurité Sanitaire des Produits de Santé (*agreement no: 2008-A00023-52*).

Cirrhotic patients were assessed for characteristics of HCC at inclusion *via* US and/or CT and/or L-MRI, plus clinical biochemistry, *i.e.*, AFP levels  $< 100 \text{ ng mL}^{-1}$  and subjected to routine follow-up regimes of up to 1 year revealed none of the cirrhotic patients were suspected with HCC. This was achieved with 6 monthly right upper quadrant US (RUQ-US) and checked levels of AFP throughout. Clinical diagnosis of cirrhosis was made either by histology of a liver biopsy or by a combination of clinic-biological signs of hepatic portal vein hypertension (PVH), and/or endoscopy of PVH or imaging of cirrhosis. Confirmed diagnosis of HCC by the pathologists relied on the EASL guidelines [15], and patients younger than 35 years were not included, nor were patients with HIV infection, extrahepatic carcinoma and unconsented patients (e.g. not been able to give written consent).

### 5.2.2 Sample Processing

For closer scrutiny from the large cohort of 817 patients, clinical matching of age, sex, Child-Pugh scores, and cause/severity was carried out by a senior medical consultant (see table 5.1). This revealed matched pairs of  $n=130$  for cirrhotic and cancerous patients. The removal of non-matched cases was done to relieve the burden of confounding factors at the analysis stage.

All samples came from 24-hour fast-orientated patients and immediately post-venepuncture, the blood samples were processed, and the serum was stored cryogenically at  $-80^{\circ}\text{C}$ . Serum samples

were collected from 2 sets of patients: cirrhotic patients without HCC (n=127) and cirrhotic patients with HCC (n=120), irrespective of the liver disease cause.

The serum samples were blind sampled by the spectroscopist. The samples were stored in a central biobank at the bio-pathology department of Reims Hospital (CHU). A secondary non-diseased control group was added for testing. These serum samples were included for analysis due to clinical inclusion by a chief gastro-hepatologist at Reims CHU. Samples were thawed at room temperature in a controlled environment with recorded humidity. 50  $\mu$ L of sera per patient were transferred in to a quartz cuvette for analysis. No serum dilution was necessary.

**Table 5.11** Patient sample demographics (cirrhotic, cancerous and normal), including disease stage (METAVIR F), number of patients, age range/mean ages and gender plus clinic-biological characteristics for diseased patients.

	Patients	Spectra	Age		M; F	BMI	HCV+	AFP	OH+
			Range/Mean/ yr	Ave		%	Ave	%	
CO	88	440	43.4-89.4 / 61.12		85;13	27.7	17	5.6	72.2
1	19		48.3-75 /	59.5	16; 3	29.4	-	-	-
2	10		47.4-71 /	58.3	8; 2	26.7	-	-	-
3	19		43.4-80.4 /	60.6	17; 2	26.4	-	-	-
4	31		49.7-89.4 /	63.9	25; 6	27.5	-	-	-
5	9		53.7-72.3 /	63.3	9; 0	28.4	-	-	-
HCC	103	515	45.4-82.5 / 62.86		97;7	28.7	14.7	1985	84.3
1	45		45.4-80 /	62.1	45; 0	29.4	-	-	-
2	6		55.6-70.3 /	62.9	4; 2	26.7	-	-	-
3	21		50.1-80.5 /	63.2	18; 3	26.4	-	-	-
4	24		50.1-82.5 /	63.7	23; 1	27.5	-	-	-
5	8		49.1-81.6 /	62.4	7; 1	28.4	-	-	-
F0	10	49	18-57 /	39.58	5; 7	-	-	-	-

1, 2, 3, 4, 5 – centres included; CO – Cirrhotic only cases; HCC – Cancer cases; F0 (non-fibrosis cases); Ave -average; information for BMI, HCV+, AFP average (measured in ng/mL) and OH+ is only available for diseased case

### 5.2.3 Macro Liquid Raman Spectroscopy

Single point Raman spectra were recorded with a LabRAM HR 300 micro-spectrometer (Horiba Jobin Yvon SAS, Villeneuve D'Ascq, France) re-aligned to bypass the microscope objective. A 40 mm macro adaptor was coupled to the spectrometer for the 3 W NIR 785 nm diode excitation laser (Toptica Photonics, Munich, Germany) to irradiate the sample (contained within the quartz cuvette). The Raman signal was collected in 180° backscatter geometry. The laser power on the sample was ~75 mW and the beam size was 3 mm. An Andor Tech CCD detector (1024 x 256 pixels, Andor Tech., Belfast, UK) was used to capture the signal. A holographic 600 lines/mm diffraction grating was employed with a confocal hole of 1000  $\mu$ m and slit size 150  $\mu$ m. The sample was acquired for 120 s with 5 integrations over the 1800-500  $\text{cm}^{-1}$  wavenumber range, with a spectral resolution of 3  $\text{cm}^{-1}$ . Prior to spectral collection, the spectrometer was calibrated

with a silicon wafer and instrument dark noise and detector linearity was checked with an in house-regime (see Figure 2.12 (2.31)).

### 5.2.4 Raman Spectral Quality Testing

Prior to pre-processing, a Raman spectral quality test (QT) was used to evaluate the SNR of the datasets on MATLAB software (version R2015a, The MathWorks, Inc., USA). In brief, two spectral regions ( $\sim 990\text{-}1010\text{ cm}^{-1}$  and  $1720\text{-}1780\text{ cm}^{-1}$ ) were chosen to represent the spectral aspects for signal (S) and noise (N). Spectra passed the QT if it exceeded a ratio value of 30, which is used in biological spectra and is line with previous studies [137]. Refer to 2.3.1 for details of the Raman quality assessments.

### 5.2.5 Spectral Pre-processing and Chemometrics

All spectra passing the standard quality and variance assessments were pre-processed in MATLAB for exploiting the chemical information and reducing the physical interferences. An outline of the spectral pre-processing steps could be seen below in Figure 5.1. All data were normalised using the vector scaling method (vector normalisation): mean-centred spectra were divided by the square root of the sum of the mean-centred intensities squared, meaning that the sum of all the intensity values squared is equal to 1. All data were then completed with zero offset, the value of which is chosen so that one spectrum point will equal to zero, often the ends of the spectrum, prior to chemometric assessment. For advanced chemometrics such as Random Forest and SVM, the data were implemented on R-Studio.

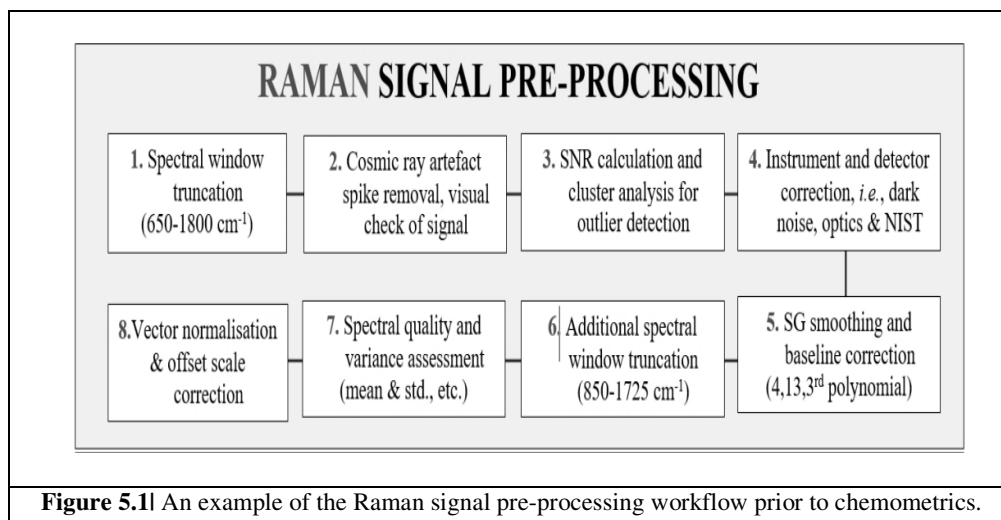


**Figure 5.1|** An example of the Raman signal pre-processing workflow prior to chemometrics.

### **5.2.6 MVA Workflow**

All datasets were then submitted to cluster analyses *via* HCA and PCA in the first instance for outlier detection and sample removal prior to more advanced chemometric assessments.

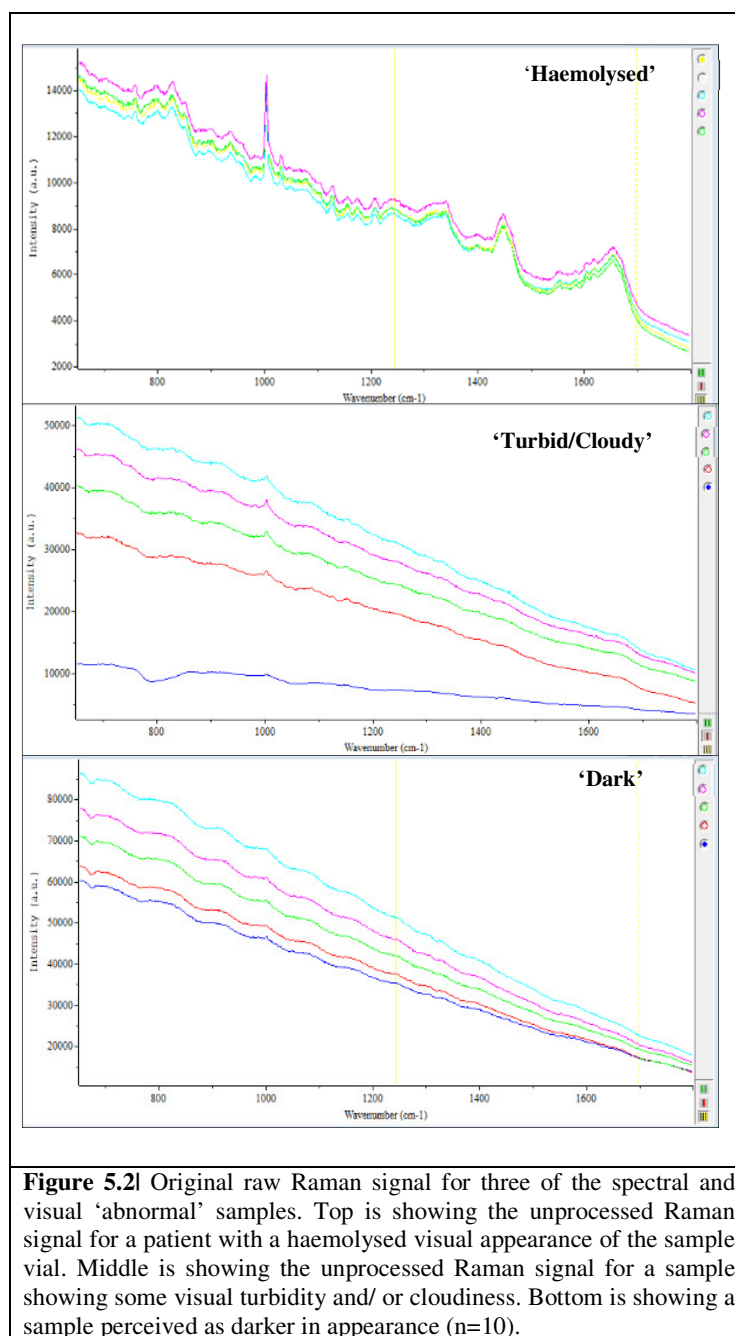
PCA was developed as an invaluable unsupervised dimension reduction and data transformation technique that was used as the starting point in discerning spectroscopic data. HCA allowed the observer to see similarities and differences amongst the data based on a dendrogram approach (full explanations of all MVA techniques are given in Chapter 2).

DFA was used to ascertain clusters in to groups following cluster analysis. Following this, more advanced machine learning algorithms were employed to find classification of the data groups, such as random forest classifiers (RF) and Gini-SVM.

## **5.3 RESULTS & DISCUSSION**

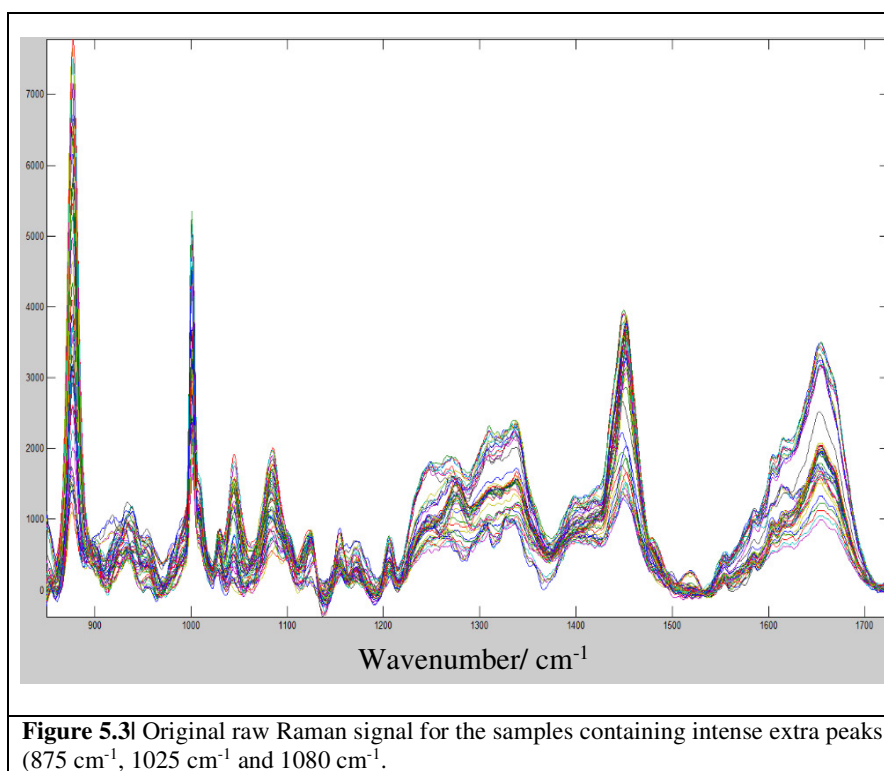
### **5.3.1 Spectral Quality & Variance Study**

At the point of spectral collection and subsequent pre-processing, physical and spectral anomalies were observed. Noted firstly at spectroscopic collection, there were some noticeable differences in the collected spectra (*in situ*) (Figure 5.2) and some visual differences when observing the samples in the cuvette prior to Raman interrogation (Figure 5.4). Some samples were cloudier and/ or darker in appearance to visual examination (by eye of the analyst) or had some aspect of haemolysis (red in colour). This immediately manifested in the real-time spectra, meaning some samples presented an aberrant baseline, some were recorded with extraneous spikes and sharp peaks and some were intractable signal-wise. These are shown in both Figure 5.2 and Figure 5.3.



Following these instances, repeat Raman collection was carried out to ensure good robust data collection. Such problematic samples were subsequently compared to the serum biochemical profile (*i.e.*, the very small standard deviation patients), and the clinic-biological characteristics of each patient. It was decided that such samples would be removed from the dataset for further analysis. Figure 5.3 shows the normalised and pre-processed spectra for the extra peak specific spectra/patients. As one can see there appears to be three significant intense peaks ( $875\text{ cm}^{-1}$ ,

1025  $\text{cm}^{-1}$  and 1080  $\text{cm}^{-1}$ ), which were unexpected (compared to the average signal of the data). Further investigations were carried out to examine and change different aspects of the experimentation setup, such as grating choice (three different gratings were tested to see if the same signal resulted). All gratings (600, 800 and 1950 lines  $\text{mm}^{-1}$ ) showed the same intense extra peaks. Secondly, the cuvette was changed as well as the depth of penetration for the laser light hitting the sample, this again showed the same signal. Lastly, to ensure the cuvette was not contaminated, a water test signal was carried out. This confirmed that only the signal of the water/cuvette was seen. Observing the clinic-biological data for the patients that presented these aberrant (compared to the bioserum profile – as seen across the general peak shape amongst all the sample) peaks, it was decided that these patients seemed to show a higher lipid/cholesterol/triglyceride reading (data not shown), so it was inconclusive whether this subset of patients properly fasted prior to giving their sample; so, they were removed from further testing. Figure 5.4 demonstrates this sample-patient data exclusion process in a schematic with visual evidence of each vial and justification for exclusion. This secondary spectral quality step was required as visual assessment of each individual sample.



Patient's signal showed some inconsistencies that did not align well with the remaining signal (when visibly observing the live spectrum on the instrumentation /computer screen). As

demonstrated below (see Figure 5.4), four criteria were chosen based on both visual checks of the sample vial, *i.e.*, apparent haemolysis (n=3), turbidity owed to a cloudy appearance of some sample vials (n=9), a darkened appearance (n=8) and the inclusion of extra bands in some patients (n=12). Figure 5.5 and figure 5.6 demonstrate some preliminary cluster analyses (HCA and PCA) which revealed the samples to be outliers.

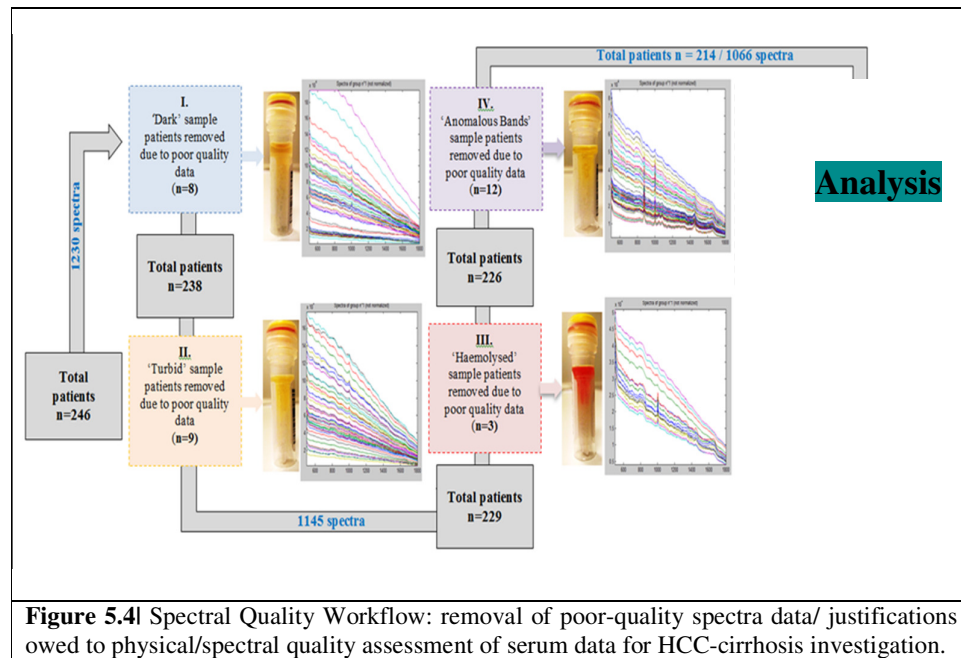


**Figure 5.4|** Spectral Quality Workflow: removal of poor-quality spectra data/ justifications owed to physical/spectral quality assessment of serum data for HCC-cirrhosis investigation.

For explorative outlier detection, two sets of cluster analyses were carried out. The first (Figure 5.5) shows all spectra plotted, but with highlighted poor-quality spectral groups (inclusive of patients with the so-called samples seen with aberrant peak). As can be seen here, the group of patients with the extra peak morphology appears to find clustering separate to that of the remainder of the patient spectra. Therefore, this result would significantly impact later MVA analyses. The remaining poor-quality spectral groups were then highlighted to show physical/chemical differences. The result is shown in Figure 5.5 (compared to all spectral groups) and Figure 5.6, which demonstrates the same result without the inclusion of the 'good quality spectra'.

Secondly, HCA cluster analysis was carried out to ascertain the similarities/differences solely between the groups of poor-quality spectra/patients. As can be seen from the dendrogram on Figure 5.6, it appears that samples given the assignment of 'turbid' and 'dark' appear to have similarities to one another (smallest branches on the dendrogram). These in turn are similar in characteristics to the 'haemolysed' patients. The most different dendrograms are the 'extra peak'

samples which are shown as the longest branch. Additionally, these extra three peaks also appear clearly in the loadings of the PCA and the plotted pre-processed normalised spectra (highlighted in grey on Figure 5.6)

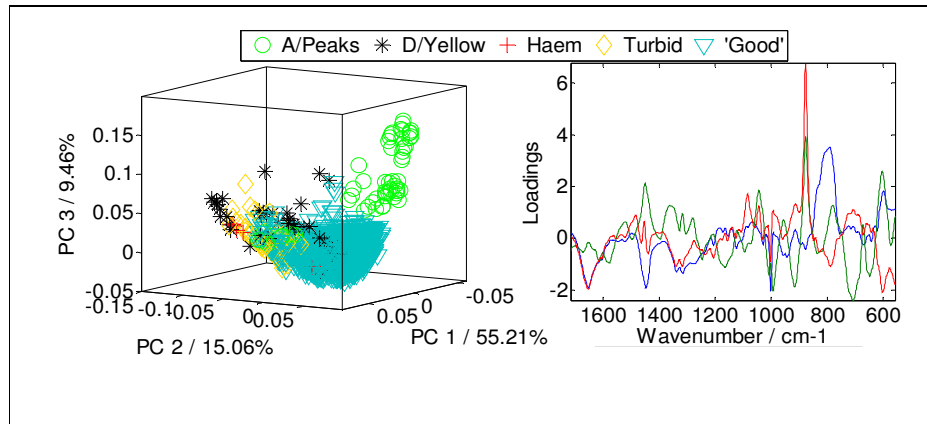


**Figure 5.5** Good quality spectra vs. poor quality spectra: Cluster analysis via PCA 3D plot (top) showing all spectra with highlighted poor-quality spectra inclusive of aberrant peak patients. Loadings are shown the right of each plot. PC1, PC2 and PC3 all explain ~80% of the data.

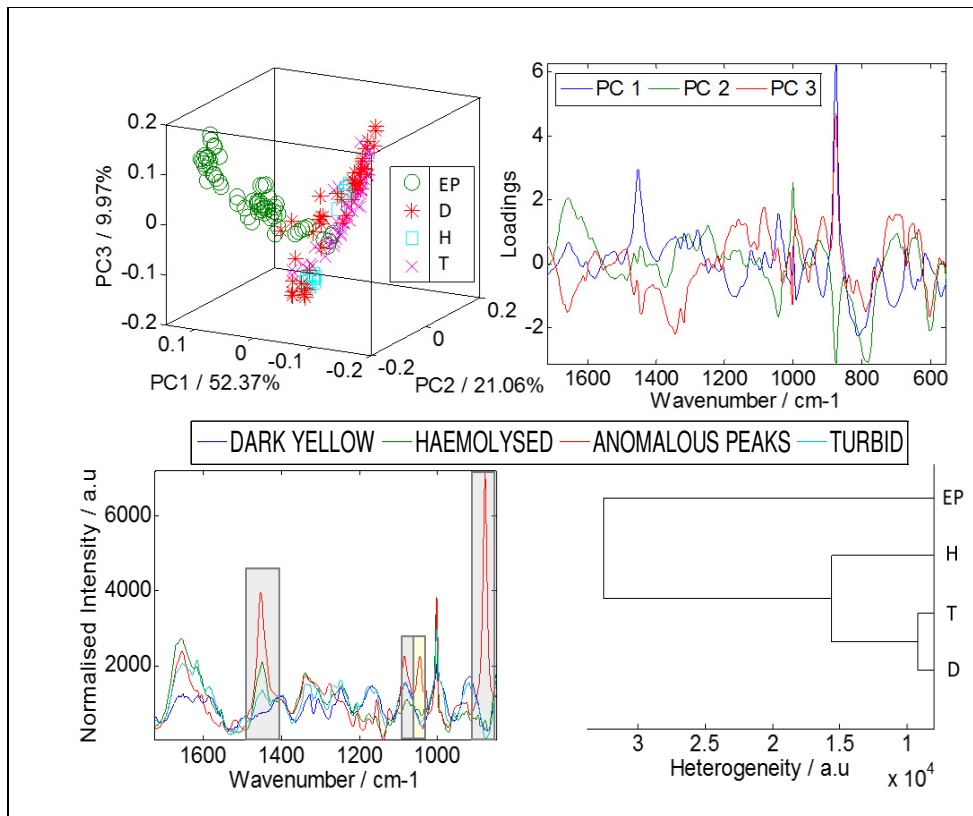
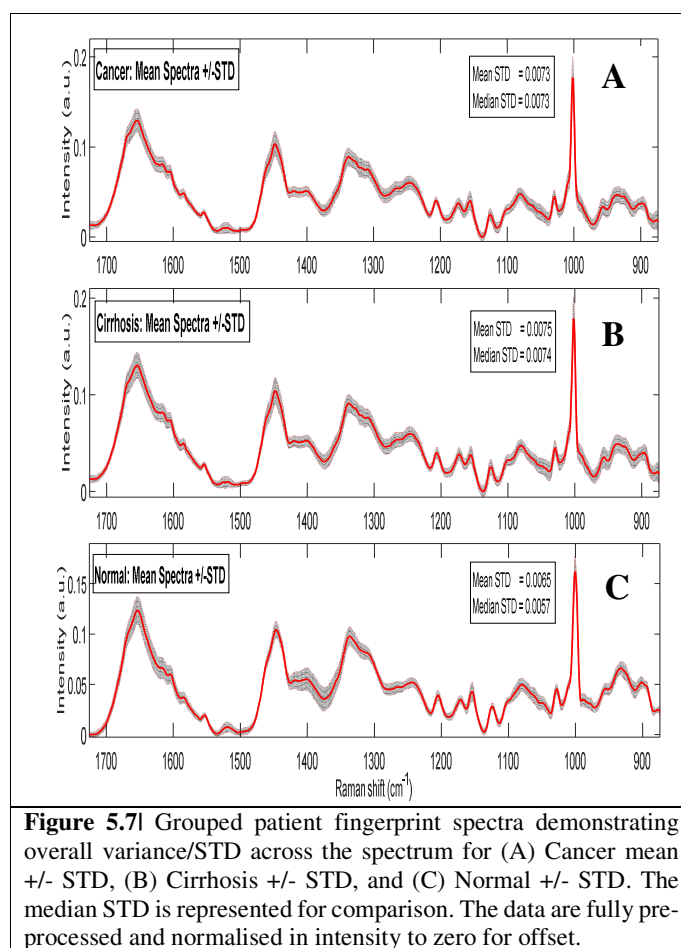


**Figure 5.6** Diagrams showing further cluster analyses via PCA and HCA for outlier detection of spectral abnormal spectra to confirming the differences and similarities of the poor-quality spectral group. PC1, PC2 and PC3 all explain ~81% of the data. Sample nomenclature: EP – ‘extraneous peaks’; H – ‘haemolysed’; T turbid/cloudy in appearance; D – dark in appearance.

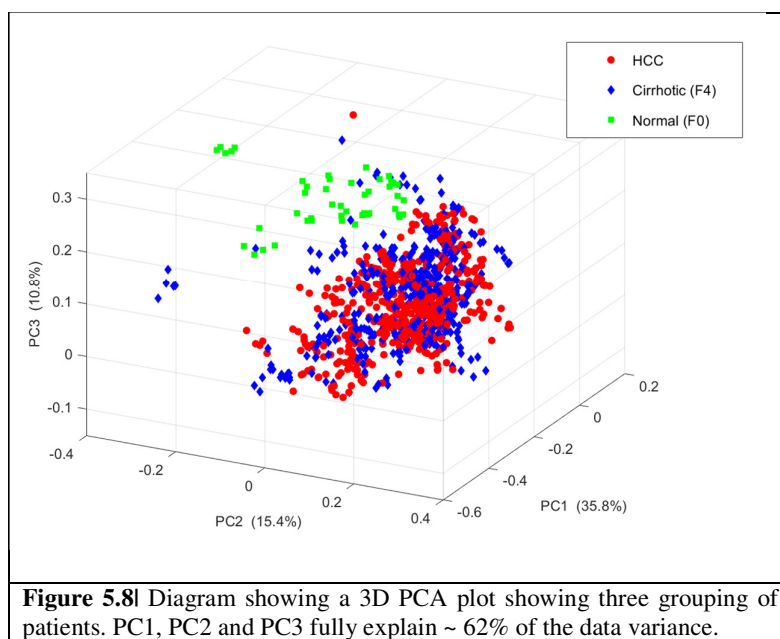
Figure 5.7 shows the total spectra (mean data) for the inclusion of further analyses, following the quality assessments. As can be seen there are three separate signals. The top signal represents the HCC patients mean spectra, the middle is the cirrhosis only patients (diseased control) and the bottom is the healthy control (F0 patients). The latter group had the smallest variance amongst the spectral groups (mean STD = 0.0065; median STD = 0.0057), followed by the other groups being on par (0.0073-0.0075). The grey cloud around the red mean signals is the STD values around the mean.



### 5.3.2 Explorative PCA of Cirrhotic, HCC and F0 Patients

Following variance analyses, the patient data was submitted for unsupervised explorative clustering by PCA. The pre-processed non-derivative fingerprint Raman spectrum was used for further MVA. Analysis of the derivatised spectra was attempted also but presented no

observable differences at this stage, nor did it add any extra value to the data. Figure 5.8 shows the PCA result by a three-way analysis in 3D space. The results from the three patient datasets (HCC, Cirrhotic and FO) are clearly visible on the plot as represented by the colours (red, blue and green). PCA was able to reveal two clusters (diseased vs. healthy), which is seen as the green (healthy patients) separating from the red/blue mixture (cirrhosis/cancer). Together, the three PCs explained ~62% of the data variance. PC loadings are shown in Figure 5.9. The negative loadings on PC2 finds the separation between healthy and diseased (1365  $\text{cm}^{-1}$ , 1348  $\text{cm}^{-1}$ , 1041  $\text{cm}^{-1}$ , and 956  $\text{cm}^{-1}$ ). The following can be tentatively assigned to a mix of the amino acid, tryptophan, adenine, plus proteins and phospholipids [209]. The tentatively assigned component loadings are assigned to the serum bio-profile (see Table 5.2)



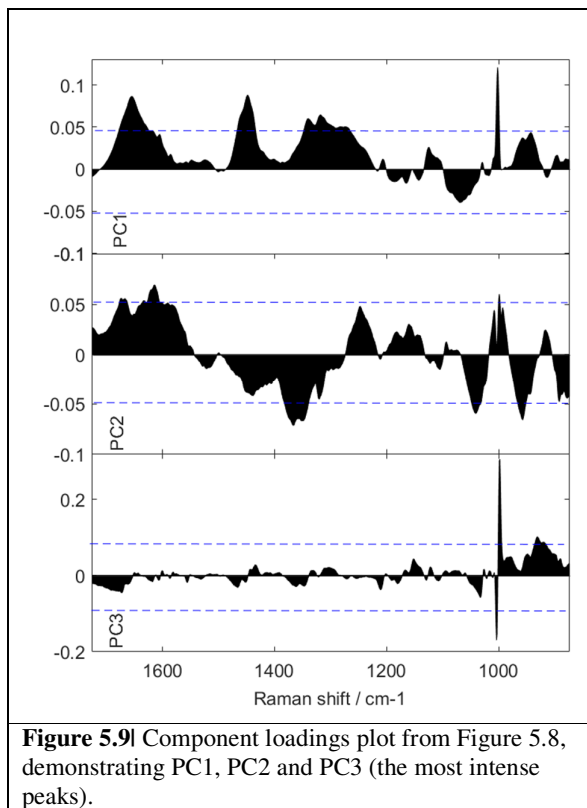


**Figure 5.9** Component loadings plot from Figure 5.8, demonstrating PC1, PC2 and PC3 (the most intense peaks).

The Raman band at  $1633\text{ cm}^{-1}$  can be attributed to antisymmetric bending of  $-\text{CH}_3$  which is assigned to lipids presents in both healthy and diseased serum. The predominant bands throughout the loadings (Figure 5.9) are observed at  $1170\text{ cm}^{-1}$  and  $1344\text{ cm}^{-1}$  are due to  $\nu(\text{C}-\text{O}-\text{C})$  antisymmetric stretching and  $\delta(\text{CH}_2)$  wagging, respectively, found in lipids and phospholipids [210]. During hepatitis, such an occurrence is associated to activated enzymes by the hepatic destruction processes [57, 211-212]. This process of alterations can occur in the concentration of the various enzymes, proteins, lipids and phospholipids that are found in blood, or here in the serum. The bands that occur at  $1633\text{ cm}^{-1}$  and  $1041\text{ cm}^{-1}$  could be due in part to quartz cuvette Raman scattering, which was used to hold the blood serum samples.

**Table 5.2** PCA: Tentatively assigned serum loadings from PC1, PC2 and PC3 (Figure 5.7) taken from the serum investigation for HCC-cirrhosis- normal patients [132, 209-210, 213]

$\tilde{\nu}/\text{cm}^{-1}$	Tentatively assigned Raman peaks	PC1	PC2	PC3
931	$\nu(\text{C-C})$ skeletal of collagen backbone (proline, hydroxyproline)			+
956	$\nu(\text{C-O-C})$ glycoside ring (carbohydrate)		-	
999	$\delta(\text{C-H})$ bend lipids		+	
998				+
1002	Phe ring breathing mode (proteins – collagen); carotenoids	+		
1004	Proteins, DNA/ Phospholipids, Phe			-
1041*	$(\nu\text{CH})$ str Phe/*Quartz contribution		-	
1170	$\nu(\text{C-O})$ , $\nu(\text{C-O-C})$ antisym. and $\delta(\text{CH}_2)$ wagging, (lipids/phospholipids)	+		
1321	$\delta(\text{CH}_3)$ $\delta(\text{CH}_2)$ wagging of proteins/nucleic acids	+		
1339	$\nu(\text{C-O})$ , $\nu(\text{C-O-C})$ antisym. $\delta(\text{CH}_2)$ wagging, (lipids/phospholipids)	+		
1344			-	
1365	$\delta(\text{C-H})$ proteins (collagen) and carbohydrates (glucose)		-	
1447	$\delta(\text{CH}_2)$ bending, collagen/lipids	+		
1594	$\nu(\text{C-N})$ , $\nu(\text{C-C})$ proteins		+	
1616	$\nu(\text{C-C})$ porphyrin		+	
1626		+		
1633*	Amide I $\nu(\text{C-O})$ , proteins; $\nu(\text{C-C})$ lipids / *Quartz contribution		+	
1656		+		
1668			+	

### 5.3.3 Discriminant Function Analysis

Figure 5.10 shows the results for the DFA. The next step in the process was to submit the data to DFA. The top 15 PCs were taken forward for the analysis that explained 99.9% of the data. DF1 and DF2 showed the best clustering. DF3 was omitted as it did not add anything further to the data. At first, when doing a binary data projection, *i.e.*, cancer vs cirrhosis, the data did not find any true separation (data not shown). However, when projecting in a third class (namely the F0 patients), the DFA algorithm found a very clear visible cluster split as shown in Figure 5.10. Here the non-diseased patients found 100% separation.

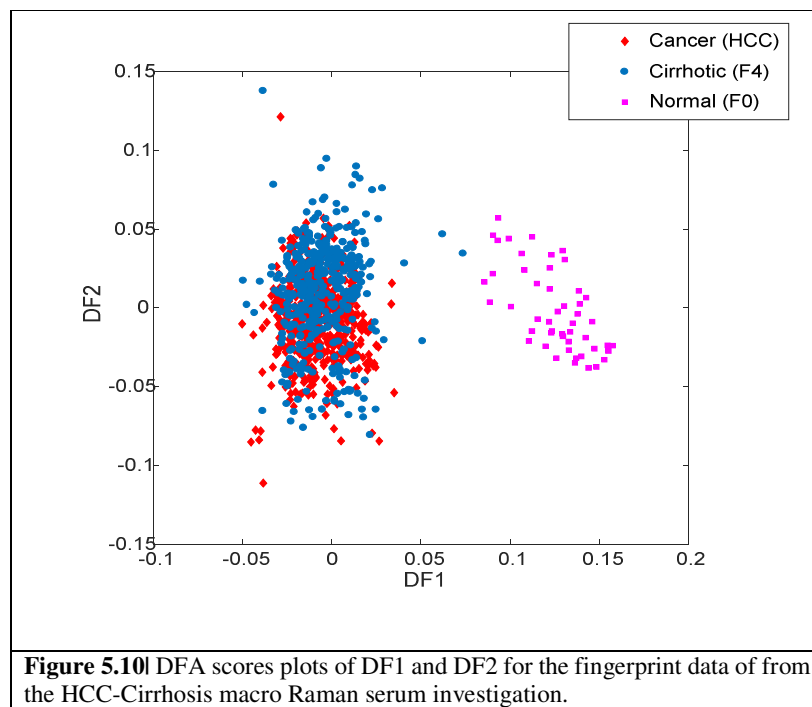


Figure 5.11 demonstrates the two loadings with a minimum threshold value for significance of inclusion (dotted line). Here, DF1 (top) shows that the phenylalanine bands around the 998-1010  $\text{cm}^{-1}$  demonstrates the most intense peaks. DF2 (bottom) shows the influence of amide III, phospholipids, phenylalanine, and beta carotene bands (1001-1180  $\text{cm}^{-1}$ ). Table 5.3 lists the tentative peak assignments.

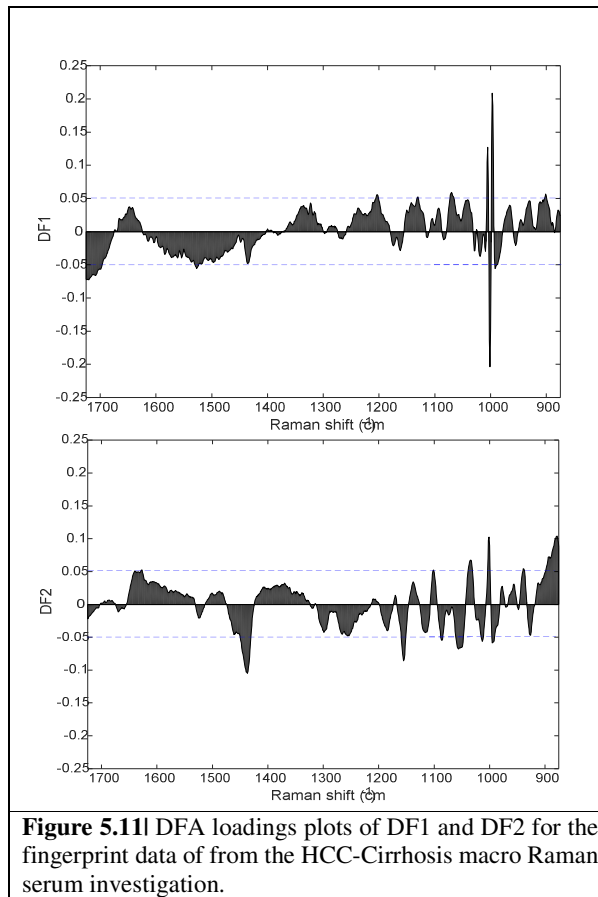
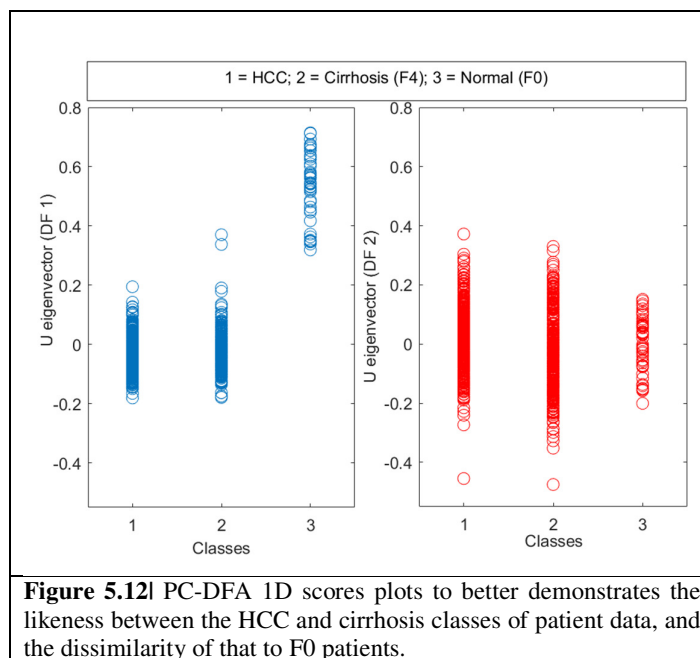


Figure 5.12 shows a linear formation of the PCA plot from Figure 5.11. Here the similarities and differences between the patient groups are evident. DF1 (in blue) shows almost perfect separation between healthy patients and diseased including cancer, whereas, DF2 struggles to show anything. Further quantification was sought using Tukey’s multiple post-hoc comparison statistical test (see Table 5.4). The results are shown below for each of the eigenvectors for DFA.



**Table 5.3** DFA: Tentatively assigned serum loadings from DF1 and DF2 (Figure 9) taken from the serum investigation for HCC-cirrhosis- normal patients [132, 209-210, 213].

$\tilde{\nu}/\text{cm}^{-1}$	Tentatively assigned Raman peaks	DF1	DF2
878	DNA, proteins, $\nu(\text{C-C})$ skeletal of collagen backbone (proline, hydroxyproline), $\nu(\text{C-O-C})$ glycoside ring (carbohydrate)		+
893			+
901		+	
938			+
992	Proteins, DNA/ Phospholipids, Phe, $\delta(\text{C-H})$ lipids		-
997		+	
1001		-	+
1004		+	
1012	Phe ring breathing mode (proteins – collagen); carotenoids		-
1033		+	
1042	Proteins/Phospholipids	+	
1055			-
1087			-
1101	Phe		+
1130		+	
1154	Phe/ $\beta$ carotene, $\nu(\text{C-O})$ , $\nu(\text{C-O-C})$ antisym. $\delta(\text{CH}_2)$ wagging, (lipids/phospholipids)		-
1203	Amide III, Phospholipids	+	
1436	$\delta(\text{CH}_2)$ (lipids)	-	-
1572	Amide III / $\beta$ carotene, $\nu(\text{C-N})$ , $\nu(\text{C-C})$ proteins	-	
1627	Amide I $\nu(\text{C-O})$ , proteins; $\nu(\text{C-C})$ str lipids		+
1702		-	
1719		-	

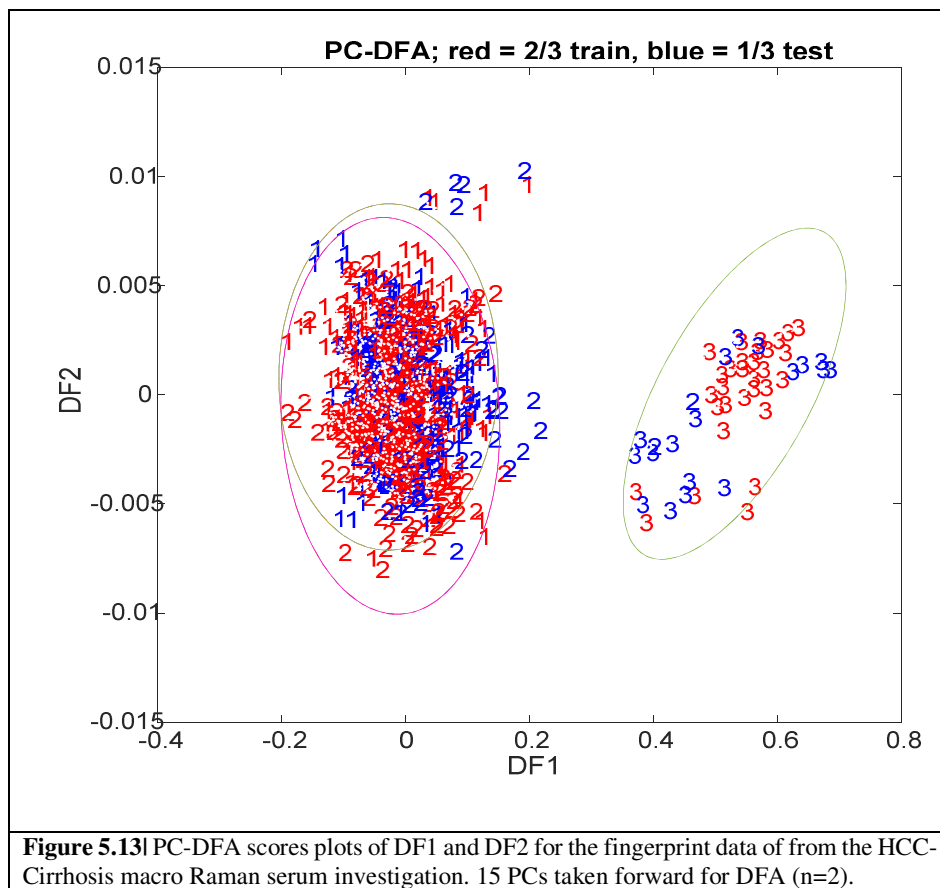
**Table 5.4** Tukey's multiple post-hoc comparison test: Results for the three scenarios (cancer vs. cirrhosis, cancer vs. normal and cirrhosis vs. normal), reported from a 1D DFA box plot (Figure 5.12).

	U Eigenvector DF1		U Eigenvector DF2	
	Mean Diff.	p value	Mean Diff.	p value
Cancer vs. Cirrhosis	-0.00405	>0.05	0.06367	<0.001
Cancer vs. Normal	-0.5675	<0.001	0.02658	>0.05
Cirrhosis vs. Normal	-0.5634	<0.001	-0.03709	>0.05

The purpose of Tukey's comparison test is to discern which groups in the sample differ. It uses the "Honest Significant Difference", a number that represents the distance between groups, to compare every mean with every other mean. Here, for cancer vs. cirrhosis we can conclude that the given result is not at all significant ( $p > 0.05$ ), whereas both the cancer vs. normal and cirrhosis vs. normal results appear much more significant ( $p < 0.001$ ), when observing DF1; that is less than 0.1% of the findings as such is by chance, therefore there is significance in the separation between patient groups.

### 5.3.4 PC-DFA: Supervised Cluster Analysis

Moving forward, a PC-DFA was carried out on the datasets. PC-DFA is a supervised data prediction algorithm based on canonical variates analysis. It aims to maximise the between group distance and minimise the intragroup distance. The first 15 PCs that explained 99.9% of the data variance were chosen for analysis, together with 2 DFs (number of DF is  $1 < \text{number of groups}$ ). The data were split in to randomised groups of 1/3 and 2/3 of all three groups of patients, ensuring that no technical repeat spectra was in more than one division for the analysis. Two-thirds of the data were used to train the model before blindly projecting the remaining 1/3 test data to validate the model. Figure 5.13 demonstrates the PC-DFA scores biplot. As can be seen there is a significant cluster split between group 3 (F0 patients), and the remaining group 1 and 2 (cancer and cirrhosis, respectively). This result only echoed what was seen with both PCA and DFA methods. However, here a 95% confidence ellipsis was also projected around the test data points. As can be seen there appears to be a mixture of both group 1 and group 2 data points (test – blue; train- red). Group 3 however, demonstrates a 100% positive classification; that is all test subjects found perfect matching with the training patients. As the other two groups were completely mixed, a classification accuracy was not relevant here. Figure 5.14 demonstrates the respective loadings profile for the PC-DFA completed. Table 5.5 lists the full spectral loadings and their tentative peak assignments.



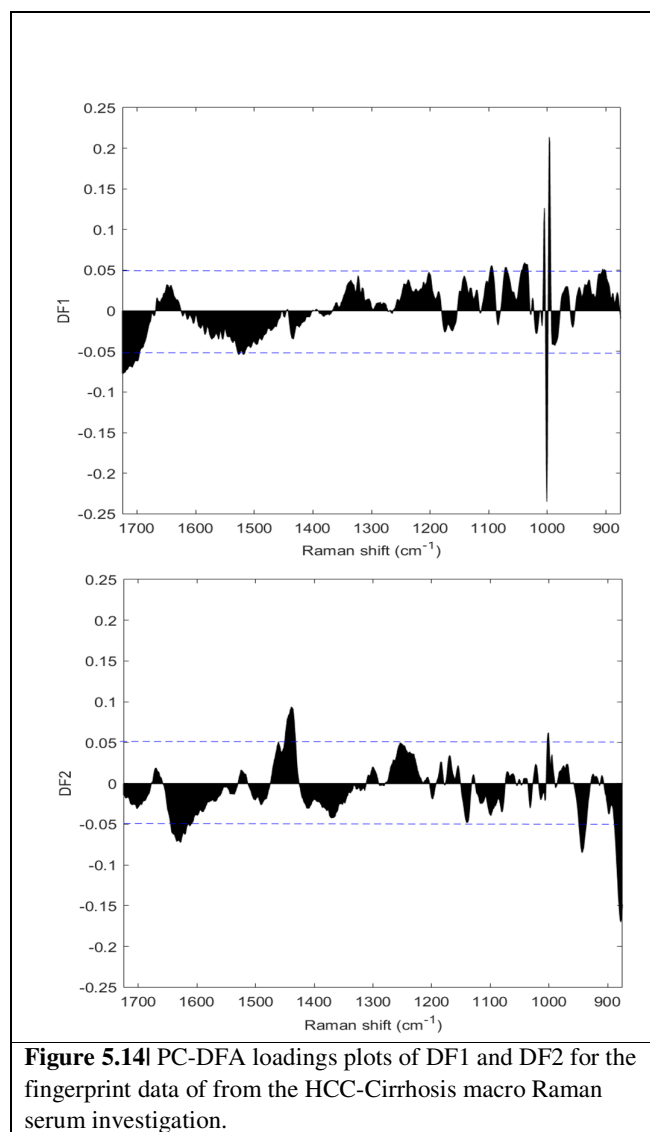


**Figure 5.14** PC-DFA loadings plots of DF1 and DF2 for the fingerprint data of from the HCC-Cirrhosis macro Raman serum investigation.

**Table 5.5** PC-DFA: Tentatively assigned serum loadings from DF1 and DF2 (Figure 12) taken from the serum investigation for HCC-cirrhosis- normal patients [132, 209-210, 213].

$\tilde{\nu}/\text{cm}^{-1}$	Tentatively assigned Raman peaks	DF1	DF2
879	Proteins (proline, hydroxyproline, tyrosine); $\nu(\text{C-C})$ collagen backbone		-
906	$\nu(\text{C-C})$ skeletal of collagen backbone (proline, hydroxyproline)	+	
945			-
997	$\nu(\text{COC})$ glycoside ring (carbohydrate)	+	
1001	Phe ring breathing mode (proteins – collagen); carotenoids	-	+
1004	Proteins, DNA/ Phospholipids, Phe	+	
1039		+	
1072		+	
1096	$\nu(\text{C-N})$ proteins	+	
1140	$\nu(\text{C-N})$ (proteins); $\nu(\text{C-O})$ (carbohydrates); $\nu(\text{C-C})$ (acyl backbone – lipids)		-
1251	Amide III ( $\nu(\text{C-N})$ , $\nu(\text{N-H})$ , $\delta(\text{C-H})$ ) (lipids/phospholipids)		+
1439	$\delta(\text{CH}_2)$ lipids, phospholipids/cholesterol		+
1461	$\delta(\text{CH}_2)$ , $\delta(\text{CH}_3)$ proteins		+
1517	$\nu(\text{C-C})$ porphyrins, carotenoid	-	
1525	$\nu(\text{C-N})$ , $\nu(\text{C-C})$ proteins	-	
1628	Amide I $\nu(\text{C-O})$ , proteins; $\nu(\text{C-C})$ lipids		-
1634			-
1700	Amide I $\nu(\text{C-O})$ proteins, $\nu(\text{C-C})$ lipids	-	
1724	$\nu(\text{C-C})$ lipids	-	

### 5.3.5 Supervised Machine Learning: RF and SVM

The data were submitted to more advanced machine learning algorithms for comparison of the result to previous analyses. The Random Forest (RF) [57] method utilised in this research was implemented on R-Studio with the specific package [212]. Random Forest (RF) is an ensemble machine learning algorithm of building a forest of uncorrelated decision trees or classification and regression trees (CART). See Figure 1.22 in Chapter 1 to understand how the RF classifier works. Figure 5.15 demonstrates the output for RF ‘Gini importance plot’. Gini importance purity index results in a collection of the most interesting/discriminating wavenumbers as a result from the RF decision trees. The plot itself shows the three patient groups (1-HCC, 2-Cirrhosis and 3-Normal) as a function of their mean Raman signals, together with their most discriminating wavenumbers. Moving forward with this allows one to explore Gini-SVM. In this case, the top 30 wavenumbers are fed in to the SVM algorithm, the grid search is tuned over and over with different iterations until the optimal cost and gamma parameters present the best overall classification accuracy across the patient spectra. The results for both the RF classifier and Gini-SVM are shown in Table 5.6.

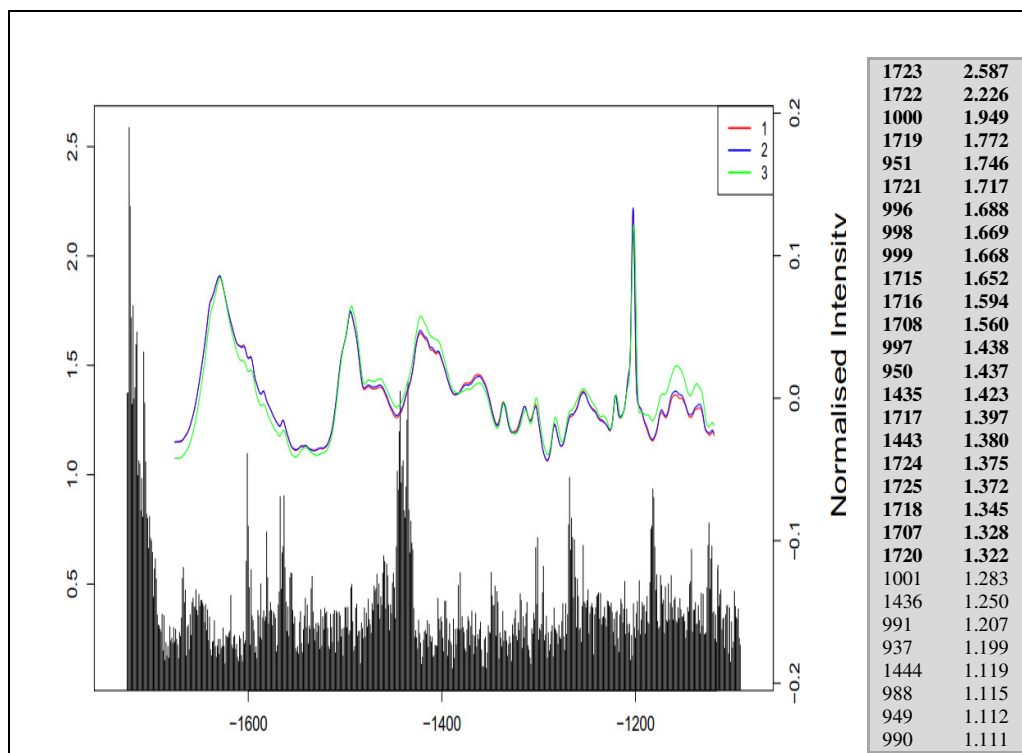


**Figure 5.15** Gini importance purity index: RF classifiers results in a list of wavenumbers that are important in describing the purity of the data. The plot demonstrates the tri-class mean signal with the importance of each of the wavenumbers across the classification (below). The wavenumbers and their importance are organised in ascending order (right).

Gini-SVM was carried out following a cost and gamma tune grid. All data frames were tried until the best data frame was discovered ( $2^{(20:10)}$ ,  $2^{(-14:16)}$ ). A radial basis function (RBF) kernel was optimised and the results were tested three times and reported as an average. Inputted to the SVM algorithm was 2/3 training dataset, with 80% divided for an internal test and 20% of the remaining 1/3 test data as an external testing dataset. Finally, a cross validation (CV) was done where  $k=5$ .

Prior to these results, a preliminary investigation was carried out to ascertain which machine learning algorithm would be the best at describing the data by way of good classification accuracies. Three algorithms were implemented (RF, SVM and genetic algorithm (GA)). Eight different pre-processing regimes were evaluated, ranging from binning numbers, polynomial baselines, vector, standard normal variate normalisations, derivatisations, wavelet de-noising and offset scaling to determine which of these combinations garnered the best sensitivity and specificity results across the three platform algorithms (data not shown). It was decided that a combination of both RF classifiers and Gini-SVM presented equally mid-high results. GA was then abandoned. Sensitivity is the ability of a test to correctly identify those with the disease (*i.e.*, true positive or ++ rate (TPR)). Whilst, specificity is the ability of a test to correctly identify

those without who are disease-free (healthy) (i.e true negative or -- rate (TNR)). The true positive rate (TPR) and true negative rate (TNR) for a good classifier should be values closest to the 100%. The formula for both is presented below in Figure 5.16. Both classifiers resulted in three binary sensitivity and specificity results.

$\text{Sensitivity} = \frac{TP}{TP+FN} = \frac{TP}{\text{diseased}}$ $\text{Specificity} = \frac{TN}{TN+FP} = \frac{TN}{\text{healthy}}$
<b>Figure 5.16</b> Formulae for sensitivity ( <i>se</i> ) and specificity ( <i>sp</i> ).

For ‘Cancer’ subjects the best sensitivity and specificity was seen with the Gini-SVM classifier. For ‘Cirrhosis’ subjects, both classifiers show similar results, whereas, for the ‘Normal’ subjects, the Gini-SVM classifier was stronger (see Table 5.6).

**Table 5.6** Classification sensitivity and specificity results for the two machine learning algorithms implemented on the patient datasets.

	<b>Top 30 WVN- RF Classifier</b>		<b>Gini-SVM Classifier</b>	
	Sens %	Spec %	Sens %	Spec %
Cancer	55.1	53.5	62.3	55.3
Cirrhosis	46.3	58.6	45.6	66.3
Normal	94.3	99.2	94.6	100

The RF classifier method was chosen for this work due to its ease in scalability, meaning that it is easily applicable to larger datasets, or if the cancer vs. cirrhosis was only tried first. In this case a third F0 patient was easily added. Second, the Gini results are easily interpreted when discerning wavenumbers were easily identified. Additionally, according to Smith *et al.* [213], RF is capable of handling outliers in the input space, which allows spectral classification without overly-heavy pre-processing regimes. In turn, this can deal well with missing or truncated values, *i.e.*, wavenumber truncation to the fingerprint region, compared to other classification methods [212].

## 5.4 CONCLUSION

Serum sampling using spectroscopy has several advantages, namely being non-invasive, easily attainable at low cost and has viable monitoring capabilities to the long-term benefit of the patient. Owing to its very nature of a complex stream of highly interesting blood products, it can reflect the internal milieu of the body with biochemical readouts or fingerprints when spectroscopically exploited. In cases of diseases, such as fibrosis, cirrhosis and tumour invasion, the analysis of the blood reveals an account of the microenvironment, which harbour biomarkers of disease. Here, this study used a novel macro Raman approach to interrogate the serum profile of cirrhotic patient serum samples either with and without HCC in their liquid formation, towards the development of a spectroscopic diagnostic/screening tool for patient welfare. RS can provide a spectral fingerprint of all molecules with the serum sample on a global scale. From this, over 10 000 spectral variables were then subjected to multivariate analysis and machine learning algorithms to ascertain the salient features amongst the data. Following an in-house pre-processing regime, clustering algorithms such as PCA and HCA were used to establish outliers within the data in the first instance. When taking forward the viable patient's spectra, PCA only showed differences amongst the healthy F0 patients against the diseased (cancer + cirrhosis) patients. Overall, no significant differences are seen when comparing on a binary dataset (cancer vs cirrhosis) *via* PCA. DFA shows similar information for the binary classification, but with a multiclass (all data), a greater separation between disease vs. normal was expressed. In contrast, DF1 shows good discrimination between cancer vs. normal ( $P < 0.001$ ) and similarly, DF2 showed some differences for cancer vs. cirrhosis *via* a Tukey's post-hoc test. PC-DFA demonstrates 100% sensitivity and specificity (99% confidence ellipses) for diseased vs. normal, but poor classification for cancer from cirrhosis. Finally, both RF and Gini-SVM demonstrate moderate-good results for this multiclass classification across the patient groups (55%, 62% (cancer), 54%, 55% (cirrhosis) and 99%, 100% (F0)).

In summary, HCC and cirrhosis are clinically and biologically very difficult to show distinctions when approximately 80% of all cirrhotic cases transform to HCC. This is also shown in the results of this study; that diseased vs. healthy shows distinct differences in the serum profile *via* RS spectroscopy from a liquid serum perspective. However, discerning cancer from a diseased population has proved challenging. Here, this study has shown the viability of using Raman spectroscopy on liquid samples without the use of a microscope function for disease screening purposes.

**| CHAPTER 6 |**

**GENERAL CONCLUSIONS  
AND PERSPECTIVES**

---

**| CHAPITRE VI |**

**CONCLUSIONS GÉNÉRALES  
ET PERSPECTIVES**

## **VI.1 RÉSUMÉ**

Ce dernier chapitre résume l'objectif principal des recherches menées dans le cadre de la thèse de doctorat. Il se termine par les aspects pertinents des recherches et met en évidence les suggestions possibles pour améliorer la portée future de ces travaux. L'objectif principal de ce doctorat de projet de recherche consistait à mettre au point une nouvelle approche spectroscopique pour mettre en place un outil de dépistage utilisable en clinique pour la détection du cancer à partir de sérum humain. Deux phases de cette recherche sont considérées de manière séquentielle: des études pour évaluer des conditions pré-analytiques et des études sur des cas concrets de maladie pour évaluer le potentiel diagnostique. Pour les études pré-analytiques, un pool de sérums humains commercialisé a été utilisé. Pour les études diagnostiques, trois groupes de patients rétrospectifs ont été étudiés ici; i) sérums de patients présentant différents stades de fibrose hépatique (F1-F4) par rapport à des sujets sains (F0), ii) sérums de patients présentant différents stades de tumeurs primitives du cerveau (normal vs glioblastome multiforme vs métastatique), et iii) sérums de patients cirrhotiques avec et sans cancer primitif du foie (carcinome hépatocellulaire).

## **VI.2 CONCLUSIONS ET PERSPECTIVES**

Le but de cette recherche était de développer la spectroscopie du biofluide, en particulier le sérum, en vue de développer un test rapide de technologie de POC. Des efforts ont été consacrés à la spectroscopie HTS-IRTF et à la spectroscopie Raman de préparations sèches et liquides de sérum humain. On pense que l'avenir de ce stade évoluera vers le développement de nouvelles biopsies liquides en vue de la recherche des signes distinctifs des profils de maladie basés sur une vaste gamme de produits. Il semblerait que la spectroscopie IR et la spectroscopie Raman sont des candidats potentiels à une implémentation en tant qu'applications cliniques de routine et que le principal point de vue de l'accès à ces applications s'orienterait vers des scénarios de soins au chevet du patient, ou à haut débit et à grande échelle dans des plateformes cliniques. Bien que cette thèse se soit concentrée sur l'analyse sérique pour identifier des processus pathologiques, elle peut être très facilement adaptée à d'autres biofluides, tels que le plasma, la salive, l'urine, les sécrétions biliaires, les larmes et le liquide céphalo-rachidien.

Un autre domaine de développement réside dans la réduction du volume d'échantillonnage et dans la recherche de mesures permettant de gagner du temps, ce qui pourrait alléger la charge pesant sur nos ressources économiques pour un système de soins de santé plus performant. Ici, les domaines de la microfluidique et de la nanofluidique sont d'un intérêt majeur. L'un des principaux objectifs est de permettre la gestion des fluides lors de la séparation des composants liquides, de sorte que davantage puisse être fait pour les tests / analyses à partir de la même acquisition d'échantillon. Développer des dispositifs micro-fabriqués compatibles avec les tests

spectroscopiques de routine peut être la solution pour une technologie sans marquage. De plus, la tendance à la miniaturisation est la norme à l'heure actuelle, de sorte que l'on peut voir les dispositifs spectroscopiques mobiles dans un avenir très proche.

Une étude prospective consisterait à examiner de grandes cohortes afin de créer de bons classificateurs. Pour évaluer l'efficacité d'une méthode, les cliniciens utilisent souvent la courbe ROC (Receiver Operator Characteristic). Cela permettra à l'analyste d'illustrer graphiquement le potentiel diagnostique d'un système de classification binaire, c'est-à-dire patient sain ou patient malade. Ce type d'analyse est directement lié au détriment / bénéfice des décisions de diagnostic. Ceci peut également ajouter de la valeur aux données spectroscopiques et mieux convaincre le milieu clinique de la richesse de l'approche spectroscopique en tant qu'outil d'aide au diagnostic, surtout dans un contexte de soins POC.

En résumé, cette thèse a comparé l'application des diverses approches de spectroscopie vibrationnelle à l'analyse des divers échantillons sériques séchés et en phase liquide. Elle a aussi évalué la capacité à les utiliser pour des applications diagnostiques. Ceci est basé sur un test de diagnostic peu invasif (phlébotomie du patient) qui pourrait être intégré au dépistage systématique et aux scénarios associés, dans le but de réduire les taux de morbidité / mortalité dans les systèmes de soins de santé. Ces résultats sont préliminaires et des recherches approfondies sont nécessaires pour bien évaluer le potentiel diagnostique de ces approches.

## **6.1 THESIS CONCLUSION**

The aim of this Ph.D. research project was to ascertain a novel spectroscopic approach towards a point-of-care (POC) screening regime for cancer detection from human serum. Two phases of this research emerged sequentially; preanalytical and diagnostic screening studies. For pre-analytical studies, commercial pooled serum was used. Diagnostically, three retrospective patient groups were studied here; i) patient sera with varying stages of hepatic fibrosis (F1-F4) compared to healthy subjects (F0), ii) patient sera with different stages of primary brain tumours (normal vs. glioblastoma multiforme vs. metastatic disease), and iii) cirrhotic patient sera with and without primary liver cancer (hepatocellular carcinoma).

Serum sampling *via* spectroscopy has several advantages, *i.e.*, non-invasive, easily accessible at low cost and has viable monitoring capabilities to benefit the patient. Blood and its products have long since been the standard for routine clinically testing as it reflects the internal milieu of the human body. Blood feeds the tissues and lies at the intersection of cellular-tissue communication and as such, a perfuse stream of highly informative secretions enables biochemical readouts or 'fingerprints' when combined with molecular spectroscopy. Such readouts should inevitably reflect the patient's healthy or diseased status. Therefore, it is for this

reason that often advanced mathematical algorithms and chemometrics are combined to uncover the fundamental descriptive and discerning variables for the analyst (out of many 1000's of variables from the spectroscopic serum profiles).

Prior to distinguishing the healthy *vs.* disease patterns, it is important to assure that variations within the biology of the samples and the preanalytical steps are kept to an absolute minimum, so as not to introduce further confounding influences in the data. To this end, various preanalytical experiments were conducted for this research. Developmental approaches were envisaged to understand possible influences on the overall serum biochemistry. Experimentations towards freeze-thaw cycles (FTC) and ambient environmental drying (ED) were conducted. The preanalytical methodologies and subsequent results were seen in the first part of chapter 3 and chapter 4.

In chapter 3, FTIR analysis *via* modalities of ATR and HTS spectroscopy were completed for the effect of FTC on pooled serum. Here, PCA demonstrated very little changes to serum profile. The FTC appeared mixed with no logical clustering seen. For both techniques, common spectral peaks were observed for the serum: proteins (amide I  $\sim 1580$ - $1680\text{ cm}^{-1}$ ; and amide II  $\sim 1500$ - $1580\text{ cm}^{-1}$ ). It was concluded that non-pertinent serum influence from FTC effects were seen on the spectral profiles. Further, the ambient ED results demonstrated the physical presence of the fern-like formation. The time points were orientated showing a sequential pattern starting from T0 (fresh drop liquid sera) towards T24 (24 h post drying). PCA loadings highlighted the prominent bands as proteins: amide I ( $\nu(\text{C-O})$  stretch  $\sim 1655\text{ cm}^{-1}$ , the N-H deformation  $\sim 1540\text{ cm}^{-1}$  and a  $\nu(\text{C-C})$  stretch  $\sim 1615\text{ cm}^{-1}$ ).

In chapter 4 the same study *via* Raman spectroscopy carried out for preanalytical variation showed similar results. Hence, no influence was seen on both the FTC (data was mixed with PCA clustering), and ambient ED study. The overall conclusion from the preanalytical studies was to successfully progress to the diagnostic investigations with the knowledge of negligible influence of FTC and ED on serum. However, both FTIR spectroscopy techniques were discerning enough to demonstrate the coffee-ring effect upon drying. Although, freezing, thawing and drying appear to have negligible effects on the data outcome, it is still important to not over-process the samples in practice, and caution is needed not to exceed high amounts of the physical effects to the samples in the first place. As with any biological sample, it could be susceptible to degradation eventually.

The diagnostic approaches were investigated and discussed in chapters 3, 4 and 5. Following down-selections of the methodological design towards diagnostic testing, focus was geared

towards the investigative veracity of the approaches, *i.e.*, macro Raman spectroscopy on liquid serum samples and HTS-FTIR transmission spectroscopy on dried serum samples.

The last part of chapter 3 discusses the study for the HTS-FTIR diagnostic high throughput approach towards dried serum analysis from two patient serum banks. Firstly, fibrosis patients (F0 – healthy; F1-F2 – early stage disease onset; F3-F4 – late stage disease onset and end-stage irreversible cirrhosis) were investigated. The results demonstrated that PCA was weak in showing differences between the data groups. However, DFA did show a slight separation between early onset fibrotic disease (F2) from advanced fibrosis/cirrhosis (F4) *via* the DF1 loading. DF2 further showed this, as explained by the negative and positive loading profiles (low-grade and high-grade disease respectively). Increased intensities in the 1530  $\text{cm}^{-1}$  region, the 1635  $\text{cm}^{-1}$  and 1748  $\text{cm}^{-1}$  bands indicated amide II, amide I ( $\alpha$ - helices), and carbonyl bonds of lipids. Other influencing loadings could be associated protein bands at  $\sim 1220 \text{ cm}^{-1}$ ,  $\sim 1550 \text{ cm}^{-1}$  and pleated sheets/aggregated protein structures. Overall, this study demonstrated that both PCA and DFA was able to show biochemical differences between some the patient disease stages. Although a PC-DFA validation was tried, it did not add anything to the data.

In a second patient bank, glioma/brain tumour patients (normal vs. GBM vs. MET) were analysed with the HT-FTIR method. Here, both PCA and DFA showed some distinctions between normal vs. disease samples (GBM + MET). DF1 found good separation between normal and metastatic patients, which is attributed to the broadband  $\text{CH}_3$  deformation of lipids at  $\sim 1348 \text{ cm}^{-1}$  and amide I of  $\alpha$ -helical protein structures at  $\sim 1640 \text{ cm}^{-1}$ . More intrinsically, the positive loadings differentiated the metastatic patients from controls based on  $\delta(\text{CH}_2)$  deformation of methylene groups and lipids at  $\sim 1440\text{-}1462 \text{ cm}^{-1}$ , amide I of  $\alpha$ -helical protein structures at  $\sim 1640 \text{ cm}^{-1}$ , and  $\nu(\text{C-O})$  of DNA/RNA at  $\sim 1075\text{-}1088 \text{ cm}^{-1}$ . The negative loadings were on two peaks, 1348  $\text{cm}^{-1}$  and 1640  $\text{cm}^{-1}$ , which correspond to the  $\text{CH}_3$  lipid deformation and the  $\alpha$ -helix protein structure of amide I, conducting to separation between healthy and diseased (MET). DF2 further demonstrated nuances between the metastatic and GBM patients. The positive loadings were attributed to the majority of GBM patients, and the negative ones to most of the metastatic patients; both with an influence from normal patients. DF2 in result was not as discriminatory as DF1.

Whilst employing a range of chemometric techniques, such as RF classifiers and SVM the data did not show any further discrimination, however when subjecting with PLS-DA leave-one-out with 10 PLS directions, it was possible to show more than 96% of correct classifications and increased sensitivities and specificities of dataset for cancer vs. normal (97.6% and 95.7%, respectively). GBM vs. MET was slightly lower in diagnostic accuracy (71.4% and 65%).

Whereas, GBM vs. NORM and MET vs. NORM presented 95.2%, 100%, 100% and 95.7%, sensitivity and specificity, respectively. Overall, this study was able to show good to very good diagnostic accuracy.

Chapter 4 of this study discussed the experimentation for the Raman diagnostic macro approach towards thawed liquid serum analysis from the same glioma/brain tumour patients (chapter 3). The DFA results (positive loadings on DF1) demonstrated a slight separation between healthy vs. cirrhotic patient spectra from F0 and F4 respectively. Such a result was attributed by loadings from the 900-1300  $\text{cm}^{-1}$  region, which encompasses the amino acids and amide III region. Although a PC-DFA validation was tried, it did not add anything more to the data. The data were submitted to both RF classifiers, Gini-SVM using an RBF kernelization and finally to a forward LDA for further interrogation. The highest sensitivity and specificity was a moderate result and so it is concluded that neither of the algorithms employed were able to provide a disease discrimination. Overall, this study demonstrated that combining advanced multivariate analysis as classification tools, is sometimes not enough to find discrimination if the disease course is highly complex and analysed in liquid phase.

In chapter 5, a large cohort of cirrhotic patients with / without complications of hepatocellular carcinoma were interrogated using the macro-Raman methodology for liquid serum preparations. The results revealed that only PCA demonstrated differences amongst the healthy F0 patients against the pathological (cancer + cirrhosis) patients. Overall, no significant differences are seen when comparing on a binary dataset (cancer vs. cirrhosis) *via* PCA. DFA showed similar information for the binary classification, but with a multiclass (all data), a greater separation between disease vs. normal was expressed. While DF1 showed good discrimination between cancer vs. normal ( $p < 0.001$ ), DF2 revealed some differences for cancer vs. cirrhosis *via* a Tukey's post-hoc test. PC-DFA demonstrated 100% sensitivity and specificity (99% confidence ellipses) for diseased vs. normal, but poor classification for cancer vs. cirrhosis. One has to be cautious with such result as overfitting could be occurring. Finally, both RF and Gini-SVM demonstrated moderate results for this multiclass classification across the patient groups (55%, 62% (cancer), 54%, 55% (cirrhosis) and 99%, 100% (F0)).

HCC and cirrhosis are clinically and biologically very difficult to distinct when approximately 80% of all cirrhotic cases transform to HCC. This is also shown in the results of this study comparing diseased vs. healthy cases. The data show distinct differences in the serum profile *via* Raman spectroscopy from a liquid serum perspective. However, discerning cancer from a diseased population is a major limitation in this study. Nevertheless, this study has clearly

attempted to demonstrate the viability of using macro-Raman spectroscopy on liquid samples without the use of a Raman microscopy for disease screening purposes.

In summary, this thesis demonstrates the ability to employ various molecular vibrational spectroscopies towards POC testing for rapid serum sampling in both dried and liquid phases. This is based upon a minimally invasive (patient phlebotomy) diagnostic test that could be embedded into routine screening and associated scenarios, in an active bid towards a reduction in morbidity / mortality rates in healthcare systems.

## **6.2 SCOPE FOR FUTURE STUDIES**

The direction of this research was to develop a biofluid/ serum spectroscopy approach towards a rapid POC testing. Whilst concerted efforts have been towards HT-FTIR and macro-Raman spectroscopy of dried and liquid preparations of human serum, it is believed that the future of this arena will move towards the development of further liquid biopsies towards the search for hallmarks of a vast range of disease profiles. It is common knowledge that both IR and Raman spectroscopy are contenders to be implemented as routine clinical applications and the main access vantage point for these would be towards bedside, or single – large scale high throughput scenarios. Whilst this thesis was focused on serum sampling for disease processes, it can be very easily adapted towards other biofluids, such as plasma, saliva, urine, bile secretions, tears and cerebral spinal fluid etc.

Another area of development lies in the scaling of the sampling volume and a further push towards time-saving measures that could lighten up the burden on our economic resources towards a brighter healthcare system. Here, the area of microfluidics and nano-fluidics are of key interest. A major aim is to enable fluid handling for liquid component separations so that more can be done for testing/analysis from the same sample acquisition. Developing micro-fabricated devices that are compatible for routine spectroscopic testing can be the answer towards an absolute label-free technology. Additionally, the trend for miniaturization is the norm at present, so one can see mobile spectroscopic devices being something of the very near future. A prospective study would be to look at large cohort studies to build good classifiers. Clinicians often use receiver operating characteristic curve, *i.e.*, ROC curve. This will allow the analyst to graphically illustrate the diagnostic ability of a binary classification system, *i.e.* normal vs. disease. This type of analysis is related in a direct way of the detriment/benefit of diagnostic decisions. Whilst the benefit clinically based, it may also add added value to the spectroscopic data and better convince the clinical area of the wealth of spectroscopic as an adjunct tool at POC settings.

## **| REFERENCES |**

1. Kimura, WD. (2017). Chapter 1. What are electromagnetic waves? In: IOP Science: *Electromagnetic waves and lasers*. Bristol, UK: Morgan & Claypool Publishers, pp.1-33.
2. Banwell, C. & McCash, E. (1994). *Fundamentals of molecular spectroscopy*. 4th ed. Berkshire, England: McGraw-Hill Publishing Co. pp.27-53.
3. Stuart, B.H (2004). *Infrared spectroscopy: fundamentals and applications*. Berkshire, England: John Wiley & Sons, Ltd. pp.1-44.
4. Schrader, B (1995). *Infrared and Raman spectroscopy: methods and applications*. Weinheim, Germany: VCH Publishers. pp.39-58.
5. Baker, MJ. Hughes, CS. Hollywood, KA. (2016). *Chapter 3. Raman spectroscopy*. In: IOP Concise Physics Biophotonics: vibrational spectroscopic diagnostics. Bristol, UK: Morgan & Claypool Publishers. pp.3.1-3.6.
6. Baker, MJ. Hussain, SR. Lovergne, L. Untereiner, V. Hughes, C. Lukaszewski, RA. Thieffin, G. Sockalingum, GD. (2016). Developing and understanding biofluid vibrational spectroscopy: a critical review. *Chemical Society Reviews*, 45(7), pp.1803-1818.
7. Baker, MJ. Hughes, C. Hollywood, K. (2016). *Biophotonics: vibrational spectroscopic diagnostics*. Bristol, UK: Morgan & Claypool Publishers, IOP eBook.
8. Sathyanarayana, DN. (2007). *Vibrational spectroscopy: theory and applications*. London: New Age International. Ebook: <https://books.google.com/books?id=SBpXpX9kxcccC&pgis=1>.
9. Christy, AA. Ozaki, Y. Gregoriou, VG. (2001). *Modern Fourier transform infrared spectroscopy*. New York: Elsevier. pp.27-39.
10. Peeran, M. Srinivasamurthy, KG. (2005). *Comparison of Raman and IR spectroscopy*. Available: <http://www.chemvista.org/ramanIR3.html>. Last accessed 12/03/2017.
11. Baker, MJ, Trevisan, J. Bassan, P. Bhargava, R. Butler, HJ. Dorling, KM. Fielden, PR. Fogarty, SW. Fullwood, NJ. Heys, KA. Hughes, C. Lasch, P. Martin-Hirsch, PL. Obinaju, B. Sockalingum, GD. Sulé-Suso, J. Strong, R. Walsh, MJ. Wood, BR. Gardner, P. & Martin, FL. (2014). Using Fourier transform IR spectroscopy to analyse biological materials', *Nature Protocols*, 9(8), pp.1771-1791. <https://doi.org/10.1038/nprot.2014.110>.
12. Skoog, DA. Leary, JJ. (1992). *Chapter 12: principles of instrumental analysis*, 4th Ed. Harcourt Brace Jovanovich. Philadelphia, PA.
13. Birkner, N., Wang, Q. (2015). *Infrared spectroscopy instrumentation*. Available: [https://chem.libretexts.org/Core/Physical\\_and\\_Theoretical\\_Chemistry/Spectroscopy/Vibrational\\_Spectroscopy/Infrared\\_Spectroscopy/How\\_an\\_FTIR\\_Spectrometer\\_Operates](https://chem.libretexts.org/Core/Physical_and_Theoretical_Chemistry/Spectroscopy/Vibrational_Spectroscopy/Infrared_Spectroscopy/How_an_FTIR_Spectrometer_Operates). Last accessed 12/04/2017.
14. Heyrovsky, J. (2013). *Institute of physical chemistry, department of spectroscopy*. Available: <http://www.jh-inst.cas.cz/~ftirlab/bruker>. Last accessed 27/06/2017.
15. Griffiths PR. de Haseth, J.A. (2007). *Fourier transform infrared spectrometry* 2nd Ed. John Wiley & Sons, Ltd. pp.12-29.
16. Pike Technologies Inc. (2014). *FT-IR sampling techniques*. Available: <https://www.piketech.com/files/pdfs/EducationalPoster.pdf>. Last accessed: 04/03/2016.
17. Mirabella, FM. (1993). *Practical Spectroscopy Series; Internal reflection spectroscopy: Theory and applications*, Marcel Dekker, Inc.; Marcel Dekker, Inc., pp.17-52.
18. Filik, J. Frogley, MD. Pijanka, JK. Wehbe, K. & Cinque, G. (2012). Electric field standing wave artefacts in FTIR micro-spectroscopy of biological materials. *Analyst*, 137, pp.853-861.
19. Baker, MJ. Hughes, CS. Hollywood, KA. (2016). *Chapter 2. Infrared spectroscopy*. In: IOP Concise Physics, Biophotonics: vibrational spectroscopic diagnostics. Bristol, UK: Morgan & Claypool Publishers. pp.2.1-2.14.
20. Butler, HJ. Ashton, L. Bird, B. Cinque, G. Curtins, K. Dorney, J. Esmonde-White, K. Fullwood, NJ. Gardner, B. Martin-Hirsch, PL. Walsh, MJ. McAinsh, MR. Stone, N. Martin, FL. (2016). Using Raman spectroscopy to characterise biological materials. *Nature Protocols*, 11, pp.664–687.
21. Settle, FA. (1997). *Handbook of instrumental techniques for analytical chemistry*, Prentice, Inc., New Jersey.

22. Smith, E. & Dent, G. (2005). *Modern Raman spectroscopy – a practical approach*. John Wiley & Sons Ltd., Chichester, pp.28-51.
23. Oxford Instruments (2020). *Learning centre asset: spectrograph properties*. Available: <https://www.oxinst.com/learning/view/article/spectrograph-properties>. Last accessed 11/02/2017.
24. Vandenberghe, P. (2013). *Practical Raman spectroscopy: an introduction*. John Wiley & Sons, Ltd. Chichester, UK.
25. Gautam, R. Vanga, S. Ariese, F. Umapathy, S. (2015). Review of multidimensional data processing approaches for Raman and infrared spectroscopy. *EPJ Techniques & Instrumentation*, 2(8), pp.1-38.
26. Lasch, P. (2012). Spectral pre-processing for biomedical vibrational spectroscopy and microspectroscopic imaging. *Chemometrics and Intelligent Laboratory Systems*, 117, pp.100-114.
27. Scaglia, E. Sockalingum, G. D. Schmitt, J. Gobinet, C. Schneider, N. Manfait, M. & Thieffin, G. (2011). Non-invasive assessment of hepatic fibrosis in patients with chronic hepatitis C using serum Fourier transform infrared spectroscopy. *Analytical Bioanalytical Chemistry*, 401, pp.2919–2925.
28. Zhang, X. Thiéfin, G. Gobinet, C. Untereiner, V. Taleb, I. Bernard-Chabert, B. Heurgue, A. Truntzer, C. Ducoroy, P. Hillon, P. Sockalingum, GD. (2013). Profiling serologic biomarkers in cirrhotic patients via high-throughput Fourier transform infrared spectroscopy: toward a new diagnostic tool of hepatocellular carcinoma. *Translational Research*, 162, pp.279-86.
29. Martens, H. Stark, E. (1991). Extended multiplicative signal correction and spectral interference subtraction - new pre-processing methods for near-infrared spectroscopy, *Journal of Pharmaceutical and Biomedical Analysis*, 9, pp.625–635.
30. Martens, H. Pram Nielsen, J. and Balling Engelsen, S. (2003). Light scattering and light absorbance separated by extended multiplicative signal correction: application to near-infrared transmission analysis of powder mixtures. *Analytical Chemistry*, 75(3), pp.394–404.
31. Afseth, NK. Kohler, A. (2012). Extended multiplicative signal correction in vibrational spectroscopy, a tutorial. *Chemometrics and Intelligent Laboratory Systems*, 117, pp.92-99.
32. Gobinet, C. Vrabie, V. Manfait, M. Piot, O. (2009). Pre-processing methods of Raman spectra for source extraction on biomedical samples: application on paraffin-embedded skin biopsies, *IEEE Translational Biomedical Engineering*, 56, pp.1371-82.
33. Zhang, ZD. Ben-Amotz, D. (2002). Removal of cosmic spikes from hyper-spectral images using a hybrid upper-bound spectrum method, *Applied Spectroscopy*, 56, pp.91–98.
34. Do Lago, C.L. Juliano, VF. Kascheres, C. (1995) Applying moving median digital filter to mass spectrometry and potentiometric titration, *Analytica Chimica Acta*, 310, pp.281–288.
35. Zhao, J. (2003). Image curvature correction and cosmic removal for high-throughput dispersive Raman spectroscopy, *Applied Spectroscopy*, 57, pp.1368–1375.
36. Phillips, GR. Harris, JM. (1990). Polynomial filters for data sets with outlying or missing observations: application to charge-coupled-device-detected Raman spectra contaminated by cosmic rays. *Analytical Chemistry*, 62, pp.2351–2357.
37. Bowley HJ. Gerrard, DL. (1986) The use of diode array detectors in conjunction with continuous wave gas lasers for anti-Stokes Raman spectroscopy, *Optics and Laser Technology*, 18, pp.33–35.
38. Rohleder, D. Kiefer, W. Petrich, W. (2004). Quantitative analysis of serum and serum ultrafiltrate by means of Raman spectroscopy, *Analyst*, 129, pp.906–911.
39. Lieber, CA. Mahadevan-Jansen, A. (2003). Automated method for subtraction of fluorescence from biological Raman spectra. *Applied Spectroscopy*, 57, pp.1363–1367.
40. Zhao, J. Lui, H. McLean, DI. Zeng, H. (2007). Automated autofluorescence background subtraction algorithm for biomedical Raman spectroscopy, *Applied Spectroscopy*, 61, pp.1225–1232.
41. Mosier-Boss, PA. Lieberman, SH. Newbery, R. (1995). Fluorescence rejection in Raman spectroscopy by shifted-spectra, edge detection, and FFT filtering techniques, *Applied Spectroscopy*, 49, pp.630–638.

42. Savitzky, A. Golay, MJE. (1964). Smoothing and differentiation of data by simplified least squares procedures. *Analytical Chemistry*. 36(8), pp.1627–1639.
43. Pearson, K. (1901). On lines and planes of closest fit to systems of points in space. *Philosophical Magazine*. 2(11), 559–572.
44. Hotelling, H. (1933). Analysis of a complex of statistical variables into principal components. *Journal of Educational Psychology*, 24, pp.417–441.
45. Thiele, S. Salzer, R. (2003). *Chapter 2: Optical spectroscopy*. In: Gauglitz, G. Vo-Dinh, T. Handbook of Spectroscopy. KGaA, Weinheim: WILEY-VCH Verlag GmbH & Co. pp.439-459.
46. Brereton, RG. (2009). *Chemometrics for pattern recognition*. John Wiley & Sons, Chichester. pp.107-289.
47. Bonnier, F. & Byrne, H. (2012). Understanding the molecular information contained in principal component analysis of vibrational spectra of biological systems. *Analyst*, 2012, pp.137, 322.
48. Ward, JH, Jr. (1963). Hierarchical grouping to optimize an objective function. *Journal of the American Statistical Association*, 58, pp.236–244.
49. MacQueen, J.B. (1967). *Some methods for classification and analysis of multivariate observations*. Proceedings of 5-th Berkeley Symposium on Mathematical Statistics and Probability", Berkeley, University of California Press, 1, pp.281-297.
50. Huberty, C. J. and Olejnik, S. (2006). *Discriminant analysis in research, in applied MANOVA and discriminant analysis*. Second Edition, John Wiley & Sons, Inc., Hoboken, NJ, USA. pp.38-74.
51. Kaiser HF, Norman, WT. (1991). Coefficients alpha for components. *Psychological Reports*; 69(1), pp.111-114.
52. Kanyongo GY. (2006). The influence of reliability on four rules for determining the number of components to retain. *Journal of Modern Applied Statistical Methods*. 5(2), pp.332-343.
53. Boser, B. Guyon, I. Vapnik, V. (1992). *A Training Algorithm for Optimal Margin Classifiers*. Proceedings of the 5th Annual Workshop on Computational Learning Theory (COLT'92), pp.144-152. Pittsburgh, PA, USA, ACM Press.
54. Rosario, B. (2004). *Applied natural language processing*. Available: <https://www.slideshare.net/ANITALOKITA/winnow-vs-perceptron>. Last accessed 14/04/2017.
55. Smola, AJ. Schölkopf, B. (2004). A Tutorial on support vector regression, *Statistics and Computing Archive*, 14(3), pp.199-222.
56. Ben-Hur, A. Weston, JA. (2010). User's guide to support vector machines. *Methods Molecular Biology*, 609, pp.223-239.
57. Breiman L. (2001). Random forests. *Journal of Machine Learning*. 45, pp.5–32.
58. Breiman L. (2004). *Consistency for a simple model of random forests*. In Technical Report 670. Department of Statistics, University of California, Berkeley, USA.
59. Ellis, DI. Crowcher, DP. Ashton, L. O'Hagan, S. & Goodacre, R. (2013). Illuminating disease and enlightening biomedicine: Raman spectroscopy as a diagnostic tool. *Analyst*, 138, p. 3871.
60. Elliott, A. & Ambrose, EJ. (1950). Evidence of chain folding in polypeptides and proteins. *Discussions Faraday Society*, 9, pp.246–251.
61. Blout, ER. & Fields, M. (1949). Absorption spectra: VII. The infra-red spectra of some nucleic acids, nucleotides, and nucleosides. *Journal Biological Chemistry*, 178, pp.335–343.
62. Diem, M. Romeo, M. Boydston-White, S. Miljkovic, M. Matthaus, C. (2004). A decade of vibrational micro-spectroscopy of human cells and tissue (1994-2004). *Analyst*, 129(10), pp.880–885.
63. Nallala, J. Diebold, MD. Gobinet, C. Bouché, O. Sockalingum, GD. Piot, O. & Manfait, M. (2014). Infrared spectral histopathology for cancer diagnosis: a novel approach for automated pattern recognition of colon adenocarcinoma. *Analyst*, 139(16), pp.4005-4015.
64. Papamarkakis, K. Bird, B. Schubert, JM. Miljkovic, M. Wein, R. Bedrossian, K. Laver, N. and Diem, M. (2010). Cytopathology by optical methods: spectral cytopathology of the oral mucosa. Laboratory Investigation, *Journal of Technical Methods and Pathology*, 90(4), pp.589–598.
65. Petricoin, EF. Belluco, C. Araujo, RP. Liotta, LA. (2006). The blood peptidome: a higher dimension of information content for cancer biomarker discovery. *Nature Reviews Cancer*, 6(12), pp.961–967.

66. Pierrakos, C. & Vincent, JL. (2010). Sepsis biomarkers: a review. *Critical Care* (London, England), 14(1), R15, pp.1-18.
67. Maddams, J. Utley, M. Moller, H. (2012). Projection of cancer prevalence in the United Kingdom, 2010-2040. *British J. Cancer*, 107, pp.1195–1202.
68. Macmillan Cancer Support. (2015). *Statistics fact sheet (external version)*. Available: [http://www.macmillan.org.uk/images/cancer-statistics-factsheet\\_tcm9-260514.pdf](http://www.macmillan.org.uk/images/cancer-statistics-factsheet_tcm9-260514.pdf). Last accessed 11/08/2015.
69. Cancer Research UK. (2015). *Survival three times higher when cancer is diagnosed early*. Available: <http://www.cancerresearchuk.org/about-us/cancer-news/press-release/survival-three-times-higher-when-cancer-is-diagnosed-early>. Last accessed 11/08/2015.
70. World Cancer Research Foundation International. (2015). *Data for cancer frequency by country*. Available: <http://www.wcrf.org/int/cancer-facts-figures/data-cancer-frequency-country>. Last accessed 11/08/2015.
71. UNICancer Group (2013). *Figures for cancer in France*. Available: <http://www.unicancer.fr/en/univancer-group/key-figures=cancer-france>. Last accessed 11/08/2015.
72. Cyclacel Pharmaceuticals Incorporated (2015). *Cell cycle in cancer*. Available: [http://www.cyclacel.com/research\\_science\\_cell-cycle.shtml](http://www.cyclacel.com/research_science_cell-cycle.shtml). Last accessed 02/02/2015.
73. Clinical Tools Incorporated (2015). *Cell division*. Available: <http://www.larasig.com/node/1559>. Last accessed 14/10/2015.
74. Tsuda, H, Akiyama, F, Terasaki, H, Hasegawa, T, Kurosumi, M, Shimadzu, M, Yamamori, S, Sakamoto, G. (2001). Detection of Her-2/neu (c-erb B-2) DNA amplification in primary breast carcinoma. *Cancer*, 92(12), pp.2965–2974.
75. Hanahan, D Weinberg, RA. (2000). The hallmarks of cancer. *Cell*, 100, pp.57–70.
76. Hanahan, D. Weinberg, RA. (2011). Hallmarks of cancer: the next generation. *Cell*, 144, pp.646–674.
77. Friedman SL. (2003). Liver fibrosis - from bench to bedside. *Journal of Hepatology*, 38, (Suppl. 1), pp.S38–S53.
78. Kumar, V. Kumar, Abbas, A. Fausto, N. and J. Aster. (2010). *Pathological basis of disease* (Eds.) Robbins and Cotran. Saunders, Elsevier Inc. pp.14-29.
79. Flemming, JA. Yang, JD. Vittinghoff, E. Kim, WR. Terrault, NA. (2014). Risk prediction of hepatocellular carcinoma in patients with cirrhosis: the ADDRESS-HCC risk model. *Cancer* 120(22), pp.3485–3493.
80. Fattovich, G. Giustina, G. Degos, F. Tremolada, F. Diodati, G. Almasio, P. Nevens, F. Solinas, A. Mura, D. Brouwer, JT. Thomas, H. Njapoum, C. Casarin, C. Bonetti, P. Fuschi, P. Basho, J. Tocco, A. Bhalla, A. Galassini, R. Noventa, F. Schalm, SW. Realzi, G. (1997). Morbidity and mortality in compensated cirrhosis type C: a retrospective follow-up study of 384 patients. *Gastroenterology* 112(2), pp.463–472.
81. Patel, K. Gordon, S. Jacobson. Hézode, C. Oh, E. Smith, KM. Pawlotsky, JM. McHutchison, JG. (2004). Evaluation of a panel of non-invasive serum markers to differentiate mild from moderate-to advanced liver fibrosis in chronic hepatitis C patients. *Journal of Hepatology*, 41(6), pp.935–942.
82. Poynard *et al.* (2012). Relative performances of Fibrotest, Fibroscan, and biopsy for the assessment of the stage of liver fibrosis in patients with chronic hepatitis C: a step toward the truth in the absence of a gold standard. *Journal Hepatology*, 56(3), pp.541-548.
83. Kleckner, MS. (1960). *Cirrhosis of the liver*. Thomas Blackwell Ltd, Michigan, USA.
84. Cancer Research UK. (2015). *Statistics on liver cancer*. Available: <http://www.cancerresearchuk.org/cancer-info/cancerstats/types/liver/uk-liver-cancer-statistics>. Last accessed 23/02/2015.
85. Gomaa, A. Khan, S. Todedano, M. Waked, I. Taylor-Robinson, SD. (2008). Hepatocellular carcinoma: epidemiology, risk factors and pathogenesis. *World Journal Gastroenterology*, 14, pp.4300–4308.
86. Pons, F. Varela, M. & Llovet, JM. (2005). Staging systems in hepatocellular carcinoma. *HPB : The Official Journal of the International Hepato Pancreato Biliary Association*, 7(1), pp.35–41.

87. Kew, MC. (2013). Aflatoxins as a cause of hepatocellular carcinoma. *Journal of Gastrointestinal Liver Disease*, 22(3), pp.305–310.
88. DiBisceglie, AM. Rustgi, VK. Hoofnagle JH. Dusheiko, JM. & Lotze, MT. (1988). Hepatocellular carcinoma. *Annals of Internal Medicine*, 108, pp.390–401.
89. Chen, CJ. Yu, MW. & Liaw, YF. (1997). Characteristics and risk factors of hepatocellular carcinoma. *Journal of Gastroenterology & Hepatology*, 12, pp.ss294–ss308.
90. Huang, WS. Liao, LY. Wang, CS. Chen, PH. Huang, WS. Liao, LY. Wang, CS. & Chen, PH. (1999). Hepatocellular carcinoma presenting with acquired porphyria: A case report and review of the literature. *Chang Keng I Hseuh Tsa Chih*, 22, pp.111–116.
91. Okuda, K. (2000). Hepatocellular carcinoma. *Journal Hepatology*, 32, pp.225–237.
92. Takayama, T. Makuuchi, M. Hirohashi, S. Al. E. Takayama, T. Makuuchi, M. Hirohashi, S. & *et al.* (1990). Malignant transformation of adenomatous hyperplasia to hepatocellular carcinoma. *Lancet*, 336, pp.1150-1153.
93. Buendia, MA. (2000). Genetics of hepatocellular carcinoma. *Seminars in Cancer Biology*, 10, (3), pp.185–200.
94. Thorgeirsson, SS. & Grisham, JW. (2002). Molecular pathogenesis of human hepatocellular carcinoma. *Nature Genetics*, 31(4), pp.339–346.
95. Kudo, M. (2010). The 2008 Okuda lecture: Management of hepatocellular carcinoma: from surveillance to molecular targeted therapy. *Journal of Gastroenterology and Hepatology*, 25(3), pp.439–452.
96. EASL-EORTC. (2012). Clinical Practice Guidelines: Management of hepatocellular carcinoma. *Journal of Hepatology*, 56(4), pp.908–943.
97. El-Serag, HB. & Mason, AC. (1999). Rising incidence of hepatocellular carcinoma in the United States. *The New England Journal of Medicine*, 340(10), pp.745–750.
98. Llovet, JM. Brú, C. Bruix, J. (1999). Prognosis of hepatocellular carcinoma: the BCLC staging classification. *Seminars in Liver Disease*, 19(3), pp.329–338.
99. Subramaniam, S. Kelley, RA. Venook, AP. (2013). A review of hepatocellular carcinoma (HCC) staging systems. *Chinese Clinical Oncology*, 2(4), pp.33-45.
100. University of Maryland Medical Center (2015). *Primary brain tumour*. Available: <https://umm.edu/health/medical/reports/articles/brain-tumors-primary>. Last accessed 11/08/2015.
101. Hatzikirou, H. Deutsch, A. Schaller C. Simon, M. Swanson, K. (2005). Mathematical modelling of glioblastoma tumour development: a review. *Mathematical Models and Methods in Applied Sciences*, 15(11), pp.1779-1794.
102. Brain Cancer Health Centre (2015). *Malignant gliomas*. Available: <http://www.webmd.com/cancer/brain-cancer/malignant-gliomas>. Last accessed 12/08/2015.
103. American Brain Tumor Association (2014). *Tumor types: Ependymoma*. Available: <http://www.abta.org/brain-tumor-information/types-of-tumors/ependymoma.html>. Last accessed 15/08/2015.
104. Louis, DN. Ohgaki, H. Wiestler, OD. Cavenee, WK. Burger, PC. Jouvet, A. Kleihues, P. (2007). The 2007 WHO classification of tumours of the central nervous system. *Acta Neuropathologica*, 114(2), pp.97-109.
105. NICE Standards (2009). *Photodynamic therapy for brain tumours*. Available: <https://www.nice.org.uk/guidance/ipg290>. Last accessed 24/08/2015.
106. Ollesch, J. Heinze, M. Behrens, T. Bruning, T. Gerwert, K. Heise, M. (2014). It's in your blood: spectral biomarker candidates for urinary bladder cancer from automated FTIR spectroscopy. *Journal of Biophotonics*, 7(3-4), pp.210–221.
107. Backhaus, J. Meuller, R. Formanski, N. Szlama, N. Meerpohl, HG. Eidt, M. Bugert, P. (2010). Diagnosis of breast cancer with infrared spectroscopy from serum samples. *Vibrational Spectroscopy*, 52, pp.173–177.
108. Owens, G. L. Gajjar, K. Trevisan, J. Fogarty, SW. Taylor, SE. Da Gama-Rose, B. & Martin, F. L. (2014). Vibrational biospectroscopy coupled with multivariate analysis extracts potentially diagnostic features in blood plasma/serum of ovarian cancer patients. *Journal of Biophotonics*, 7(3-4), pp.200–209.

109. Gajjar, K. Trevisan, J. Owens, G. Keating, P.J. Wood, N.J. Stringfellow, H.F. & Martin, F.L. (2013). Fourier-transform infrared spectroscopy coupled with a classification machine for the analysis of blood plasma or serum: a novel diagnostic approach for ovarian cancer. *Analyst*, 138, pp.3917-3926.
110. Hands, J.R. Abel, P. Ashton, K.M. Dawson, T. Davis, R.W. McIntosh, A.J. & Baker, M.J. (2013). Investigating the rapid diagnosis of gliomas from serum samples using infrared spectroscopy and cytokine and angiogenesis factors. *Analytical Bioanalytical Chemistry*, 405, pp.73477-73495.
111. Hands, J.R. Dorling, K.M. Abel, P. Ashton, K.M. Brodbelt, A. Davis, C. Baker, M.J. (2014). Attenuated total reflection Fourier transform infrared (ATR-FTIR) spectral discrimination of brain tumour severity from serum samples. *Journal of Biophotonics*, 7(3-4), pp.189-199. doi: 10.1002/jbio.201300149.
112. Schmitt, J. Beekes, M. Brauer, A. Udelhoven, T. Lasch, P. & Naumann, D. (2002). Identification of scrapie infection from blood serum by Fourier transform infrared spectroscopy. *Analytical Chemistry*, 74, pp.3865-3868.
113. Lasch, P. Schmitt, J. Beekes, M. Udelhoven, T. Eiden, M. Fabian, H. & Naumann, D. (2003). Antemortem identification of bovine spongiform encephalopathy from serum using infrared spectroscopy. *Analytical Chemistry*, 75(23), pp.6673-6678.
114. Martin, T.C. Moecks, J. Belousov, A. Cawthraw, S. Dolenko, B. Eiden, M. Petrich, W. (2004). Classification of signatures of Bovine Spongiform Encephalopathy in serum using infrared spectroscopy. *Analyst*, 129(10), pp.897-901.
115. Staib, A. Dolenko, B. Fink, D.J. Früh, J. Nikulin, A.E. Otto, M. Petrich, W. (2001). Disease pattern recognition testing for rheumatoid arthritis using infrared spectra of human serum. *Pharmacogenomics*, 308(1-2), pp.79-89.
116. Peng, L. Wang, G. Yao, H.L. Huang, S. Wang, Y. Tao, Z. Li, Y. (2009). FTIR-HATR to identify beta-thalassemia and its mechanism study. *Guang Pu Xue Yu Guang Pu Fen Xi Guang Pu*, 29(5), pp.1232-1236.
117. Petrov, M.S. Gordetzov, A.S. & Kukosh, M.V. (2007). Early prediction of severity in acute pancreatitis using infrared spectroscopy of serum. *Pancreatology*, 7(5-6), pp.451-458.
118. Perez-Guaita, D. Ventura-Gayete, J. Perez-Rambia, C. Sancho-Andreu, M. Garrigues, S. De la Guardia, M. (2012). Protein determination in serum and whole blood by attenuated total reflectance infrared spectroscopy. *Analytical Bioanalytical Chemistry*, 404(3), pp.649-656.
119. Sheng, D. Liu, X. Li, W. Wang, X. (2013). Distinction of leukemia patients' and healthy persons' serum using FTIR spectroscopy. *Spectrochimica Acta A. Molecular Biomolecular Spectroscopy*, 15(101), pp.228-232.
120. Peuchant, E. Richard-Harston, S. Bourdel-Marchasson, I. Dartigues, J.F. Letenneur, L. Barberger-Gateau, P. & Daniel, J.Y. (2008). Infrared spectroscopy: a reagent-free method to distinguish Alzheimer's disease patients from normal-aging subjects. *Translational Research: The Journal of Laboratory and Clinical Medicine*, 152(3), pp.103-112.
121. Carmona, P. Molina, M. Calero, M. Bermejo-Pareja, F. Martínez-Martín, P. & Toledano, A. (2013). Discrimination analysis of blood plasma associated with Alzheimer's disease using vibrational spectroscopy. *Journal of Alzheimer's disease*, 34(4), pp.911-920.
122. Griebe, M. Daffertshofer, M. Stroick, M. Syren, M. Ahmad-Nejad, P. Neumaier, M. & Fatar, M. (2007). Infrared spectroscopy: A new diagnostic tool in Alzheimer disease. *Neuroscience Letters*, 420(1), pp.29-33.
123. Lacombe, C. Untereiner, V. Gobinet, C. Zater, M. Sockalingum, G.D. Garnotel, R. (2015). Rapid screening of classic galactosemia patients: a proof-of-concept study using high-throughput FTIR analysis of plasma. *Analyst*, 140(7), pp.2280-2286.
124. Untereiner, V. Sockalingum, G.D. Garnotel, R. Gobinet, C. Ramaholimihaso, F. Ehrhard, F. Thiéfin, G. (2014). Bile analysis using high-throughput FTIR spectroscopy for the diagnosis of malignant biliary strictures: a pilot study in 57 patients. *Journal of Biophotonics*, 7(3-4), pp.241-253.

125. Eysel, HH, Jackson, M. Nikulin, A. Somorjai, RL. Thomson, GTD. Mantsch, H.H. (1997). A novel diagnostic test for arthritis: Multivariate analysis of infrared spectra of synovial fluid. *Biospectroscopy*, 3(2), pp.161–167.
126. Scott, D. A. Renaud, D. E. Krishnasamy, S. Meriç, P. Buduneli, N. Cetinkalp, S. Liu, KZ. (2010). Diabetes-related molecular signatures in infrared spectra of human saliva. *Diabetology & Metabolic Syndrome*, 2, 48 (An abstract).
127. Whiteman, SC. Yang, Y. Jones, JM. Spiteri, MA. (2008). FTIR spectroscopic analysis of sputum: preliminary findings on a potential novel diagnostic marker for COPD. *Therapeutic Advances in Respiratory Disease*, 2(1), pp.23–31.
128. Travo, A. Paya, C. Deleris, G. Colin, J. Mortemousque, B. Forfar, I. (2013). Potential of FTIR spectroscopy for analysis of tears for diagnosis purposes. *Analytical Bioanalytical Chemistry*, 406, pp.2367–2376.
129. Graça, G. Moreira, AS. Correia, AJV. Goodfellow, BJ. Barros, AS. Duarte, IF. Gil, AM. (2013). Mid-infrared (MIR) metabolic fingerprinting of amniotic fluid: A possible avenue for early diagnosis of prenatal disorders? *Analytica Chimica Acta*, 764, pp.24–31.
130. Liu, KZ. & Mantsch, HH. (1999). Simultaneous quantitation from infrared spectra of glucose concentrations, lactate concentration and lecithin/sphingomyelin ratio in amniotic fluid. *American Journal of Obstetrics & Gynecology*, 180(696), pp.702–708.
131. Petrich, W. Lewandrowski, KB. Muhlestein, JB. Hammond, MEH. Januzzi, JL. Lewandrowski, EL. Zerbacka, R. (2009). Potential of mid-infrared spectroscopy to aid the triage of patients with acute chest pain. *Analyst*, 134, pp.1092–1098.
132. Pichardo-Molina, JL. Frausto-Reyes, C. Barbosa-Garcia, O. Heurta-Franco, R. Gonzalez-Trujillo, J. L. Ramirez-Alvarado, CA. Medina-Gutierrez, C. (2007). Raman spectroscopy and multivariate analysis of serum samples from breast cancer patients. *Lasers in Medical Sciences*, 22(4), pp.229–236.
133. Harris, AT. Rennie, A. Waqar-Uddin, H. Wheatley, SR. Ghosh, SK. Martin-Hirsch, DP. Upile, T. (2010). Raman spectroscopy in head and neck cancer. *Head Neck Oncology*, 2, pp.26–31.
134. Sahu, A. Nandakumar, N. Sawant, S. & Krishna, CM. (2015). Recurrence prediction in oral cancers: a serum Raman spectroscopy study. *Analyst*, 140(7), pp.2294–2301.
135. Sahu, A. Dalai, K. Naglot, S. Aggarwal, P. Krishna, M. (2013). Serum based diagnosis of asthma using Raman spectroscopy: An early phase pilot study. *Plos One*, 8(11), p. e7892.
136. González-Solís, JL. Martínez-Espinosa, JC. Torres-González, LA. Aguilar-Lemarroy, A. Jave-Suárez, LF, & Palomares-Anda, P. (2013). Cervical cancer detection based on serum sample Raman spectroscopy. *Lasers in Medical Science*, 29(3), pp.979–985.
137. Taleb, I. Thieffin, G. Gobinet, C. Untereiner, V. Bernard-Chabert, B. Heurgue, A. Sockalingum, GD. (2013). Diagnosis of hepatocellular carcinoma in cirrhotic patients: a proof-of-concept study using serum micro-Raman spectroscopy. *Analyst*, 138, pp.4006–4012.
138. Neugebauer, U. Trenkmann, S. Bocklitz, T. Schmerler, D. Kiehntopf, M. Popp, J. (2014). Fast differentiation of SIRS and sepsis from blood plasma of ICU patients using Raman spectroscopy. *Journal of Biophotonics*, 7(3-4), pp.232–240.
139. Ryzhikova, E. Kazakov, O. Halamkova, L. Celmins, D. Malone, P. Molho, E. Lednev, IK. (2015). Raman spectroscopy of blood serum for Alzheimer's disease diagnostics: specificity relative to other types of dementia. *Journal of Biophotonics*, 8(7), pp.584–596.
140. Esmonde-White, KA. Mandair, GS. Raaii, F. Jacobson, JA. Miller, BS. Urquhart, AG. Morris, MD. (2009) Raman spectroscopy of synovial fluid as a tool for diagnosing osteoarthritis. *Journal of Biomedical Optics*, 14(3), p. 034013.
141. Bispo, JA. M.Silveira, L. Vieira, E. (2013). Determining the amounts of urea and glucose in urine of patients with renal complications from diabetes mellitus and hypertension by near-infrared Raman spectroscopy. In (Ed). S. Fernandes, AB, GL. Coté, SPIE BiOS. *International Society for Optics and Photonics*. p. 85910T.
142. Filik, J. Stone, N. (2008). Analysis of human tear fluid by Raman spectroscopy. *Analytica Chimica Acta*, 616(2), pp.177–184.

143. Lamcharfi, E. Cohen-Solal, C. Marquet, M. Lutton, C. Dupre, J. Meyer, C. (1997). Determinations of molecular associations of some hydrophobic and hydrophilic bile acids by infrared and Raman spectroscopy. *Journal European Biophysics*, 54(4), pp.285–291.
144. Lin, J. Chen, R. Feng, S. Pan, J. Li, Y. Chen, G. Zeng, H. (2011). A novel blood plasma analysis technique combining membrane electrophoresis with silver nanoparticle-based SERS spectroscopy for potential applications in non-invasive cancer detection. *Nanomedicine: Nanotechnology, Biology and Medicine*, 7(5), pp.655–663.
145. Lin, D. Feng, S. Pan, J. Chen, Y. Lin, J. Chen, G. Chen, R. (2011). Colorectal cancer detection by gold nanoparticle based surface-enhanced Raman spectroscopy of blood serum and statistical analysis. *Optics Express*, 19(14), pp.13565–13577.
146. Feng, S. Chen, R. Lin, J. Pan, J. Chen, G. Li, Y. Zeng, H. (2010). Nasopharyngeal cancer detection based on blood plasma surface-enhanced Raman spectroscopy and multivariate analysis. *Biosensors and Bioelectronics*, 25(11), pp.2414–2419.
147. Li, X. Yang, T. Lin, J. (2012). Spectral analysis of human saliva for detection of lung cancer using surface-enhanced Raman spectroscopy. *Journal of Biomedical Optics*, 17(3), 037003 (An abstract).
148. Bonifacio, A. Dalla Marta, S. Spizzo, R. Cervo, S. Steffan, A. Colombatti, A. Sergo, V. (2014). Surface-enhanced Raman spectroscopy of blood plasma and serum using Ag and Au nanoparticles: a systematic study. *Analytical and Bioanalytical Chemistry*, 406(9-10), pp.2355–2365.
149. Choi, S. Moon, SW. Shin, JH. Park, HK. & Jin, KH. (2014). Label-free biochemical analytic method for the early detection of adenoviral conjunctivitis using human tear biofluids. *Analytical Chemistry*, 86(22), pp.11093–11099.
150. Del Mistro, G. Cervo, S. Mansutti, E. Spizzo, R. Colombatti, A. Belmonte, P. Bonifacio, A. (2015). Surface-enhanced Raman spectroscopy of urine for prostate cancer detection: a preliminary study. *Analytical and Bioanalytical Chemistry*, 407(12), pp.3271–3275.
151. Pike Technologies, Inc. (2014). *FT-IR sampling techniques*. Available ([http://www.piketech.com/files/pdfs/MIRacle\\_PDS\\_2015.pdf](http://www.piketech.com/files/pdfs/MIRacle_PDS_2015.pdf)). Last accessed 04/03/2016.
152. Lovergne, L. Clemens, G. Lukaszewski, R. Untereiner, V. Sockalingum, GD. Baker, MJ. (2015). Investigating optimum sample preparation for infrared spectroscopic serum diagnostics. *Analytical Methods*, 7, pp.7140-7149.
153. Filik, J. & Stone, N. (2007). Drop coating deposition Raman spectroscopy of protein mixtures. *Analyst*, 132, (6), pp.544–550.
154. Andor Technologies. (2011). *Spectrograph properties*, Available: <http://www.andor.com/learning-academy/spectrograph-properties-basic-principles-of-a-spectrograph>. Last accessed 11/02/2017.
155. InPhotonics (2006). *Raman fibre optic probes*. Available: <http://www.inphotonics.com/opticallayout.htm>. Last accessed 03/03/2016.
156. Horiba Ltd. (2017) *HE spectrograph*. Available: (<http://www.horiba.com/uk/scientific/products/raman-spectroscopy/raman-spectrometers/modular-and-fiber-coupled-raman/details/he-spectrograph-144/>). Last accessed 14/02/2017.
157. Bruix, J. Sherman, M. Llovet, JM. *et al.* (2001). Clinical management of hepatocellular carcinoma: conclusions of the Barcelona-2000 EASL conference: European Association for the Study of the Liver. *Journal of Hepatology*, 35, pp.421-430.
158. Deegan RD. Bakajin, O. Dupont, T. Huber, G. Nagel, S. Witten, T. (1997). Capillary flow as the cause of ring stains from dried liquid drops. *Nature*, 389, pp.827-829.
159. Ristenpart, W. Kim, P. Domingues, C. Wan, J. and Stone, H. (2007). Influence of substrate conductivity on circulation reversal in evaporating drops. *Physical Review Letters*, 99, pp.234-252.
160. Yunker, PJ, Still, T. Loh, MA. Yodh, A. (2011). Suppression of the coffee-ring effect by shape-dependent interactions. *Nature*, 476, pp.308-311.
161. Esmonde-White, KA. Esmonde-White, FW. Morris, MD. Roessler, BJ. (2014). Characterization of biofluids prepared by sessile drop formation. *Analyst*, 139(11), pp.2734-2741.

162. Ollesch, J. Drees, SL. Heise, HM. Behrens, T. Brüning, T. and Gerwert, K. (2013). FTIR spectroscopy of biofluids revisited: an automated approach to spectral biomarker identification. *Analyst*, 138(14), pp.4092-4102.
163. Plebani, M. Carraro, P. (1997). Mistakes in a stat laboratory: types and frequency. *Clinical Chemistry*. 43, pp.348-351.
164. Schleicher, E. (2006). Clinical chemistry laboratory: current status, problems and diagnostic prospects. *Analytical Bioanalytical Chemistry*, 384, pp.124-131.
165. Lovergne, L. Bouzy, P. Untereiner, V. Garnotel, R. Baker, MJ. Thiéfin, G. Sockalingum, GD. (2016). Biofluid infrared spectro-diagnostics: pre-analytical considerations for clinical applications. *Faraday Discussions*, 187, pp.521-537.
166. Bedossa, P. Poynard, T. (1996). An algorithm for the grading of activity in chronic hepatitis C. The METAVIR Cooperative Study Group. *Journal of Hepatology*, 24, pp.289-293.
167. Burnett, NG. Jefferies, SJ. Benson, RJ. Hunt, DP. Treasure, FP. (2005). Years of lives lost (YLL) is an important measure of population-burden and should be considered when allocating research funds. *British Journal of Cancer*, 92, pp.241-245.
168. Cancer Research UK. (2018). *Statistics and outlook for brain tumours*. Available from: <https://www.cancerresearchuk.org/about-cancer/brain-tumours/survival>. Last accessed 12/02/2018.
169. Silcocks, P. Steward, J. Woods, H. (2005). *Brain, Chapter 4* in: Quinn, M. Wood, H. Cooper, N.M and Rowan, S. (eds) *Cancer Atlas of the United Kingdom and Ireland 1991-2000: Studies on Medical and Population Subjects No 68*. The Office of National Statistics, London; Palgrave Macmillan.
170. Stupp, R. Tonn, JC, Brada, M. Pentheroudakis, G. (2010), High-grade malignant glioma: ESMO Clinical Practice Guidelines for diagnosis, treatment and follow-up. *Annual of Oncology*, 21(5), pp.190-193.
171. Bruner, JM. Inouye, L. Fuller, GN. Langford, LA. (1997). Diagnostic discrepancies and their clinical impact in a neuropathology referral practice. *Cancer*, 79(4), pp.796-803.
172. Sobottka, SB. Geiger, K.D., Salzer, R. Schackert, G. Krafft, C. (2009). Suitability of infrared spectroscopic imaging as an intraoperative tool in cerebral glioma surgery. *Analytical Bioanalytical Chemistry*, 3931, pp.87-195.
173. Hands, JR. Clemens, C. Stables, R. Ashton, K. Brodbelt, A. Davis, C. Dawson, TP. Jenkinson, MD. Lea, RW. Walker, C. and Baker, MJ. (2016). Brain tumour differentiation: rapid stratified serum diagnostics via attenuated total reflection Fourier-transform infrared spectroscopy. *Journal of Neurooncology*, 127, pp.463-472.
174. Maquelin, K. Kirschner, C. Choo-Smith, LP. van den Braak, N. Endtz, HP. Naumann, D. and Puppels, GJ. (2002) Identification of medically relevant microorganisms by vibrational spectroscopy. *Journal of Microbiological Methods*, 51, pp.255-271.
175. Patel, II. Harrison, WJ. Kerns, JG. Filik, J. Wehbe, K. Carmichael, PL, Scott, AD. Philpott, MP. Frogley, MD. Cinque, G. Martin, FL. (2012). Isolating stem cells in the inter-follicular epidermis employing synchrotron radiation-based Fourier-transform infrared microspectroscopy and focal plane array imaging. *Analytical Bioanalytical Chemistry*, 404, pp.1745-1758.
176. Thumanu, K. Sangrajang, S. Khuhaprema, T. Kalalak, A. Tanthanuch, W. Pongpiachan, S. Heraud, P. (2014). Diagnosis of liver cancer from blood sera using FTIR microspectroscopy: a preliminary study. *Journal of Biophotonics*, 3/4, pp.222-231.
177. Gupt, D. and Lis, GG. (2010). Pretreatment serum albumin as a predictor of cancer survival: A systematic review of the epidemiological literature. *Nutrition Journal*. 9, pp.69-78.
178. Jiang, J. Nilsson-Ehrle, P. Xu, N. (2006). Influence of liver cancer on lipid and lipoprotein metabolism. *Lipids in Health and Disease*, 5(4), pp.17-26.
179. Adkins JN, Varnum SM, Auberry KJ, Moore RJ, Angell NH, Smith RD, Springer, DL, Pounds, JG. (2002). Towards a human blood serum proteome: analysis by multidimensional separation coupled with mass spectrometry. *Molecular Cell Proteomics* 1(12), pp.947-955.
180. Pieper, R. *et al.* (2003). The human serum proteome: Display of nearly 3700 chromatographically separated protein spots on two-dimensional electrophoresis gels and identification of 325 distinct proteins. *Proteomics*, 3, pp.1345-1364.

181. Zhang, AH. Sun, H. Yan, GL. Han, Y. Wang, XJ. (2013). Serum proteomics in biomedical systematic review. *Applied Biochemistry and Biotechnology*, 170(4), pp.774-786.
182. Dunn, WB. *et al.* (2015). Molecular phenotyping of a UK population: defining the human serum metabolome. *Metabolomics*. 11, pp.9-26.
183. Taylor, SE. Cheung, KT. Patel, II. Trevisan, J. Stringfellow, HF. Ashton, KM. Wood, NJ. Keating, PJ. Martin-Hirsch, PL. Martin, FL (2011). Infrared spectroscopy with multivariate analysis to interrogate endometrial tissue: a novel and objective diagnostic approach. *British Journal of Cancer*, 104(5), pp.790-797.
184. Poon, KW. Lyng, FM. Knief, P. Howe, O. Meade, AD. Curtin, JF. Byrne, HJ. Vaughan, J. (2012). Quantitative reagent-free detection of fibrinogen levels in human blood plasma using Raman spectroscopy. *Analyst* 137(8), pp.1807-1814.
185. Bonnier, F. Baker, MJ. Byrne, HJ. (2014). Vibrational spectroscopic analysis of body fluids: avoiding molecular contamination using centrifugal filtration. *Analytical Methods*, 14, pp.5155-5160.
186. Nagase, Y. Yoshida, S. Kamiyama, K. (2005). Analysis of human tear fluid by Fourier transform infrared spectroscopy. *Biopolymers*, 79, (1), pp.18-27.
187. Borchman, D. Foulks, GN. Yappert, MC. Tang, D. Ho, DV. (2007). Spectroscopic evaluation of human tear lipids. *Chem. Phys. Lipids*, 147(2), pp.87-102.
188. Mitchell, BL. Yasui, Y. Ci, C. Fitzpatrick, AL. Lampe, PD. (2005). Impact of freeze-thaw cycles and storage time on plasma samples used in mass spectrometry-based biomarker discovery projects. *Cancer Information*, 1, pp.98-104.
189. Atlanta Biologicals (2017). *Technical bulletin: heat inactivation of serum*. Available: <https://research.missouri.edu/cic/files/tb-hi.pdf>. Last accessed 12/08/2017.
190. Dubrownny, N, Smith, S, Hanna, S. (2005). From vein to the analyser: sample handling impact. BD-BCI workshop. *AACC annual meeting*.
191. Bonnier, F. Petitjean, F. Baker, MJ. Byrne, HJ. (2014). Improved protocols for vibrational spectroscopic analysis of body fluids. *Journal of Biophotonics* 7, pp.167-179.
192. De Gelder, J. De Gussem, K. Vandenabeele, P. Moens, L. (2007). Reference database of Raman spectra of biological molecules. *Journal of Raman Spectroscopy*, 38(9), pp.1133-1147.
193. Rygula, A. Majzner, K. Marzec, KM. Kaczor, A. Pilarczyk, M. Baranska, M. (2013). Raman spectroscopy of proteins: a review. *Journal of Raman Spectroscopy*, 44, pp.1061-1076.
194. Draux, F. Jeannesson, P. Beljebbar, A. Tfayli, A. Fourre, N. Manfait, M. Sockalingum, GD. (2009). Raman spectral imaging of single living cancer cells: a preliminary study. *Analyst*, 134(3), pp.542-8.
195. Ortiz, C. Zhang, D. Xie, Y. Ribbe, AE. & Ben-Amotz, D. (2006). Validation of drop coating deposition Raman method of protein analysis. *Analytical Biochemistry*, 353(2), pp.157-166.
196. Ivanov, I. Zhbankov, RG. Korolenko, EA. Korolik, EV. Meleshchenko, LA. Marchewka, M. and Ratajczak, H. (1994). Infrared and Raman spectroscopic studies of the structure of human serum albumin under various ligand loads. *Journal of Applied Spectroscopy*, 60, pp.30, (5-3116)
197. Hughes, C. Brown, M. Clemens, G. Henderson, A. Monjardez, G. Clarke, NW. Gardner, P. (2014). Assessing the challenges of Fourier transform infrared spectroscopic analysis of blood serum. *Journal of Biophotonics* 7, pp.180-188.
198. Hsieh, S.-Y. Chen, RK, Pan, YH & Lee, HL. (2006). Systematical evaluation of the effects of sample collection procedures on low-molecular-weight serum/plasma proteome profiling. *Proteomics*, 6(10), pp.3189-3198.
199. Timms, JF. Arslan-Low, E. Gentry-Maharaj, A. *et al.* (2007). Preanalytic influence of sample handling on SELDI-TOF serum protein profiles. *Clinical Chemistry*, 53(4), pp.645-56.
200. Yin P, Lehmann R, Xu G. (2015). Effects of pre-analytical processes on blood samples used in metabolomics studies. *Analytical Bioanalytical Chemistry*, 407, pp.4879-4792.
201. Cuhadar, S. Koseoglu, M. Atay, A. Dirican, A. (2013). The effect of storage time and freeze-thaw cycles on the stability of serum samples. *Biochemia Medica*, 23(1), pp.70-77.
202. Cao, E. Chen, Y. Cui, Z. Foster, PR. (2003). Effect of freezing and thawing rates on denaturation of proteins in aqueous solutions. *Biotechnology and Bioengineering*, 82, pp.685-690.

203. Sherman, M. Burak, K. Maroun, J. Metrakos, P. Knox, JJ. *et al.* (2011). Multidisciplinary Canadian consensus recommendations for the management and treatment of hepatocellular carcinoma. *Current Oncology*, 18, pp.228-240.
204. Schraiber L dos S, de Mattos AA, Zanutelli ML, *et al.* (2016). Alpha-fetoprotein level predicts recurrence after transplantation in hepatocellular carcinoma. Fan, H, ed. *Medicine*. 95, pp.2478-2485.
205. Yim SH, Chung YJ. (2010). An overview of biomarkers and molecular signatures in HCC, *Cancers*, 2, pp.809-823.
206. Llovet, JM. Brú, C. & Bruix, J. (1999). Prognosis of hepatocellular carcinoma: the BCLC staging classification. *Seminars in Liver Disease*, 19(3), pp.329–338.
207. Vroman, L. Adams, AL. Fischer, GC. Munoz, PC. (1980). Interaction of high molecular weight kininogen, factor XII, and fibrinogen in plasma at interfaces. *Blood*. 55(1), pp.156–159.
208. Nishikawa, Y. Ukida, M. Matsuo, R. Omori, N. and Tsuji, TY. (1994). Ca<sup>2+</sup> influx initiates death of hepatocytes injured by activation of complement, *Liver*, 14, pp.200–205.
209. Kedderis, GL. (1996). Biochemical basis of hepatocellular injury. *Toxicological Pathology*, 24(1), pp.77–83.
210. Kraus-Friedmann, N. (1990). Calcium sequestration in the liver. *Cell Calcium* 11(10), pp.625–640.
211. Saade, J. Pacheco, MTT, Roderigues, MR. and Silveira Jr, L. (2008). Identification of hepatitis C in human blood serum by near-infrared Raman spectroscopy. *Spectroscopy*, 22, pp.387–395.
212. Liaw, A. and Wiener, M. (2002). Classification and regression by Random forest. *R news*, 2, pp.18-22.
213. Smith, BR. Ashton, KM. Brodbelt, A. Dawson, T. Jenkinson, MD. Hunt, NT. Palmer, DS, Baker, MJ. (2016). Combining random forest and 2D correlation analysis to identify serum spectral signatures for neuro-oncology. *Analyst*, 141(12), pp.3668-3678.

**| PRESENTATIONS  
AND  
PUBLICATIONS |**

# Serum Spectroscopy: Freeze-Thaw and Drying Sample Preparation

Shawn Hussain<sup>1,2</sup>, Allison E. Jones<sup>2</sup>, Ganesh D. Sockalingum<sup>1</sup>, Matthew J. Baker<sup>3</sup>

<sup>1</sup>MÉDIAN Biophotonique et Technologies pour la Santé, Université de Reims Champagne-Ardenne, FRE CNRS 3481 MEDyC, UFR de Pharmacie, SFR Cap Santé, 51096 Reims Cedex, France.

<sup>2</sup>Centre for Materials Science, Division of Chemistry, School of Forensic and Investigative Sciences, JB Firth Building, University of Central Lancashire, Preston, England, PR1 2HE.

<sup>3</sup>WestCHEM, Department of Pure and Applied Chemistry, University of Strathclyde, Glasgow G1 1XL, UK.

Email: shawn.hussain@univ-reims.fr

AIM

To understand the effects of freeze-thaw and environmental drying using transmission, ATR-FTIR, and Raman micro-spectroscopy on human serum content

INTRODUCTION

- Biospectroscopy is quickly becoming an effective tool within medical diagnostics. Recent global developments within biomedical spectroscopy, means we are realising the potential of biofluid and serum analysis for rapid biochemical snapshots for underlying disease functionality; an endeavour previously focused on tissues.
- Serum spectroscopy sample preparation is still unexplored. To date focus is towards serum diagnostics for health and pathology, however, little is known about serum sample stability for freeze-thaw and environmental drying.
- Potential molecular changes in sample integrity due to freeze-thaw cycles and serum environmental ageing will be observed using both Raman and infrared spectroscopy.

METHODOLOGY

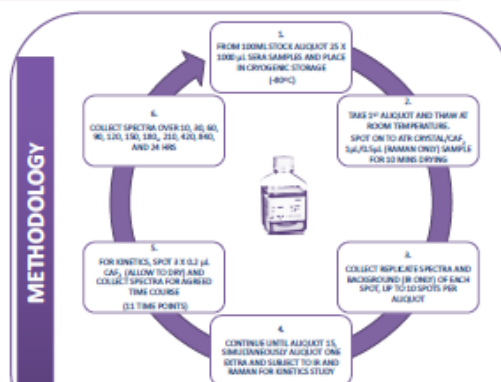


Fig 1. Experimental 6 step procedural plan to test the effect of freeze-thaw/drying on human mixed pooled serum samples. NB. Step 6 denotes end of cycle.

## SPECTRAL & DATA ANALYSIS FLOW-THROUGH

**INFRARED PARAMETERS**

ATR - Ge crystal, (4cm<sup>-1</sup>) resolution, 32 coadded scans - 3 spots, 600-4000cm<sup>-1</sup>

Spectral collection on FTIR Cary 600 (fig 2)

1 µL pipetted on to crystal (9 spots/ aliquot)-air dried for FT & K study

0.2 µL pipetted on CaF<sub>2</sub> substrate, dried and spectra collected in triplicate 11 (fig 1), with 4cm<sup>-1</sup> resolution over 600-4000cm<sup>-1</sup> for transmission kinetics study

Fig 2. FTIR Agilent Cary 600 series at UCLan.

**RAMAN PARAMETERS**

Calibration on silicon to 520.8 cm<sup>-1</sup>

Spectral collection on LabRam 800 (fig 3)

785 nm laser at 100% filter, 100 hole, 400 slit, collect spectra between 500 - 2000 cm<sup>-1</sup> for 20 seconds for both freeze-thaw and drying studies

Pipette 0.5µL directly on CaF<sub>2</sub> substrates - allow 10 minutes air drying, then record spectra in triplicate

Fig 3: Horiba Jobin-Yvon LabRAM HR800 spectrometer at UCLan.

**DATA COLLECTION & PROCESSING**

Raman pre-processing will be carried out using LabSpec 6 spectroscopy software suite (HORIBA Scientific) and MATLAB version 7.8.0 (R2009a) (The Math-Works, Inc., USA) using in-house written software

Raman data will be background subtracted (5<sup>th</sup> order polynomial and smoothed using 7 point s) (LabSpec 6), vector normalised, and PC-based noise reduced (MATLAB)

IR spectra will be vector normalised and PC-based noise reduced for both freeze-thaw and drying studies

The fingerprint region (1000-1800cm<sup>-1</sup>) will be selected for MVA

PCA and PC-DFA will be performed on the data sets, followed by standard deviation for freeze-thaw cycle

# Serum Spectroscopy: Freeze-thaw Sample Preparation for Serum Stability and Kinetics

Shawn Hussain<sup>1</sup>, Graeme Clemens<sup>1</sup>, Ganesh D. Sockalingum<sup>2</sup>, Matthew J. Baker<sup>3</sup>

<sup>1</sup>Centre for Materials Science, Division of Chemistry, School of Forensic and Investigative Sciences, JB Path Building, University of Central Lancashire, Preston, England, PR1 2HE

<sup>2</sup>MCDM (Biophysique et Technologie pour la Santé), Université de Reims Champagne-Ardenne, FRE CNRS 3491 MEDyG, UFR de Pharmacie, SFR Cap Santé, 81000 Reims Cedex, France.

<sup>3</sup>MedChem, Department of Pure and Applied Chemistry, University of Strathclyde, Glasgow G1 1DL, UK

Email: shussain1@uclan.ac.uk



**AIM**  
To understand the effects of freeze-thaw and environmental drying employing transmission, ATR-FTIR, and Raman micro-spectroscopy on human serum content

## INTRODUCTION

- Biospectroscopy is quickly becoming an effective tool within medical diagnostics. Recent global developments within biomedical spectroscopy, means we are realising the potential of biofluid and serum analysis for rapid biochemical snapshots for underlying disease functionality; an endeavour previously focused on tissues.
- Serum spectroscopy sample preparation is still unexplored. To date focus is towards serum diagnostics for health and pathology, however, little is known about serum sample stability for freeze-thaw and environmental drying.
- Potential molecular changes in sample integrity due to freeze-thaw cycles and serum environmental ageing will be observed using both Raman and infrared spectroscopy.

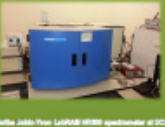
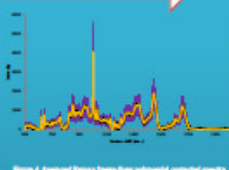
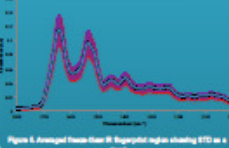
## METHODOLOGY



- Raman micro-spectroscopy, transmission and ATR-FTIR spectra were collected from the serum after drying for 10 minutes
- Transmission and ATR-FTIR spectra were collected at 4cm<sup>-1</sup> resolution, with 32 co-added scans over 600-4000cm<sup>-1</sup> for both freeze-thaw and drying studies (see Figure 1 for full procedure)
- Raman measurements (500-2000 cm<sup>-1</sup>, 785nm laser, 600 g/mm grating, 100% filter) were collected for 20 seconds

Figure 1. Experimental flow procedural plan to test the effect of freeze-thawing on human serum protein when subjected to 10 days 4 months and 1 year.

## SPECTRAL & DATA ANALYSIS FLOW-THROUGH

INFRARED PARAMETERS	RAMAN PARAMETERS	DATA COLLECTION & PROCESSING
<ul style="list-style-type: none"> <li>ATR - Ge crystal (4cm<sup>-1</sup>) resolution, 32 co-added scans every 3 spots, measured over 600-4000cm<sup>-1</sup></li> <li>Spectral collection on FTIR Cary 600 (see figure 2)</li> <li>1 µL pipetted on to crystal (2 spots per aliquot) and dried for freeze-thaw stability study</li> <li>0.2 µL pipetted on CaF<sub>2</sub> substrate, dried and spectra collected in HyRate II (see Figure 1), with 4cm<sup>-1</sup> resolution over 600-4000cm<sup>-1</sup> for transmission kinetics study</li> </ul>  <p>Fig 2. FTIR Agilent Cary 600 spectrometer at UCLan</p>	<ul style="list-style-type: none"> <li>Calibration on silicon to 520.6 cm<sup>-1</sup></li> <li>Spectral collection on LabRam 800 (see Figure 3)</li> <li>785 nm laser at 100% flux 100 hole, 400 slit, collected spectra between 500 - 3000 cm<sup>-1</sup> for 20 seconds for both freeze-thaw and drying studies</li> <li>Pipette 0.5 µL directly on CaF<sub>2</sub> substrate - allow 10 minutes to dry, then record spectra in HyRate II</li> </ul>  <p>Fig 3. Thermo Jobin-Yvon LabRam 800 Raman spectrometer at UCLan</p>	<ul style="list-style-type: none"> <li>Raman pre-processing was carried out using LabSpec 6 spectroscopy software suite (HORIBA Scientific) and MATLAB version 7.8.0 (R2008a) (The Math-Works, Inc., USA) using in-house written software</li> <li>Raman data was background subtracted (9<sup>th</sup> order polynomial and smoothed using 7 point <math>\sigma</math>) (LabSpec 6), vector normalised, and PO-based noise reduced (MUTLAB)</li> <li>IR spectra were vector normalised and PO-based noise reduced for both freeze-thaw and drying studies</li> <li>The fingerprint region (1000-1800cm<sup>-1</sup>) was selected for PCA</li> <li>PCA and PO-PCA were performed on the data sets, followed by standard deviation for freeze-thaw cycle (see Figure 4 and 5)</li> </ul>  <p>Figure 4. Average Raman freeze-thaw post-thaw corrected spectra (background subtracted) showing 97% on a scale</p>  <p>Figure 5. Average freeze-thaw IR fingerprint region showing 97% on a scale</p>

### Infrared & Raman Drying Kinetics Study

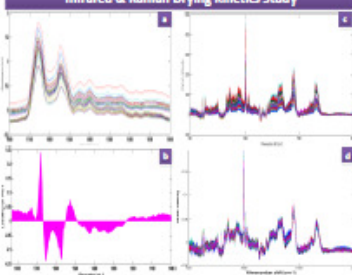


Figure 6. (a) IR fingerprint region cut spectra for kinetic study (n=22). (b) IR fingerprint region cut spectral scaling on PCA. (c) Raman spectra vector normalised, 7 point smoothed (PO-PCA). (d) Raman drying spectra pre-processed with polynomial, smoothing, vector normalisation and PO based noise reduction.

## RESULTS

### Infrared & Raman Freeze-thaw Stability Study

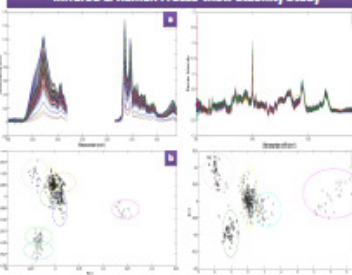


Figure 7. (a) IR fingerprint region cut spectra (n=22). (b) PO-PCA scores 1 and 2 showing separation of freeze-thaw 10 cycles in clusters. (c) showing 9<sup>th</sup> order 7 point smoothed polynomial corrected, vector normalised and PO based noise reduced Raman freeze-thaw cycles (n=22). (d) PO-PCA showing Raman freeze-thaw cycles (1-10) and 100% 10 cycle (n=22). 97% noise are applied to the spectra only.

### FUTURE WORK

IR and Raman spectral models will be blind tested with further spectral data sets

Further statistical evaluation will be carried out and the drying kinetics study will be run again for 24 hours



### 3. Poster presented at CLIRCON17, Manchester, UK and at Raman4Clinics,

#### Castelldefels, Spain

– won 1<sup>st</sup> prize for best research poster



## A SPECTROSCOPIC INVESTIGATION OF LIVER FIBROSIS VIA A LIQUID MACRO RAMAN APPROACH



S. R. Hussain<sup>1,2</sup>, A. E. Jones<sup>2</sup>, M. J. Baker<sup>3</sup>, A. Beljebbar<sup>1</sup>, G. Thiéfin<sup>1,4</sup>, G. D. Sockalingum<sup>1</sup>



<sup>1</sup> Université de Reims Champagne-Ardenne, CNRS UMR 7369-MEDyC, MeDIAN-Biophotonique et Technologies pour la Santé, UFR de Pharmacie, 51 rue Cognacq-Jay, 51096 Reims Cedex, France.  
<sup>2</sup> Centre for Materials Science, Division of Chemistry, JB Firth Building, University of Central Lancashire, Preston, PR1 2HE, UK.  
<sup>3</sup> WESTChem, Department of Pure and Applied Chemistry, Technology and Innovation Centre, 99 George Street, University of Strathclyde, Glasgow, G1 1RD, UK.  
<sup>4</sup> Service d'Hépatogastroentérologie, Centre Hospitalo-Universitaire de Reims, Hôpital R Debré, 51092 Reims Cedex, France

\*e-mail: [shussain3@uclan.ac.uk](mailto:shussain3@uclan.ac.uk), [matthew.baker@strath.ac.uk](mailto:matthew.baker@strath.ac.uk) & [gunesch.sockalingum@univ-reims.fr](mailto:gunesch.sockalingum@univ-reims.fr)



Introduction

- Hepatic fibrosis (HF or liver fibrosis, LF) results from a wound-healing response to repeated injury<sup>1</sup>, i.e. viral hepatitis or non-alcoholic steatohepatitis (NASH)<sup>2</sup>
- Initiation of an inflammatory response leads to a decrease of extracellular matrix (ECM) proteins at the injury site, with replacement of necrotic/apoptotic cells with parenchymal cells in the normal response. However, persistent injury/liver regeneration, eventually hepatocytes replaced by more ECM proteins, such as fibrillar collagen.
- Fibrosis – graded on a 5-point scale from F0 to F4 (see Fig. 1). Differentiation of the fibrosis stages via non-invasive methods, such as vibrational spectroscopy, i.e. Raman spectroscopy<sup>3</sup>, is vital for both the clinicians' and patient benefit, as fibrosis is a precursor for cirrhosis and hepatocellular carcinoma (HCC)<sup>4,5</sup>. Chronic Hepatitis C viral (eHCV) infection is the leading cause of hepatic scarring/fibrosis<sup>6,7</sup>.
- Currently – no "Gold Standard" screening regime<sup>8</sup> and biopsy is an invasive diagnostic technique with associated with morbidity, possible mortality, relatively high costs and has the potential for sample error, i.e. observer variation<sup>9</sup>.
- FibroTest & FibroScan are routine biomarker and imaging diagnostic tests and have been shown to more accurate at advanced fibrosis stages<sup>6</sup> – so further developments are needed. Here, we propose a macro Raman approach employed on liquid serum from patients of varying stages of fibrosis for disease fingerprint detection and HF staging. A population of HF patients were investigated and analysed with multivariate analysis (MVA), such as PCA and PC-DFA.

**Fibrosis Stage**  
*(Degree of Inflammation/Scarring)*

F0	no fibrosis
F1	expansion of portal tracts
F2	expansion of most portal tracts and occasional bridging
F3	expansion of most portal tracts, marked bridging and occasional nodules
F4	cirrhosis (end stage irreversible scarring)

Fig. 1 METAVIR score

**Aim: To develop a macro Raman approach for hepatic fibrosis detection and staging from liquid biofluid**

Experimentation

**DATA COLLECTION**

Raman measurements with a Horiba Jobin-Yvon LabRam HR 300 spectrometer. The following setup was used:

- Spectral acquisition: 1800-500 cm<sup>-1</sup>
- Excitation laser: 785 nm diode (300 mW)
- Laser power: ~75 mW
- Diffraction grating: 950 lines/mm
- Spectral resolution: ~3 cm<sup>-1</sup>
- Slit/hole: 150/1000 μm
- Integrations: 5 x 120 s.
- Substrate: Quartz cuvette

Fig. 2 Illustration of a macro Raman liquid collection approach (beam size ~3mm)

**PRE-PROCESSING**

- Nonlinear Response (Dark Noise, Detector Optics, NS1, Silicon Calibration)
- Quality/Variance Testing and Outlier Removal
- Wavenumber Truncation

→ Savitzky-Golay (3,15) Smoothing  
 → 2<sup>nd</sup> Poly-normal Baseline Correction  
 → Differentiation (1<sup>st</sup> = Optional)  
 → Vector Normalisation  
 → tSNE Correction

**MULTIVARIATE ANALYSIS**

→ PCA  
 → PC-DFA

Results, Conclusions & Future Works

Forty-two patients were investigated and pre-processed and analysed with Principal Component Analysis (PCA) and Principal Component - Discriminant Function Analysis (PC-DFA). Fig. 3 to 5 demonstrates the PCA and PC-DFA classification results.

Fig. 3 Fibrosis dataset via PCA 1<sup>st</sup> scores biplot and loadings plot plus 3 labels used for interpretation and binary classification, i.e. label 1 (individuals), label 2 by the METAVIR score, and label 3 (grouped fibrosis stages, i.e. A = F0-1, B = F2, and C = F3-4). PC 1 and 3 loading components, demonstrating the underlying chemistry of the scores biplots.

**Mean group spectra and discriminant features**

Fig. 4 Mean group spectra for 5 METAVIR stages with most discriminant features as highlighted by a Kruskal-Wallis test (p < 0.05) (in blue).

Raman shift / cm <sup>-1</sup>	tentative Assignments <sup>8</sup>	DF1 / DF2
881	Dic. P= and polysaccharides	1*
932-937	C-C skeletal of collagen backbone (proline, hydroxyproline)	1*
1062-2	Phenyl ring breathing mode (mainly collagen)	1*
1050	Carotenoids, Phe	1*, 2*
1076-98	C-N proteins	2*
1110-71	C-N (proline), C-O (carbohydrates), C-C skeletal str.	1*, 2*, 2*
1155	Protein amide I (C-C stretch mode), C-CU, N-H, protein	1*
1245	Amide III (C-N-H), C-C-C-N def. (lipid-phospholipids)	1*
1310, 1355	Thiopyranes (fatty acids), C-H, CH <sub>2</sub> def. (CH <sub>2</sub> CH <sub>2</sub> isomers, saturated, collagen, nucleic acids)	2*
1447	CH <sub>2</sub> deformation (lipids and proteins), Fatty acids	1*
1554	Carotenoid C-C conjugated C-C-C stretching, Phe, hydroxyproline	2*, 2*
1581	Amide I (C=O) stretch	1*
1688	Amide I (C=O) stretch, C-C str (lipids)	1*

Fig. 4 PC-DFA binary classification demonstrates a strong positive predictive value for none to low levels of fibrosis but poor values for advanced staging. 50 PCs were projected in to 3 DF's space with total explained variance of 99.87%.

Fig. 5 PC-DFA binary classification of fibrosis patients demonstrating scores biplot and loadings plus testing accuracy values for sensitivity and specificity. F2 patients removed due to analysis of extreme ends of disease scale.

Here, 42 fibrosis patients (F0-F4) were analysed based on their FibroTest results for eHCV infection. For data analysis different interrogation of the patient groups were assigned, based on a three tier label and binary classification. Routine data pre-processing and PCA for initial data clustering was carried out. PC-DFA showed moderate to good results for the binary classification with F2 patients removed.

These results demonstrate a strong positive predictive value for the F0-F1, but poor value for advanced stages. The most discriminant features of the fibrosis were found to be in the lower frequency region of the fingerprint aspect, and contributions from lipids, proteins, DNA, tryptophan, phenylalanine, tyrosine and nucleic acids (~900-1350 cm<sup>-1</sup>).

Future works indicated for this project are Random Forest (RF) classifiers to determine the best discriminant features, which will then be turned to a support vector machine (SVM) model. It is believed that the GINI-fed SVM from RF classifiers will be able to highlight a greater degree of separation with increases in sensitivity and specificity.

**Acknowledgements:** We would like to acknowledge the Champagne-Ardenne Regional Council and the UCLan, Centre for Material Science, for joint PhD funding and the UCLan PACT Technological Platform for providing instrument facilities. Professor Gérard Thiéfin is greatly acknowledged for the samples for this work. Dr. Beljebbar is thanked for his expertise on using the LabRam HR 300 and experimental setup.

**References:**  
 1. Friedman M., *J. Hepatol.* 2010; 52: 832-843.  
 2. Kojouharova K., *J. Hepatol.* 2010; 52: 832-843.  
 3. Flannigan J., *J. Hepatol.* 2010; 52: 832-843.  
 4. Fattovich G., *Gastroenterology* 1997; 112: 3.  
 5. Patel et al., *J. Hepatol.* 2009; 51: 6.  
 6. Daynard et al., *J. Hepatol.* 2012; 56: 7.  
 7. Hani et al., *Cancer Lett* 1995; 86: 8.  
 8. Lima et al., *Lancet Med Sci* 2011; 15: 20.

## 4. Poster presented at SPEC Montreal, Canada,



# MONITORING THE EFFECT OF FREEZE-THAW CYCLES IN LIQUID AND DRIED DROP SERUM BY MICRO-RAMAN SPECTROSCOPY



S. R. Hussain<sup>1,2</sup>, A. E. Jones<sup>2</sup>, M. J. Baker<sup>3\*</sup>, G. D. Sockalingum<sup>1\*</sup>

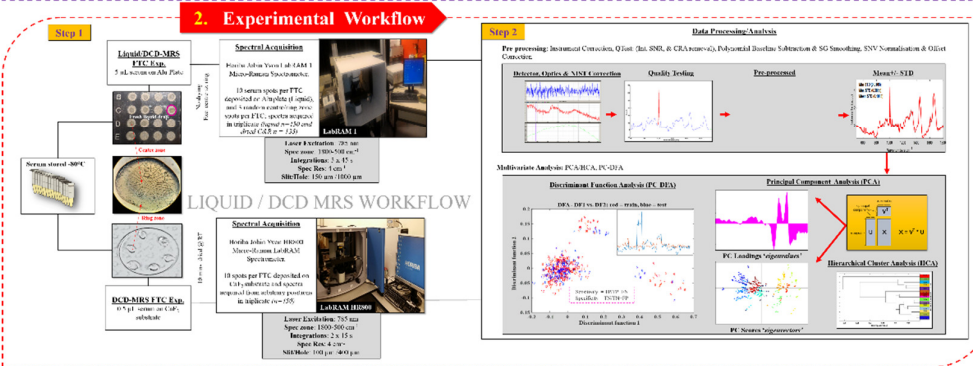
<sup>1</sup> Université de Reims Champagne-Ardenne, CNRS UMR 7369-MEDyC, MEdIAN-Biophotonique et Technologies pour la Santé, UFR de Pharmacie, 51 rue Cognacq-Jay, 51096 Reims Cedex, France. <sup>2</sup> Centre for Materials Science, Division of Chemistry, JB Firth Building, University of Central Lancashire, Preston, PR1 2HE, UK. <sup>3</sup> WISTChem, Department of Pure and Applied Chemistry, Technology and Innovation Centre, 99 George Street, University of Strathclyde, Glasgow, G1 1RD, UK

\*e-mail: [shahen.hussain@univ-reims.fr](mailto:shahen.hussain@univ-reims.fr), [matthew.baker@strath.ac.uk](mailto:matthew.baker@strath.ac.uk) & [ganes.h.sockalingum@univ-reims.fr](mailto:ganes.h.sockalingum@univ-reims.fr)

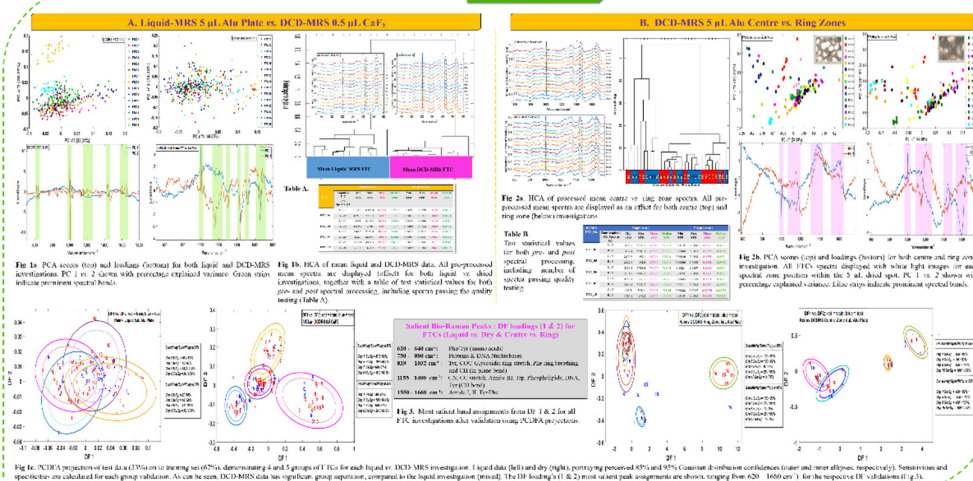
### 1. Introduction

Raman spectroscopy (RS) is a label-free, non-destructive and minimally invasive technique that has been used in a number of proof-of-principle studies to develop diagnostic biofluid spectroscopy. However, little is known about serum stability prior to the spectroscopic workflow. Clinical utility via RS is underway, however pre-analytical variabilities need to be understood, first. In most studies fresh samples are not readily available and it is commonplace to work on frozen stored samples. The effect of freeze-thaw cycles (FTC) is therefore an important parameter to take into consideration and in the present study we seek to observe *via* micro-Raman spectroscopy (MRS) the related spectral variability and any associated biochemical changes by employing two biofluid protocols: liquid serum and drop-coating deposition MRS (DCD-MRS).

**Aim: To monitor the effect of human serum FTC *via* liquid and DCD-MRS**



### 3. Results



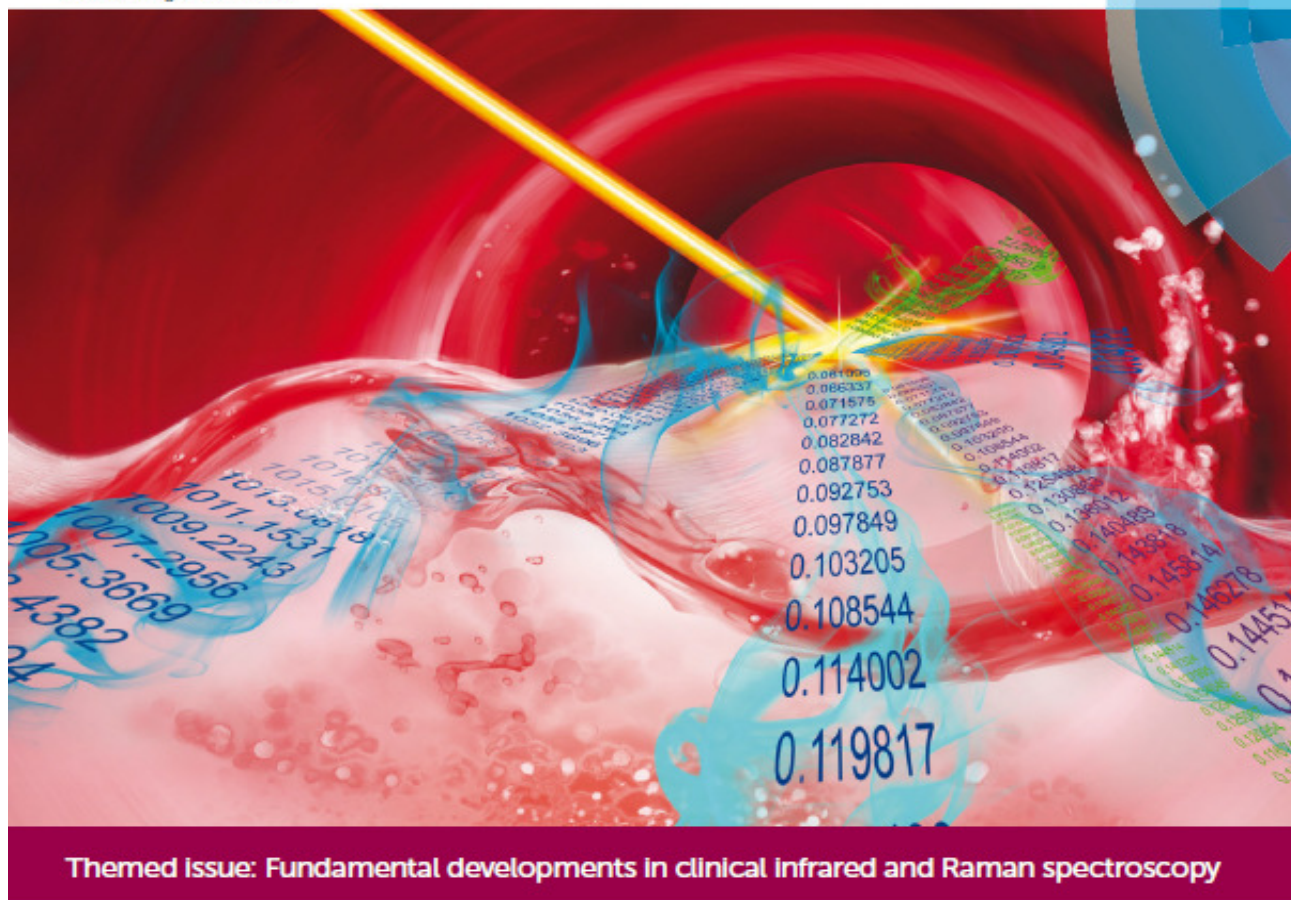
### 4. Conclusion & Future Perspectives

The results obtained on the discrimination between the FTCS shows the potential of RMS coupled with PC-DFA. The liquid investigation showed less discrimination compared to DCD-MRS; which appeared to show moderate to good FTCS separation. Furthermore, the center vs. ring zone data also gave similar sensitivities and specificities; the center being marginally better. Overall, such variability can be attributed to possible changes of the lipid and protein structures of the serum. Given the results here, it could be suggested that serum viability at the pre-clinical level, is structurally affected after nominal FTCS, thus excessive FTCS should be minimized when possible, in future experimentation.

**Acknowledgments:** We would like to acknowledge the Champagne-Ardenne Regional Council and the University of Central Lancashire, Centre for Material Science, for research funding and the URCA PICT Technological Platform for providing instrument facilities.

# Chem Soc Rev

Chemical Society Reviews  
www.rsc.org/chemsocrev



Themed Issue: Fundamental developments in clinical infrared and Raman spectroscopy

ISSN 0306-0012



REVIEW ARTICLE  
Matthew J. Baker, Ganesh D. Sockalingum et al.  
Developing and understanding biofluid vibrational spectroscopy: a critical review

**175** YEARS



Cite this: DOI: 10.1039/c5cs00585j

## Developing and understanding biofluid vibrational spectroscopy: a critical review

Matthew J. Baker,<sup>†\*a</sup> Shawn R. Hussain,<sup>‡bc</sup> Lila Lovergne,<sup>‡ab</sup> Valérie Untereiner,<sup>bcd</sup> Caryn Hughes,<sup>e</sup> Roman A. Lukaszewski,<sup>f</sup> Gérard Thiéfin<sup>dg</sup> and Ganesh D. Sockalingum<sup>†\*ab</sup>

Vibrational spectroscopy can provide rapid, label-free, and objective analysis for the clinical domain. Spectroscopic analysis of biofluids such as blood components (e.g. serum and plasma) and others in the proximity of the diseased tissue or cell (e.g. bile, urine, and sputum) offers non-invasive diagnostic/monitoring possibilities for future healthcare that are capable of rapid diagnosis of diseases via specific spectral markers or signatures. Biofluids offer an ideal diagnostic medium due to their ease and low cost of collection and daily use in clinical biology. Due to the low risk and invasiveness of their collection they are widely welcomed by patients as a diagnostic medium. This review underscores recent research within the field of biofluid spectroscopy and its use in myriad pathologies such as cancer and infectious diseases. It highlights current progresses, adverts, and pitfalls within the field and discusses future spectroscopic clinical potentials for diagnostics. The requirements and issues surrounding clinical translation are also considered.

Received 27th July 2015

DOI: 10.1039/c5cs00585j

www.rsc.org/chemsocrev

### Introduction

Biophotonic techniques are widely used in research for developing new modalities with the aim to improve patient healthcare *via* better diagnosis, prognosis, and surveillance. Vibrational spectroscopy holds such promises because the “molecular fingerprint” that it provides represents a snapshot of the sample biomolecular composition and variations therein can be exploited to identify different pathologies.<sup>1,2</sup> Its sensitivity to such variations makes it possible to probe pathophysiological processes in cells and tissues as demonstrated by many reports for more than a decade,<sup>3</sup> leading to the concepts of “spectral cytopathology” and

“spectral histopathology”.<sup>4–6</sup> With the advances in spectroscopic/imaging technologies and data processing techniques, cells and tissues can be analysed rapidly and non-invasively to identify disease-related abnormalities. Indeed, some promising studies have reported the added value of vibrational spectroscopy to deliver an objective diagnosis but they were performed on a limited number of patients.<sup>7</sup> In spite of these advances in cell and tissue spectroscopy, the technique has not yet been able to overcome the experimental research phase in order to be transferable from bench to bedside. This is mainly due to the lack of standardisation and validation in large clinical trials and multicentre actions. Access to large sample sets with ethical approval is also a limitation. We believe that spectroscopic diagnosis/prognosis *via* biofluids represents an interesting alternative to cells and tissues. Presently, there is limited research representing high-powered clinical studies for biofluid spectroscopy, yet through the use of animal systems several studies from Naumann's group have set the precedent for studies involving large sample numbers; instilling confidence in the high sensitivity and specificity model outcomes by using several hundred animals per study.<sup>8–10</sup>

The quest for disease markers through “liquid biopsies” is a fast emerging field and has only been recently explored by spectroscopic approaches. Blood components like serum and plasma are routinely used for blood testing as they contain biomarkers that are useful for disease diagnostics. For example, in diseases like cancer, they are known to be a rich source of information and represent readouts of the ongoing cellular and extracellular events.<sup>11</sup> Further, they are easily accessible and

<sup>a</sup> WESTChem, Department of Pure and Applied Chemistry, Technology and Innovation Centre, University of Strathclyde, 99 George Street, Glasgow, G1 1RD, UK. Email: matthew.baker@strath.ac.uk; Web: www.twitter.com/ChemistryBaker

<sup>b</sup> Equipe MÉDIAN-Biophotonique et Technologies pour la Santé, Université de Reims Champagne-Ardenne, CNRS UMR 7369-MEDyC, UFR de Pharmacie, 51 rue Cognacq-Jay, 51096 Reims Cedex, France. Email: ganesh.sockalingum@univ-reims.fr

<sup>c</sup> Centre for Materials Science, Division of Chemistry, JB Firth Building, University of Central Lancashire, Preston, PR1 2HE, UK

<sup>d</sup> Plateforme en Imagerie Cellulaire et Tissulaire, Université de Reims Champagne-Ardenne, 51 rue Cognacq-Jay, 51096 Reims Cedex, France

<sup>e</sup> Manchester Institute of Biotechnology, University of Manchester, 131 Princess Street, Manchester, M1 7DN, UK

<sup>f</sup> Chemical Biological Radiological Division, DSTL, Porton Down, Salisbury, Wiltshire, SP4 0JQ, UK

<sup>g</sup> Service d'Hépatogastroentérologie, CHU de Reims, Hôpital Robert Debré, 51092 Reims Cedex, France

<sup>†</sup> Both authors contributed to the work and project supervision equally.

<sup>‡</sup> Both authors contributed equally to this work.

minimally invasive for patients making large studies feasible. Other organ-specific biofluids in the proximity of the diseased cells or tissues like bile, urine, sputum, and cerebrospinal fluid are also of interest for diagnostic purposes. Recent trends tend to indicate that the use of single or few biomarkers has fallen out in favour of multiple biomarkers<sup>12</sup> and in this context the role of vibrational spectroscopic methods can be determinant as the information provided contains data on global sample biomolecular composition providing a chemical 'fingerprint' or 'signature' of the sample. We will focus on the ability of vibrational spectroscopic analysis to illuminate these disease signatures (disease pattern recognition) for diagnostic purposes as opposed to the quantitative determination of specific macromolecules within the biofluid.<sup>13–15</sup>

This critical review, from both the spectroscopic and clinical points of view, considers the issues encountered during translational research aimed at assessing the potentials of infrared and Raman approaches as rapid and label-free diagnostic methods for biological fluids. In addition, the techniques can be adapted to a variety of diseases and therefore represent a cost-effective investment for healthcare systems. This approach could provide a dynamic diagnostic environment that will enable rapid diagnostics leading to earlier treatment. In addition, the ability to accurately and rapidly monitor disease will allow for closer patient follow-up and earlier change in treatment if needed. This would enable patients to access treatment earlier with reductions in mortality and morbidity.

## Vibrational spectroscopy

Vibrational spectroscopy relates to specific optical techniques of infrared (IR) and Raman spectroscopy. These techniques

probe intramolecular vibrations and rotations of the sample when irradiated with light.<sup>16</sup> The light-matter relationship is underpinned by the electromagnetic theory postulated by Maxwell.<sup>17</sup> Vibrational spectroscopy has been used for analysing a myriad of samples in chemical, physical and biological applications.

The Raman effect constitutes the spontaneous inelastic light scattering process of photons following the interaction of a monochromatic radiation (e.g., laser source) with the sample. During this interaction both elastic and inelastic scattering processes take place. A high proportion of the photons are elastically scattered with no change in energy (so no molecular information), known as Rayleigh scattering.<sup>17</sup> When photons transfer energy to the molecules as vibrational energy, the energy loss of the scattered photons corresponds to the vibrational energy levels of the molecules. This is known as the Raman-Stokes scattering. The incident photons can in turn receive energy from vibrating molecules, and therefore their frequencies increase, described as the Raman anti-Stokes scattering. Fig. 1 shows the transitions involved during these three processes. In spontaneous Raman, the Stokes scattering is generally used due to its higher sensitivity.

Infrared spectroscopy (IR) is broadly defined as the study of absorption characteristics arising from the molecular motion of materials due to atomic displacement<sup>4</sup> upon intimate interaction with an infrared source.<sup>18</sup> Depending on the modality of choice, the radiation can be either transmitted, internally reflected, reflected, or transacted (a combination of transmission and reflectance). During the light-matter interaction, infrared light causes a molecule to enter a higher vibrational state due to the transfer of 'quanta' or 'packets' of energy at certain wavelengths dependent upon the composition of the matter under analysis. Fig. 1 illustrates the energy level transition involved in the IR

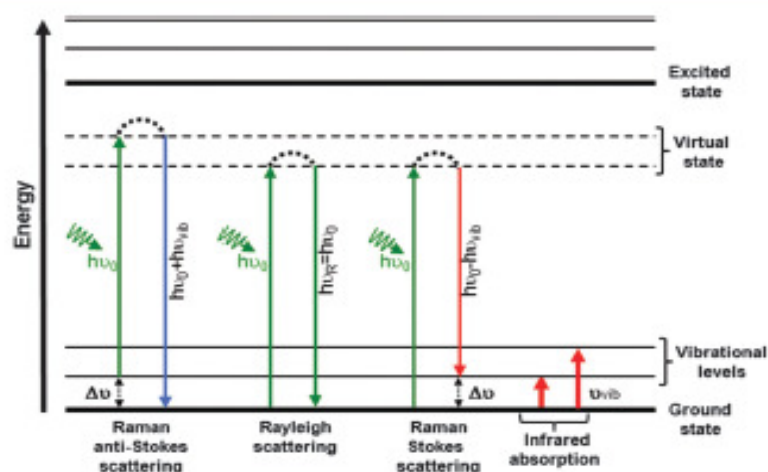


Fig. 1 Energy diagram showing transitions involved during infrared absorption, Rayleigh, Raman Stokes and anti-Stokes scattering. This Jablonski diagram shows that the same vibrational states of a given molecule can be probed via two different routes; one directly measures the absolute frequency (IR absorption) and the other measures the relative frequency or Raman shift (Stokes and anti-Stokes).  $h\nu_0$  = incident laser energy,  $h\nu_{vib}$  = vibrational energy,  $\Delta\nu$  = Raman shift,  $\nu_{vib}$  = vibrational frequencies.

absorption process compared to Raman scattering showing that vibrational energy levels can be probed with both techniques using different physical processes. These transitions result in a spectrum constituted of peaks/bands that can be interpreted qualitatively (peak position) and quantitatively (peak intensity/area, relative intensity). For IR spectroscopy the bands arise from a change in the electric dipole moment of the molecules, whereas Raman is associated with a change in the molecular polarisability.

Constituent chemical molecular bonds present many forms of vibrations which occur at different energies corresponding to different allowed transitions. IR and Raman spectroscopies are complementary and provide a "fingerprint" or "signature" of the molecules contained within the sample depending on whether their bonds exhibit Raman or IR activities. Certain vibrations that are allowed in Raman may be forbidden in IR and *vice versa*. For a full treatise of fundamental spectroscopy studies, the authors direct the reader to two reviews by Barth and Harris on IR spectroscopy<sup>19</sup> and Long on Raman spectroscopy.<sup>20</sup>

## Biological and biomedical vibrational spectroscopy

There is a continuing effort devoted to the exploration of new technologies that can detect early signs of diseases and therefore significantly reduce mortality and morbidity. This depends on the ability to detect biochemical/morphological changes at an early stage of the disease or before the disease becomes symptomatic. Detection of biomarkers plays an important role in this exploration, and in the case of cancer for example, they cover a broad range of biochemical entities, such as nucleic acids, proteins, carbohydrates, lipids, small metabolites, and cytogenetic and cytokinetic parameters, as well as entire circulating tumour cells found in body fluids. They can be used for risk assessment, diagnosis, prognosis, and for the prediction of treatment efficacy and toxicity and disease recurrence.

Over the last 20 years, there has been an exponential increase in the number of studies dedicated to identification of new cancer (Fig. 2a) and infectious disease (Fig. 2b) biomarkers, mainly because of the tremendous development of high throughput molecular technologies and associated bioinformatics. However, among the huge amount of candidate biomarkers, only a limited number have been validated for use in medical practice. A recent paper states that in DNA and proteomic research, out of 1000 biomarkers discovered less than 100 have been validated for routine clinical practice.<sup>21</sup>

Vibrational spectroscopy can contribute in bringing a new way for searching biomarkers, namely "spectral signatures" or "spectral biomarkers", which reflect the total biochemical composition of the studied sample as it has been employed for cell and tissue analysis since the pioneering work by Mantsch, Naumann and Diem, to list just a few.

Biological samples are frequently analysed *via* the transmission mode in the mid-IR region, where most molecules absorb

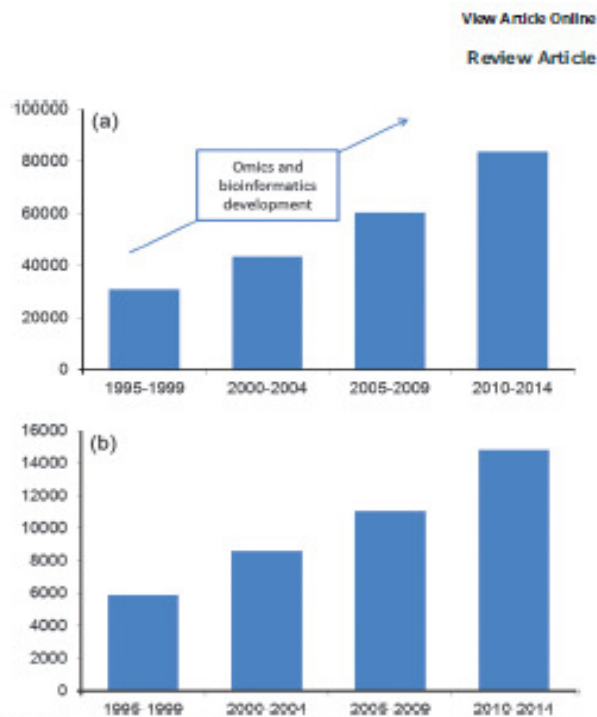


Fig. 2 Number of publications returned in PubMed when inputting the terms "cancer biomarker" (a) and "infection biomarkers" (b).

and the molecular absorbance is proportional to concentration, obeying Beer-Lambert's law for non-scattering samples. Mid-IR absorption features between approximately 4000 and 400  $\text{cm}^{-1}$  (2.5 to 25  $\mu\text{m}$ ). Fig. 3 illustrates an example of an FTIR spectrum of a breast tissue with the assignment of some important biomolecules. The spectrum can be divided into four regions where the main macromolecules absorb:  $-\text{CH}_2$  and  $-\text{CH}_3$  groups of fatty acids and proteins (3050–2800  $\text{cm}^{-1}$ ); C=O stretching vibrations mainly from lipid esters (1800–1700  $\text{cm}^{-1}$ ); C–O, N–H, and C–N modes from Amide I and II protein bands (1700–1500  $\text{cm}^{-1}$ ); phosphate vibrations from nucleic acids (1225 and 1080  $\text{cm}^{-1}$ ); and carbohydrate absorptions (1200–900  $\text{cm}^{-1}$ ). Libraries housing spectra from biological and biochemical samples have been collected over the years.

Over the years, variants of IR spectroscopic technologies have been tested. A recent review highlights the use of IR techniques to probe the functionality of biological and biomimetic systems.<sup>22</sup> Their applications to study biological and biomedical specimens have continuously increased.<sup>23,24</sup> When used to analyse biofluids, the mid-IR or near-IR spectroscopies would be performed on drying samples to negate the overwhelming water band from obscuring spectra and to increase automation.<sup>25</sup>

Another method of obtaining an IR spectrum is when the sample is placed on a highly reflecting surface, typically aluminium/teflon coated substrates or a glass slide with tin oxide-based silver reflective coating called low *e*-slides (e.g., MirIR). In this case the process is termed transflection because the IR beam passing through the sample is reflected off the slide and passes

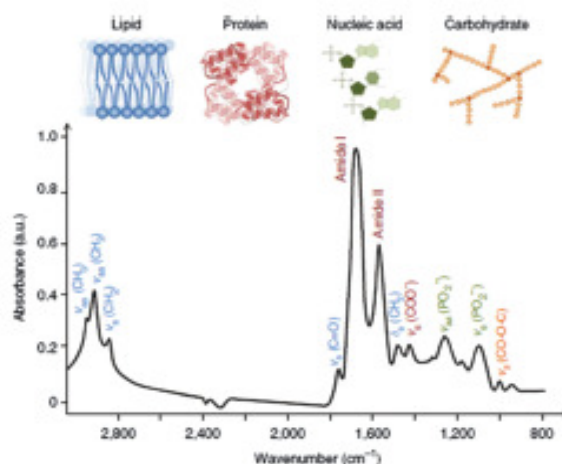


Fig. 3 FTIR biological spectrum showing frequent biomolecular band assignments from 3000–800  $\text{cm}^{-1}$ , where  $\nu$  = stretching vibrations,  $\delta$  = bending vibrations,  $s$  = symmetric vibrations and  $as$  = asymmetric vibrations. Illustration taken from transmission spectra on human breast ductal carcinoma prepared on 1 mm thick  $\text{BaF}_2$  slides.<sup>4</sup> The 3000–2800  $\text{cm}^{-1}$  region originates mostly from lipids ( $\text{C-H}$ ,  $\text{CH}_2$  and  $\text{C-H}_3$  stretching modes), but protein absorption of the same modes also contribute to these absorption bands.

again through the sample before detection. These substrates have very low cost but recently they have been shown to cause significant spectral intensity variations, due to an electric free standing wave artefact (EFSW)<sup>26,27</sup> which could be misinterpreted as composition variations while it is the sample thickness variation that is questionable. The fundamental question when using low  $e$ -slides is whether the spectral variations observed due to the EFSW impact on the discriminant spectral differences. In case of thin samples such as air-dried cellular monolayers, recent research by Cao *et al.* has shown that the same classification was obtained when performing transmission and transfection measurements.<sup>28</sup>

Attenuated total reflectance (ATR) FTIR spectroscopy is a promising modality for biological sample analysis. The guided IR beam propagates through a high refractive index crystal surface producing an evanescent standing wave that penetrates the sample by a few microns. However for appropriate use, several issues need to be considered, such as contact between the ATR crystal and the sample, the beam penetration depth and image distortion due to high refractive indices.<sup>25,29</sup>

Despite its molecular specificity, FTIR spectroscopy suffers from some shortcomings which limit its application to the measurement of biological samples and their dynamic behaviour. An important one is sensitivity, in particular in thin samples as a result of the Beer–Lambert's law. Signal amplification can be achieved by the plasmonic resonances of nano-scale metallic particles,<sup>30</sup> resulting in the phenomena of surface-enhanced infrared absorption (SEIRA),<sup>31</sup> in analogy with surface-enhanced Raman scattering (SERS).<sup>32</sup> Early SEIRA studies utilised metal island films<sup>22,31</sup> and dried samples, but today plasmonic

chip-based technology enables the *in situ* monitoring of protein and nanoparticle interactions in aqueous media, at high sensitivity in real time.<sup>33</sup>

One method of choice for cell and tissue analysis has been IR microscopy. The coupling of an FTIR spectrometer with a microscope has helped to perform microanalysis and gain in spatial resolution  $\sim 15$ – $20 \mu\text{m}$  with a thermal source and  $\sim 5$ – $10 \mu\text{m}$  with a synchrotron source using single element detectors. These systems are limited by low sensitivities and time-consuming experiments (several hours) as they remain a point by point acquisition. In the 1990s, the advent of imaging devices with multi-element detectors combined with aperture less microscopes, high-tech automation and faster computers, have drastically reduced the data acquisition times (few hours) with resolution going down to  $\sim 2 \mu\text{m}$  per pixel with liquid nitrogen cooled focal plane array detectors. Many research groups have demonstrated the efficacy of employing this to a clinical setting on biopsy samples; minimising subjectivity and increasing diagnostic accuracy.<sup>4</sup> In spite of these progresses, such instruments remain research machines and are not adapted to be used as benchtop techniques for routine analysis in a clinical setting.

The launching of new IR imaging devices incorporating high-intensity tunable quantum cascade lasers (QCL) could revolutionise the way clinical IR images are acquired.<sup>34</sup> High-throughput IR chemical imaging is now in its early days, and needs to be tested and validated. However, a gain of three orders of magnitude in acquisition time has recently been reported for large samples by Bhargava's group.<sup>35</sup> Combining signal enhancement from SEIRA and fast imaging using a QCL source with small bandwidths, a recent study claimed a  $\sim 200$  fold gain in imaging time.<sup>36</sup>

The Raman shift covers the range between 0 and 4000  $\text{cm}^{-1}$ . Raman spectroscopy can be used in the confocal mode and with the resonance and surface-enhanced modalities. Applications of Raman microscopy for probing biological systems have been continuously expanding over the years along with IR spectroscopy.<sup>37</sup> Its high spatial resolution ( $\sim 0.5 \mu\text{m}$  with green lasers), compatibility with aqueous environment,<sup>38,39</sup> and *in vivo* amenability<sup>40–43</sup> makes it a good candidate for biological and biomedical research. Akin to FTIR, it also provides high content biomolecular information. Microspectroscopy with immersion measurements can be used to enhance the signal to background ratio enabling higher quality data acquisition as demonstrated by Bonnier *et al.*<sup>44</sup>

Due to its advantages, label-free, high spectral specificity, limited water signal, and the fact that most biological molecules are Raman active, Raman has been deployed to *in vitro* cell and tissue studies, but now significant developments of *in vivo* work due to the compatibility with fibres has enabled Raman endoscopy in a label-free manner and *in vivo* Raman probes/endoscopes have made direct tissue analysis possible.<sup>45</sup>

New fields of measurement and implementation possibilities have multiplied due to recent hardware developments, improved sampling methods, and advances in the design of Raman technology alongside developments and advances in

multivariate data analysis. It has been possible to uncover subtle disease-related spectral changes and exploit them in classification models. However, an important drawback of Raman spectroscopy is that the effect is inherently weak as a very small proportion of incident photons are scattered ( $\sim 1$  in  $10^9$ ) with a corresponding change in frequency.<sup>17</sup> This together with the fact that to date most of the commercial systems use dispersive configurations adds another limitation compared to fast IR imaging systems, and makes Raman imaging of biological specimens a slower process. These limitations can be partly circumvented with other Raman modalities based on Resonant Raman Scattering (RRS) and Surface-Enhanced Raman Scattering (SERS) to enable gains in detection sensitivity.<sup>17</sup> In SERS technology, the use of functionalised metal nanosurfaces has allowed optimising the enhancement to several orders of magnitude depending on the metal substrate. Metal nanoparticle arrays and single nanoparticles have been utilized for high-throughput detection.<sup>46</sup> SERS has been applied in different areas in the chemical and biological fields<sup>47</sup> and its very high sensitivity has allowed single molecule detection.<sup>48</sup> Until recently, SERS was not widely applied to biomedical research because of issues linked to complexity of the biological medium, biocompatibility, reproducibility, and short shelf life. However, using silver and gold colloids as SERS substrates, Bonifacio *et al.* recently showed that repeatable spectra could be obtained from protein-free blood serum and plasma.<sup>49</sup>

Furthermore, non-linear Raman spectroscopy has been developed to be applied to biomedical analysis like Stimulated Raman Scattering (SRS) and Coherent Anti-Stokes Raman Scattering (CARS), for rapid image acquisition (one Raman band at a time) with higher sensitivities than spontaneous Raman.<sup>50–52</sup> For non-linear Raman, it is important to know which marker band(s) are useful, in analogy to the application of Discrete Frequency-IR (DF-IR) as enabled by the use of QCL sources.

Other areas of current interest for Raman spectroscopy are exploring the sampling depth and location of spectral information. For instance, seminal research conducted by Stone, Matousek and collaborators demonstrated the principle of spatially offset Raman spectroscopy (SORS) for subsurface analysis towards *in vivo* breast cancer<sup>53,54</sup> and deep Raman measurements using liquid tissue phantoms to mimic non-invasive cancer screening applications *in vivo*.<sup>55</sup> Through-tissue sensitivity was increased *via* SESORS measurements at several millimetres depth, *i.e.*, combining SORS with nano-tagged SERS particles.<sup>56–59</sup>

Building on the research described above, the field of biospectroscopy has continuously progressed and expanded to complex biological systems such as biofluids<sup>60</sup> with a major focus on the development of a potential diagnostic/prognostic tool with remarkable scope and future clinical promises.

With the global disease burden set to rise, a more rapid, non-invasive, label-free, non-destructive, automatic and cost effective diagnostic technique like vibrational spectroscopy would revolutionise the clinical environment. Its utility as a biofluid diagnostic tool is heavily reliant on the principle that cellular and tissue dysfunction or irregularities affect the biochemical

make-up of biofluids, manifesting as protein, carbohydrate, lipid, and nucleic acid subtle differences.<sup>16</sup>

Over the last decade, developments in this field have been ongoing in order to fulfil these objectives and ultimately leading to better diagnostics and time to results to improve patient outcomes, offer more efficient public services, and reduce health costs.

## Biomarkers in body fluids

According to the National Institutes of Health definition, a biomarker is “a characteristic that is objectively measured and evaluated as an indicator of normal biologic processes, pathogenic processes or pharmacologic responses to a therapeutic intervention”.<sup>61</sup> In line with this definition, there is a large range of clinical situations where the biomarkers are of paramount importance for the patient's management: screening of patients at risk of the disease or with the disease at an early stage, differential diagnosis of the disease with other conditions, prognosis of the disease independently of the treatment, prediction of the response to treatment, and monitoring of disease evolution (Fig. 4).

Molecular biomarkers may be detectable in tissues and biofluids. Fig. 5 illustrates the case for cancer where tissue biomarkers can be used for cytological or pathological assessment of the disease or for molecular or spectral imaging techniques. The tumour is vascularised and markers are shed into the bloodstream. Another health issue is the early detection of biomarkers for the diagnosis of infectious diseases coming either from the host or from the pathogen. From the initial interaction onwards the majority of biomarkers available to measure are derived from the host since pathogen numbers are very low and the host is able to utilize components of both the innate and adaptive host response to drive an appropriate response. In serious infection, when pathogens are able to overcome the early host response to their presence, their numbers increase at an exponential rate resulting in significant mortality rates. In such cases, the relative concentration of microbial biomarkers increase over time whilst biomarkers associated with the ongoing, yet ineffective,

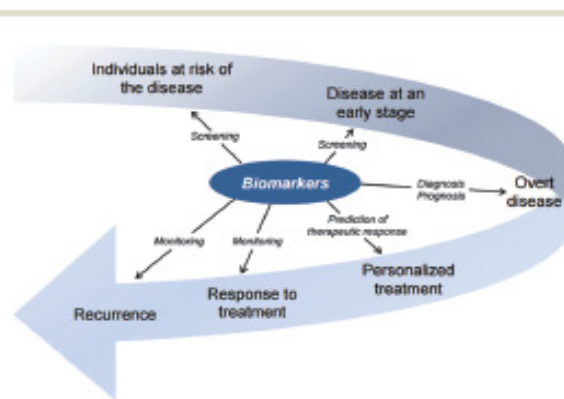


Fig. 4 Schematic of biomarker use in clinical practice.

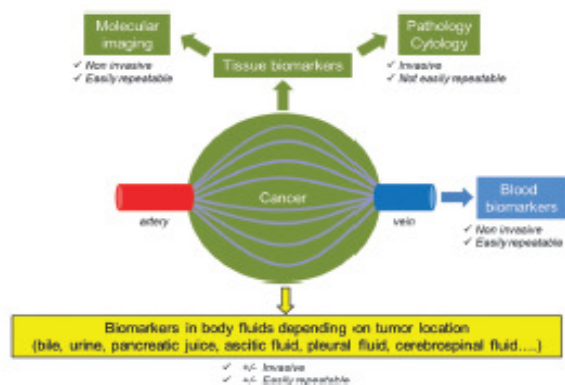


Fig. 5 Example of potential tumour-site related biomarkers.

host response are still readily detectable (Fig. 6). Preliminary evidence has been produced which indicates that it is possible to identify the presence of an infectious organism through analysis of host biomarker signatures before patients become symptomatic.<sup>62</sup> Thus, the concept of searching for such signatures in host biofluids pre-symptomatically appears as a promising avenue for exploration in order to enable early therapeutic intervention.

Regarding biofluids, blood and its constituents appear the most convenient for biomarker/biosignature detection given its ease of availability and the possibility to repeat the test as often as necessary to monitor disease progression or response to treatment.

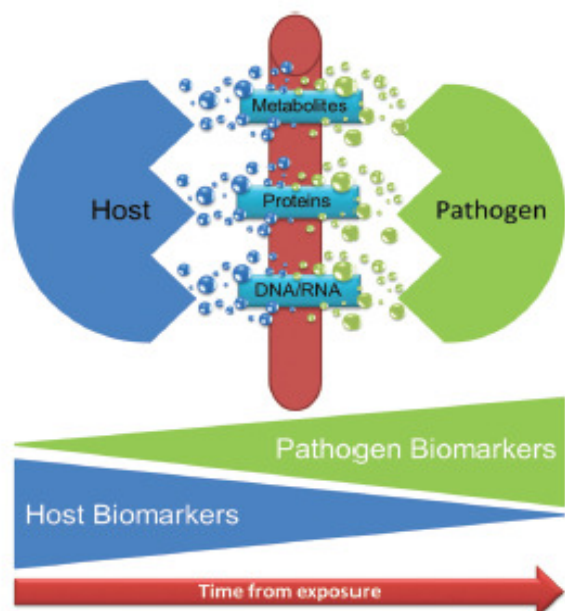


Fig. 6 The relative contribution of host and microbial derived biomarkers to enable diagnosis of infection.

Blood serum houses more than 20 000 different proteins. It perfuses all body organs meaning it contains a large range of proteomes from surrounding tissues and cells, making it the most complex biofluid.<sup>63</sup> The low molecular weight fraction serum component of blood, known as the ‘peptidome’ is information rich for diagnostic purposes.<sup>11</sup> Other biofluids (bile, urine, sputum, pancreatic juice, and ascitic, pleural, cerebrospinal fluids), in direct contact with the diseased tissue, are of great interest as media to detect biomarkers/biosignatures that are secreted or shed locally. These are expected to be present in higher concentration in these fluids than in the blood. In addition, their identification may be facilitated by a less complex molecular composition of local biofluids compared with blood. Although some biofluids such as urine share with blood samples ease of availability and repeatability, analysis of other biofluids requires an invasive procedure, which limits their repeated use in the clinical setting. An example is cerebrospinal fluid which requires a lumbar puncture for collection.

Whilst biomedical vibrational spectroscopy has been developed initially mainly for cell and tissue analysis, it has been also applied more recently to biofluids for biomarker discovery, generating a number of pilot studies with promising results as presented below. The challenge is now to translate the results of these exploratory studies to the routine clinical practice.

## Biofluid spectroscopy

The search for disease markers in biofluids *via* photonic approaches is a fast emerging field and has only been recently explored by vibrational spectroscopic approaches. Biofluids are easily accessible and minimally invasive for patients making large studies feasible. Like cells and tissues, biofluids exhibit vibrational spectra that have characteristic bands reflecting their biomolecular composition. Fig. 7 compares the FTIR spectra of some dried biofluids (serum, plasma, and bile) obtained with a high-throughput module in the transmission mode. IR spectra of serum and plasma present very close profiles with subtle differences that are difficult to depict visibly. This is explained by the fact that serum is essentially plasma with the clotting factors of blood removed. The assignment of the main bands is provided in Table 1.

The bile spectrum differs through a higher lipid and carbohydrate content and by relative intensity changes of the protein amide I/amide II bands.<sup>64</sup>

Raman spectroscopy gives complementary information to IR. Besides the main macromolecules like proteins, lipids, and carbohydrates, other modes originating from amino acids for example are active. The assignment of the main bands is indicated in Fig. 8 showing an example of a typical Raman serum spectrum taken from a dried drop.

### Serum and plasma

At present, the majority of the biofluid spectroscopy research has focused on serum and plasma. This is most likely due to

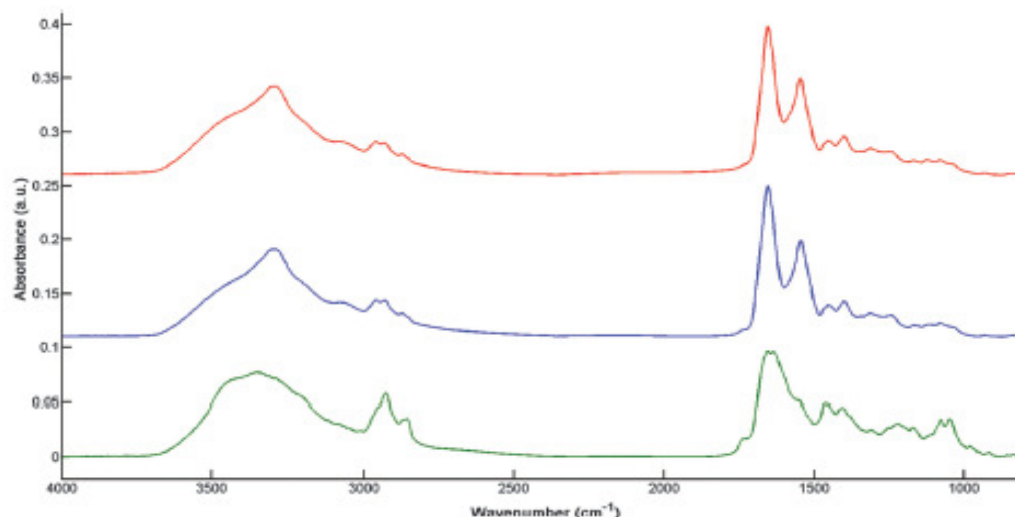


Fig. 7 Comparison between HT-FTIR spectra of different biofluids: serum (red curve), plasma (blue curve), and bile (green curve). Spectra are background corrected and normalised. Note: serum and bile were collected in dry tubes while for plasma samples lithium heparin tubes were used.

Table 1 Assignment of the major absorption bands of a plasma FT-IR spectrum<sup>80</sup>

Bands (cm <sup>-1</sup> )	Major assignments for plasma contents
3300	$\nu$ (N-H) of proteins (amide A band)
3055–3090	$\nu$ (=CH) of lipids
2950–2960	$\nu_{\text{as}}(\text{CH}_2)$ of lipids
2920–2930	$\nu_{\text{s}}(\text{CH}_2)$ of lipids
2865–2880	$\nu_{\text{s}}(\text{CH}_2)$ of lipids
2840–2860	$\nu_{\text{d}}(\text{CH}_2)$ of lipids
1730–1760	$\nu$ (C=O) of fatty acids
1660	$\nu$ (C=O) of proteins (amide I band)
1550	$\delta$ (N-H) of proteins (amide II band)
1400	$\nu$ (COO <sup>-</sup> ) of amino acids
1240	$\nu_{\text{as}}(\text{P=O})$ of nucleic acids
1170–1120	$\nu$ (C-O) and $\nu$ (C-O-C) of carbohydrates

$\nu$ : stretching vibrations,  $\delta$ : bending vibrations, s: symmetric, as: asymmetric. Taken from Lacombe *et al.*, *Analyst*, 2015, **140**, 2280.

the prevalence of these types of samples within current biobank stocks or the fact that ethics are already established to collect these samples and all that is required is an addendum stating a separate use of the material.

**Malignant diseases.** Currently, in the field of oncology, most investigations are proof-of-principle studies showing the potentials of FTIR/Raman spectroscopy to identify different types of cancer from serum samples with high degrees of accuracy. HT-FTIR spectroscopy in transmission mode was used to discriminate urinary bladder cancer patients from patients with urinary tract infection with linear discriminant analysis (LDA) or random forest (RF) classifiers.<sup>65</sup> Using blood serum, Backhaus *et al.* distinguished between breast cancer and controls with a very high sensitivity and specificity.<sup>66</sup> Chemometrics combining support vector machine (SVM) classification and leave-one-out cross validation was employed by Zhang *et al.* to separate cirrhotic patients with or without hepatocellular carcinoma.<sup>67</sup>

Equally important is the possibility to identify liver fibrosis stages prior to the development of hepatocellular carcinoma, which are crucial for the clinical management. A study by Scaglia *et al.* revealed that patients with extensive fibrosis (F3/F4 stages) could be distinguished from those with no fibrosis (F0 stage) on the basis of their FTIR serum spectra using a combination of discriminant wavenumbers.<sup>68</sup> Studies using ATR-FTIR spectroscopy coupled with classification machine discriminated ovarian<sup>69</sup> and endometrial cancers.<sup>70</sup> It also allowed differentiating glioblastoma multiforme (GBM) from healthy control and low grade gliomas and GBM *versus* healthy control.<sup>71,72</sup>

Applications of Raman spectroscopy to the study of various biofluids from cancer patients are in continuous progress. Sahu *et al.* analysed serum samples and could differentiate oral cancer patients from controls.<sup>73</sup> More recently, they reported that Raman serum spectroscopy was capable to predict the probability of recurrence in this cancer.<sup>74</sup> Other studies have shown the potential of Raman spectroscopy for differentiating normal subjects from patients with breast,<sup>75</sup> colorectal,<sup>76</sup> or cervical<sup>77</sup> cancers. A proof-of-concept study using micro-Raman spectroscopy applied to the sera of 71 cirrhotic patients showed that it could be an alternative method for discriminating cirrhotic patients with and without hepatocellular carcinoma.<sup>78</sup> On the other hand, SERS of serum or plasma has also been shown as a promising tool for the diagnosis of various types of cancer such as nasopharyngeal,<sup>79–81</sup> digestive,<sup>80,82–84</sup> and prostate cancers.<sup>85</sup>

**Non-malignant diseases.** Serum and plasma have been also employed to diagnose other diseases using biospectroscopy. For example, Raman serum data allowed to differentiate Alzheimer's disease from other dementia<sup>86</sup> and Carmona *et al.* used plasma Raman spectral data to grade mild, moderate, and severe Alzheimer cases.<sup>87</sup> *Via* FTIR spectroscopy of plasma,

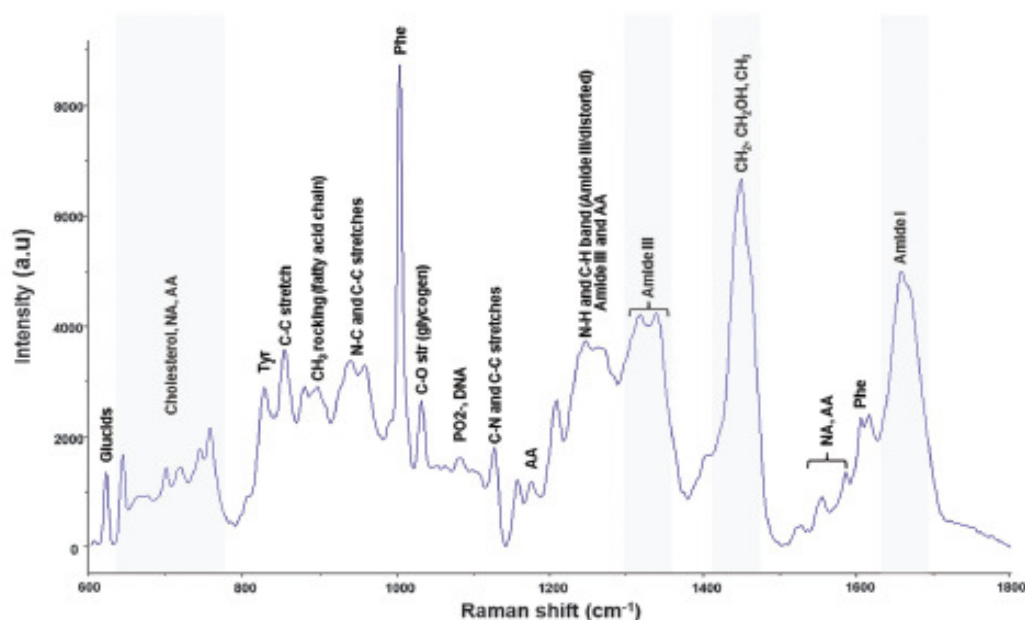


Fig. 8 Typical Raman spectrum of dried serum drop with spectral assignments. Spectrum was measured on a calcium fluoride window with a 785 nm laser excitation with an acquisition time of  $2 \times 30$  seconds.

Peuchant *et al.* have shown that patients with Alzheimer's disease could be well delineated from normal ageing subjects used as controls.<sup>88</sup>

Recent plasma data published by Lacombe *et al.* clearly showed that HT-FTIR spectroscopy could be an interesting alternative technique in neonatal screening of rare diseases such as classic galactosemia. Promising results indicated that healthy/diabetic, healthy/galactosemic, and diabetic/galactosemic patients could be discriminated with good sensitivity and specificity.<sup>89</sup>

Few large studies have been reported. An example is the study led by Petrich's group showing the potential of mid-infrared spectroscopy in the triage of patients with acute chest pain.<sup>90</sup> This study included 1429 serum samples from 389 patients reporting to two US hospitals (Massachusetts General and Latter Day Saints, Utah) consisted of 104 suffering from acute myocardial infarction (AMI), 136 from unstable angina pectoris, and 149 from chest pain of other sources. FTIR measurements were performed in the transfection mode. Using a threshold value generated from a robust linear discriminant analysis, they achieved high sensitivity and specificity enabling triage of patients with AMI, those most at need within the accident and emergency setting, compared to the other sources of chest pain. They hypothesise on the involvement of carbohydrates as discriminant features, possibly a glycation reaction. Interestingly, their results were comparable to the performance of routine cardiac laboratory markers within the same study population. They conclude on the potential of FTIR to aid the diagnostic procedure as early as within the first 6 hours after the onset of chest pain.

Blood plasma from patients has been investigated with Raman spectroscopy as dried drops to identify a reliable biomarker that can differentiate sepsis patients from those with non-infectious systemic inflammatory response syndrome. Neugebauer *et al.* reported on the high sensitivity and specificity that can be achieved.<sup>91</sup> The possibility of separating the two groups of patients is crucial because a stratification of at risk patients can be established for a rapid delivery of appropriate treatment.

Finally, following the results obtained in a model of infected cultured cells, SERS appears as a promising approach for malaria parasite detection from whole blood.<sup>92</sup>

#### Other biofluids

Other biofluids non-invasively accessible (urine, saliva, sputum, and tears) and invasively accessible (bile, synovial fluid, cerebrospinal fluid, and amniotic fluid) have been investigated by vibrational spectroscopy for diagnostic purposes.

Somorjai *et al.* were able to distinguish urine samples from normal renal transplants and rejected allografts, applying IR spectroscopy and a three-stage classification strategy.<sup>93</sup> A Raman spectroscopic analysis combined with PCA and quadratic discriminant analysis (QDA) performed on urine, has allowed identification of spectral biomarkers predictive of complications and kidney failure in the urine of diabetic and hypertensive patients.<sup>94</sup> Finally, in the field of oncology, Del Mistro *et al.* reported that SERS using Au nanoparticle substrates had the potential to detect in urine spectral biomarkers of prostate cancer.<sup>95</sup>

Another approach by FTIR spectroscopy associated with LDA on saliva has reported the correct classification of diabetic

patients from healthy control.<sup>96</sup> SERS of saliva showed the ability to predict lung cancer by monitoring the decrease of proteins and nucleic acids with 80%, 78%, and 83% accuracy, sensitivity, and specificity respectively.<sup>97</sup> A preliminary study using SERS on saliva suggested the possibility of a quick detection of AIDS but these results obtained on a small number of patients deserve to be confirmed on a larger population.<sup>98</sup>

An exploratory study has shown that FTIR spectroscopy applied to sputum could be a useful approach for the diagnostic of the chronic obstructive pulmonary disease.<sup>99</sup> Investigating the potential of human tears for the diagnosis of ocular diseases, Travo *et al.* have shown the discrimination of patients with keratoconus (degenerative disorder affecting the cornea) from healthy control and also between patients at an early or advanced stage of disease by HT-FTIR and PCA.<sup>100</sup> Additionally, Choi *et al.* report that SERS can be used for diagnosis of adenoviral conjunctivitis from tears.<sup>101</sup>

Using HT-FTIR spectroscopy in association with support vector machine (SVM) classification and leave-one-out cross validation (LOOCV), Untereiner *et al.* have shown that bile samples of patients with malignant biliary strictures were differentiated from those with benign biliary diseases.<sup>64</sup>

Eysel *et al.* using FTIR spectroscopy and LDA with LOOCV on synovial fluid were able to differentiate samples from joints affected by rheumatoid arthritis, osteoarthritis, spondyloarthropathies, and meniscal injuries.<sup>102</sup> Also from synovial fluid samples, a Raman spectroscopic study associated with a *k*-means analysis has shown discrimination between patients with osteoarthritis of low or high severity.<sup>103</sup>

Liu *et al.* have investigated the amniotic fluid potential for fetal lung development assessments by IR spectroscopy. The lecithin/sphingomyelin (lung surfactants) and lung surfactant/albumin ratio measurements by IR spectroscopy were quantitatively and qualitatively correlated to those obtained by thin-layer chromatography and fluorescence depolarization, two clinical methods used to determine fetal lung surfactant maturity in amniotic fluid.<sup>104</sup> Prenatal disorders from amniotic fluids have also been investigated by ATR-FTIR spectroscopy revealing spectral profile changes between amniotic fluids from pregnancies with fetal malformations, preterm delivery and healthy term pregnancies.<sup>105</sup>

Griebe *et al.* were able by FTIR spectroscopy to distinguish patients with Alzheimer's disease from healthy controls using cerebrospinal fluid.<sup>106</sup>

### Translation

With a few exceptions, all the mentioned proof-of-concept studies have been carried out on rather small populations and have shown promises for clinical utility and highlight the potential of vibrational spectroscopy for spectral diagnostics. To our knowledge, two major programmes for large scale clinical trials in remote settings are ongoing using hand-held FTIR modalities. The first campaign led by Wood *et al.* concerns the screening of population in Thailand for malarial diagnosis (<http://monash.edu/news/show/infrared-light-puts-malaria-to-the-test>).

A similar approach is being taken in the UK with the establishment of Glyconics Ltd. Glyconics is using sputum to

diagnose Chronic Obstructive Pulmonary Disorder and are moving towards clinical validation of handheld ATR-FTIR on a subset of the UK population (<http://www.glyconics.com/technology.asp>).

These steps towards actual clinical environment testing is pushing the field to the forefront of the application and will illuminate the utility of these techniques as well as barriers to clinical implementation that need to be overcome.

## Multivariate analysis

It is becoming more and more evident that vibrational spectroscopy represents an interesting approach to explore the diagnostic potentials of circulating biomarkers/biosignatures in various body fluids.<sup>60</sup> Along with the technological development, the front-end sample preparation challenges and approaches, and the data acquisition procedures, the pre-processing and post-processing of spectral data are equally important for the deployment of various biofluid classes into diagnostics development. Vibrational spectroscopic data are inherently multivariate by nature and their pre- and post-processing require multivariate data analysis approaches.

Different instruments from different manufacturers have different responses and spectral distortions and backgrounds have to be taken into account *via* pre-processing algorithms in order to compare data from different studies for example. The pre-processing should therefore be able to give accurate, robust and reliable data. These considerations should also include how the sample is prepared and conditioned, the optical substrate used, and the acquisition mode used in order to post-process reliable data. The way the sample is dried or acquired (e.g. transmission or reflection) will also pre-empt the pre-processing procedures. For example, rapid drying of serum can produce a granulating effect which then causes more scattering/dispersion artefacts and a specific correction has to be implemented. It is clear that pre-processing is not the same for infrared and Raman spectra of biofluids because the physical phenomena involved are, respectively, absorption and scattering. In FT-IR spectroscopy the use of an interferometer ensures an excellent intensity and wavenumber calibration. In addition, a background signal is regularly recorded and automatically subtracted to obtain the sample spectrum. For Raman, a day-to-day calibration procedure needs to be implemented to correct for instrument response, and to calibrate the wavenumber and intensity axes. Other experimental considerations include the need to subtract substrate contributions and other physical phenomena such as fluorescence and heating. Biofluid vibrational spectra are therefore corrected, derived (or not), then normalized. As a general rule, it is also important to include prior to the pre-processing steps, a quality test to remove spectra with a poor signal/noise ratio (threshold to be defined depending on the sample nature) and a validated outlier removal routine before post-processing.

The post-processing step includes data mining and the construction of classifiers. Very often, the spectral differences

between normal and pathological states are very subtle and the next step is to perform data mining, *i.e.*, a process used to extract the salient information from the spectral data. By using specific algorithms, patterns can be found in large batches of data. Thus, such feature selection procedures can help to identify discriminant spectral features to discriminate between patient groups.<sup>67</sup> However, it is important to note that data mining depends on effective data collection, the size of the datasets, and as well as their pre-processing.

To build classification models, several multivariate approaches have been used and as of today there is no general consensus on which method is the best. In other research fields, numerous linear and non-linear supervised algorithms have been evaluated and a combination of methods like SVM and PLS-DA has been shown to enhance the sensitivity and specificity of the classifiers.<sup>107</sup> Generally, building the classifier should include a calibration phase (training phase), an internal validation phase, and an external validation phase (blind testing phase). One of the important issues encountered is the size of the datasets used as a small dataset that does not accurately describe the patient population can lead to under- or over-fitting and impact the classifier outcome. For a classifier to be robust, it is important to have a large number of class-representative patient samples. In addition, the external validation requires a dataset that has not been used in the two previous steps of calibration and internal validation (based upon patient spectra and not replicate spectra from the same patient *i.e.* a spectrum from the same patient should not be in the calibration/internal validation and external validation phases). The leave-one-out cross validation method is often used for these models. It is important to note that all spectra from a given patient must be removed in this process in order to enable a valid outcome. Considering all individual spectra, mean spectra or median spectra as input datasets of the classifier should also be taken into consideration although it has been found that when spectra are highly reproducible and after applying a quality control test plus an appropriate outlier removal, the results are comparable.<sup>64</sup>

The workflow in Fig. 9 illustrates different steps, for both IR and Raman spectroscopies, starting from sample preparation to data pre- and post-processing and the building of classifiers for diagnostics. The issues dealing with pre-processing and post-processing procedures generally used are described in a more detailed manner in a dedicated review elsewhere in this special issue.

## Requirements for clinical implementation

Over the last 20 years, the number of studies dedicated to identification of new biomarkers has increased exponentially, mainly because of the tremendous development of high-throughput molecular technologies and associated bioinformatics. However, among the huge amount of candidate biomarkers, only a limited number have been validated for use in medical practice.<sup>308</sup>

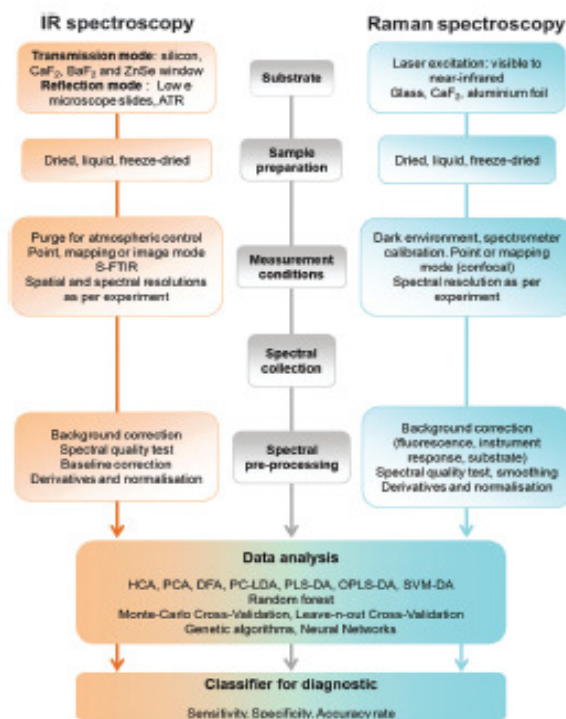


Fig. 9 Workflow of biofluid spectroscopy from substrate choice through sample preparation to spectral measurements and data analysis with diagnostic classifiers.

The origin of this discrepancy has been extensively analyzed in the field of proteomics and genomics. Methodological flaws have been identified in the process of their identification and/or clinical validation and recommendations have been set forth to overcome these inadequacies.<sup>109–113</sup> Studies based on vibrational spectroscopy are subject to the same problems. As for other high throughput technologies, the huge amount of data generated by spectroscopic analysis exposes this analysis to a significant risk of false positive findings. This risk should be minimized by rigorously controlling sample and patient related factors in the exploratory phase and by standardizing the conditions of spectral acquisition, processing and analysis (preanalytic/analytic validity). Subsequently, the findings from pilot studies need to be confirmed in independent large cohort of samples (clinical validity) and finally the benefit of using the biomarker/biosignature in the clinical decision-making setting should be clearly demonstrated as well as its favourable medico-economic profile. Only after this process, a newly discovered biomarker can pretend to reach the routine clinical use.<sup>309–313</sup>

### Preanalytic/analytic validity

In the preanalytic step, attention should be paid to validate sample-related factors and patient-related factors. Standardization of specimen collection and storage is crucial to reach

experimental reproducibility not only in an individual laboratory but also between different laboratories. In addition, investigators should be aware of the risks of contamination during sample handling. In a recent SERS study,<sup>49</sup> EDTA, citrate and Li-Heparin used as anticoagulants for plasma collection have been shown to exhibit confounding peaks. When using filtered plasma (with a 3 kDa cut-off), contrary to EDTA and citrate, Li-Heparin was filtered out and no longer interfered with the spectral information. FTIR studies have shown that EDTA and citrate spectral contributions can be circumvented using dialysed plasma. In contrast, no interference in FTIR spectra was observed when directly analysing plasma from Li-Heparin tubes.<sup>114</sup> Due to these limitations, serum is often preferred to plasma in spectroscopic analysis. Factors related to patients are of paramount importance to limit the risk of false positives. Inappropriate selection of case patients and control subjects is a common pitfall in spectroscopic studies as widely reported in other high throughput technologies.<sup>108,115</sup> When comparison groups are not matched for example for age, sex and physical conditions such as hormonal status or pathologies other than the disease of interest, the results may be biased and differences identified between groups may be linked to these confounding factors rather than to the disease of interest.<sup>109</sup>

Analytic validity includes the technical aspects of the biomarker assessment. In the field of vibrational spectroscopy, the interaction of light with biological molecules is subject to a certain number of drawbacks which should be overcome to meet the criteria of accuracy, reproducibility and robustness.

The most common protocol for spectral analysis of biofluids is the drying of drop deposits. A shortcoming of this method is the heterogeneous drop deposition characterized by the well-known coffee-ring effect, due to the migration of macromolecules towards the periphery of the drop.<sup>116–118</sup> In order to clarify the dynamics of such deposition, Esmonde-White *et al* used both imaging and Raman spectroscopy to demonstrate that substrate and fluid concentration have a profound effect on dried drop morphology. They showed that the substrate did not affect the chemical composition within the outer ring of the drop whereas the macromolecular concentration has an impact on the spatial distribution of proteins.<sup>119</sup> Using HT-FTIR, Lovregne *et al* have recently confirmed the impact of serum dilution on the deposition pattern as illustrated in Fig. 10.<sup>120</sup> Without dilution, serum spectra were saturated, due to the acquisition in the transmission sampling mode. The 3-fold dilution was shown to be the most suitable for spectral analysis with a good reproducibility and absorbance intensity. The signal/noise ratio was degraded with higher fold dilutions which precludes the analysis of molecules present at a low concentration in the serum. The heterogeneous deposition of macromolecules in the outer ring should be taken into account when using mode point spectroscopic assessment. It has been reported that this issue can be overcome by averaging spectra taken at different points of the outer ring.<sup>121</sup> Another possibility to avoid the coffee-ring effect is to perform an analysis on a film composed of an array of reduced-size dry drops each formed from 200 pL of serum.<sup>122</sup> The strict control of experimental

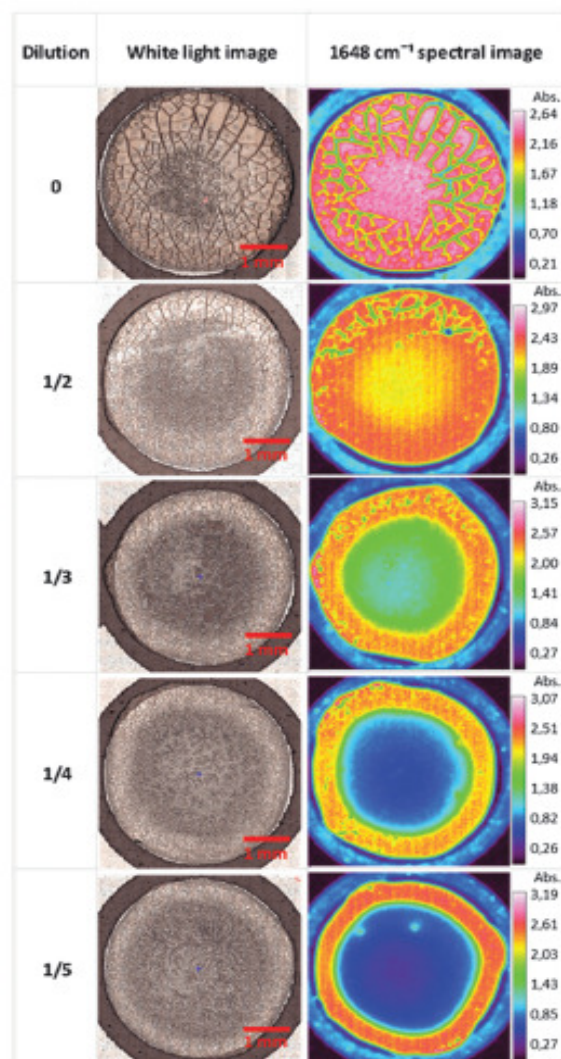


Fig. 10 Analysis of dried serum drops and coffee ring effect with different dilutions: white light images (left) and chemical images constructed on the amide I protein band (right).

parameters of drop deposition appears as a major prerequisite to obtain reproducible results.<sup>119</sup> This may be obtained at best by an automated sampling approach as described by Ollesch *et al*. Using this approach, these authors have reported a higher reproducibility of spectral data compared to a non-automated sampling.<sup>122</sup>

ATR-FTIR spectroscopy has been shown to be an interesting approach for the analysis of biofluids as samples can be directly applied onto the ATR crystal without any dilution. However, currently there is no automated device available so that spectral acquisition is time consuming, about 9 times longer than with automated HT-FTIR spectroscopy.<sup>120</sup> The lack of automation is

## Review Article

a limiting factor for the transposition of ATR-FTIR spectroscopy into a high-throughput clinical application.<sup>123</sup> This may also be possible when using a high throughput source such as a QCL during a DF-IR approach. However, for limited patient cases, in a hand-held mode it offers advantages of ease of use and ease of sample preparation with no modification/adulteration of the sample. Identically, Raman spectroscopy is also of great interest for biofluid spectroscopy particularly due to developments in hand held technology and immersion Raman which could enable hand held analysis of 'wet' serum, negating the need for a drying step.

The technical standardization of spectral acquisition makes sense if reproducible results can be obtained in different laboratories. This external validation is essential on the way towards clinical validity. The inter-instrument transferability is also a challenge that needs to be faced. Finally, the need for automated instruments underline the necessity of a close collaboration between research scientists, clinical practitioners and industrial partners in order to optimize currently available products according to a specific biomedical purpose.<sup>1</sup>

Beside the need of standardized spectral acquisition, there is also a need to validate the design of pilot studies including the chemometric analysis. Proof-of-concept studies raise the question of appropriate selection of case patients and controls as discussed below and also the question of sample size. In contrast with classical statistics, there is no simple method to calculate sample size in biospectroscopic studies. However, Beleites *et al.* have proposed in a recent report to use learning curves to determine the appropriate sample size needed to build good classifiers with specified performances.<sup>124</sup> When the number of patients is too limited to divide the population in one training set and one independent validation set, cross validation methods should be used to avoid the high risk of overfitting.<sup>125</sup>

#### Clinical validity

The next step after the phase of pre-analytic/analytic validation is to confirm the diagnostic performance of the biomarker on an independent population of a large number of patients. This means large multicenter randomized control trials where the sensitivity and the specificity of the putative biomarker may be evaluated against the gold standard diagnostic/screening procedure. These studies, particularly the criteria to include case patients and controls, should be carefully designed to demonstrate whether the biomarker is applicable to its specific purpose which may be screening, differential diagnosis, prognosis, treatment response prediction or monitoring of a disease (Fig. 4).

A common mistake is to validate a marker in the diagnostic setting of a disease and then to extrapolate its performance to the screening context. Candidate biomarkers are tested in pilot studies performed in small numbers of patients with patent disease already diagnosed using golden standard methods. It is crucial to validate the value of these markers in the screening context *i.e.* for early diagnosis in large populations of patients at risk of the disease. The biomarker sensitivity and specificity

in the screening target population are usually much lower than in patients with patent disease. In the context of population screening, high specificity is of paramount importance to avoid false positive results, which means patients will be subject to additional diagnostic procedures, potentially invasive and costly for the society. This underlines the necessity of selecting case patients and control subjects according to the clinical setting where the biomarker is intended to be used.<sup>109</sup>

A methodology to avoid patient selection bias in screening studies has been proposed by Pepe *et al.*<sup>109,111,126</sup> In the so-called PROBE study design, samples are collected prospectively in a cohort of patients before the knowledge of the final diagnosis. Once the outcome data becomes available and the diagnosis established, the sample cohort can be used retrospectively by randomly selecting cases and controls. This methodology is promoted by the research consortium "Early Detection Research Network" from the National Cancer Institute to establish specimen reference sets. It has proved efficient for rapid evaluation of potential biomarkers.<sup>110</sup>

#### Clinical utility

A crucial point in the process of biomarker validation before its adoption in routine clinical practice is to demonstrate its clinical decision-making usefulness at an acceptable cost for the society.<sup>109</sup> This means that the positive and negative predictive values of the biomarker should be evaluated in the "real life" patient population since these indicators are dependent on the prevalence of the disease of interest. The difference between clinical validity and clinical utility is illustrated by the debate about the usefulness of Prostatic Specific Antigen (PSA)-based screening program. It is well established that PSA-based screening programs significantly increase the detection of prostate cancer at an early stage.<sup>127</sup> However, there is also evidence that PSA-based screening carries a high risk of over-diagnosis leading to overtreatment in a significant number of men with early cancer that will never become symptomatic during their life time.<sup>128</sup> Whether the benefits of early detection of asymptomatic prostate cancer outweigh the harms related to over-diagnosis and overtreatment is highly controversial. There is no consensus regarding the clinical relevance of a PSA-based screening program.<sup>129</sup> This emphasizes that, in addition to its diagnostic performance, the biomarker clinical utility has to be demonstrated before its clinical implementation. The clinical utility refers to the balance of benefits to harms and the medicoeconomic evaluation. For this purpose, a validation study should be performed in a large number of unselected patients with clinical endpoints clearly defined to demonstrate the benefit of using a biomarker including quality of life for the patient and socioeconomic aspects for the society.<sup>109</sup>

## Conclusion

The difficulty in translating biomedical spectroscopy to the clinic is fundamentally based on the fact that after over more than two decades of research, not enough has been done to

fully understand the accuracy of these tests with appropriate considerations applied to control groups and limitations of the clinical environment. In addition there is a need to perform large-scale studies to evaluate the spectroscopic tests' efficacy within the clinic. These approaches would enable this technology to be acceptable to the medical community through a "hearts and minds" approach. The particular requirements of a clinical spectrometer should be implemented for different clinical settings. Its instrumental requirements (e.g. detector sensitivity and source throughput) and how accurately it can diagnose disease or perform treatment monitoring must be validated.

This review has highlighted the potential of biomedical vibrational spectroscopy to analyse biofluids. However, care should be taken for biofluid spectroscopy not to suffer from the identified pitfalls. As the field of biofluid spectroscopy is further researched, a lot of commitment from different stakeholders (researchers, clinicians, and instrument manufacturers) will be necessary to demonstrate its real potential as a rapid, novel, and robust technology to pinpoint "spectral biomarkers/signatures" that can be useful for diagnostic purposes and to predict clinical outcomes, with the promise that the test can be done periodically at low cost for monitoring care.

The initiatives via current networks like the EPSRC CLIRSPEC (<http://clirspec.org/>), the Raman4Clinics European COST action (<http://www.raman4clinics.eu/raman4clinics-a-european-cost-action/>) and the 1<sup>st</sup> International Society for Clinical Spectroscopy (CLIRSPEC) are currently gearing research, facilities and communities in the clinical spectroscopy arena to achieve these objectives.

## Acknowledgements

MJB acknowledges EPSRC, AHRC, Royal Society, Rosemere Cancer Foundation, Brain Tumour North West, and Sydney Driscoll Neuroscience Foundation. The Defence and Science Technology Laboratory (Dstl, UK), the Direction Générale de l'Armement (DGA, France), and the Champagne-Ardenne Regional Council are acknowledged for research funding and the URCA PICT Technological Platform for technical support.

## References

- H. J. Byrne, M. Baranska, G. J. Puppels, N. Stone, B. Wood, K. M. Gough, P. Lasch, P. Heraud, J. Sulé-Suso and G. D. Sockalingum, *Analyst*, 2015, **140**, 2066–2073.
- M. Diem, P. R. Griffiths and J. M. Chalmers, *Vibrational spectroscopy for medical diagnosis*, Wiley, Chichester, 2008.
- M. Diem, M. Romeo, S. Boydston-White, M. Miljković and C. Matthäus, *Analyst*, 2004, **129**, 880–885.
- M. J. Baker, J. Trevisan, P. Bassan, R. Bhargava, H. J. Butler, K. M. Dorling, P. R. Fielden, S. W. Fogarty, N. J. Fullwood and K. A. Heys, *Nat. Protoc.*, 2014, **9**, 1771–1791.
- J. Nallala, M.-D. Diebold, C. Gobinet, O. Bouché, G. D. Sockalingum, O. Piot and M. Manfait, *Analyst*, 2014, **139**, 4005–4015.
- K. Papamarkakis, B. Bird, J. M. Schubert, M. Miljković, R. Wein, K. Bedrossian, N. Laver and M. Diem, *Lab. Invest.*, 2010, **90**, 589–598.
- C. Kendall, N. Stone, N. Shepherd, K. Geboes, B. Warren, R. Bennett and H. Barr, *J. Pathol.*, 2003, **200**, 602–609.
- P. Lasch, M. Beekes, J. Schmitt and D. Naumann, *Anal. Bioanal. Chem.*, 2007, **387**, 1791–1800.
- P. Lasch, J. Schmitt, M. Beekes, T. Udelhoven, M. Eiden, H. Fabian, W. Petrich and D. Naumann, *Anal. Chem.*, 2003, **75**, 6673–6678.
- J. Schmitt, M. Beekes, A. Brauer, T. Udelhoven, P. Lasch and D. Naumann, *Anal. Chem.*, 2002, **74**, 3865–3868.
- E. F. Petricoin, C. Belluco, R. P. Araujo and L. A. Liotta, *Nat. Rev. Cancer*, 2006, **6**, 961–967.
- C. Pierrakos and J.-L. Vincent, *Crit. Care*, 2010, **14**, R15.
- D. Qi and A. J. Berger, *Appl. Opt.*, 2007, **46**, 1726–1734.
- J. M. Reyes-Goddard, H. Barr and N. Stone, *Photodiagn. Photodyn. Ther.*, 2005, **2**, 223–233.
- D. Rohleder, W. Kiefer and W. Petrich, *Analyst*, 2004, **129**, 906–911.
- R. A. Shaw, S. Low-Ying, A. Man, K.-Z. Liu, C. Mansfield, C. B. Rileg and M. Vijarnsom, *Biomedical Vibrational Spectroscopy*, John Wiley and Sons, Inc, Hoboken, NJ, 2008, pp. 79–103.
- C. N. Banwell and E. M. McCash, *Fundamentals of molecular spectroscopy*, McGraw-Hill, London, 1983.
- P. Dumas, G. D. Sockalingum and J. Sule-Suso, *Trends Biotechnol.*, 2007, **25**, 40–44.
- A. Barth and P. I. Harris, *Biological and biomedical infrared spectroscopy*, IOS press, 2009.
- D. Long, *J. Raman Spectrosc.*, 2008, **39**, 316–321.
- G. Poste, *Nature*, 2011, **469**, 156–157.
- K. Ataka, T. Kottke and J. Heberle, *Angew. Chem., Int. Ed.*, 2010, **49**, 5416–5424.
- D. I. Ellis and R. Goodacre, *Analyst*, 2006, **131**, 875–885.
- C. Kendall, M. Isabelle, F. Bazant-Hegemark, J. Hutchings, L. Orr, J. Babrah, R. Baker and N. Stone, *Analyst*, 2009, **134**, 1029–1045.
- S. G. Kazarian and K. Chan, *Appl. Spectrosc.*, 2010, **64**, 135A–152A.
- P. Bassan, A. Sachdeva, J. Lee and P. Gardner, *Analyst*, 2013, **138**, 4139–4146.
- J. Filik, M. D. Frogley, J. K. Pijanka, K. Wehbe and G. Cinque, *Analyst*, 2012, **137**, 853–861.
- J. Cao, E. S. Ng, D. McNaughton, E. G. Stanley, A. G. Elefanty, M. J. Tobin and P. Heraud, *Analyst*, 2013, **138**, 4147–4160.
- B. Schrader, *Infrared and Raman spectroscopy: methods and applications*, John Wiley & Sons, 2008.
- L. Novotny and N. Van Hulst, *Nat. Photonics*, 2011, **5**, 83–90.
- M. Osawa, K.-I. Ataka, K. Yoshii and Y. Nishikawa, *Appl. Spectrosc.*, 1993, **47**, 1497–1502.
- M. Moskovits, *Rev. Mod. Phys.*, 1985, **57**, 783.
- R. Adato and H. Altug, *Nat. Commun.*, 2013, **4**, 2154.

- 34 G. Clemens, B. Bird, M. Weida, J. Rowletteb and M. J. Bakera, *Spectrosc. Eur.*, 2014, **26**, 14–19.
- 35 K. Yeh, S. Kenkel, J.-N. Liu and R. Bhargava, *Anal. Chem.*, 2014, **87**, 485–493.
- 36 A. Hasenkampf, N. Kröger, A. Schönhals, W. Petrich and A. Pucci, *Opt. Express*, 2015, **23**, 5670–5680.
- 37 F. S. Parker, in *Applications of infrared, Raman, and resonance Raman spectroscopy in biochemistry*, ed. F. S. Parker, Springer, New York, 1983, pp. 315–347.
- 38 F. Draux, P. Jeannesson, A. Beljebbar, A. Tfayli, N. Foure, M. Manfait, J. Sulé-Suso and G. D. Sockalingum, *Analyst*, 2009, **134**, 542–548.
- 39 I. Notingher and L. L. Hench, *Expert Rev. Med. Devices*, 2006, **3**, 215–234.
- 40 T. Bakker Schut, M. Wijes, H. Sterenborg, O. Speelman, J. Roodenburg, E. Marple, H. Bruining and G. Puppels, *Anal. Chem.*, 2000, **72**, 6010–6018.
- 41 C. Fulljames, N. Stone, D. Bennett and H. Barr, *Ital. J. Gastroenterol. Hepatol.*, 1999, **31**, 695–704.
- 42 A. Mahadevan-Jansen, M. F. Mitchell, N. Ramanujam, U. Utzinger, U. Utzinger and R. Richards-Kortum, *Photochem. Photobiol.*, 1998, **68**, 427–431.
- 43 M. G. Shim, L. M. Wong Kee Song, N. E. Marcon and B. C. Wilson, *Photochem. Photobiol.*, 2000, **72**, 146–150.
- 44 F. Bonnier, S. M. Ali, P. Knief, H. Lambkin, K. Flynn, V. McDonagh, C. Healy, T. Lee, F. M. Lyng and H. J. Byrne, *Vib. Spectrosc.*, 2012, **61**, 124–132.
- 45 H. Barr, C. Kendall, J. Hutchings, F. Bazant-Hegemark, N. Shepherd and N. Stone, *Surgeon*, 2011, **9**, 119–123.
- 46 J. N. Anker, W. P. Hall, O. Lyandres, N. C. Shah, J. Zhao and R. P. Van Duyne, *Nat. Mater.*, 2008, **7**, 442–453.
- 47 D. Graham and R. Goodacre, *Chem. Soc. Rev.*, 2008, **37**, 883–884.
- 48 K. Kneipp, Y. Wang, H. Kneipp, L. T. Perelman, I. Itzkan, R. R. Dasari and M. S. Feld, *Phys. Rev. Lett.*, 1997, **78**, 1667.
- 49 A. Bonifacio, S. Dalla Marta, R. Spizzo, S. Cervo, A. Steffan, A. Colombatti and V. Sergo, *Anal. Bioanal. Chem.*, 2014, **406**, 2355–2365.
- 50 C. Krafft and J. Popp, *Anal. Bioanal. Chem.*, 2015, **407**, 699–717.
- 51 I. W. Schie, C. Krafft and J. Popp, *Analyst*, 2015, **140**, 3897–3909.
- 52 M. Winterhalder and A. Zumbusch, *Adv. Drug Delivery Rev.*, 2015, **89**, 135–144.
- 53 A. S. Haka, Z. Volynskaya, J. A. Gardecki, J. Nazemi, J. Lyons, D. Hicks, M. Fitzmaurice, R. R. Dasari, J. P. Crowe and M. S. Feld, *Cancer Res.*, 2006, **66**, 3317–3322.
- 54 N. Stone and P. Matousek, *Cancer Res.*, 2008, **68**, 4424–4430.
- 55 M. Z. Vardaki, B. Gardner, N. Stone and P. Matousek, *Analyst*, 2015, **140**, 5112–5119.
- 56 M. D. Keller, E. Vargis, N. de Matos Granja, R. H. Wilson, M.-A. Mycek, M. C. Kelley and A. Mahadevan-Jansen, *J. Biomed. Opt.*, 2011, **16**, 077006.
- 57 P. Matousek and N. Stone, *J. Biophotonics*, 2013, **6**, 7–19.
- 58 B. Sharma, K. Ma, M. R. Glucksberg and R. P. Van Duyne, *J. Am. Chem. Soc.*, 2013, **135**, 17290–17293.
- 59 N. Stone, R. Baker, K. Rogers, A. W. Parker and P. Matousek, *Analyst*, 2007, **132**, 899–905.
- 60 M. J. Baker, *Special Issue: Photonic Biofluid Diagnostics*, Wiley-VCH Verlag GmbH & Co, Weinheim, 2014.
- 61 W. Colbum, V. G. DeGruttola, D. L. DeMets, G. J. Downing, D. F. Hoth, J. A. Oates, C. C. Peck, R. T. Schooley, B. A. Spilker and J. Woodcock, *Clin. Pharmacol. Ther.*, 2001, **69**, 89–95.
- 62 R. A. Lukaszewski, A. M. Yates, M. C. Jackson, K. Swingler, J. M. Scherer, A. Simpson, P. Sadler, P. McQuillan, R. W. Titball and T. J. Brooks, *Clin. Vaccine Immunol.*, 2008, **15**, 1089–1094.
- 63 R. S. Tirumalai, K. C. Chan, D. A. Prieto, H. J. Issaq, T. P. Conrads and T. D. Veenstra, *Mol. Cell. Proteomics*, 2003, **2**, 1096–1103.
- 64 V. Untereiner, G. Dhruvananda Sockalingum, R. Gamotel, C. Gobinet, F. Ramaholimihaso, F. Ehrhard, M. D. Diebold and G. Thiéfin, *J. Biophotonics*, 2014, **7**, 241–253.
- 65 J. Ollesch, M. Heinze, H. M. Heise, T. Behrens, T. Brüning and K. Gerwert, *J. Biophotonics*, 2014, **7**, 210–221.
- 66 J. Backhaus, R. Mueller, N. Formanski, N. Szlama, H.-G. Meerpohl, M. Eidt and P. Bugert, *Vib. Spectrosc.*, 2010, **52**, 173–177.
- 67 X. Zhang, G. Thiéfin, C. Gobinet, V. Untereiner, I. Taleb, B. Bernard-Chabert, A. Heurgué, C. Truntzer, P. Ducoroy and P. Hillon, *Transl. Res.*, 2013, **162**, 279–286.
- 68 E. Scaglia, G. D. Sockalingum, J. Schmitt, C. Gobinet, N. Schneider, M. Manfait and G. Thiéfin, *Anal. Bioanal. Chem.*, 2011, **401**, 2919–2925.
- 69 G. L. Owens, K. Gajjar, J. Trevisan, S. W. Fogarty, S. E. Taylor, D. Gama-Rose, P. L. Martin-Hirsch and F. L. Martin, *J. Biophotonics*, 2014, **7**, 200–209.
- 70 K. Gajjar, L. D. Heppenstall, W. Pang, K. M. Ashton, J. Trevisan, I. I. Patel, V. Llabjani, H. F. Stringfellow, P. L. Martin-Hirsch and T. Dawson, *Anal. Methods*, 2013, **5**, 89–102.
- 71 J. R. Hands, P. Abel, K. Ashton, T. Dawson, C. Davis, R. W. Lea, A. J. McIntosh and M. J. Baker, *Anal. Bioanal. Chem.*, 2013, **405**, 7347–7355.
- 72 J. R. Hands, K. M. Dorling, P. Abel, K. M. Ashton, A. Brodbelt, C. Davis, T. Dawson, M. D. Jenkinson, R. W. Lea and C. Walker, *J. Biophotonics*, 2014, **7**, 189–199.
- 73 A. Sahu, S. Sawant, H. Mamgain and C. M. Krishna, *Analyst*, 2013, **138**, 4161–4174.
- 74 A. Sahu, N. Nandakumar, S. Sawant and C. M. Krishna, *Analyst*, 2015, **140**, 2294–2301.
- 75 J. Pichardo-Molina, C. Frausto-Reyes, O. Barbosa-García, R. Huerta-Franco, J. González-Trujillo, C. Ramírez-Alvarado, G. Gutiérrez-Juárez and C. Medina-Gutiérrez, *Lasers Med. Sci.*, 2007, **22**, 229–236.
- 76 X. Li, T. Yang and S. Li, *Appl. Opt.*, 2012, **51**, 5038–5043.
- 77 J. L. González-Solís, J. C. Martínez-Espinosa, L. A. Torres-González, A. Aguilar-Lemarroy, L. F. Jave-Suárez and P. Palomares-Anda, *Lasers Med. Sci.*, 2014, **29**, 979–985.

- 78 I. Taleb, G. Thiéfin, C. Gobinet, V. Untereiner, B. Bernard-Chabert, A. Heurgué, C. Truntzer, P. Hillon, M. Manfait and P. Ducoroy, *Analyst*, 2013, **138**, 4006–4014.
- 79 S. Feng, R. Chen, J. Lin, J. Pan, G. Chen, Y. Li, M. Cheng, Z. Huang, J. Chen and H. Zeng, *Biosens. Bioelectron.*, 2010, **25**, 2414–2419.
- 80 S. Li, Y. Zhang, Q. Zeng, L. Li, Z. Guo, Z. Liu, H. Xiong and S. Liu, *Laser Phys. Lett.*, 2014, **11**, 065603.
- 81 D. Lin, J. Pan, H. Huang, G. Chen, S. Qiu, H. Shi, W. Chen, Y. Yu, S. Feng and R. Chen, *Sci. Rep.*, 2014, **4**, 475.
- 82 S. Feng, R. Chen, J. Lin, J. Pan, Y. Wu, Y. Li, J. Chen and H. Zeng, *Biosens. Bioelectron.*, 2011, **26**, 3167–3174.
- 83 H. Ito, H. Inoue, K. Hasegawa, Y. Hasegawa, T. Shimizu, S. Kimura, M. Onimaru, H. Ikeda and S.-E. Kudo, *Nanomedicine: Nanotechnol. Biol. Med.*, 2014, **10**, 599–608.
- 84 D. Lin, S. Feng, J. Pan, Y. Chen, J. Lin, G. Chen, S. Xie, H. Zeng and R. Chen, *Opt. Express*, 2011, **19**, 13565–13577.
- 85 S. Li, Y. Zhang, J. Xu, L. Li, Q. Zeng, L. Lin, Z. Guo, Z. Liu, H. Xiong and S. Liu, *Appl. Phys. Lett.*, 2014, **105**, 091104.
- 86 E. Ryzhikova, O. Kazakov, L. Halamkova, D. Celmins, P. Malone, E. Molho, E. A. Zimmerman and I. K. Lednev, *J. Biophotonics*, 2015, **8**, 584–596.
- 87 P. Carmona, M. Molina, M. Calero, F. Bermejo-Pareja, P. Martínez-Martín and A. Toledano, *J. Alzheimers Dis.*, 2013, **34**, 911–920.
- 88 E. Peuchant, S. Richard-Harston, I. Bourdel-Marchasson, J.-F. Dartigues, L. Letenneur, P. Barberger-Gateau, S. Arnaud-Dabernat and J.-Y. Daniel, *Transl. Res.*, 2008, **152**, 103–112.
- 89 C. Lacombe, V. Untereiner, C. Gobinet, M. Zater, G. D. Sockalingum and R. Gamotel, *Analyst*, 2015, **140**, 2280–2286.
- 90 W. Petrich, K. Lewandrowski, J. Muhlestein, M. Hammond, J. Januzzi, E. Lewandrowski, R. Pearson, B. Dolenko, J. Früh and M. Haass, *Analyst*, 2009, **134**, 1092–1098.
- 91 U. Neugebauer, S. Trenkmann, T. Bockditz, D. Schmerker, M. Kiehntopf and J. Popp, *J. Biophotonics*, 2014, **7**, 232–240.
- 92 N. L. Garrett, R. Sekine, M. W. Dixon, L. Tilley, K. R. Bamberg and B. R. Wood, *Phys. Chem. Chem. Phys.*, 2015, **17**, 21164–21168.
- 93 R. Somorjai, B. Dolenko, A. Nikulin, P. Nickerson, D. Rush, A. Shaw, M. Glogowski, J. Rendell and R. Deslauriers, *Vib. Spectrosc.*, 2002, **28**, 97–102.
- 94 J. A. M. Bispo, E. E. de Sousa Vieira, L. Silveira and A. B. Fernandes, *J. Biomed. Opt.*, 2013, **18**, 087004.
- 95 G. Del Mistro, S. Cervo, E. Mansutti, R. Spizzo, A. Colombatti, P. Belmonte, R. Zucconelli, A. Steffan, V. Sergio and A. Bonifacio, *Anal. Bioanal. Chem.*, 2015, **407**, 3271–3275.
- 96 D. A. Scott, D. E. Renaud, S. Krishnasamy, P. Merić, N. Buduneli, Ş. Çetinkalp and K.-Z. Liu, *Diabetol. Metab. Syndr.*, 2010, **2**, 48.
- 97 X. Li, T. Yang and J. Lin, *J. Biomed. Opt.*, 2012, **17**, 0370031.
- 98 W. Yan, H. Lin, L. Jinghua, Q. Dian, C. Anyu, J. Yi, G. Xun, L. Chunwei, H. Wen and W. Hong, *IEEE*, 2009, 885–887.
- 99 S. Whiteman, Y. Yang, J. Jones and M. Spiteri, *Ther. Adv. Respir. Dis.*, 2008, **2**, 23–31.
- 100 A. Travo, C. Paya, G. Déléris, J. Colin, B. Mortemousque and I. Forfar, *Anal. Bioanal. Chem.*, 2014, **406**, 2367–2376.
- 101 S. Choi, S. W. Moon, J.-H. Shin, H.-K. Park and K.-H. Jin, *Anal. Chem.*, 2014, **86**, 11093–11099.
- 102 H. Bysel, M. Jackson, A. Nikulin, R. Somorjai, G. Thomson and H. Mantsch, *Biospectroscopy*, 1997, **3**, 161–167.
- 103 K. A. Esmonde-White, G. S. Mandair, F. Raaij, J. A. Jacobson, B. S. Miller, A. G. Urquhart, B. J. Roessler and M. D. Morris, *J. Biomed. Opt.*, 2009, **14**, 034013.
- 104 K.-Z. Liu, T. C. Dembinski and H. H. Mantsch, *Am. J. Obstet. Gynecol.*, 1998, **178**, 234–241.
- 105 G. Graça, A. S. Moreira, A. J. V. Correia, B. J. Goodfellow, A. S. Barros, I. F. Duarte, I. M. Carreira, E. Galhano, C. Pita and M. do Céu Almeida, *Anal. Chim. Acta*, 2013, **764**, 24–31.
- 106 M. Griebel, M. Daffertshofer, M. Stroick, M. Syren, P. Ahmad-Nejad, M. Neumaier, J. Backhaus, M. G. Hennerici and M. Fatar, *Neurosci. Lett.*, 2007, **420**, 29–33.
- 107 V. Gaydou, A. Lecellier, D. Toubas, J. Mounier, L. Castrec, G. Barbier, W. Ablain, M. Manfait and G. Sockalingum, *Anal. Methods*, 2015, **7**, 766–778.
- 108 E. P. Diamandis, *J. Natl. Cancer Inst.*, 2010, **102**, 1462–1467.
- 109 M. J. Duffy, C. M. Sturgeon, G. Sölétormos, V. Barak, R. Molina, D. F. Hayes, E. P. Diamandis and P. M. Bossuyt, *Clin. Chem.*, 2015, **61**, 809–820.
- 110 Z. Feng, J. Kagan, M. Pepe, M. Thomquist, J. A. Rinaudo, J. Dahlgren, K. Krueger, Y. Zheng, C. Patriotis and Y. Huang, *Clin. Chem.*, 2013, **59**, 68–74.
- 111 M. S. Pepe, R. Etzioni, Z. Feng, J. D. Potter, M. L. Thompson, M. Thornquist, M. Winget and Y. Yasui, *J. Natl. Cancer Inst.*, 2001, **93**, 1054–1061.
- 112 N. L. Henry and D. F. Hayes, *Mol. Oncol.*, 2012, **6**, 140–146.
- 113 S. M. Teutsch, L. A. Bradley, G. E. Palomaki, J. E. Haddow, M. Piper, N. Calonge, W. D. Dotson, M. P. Douglas and A. O. Berg, *Genet. Med.*, 2009, **11**, 3–14.
- 114 C. Lacombe, PhD thesis, University of Reims Champagne-Ardenne, France, 2013.
- 115 P. Yin, R. Lehmann and G. Xu, *Anal. Bioanal. Chem.*, 2015, 1–14.
- 116 R. D. Deegan, O. Bakajin, T. F. Dupont, G. Huber, S. R. Nagel and T. A. Witten, *Nature*, 1997, **389**, 827–829.
- 117 W. Ristenpart, P. Kim, C. Domingues, J. Wan and H. Stone, *Phys. Rev. Lett.*, 2007, **99**, 234502.
- 118 P. J. Yunker, T. Still, M. A. Lohr and A. Yodh, *Nature*, 2011, **476**, 308–311.
- 119 K. A. Esmonde-White, F. W. Esmonde-White, M. D. Morris and B. J. Roessler, *Analyst*, 2014, **139**, 2734–2741.
- 120 L. Lovergne, G. Clemens, V. Untereiner, R. A. Lukaszewski, G. D. Sockalingum and M. J. Baker, *Anal. Methods*, 2015, **7**, 7140–7149.
- 121 J. Filik and N. Stone, *Analyst*, 2007, **132**, 544–550.
- 122 J. Ollesch, S. L. Drees, H. M. Heise, T. Behrens, T. Brüning and K. Gerwert, *Analyst*, 2013, **138**, 4092–4102.

## Review Article

- 123 C. Hughes, M. Brown, G. Clemens, A. Henderson, G. Monjardez, N. W. Clarke and P. Gardner, *J. Biophotonics*, 2014, **7**, 180–188.
- 124 C. Bekeites, U. Neugebauer, T. Bocklitz, C. Krafft and J. Popp, *Anal. Chim. Acta*, 2013, **760**, 25–33.
- 125 D. Pérez-Guaita, J. Kuligowski, S. Garrigues, G. Quintás and B. R. Wood, *Analyst*, 2014, **140**, 2422.
- 126 M. S. Pepe, Z. Feng, H. Janes, P. M. Bossuyt and J. D. Potter, *J. Natl. Cancer Inst.*, 2008, **100**, 1432–1438.
- 127 F. H. Schröder, J. Hugosson, M. J. Roobol, T. L. Tammela, S. Ciatto, V. Nelen, M. Kwiatkowski, M. Lujan, H. Lilja and M. Zappa, *N. Engl. J. Med.*, 2009, **360**, 1320–1328.
- 128 V. A. Moyer, *Ann. Intern. Med.*, 2012, **157**, 120–134.
- 129 J. Cuzick, M. A. Thorat, G. Andriole, O. W. Brawley, P. H. Brown, Z. Culig, R. A. Eeles, L. G. Ford, F. C. Hardy and L. Holmberg, *Lancet Oncol.*, 2014, **15**, e484–e492.